Spatial Sound Field Modeling and Noise Cancellation for Drones

Hanwen Bi

Master of Engineering, The Australian National University

A thesis submitted for the degree of

Doctor of Philosophy

The Australian National University

School of Engineering

June 2025

To family, friends, and the wonderful universe we are intimately connected with

Declaration

The contents of this thesis are the results of original research and have not been submitted for a higher degree to any other university or institution. Much of this work has either been published or submitted for publication as journal papers and conference proceedings. Following is a list of these papers.

Journal Publications

- **H. Bi**, S. Xu, F. Ma, T. D. Abhayapala, and P. N. Samarasinghe, "Limitations and performance analysis of spherical sector harmonics for sound field processing," *Applied Sciences*, vol. 14, no. 22, p. 10633, Nov. 2024. [Online]. Available: `https://doi.org/10.3390/app142210633`
- **H. Bi** and T. D. Abhayapala, "Point neuron learning: a new physics-informed neural network architecture," *EURASIP Journal on Audio, Speech, and Music Processing*, vol. 2024, no. 56, Dec. 2024. [Online]. Available: `https://doi.org/10.1186/s13636-024-00376-0`
- **H. Bi**, Y. Zhang, T. D. Abhayapala, and P. N. Samarasinghe, "Directional Active Noise Control for Drone Noise," *JASA Express Lett*, 1 December 2025; 5 (12): 124801. [Online]. Available: `https://doi.org/10.1121/10.0039953`

Conference Proceedings

- **H. Bi**, F. Ma, T. D. Abhayapala, and P. N. Samarasinghe, "Spherical sector harmonics based soundfield radial extrapolation and robustness analysis," in *IEEE International Conference on Acoustics, Speech and Signal Processing (ICASSP)*, Rhodes Island, Greece, Jun. 4–10, 2023, pp. 1–5. doi: `https://doi.org/10.1109/ICASSP49357.2023.1009541`
- **H. Bi**, F. Ma, T. D. Abhayapala, and P. N. Samarasinghe, "Spherical sector harmonics based directional drone noise reduction," in *International Workshop on Acoustic Signal Enhancement (IWAENC)*, Bamberg, Germany, Sep. 2022, pp. 1–5. doi: `10.1109/IWAENC53105.2022.9914790`
- **H. Bi**, F. Ma, T. D. Abhayapala, and P. N. Samarasinghe, "Spherical array based drone noise measurements and modelling for drone noise reduction via propeller phase control," in *IEEE Workshop on Applications of Signal Processing to Audio and Acoustics (WASPAA)*, New Paltz, NY, USA, Oct. 17–20, 2021, pp. 286–290. doi: `https://doi.org/10.1109/WASPAA52581.2021.9632719`

The following works are also completed during my Ph.D. study, but not included in this thesis:

- X. Chen, **H. Bi**, W.-T. Lai, and F. Ma, "Monaural speech enhancement on drone via adapter based transfer learning," in *International Workshop on Acoustic Signal Enhancement (IWAENC)*, Aalborg, Denmark, Sept. 9–12, 2024, pp. 85–89. doi: `https://doi.org/10.1109/IWAENC61483.2024.10694014`

The research work presented in this thesis has been performed jointly with Prof. Thushara D. Abhayapala, Assoc. Prof. Prasanga N. Samarasinghe, Dr. Fei Ma, Shaoheng Xu, and Yile Zhang. Approximately 75% of this work is my own.

Hanwen Bi
School of Engineering
The Australian National University
Canberra ACT 2601
June 2025

Acknowledgements

Without the support of a number of individuals and organisations, this work would not have been completed. I would like to acknowledge and thank each of the following:

- First and foremost, my supervisor, Prof. Thushara Abhayapala, for his support, patience, and invaluable guidance throughout this research journey. His mentorship has shaped me into an independent researcher and provided countless opportunities for learning and growth. I am also deeply grateful to my co-supervisors, Assoc. Prof. Prasanga Samarasinghe and Dr. Fei Ma, for their insightful feedback, constructive guidance, and continuous encouragement over the years.
- The Australian National University and ARC DP grant for providing scholarships. I would also like to thank the School of Engineering for providing the facilities and resources that fostered a productive research environment.
- My industry mentor, Dr. Yi Ren at SONY, Japan, for welcoming me to the audio group during my internship and for his collaboration and support on aspects of this work.
- Dr. Jihui (Aimee) Zhang, for her expert guidance and generous support during my teaching experience in ENGN4213/6213 Digital Systems and Microprocessors. I also thank Dr. Huiyuan (June) Sun for supervising my Master's research project.
- My colleagues in the Audio and Acoustic Signal Processing group, for fostering a collaborative and stimulating research environment. Special thanks to Shaoheng Xu, Wei-Ting Lai, Angela Zhang, Huawei Zhang, and Frank Wang for the engaging research discussions and our time playing basketball together, and to Xiaoli Tang for the true friendship.
- My family and friends, for their constant love, motivation, and belief in me.
- Finally, to my wife Tianshu Yang, for being by my side through all the challenges of this Ph.D. journey. Thank you for your unwavering support and love.

Abstract

This thesis advances the modeling and reduction of drone noise through the use of on-board microphones and directional active noise control (ANC) systems. In recent years, small-scale unmanned aerial vehicles (UAVs), commonly known as drones, have become increasingly prevalent across a wide array of applications, including parcel delivery, mapping, and emergency response. Despite their growing utility, drone operations contribute significantly to environmental noise pollution, posing risks to both daily comfort and public health. Consequently, the development of effective drone noise mitigation techniques has become a pressing concern.

To address this challenge, the thesis first introduces novel methods for drone noise modeling based solely on on-board microphone measurements. These methods generalize the drone noise modeling task as a sound field extrapolation problem. A sound field extrapolation framework based on spherical sector harmonics is proposed, and a comprehensive theoretical analysis is conducted to support its application to sectorial sound field reconstruction. Furthermore, the method is enhanced through the derivation of an explicit mapping between spherical and spherical sector harmonics, improving both accuracy and flexibility.

To overcome geometric limitations in microphone placement, we further develop a physics-informed neural network (PINN) architecture called the point neuron network. This model embeds the fundamental solution of the wave equation into its structure, ensuring physical consistency. The network handles complex-valued signals directly, improves interpretability, and generalizes effectively across various acoustic conditions. Unlike existing approaches, it does not rely on pre-collected datasets and remains robust to sensor noise and irregular sensor configurations.

Building upon the proposed modeling approaches, we develop two directional drone ANC systems that target noise propagation in specific far-field regions. The first system is based on the spherical sector harmonics extrapolation framework and incorporates constraints on payload and power consumption. We analyze the secondary-to-primary source power ratio for different secondary source configurations by simulations. Additionally, we enhance the ANC algorithm to relax the geometric requirements of the monitoring microphone array and validate the system's performance through hardware experiments.

Complementing these systems, we introduce a propeller phase control method aimed at reducing tonal drone noise in the downward far-field region. By adjusting the relative phase of multiple propellers, this technique achieves destructive interference in targeted directions, thereby reducing noise radiation without additional hard-

ware.

Overall, the contributions presented in this thesis constitute a comprehensive framework for drone noise modeling and directional noise reduction, offering physically grounded, practically feasible, and experimentally validated solutions to a critical problem in drone operations. Furthermore, the point-neuron learning framework and the spherical sector harmonic-based extrapolation method presented in this thesis are applicable to a broad range of sound field-related problems, including sound field reproduction, interpolation, and extrapolation.

Abbreviations and Acronyms

ANC	Active Noise Control
UAVs	Unmanned Aerial Vehicles
PINN	Physics-informed Neural Network
CFD	Computational Fluid Dynamics
FW-H	Ffowcs Williams-Hawkings
FxLMS	Filtered-x Least Mean Square
BPFs	Blade-passage Frequencies
BVI	Blade–vortex Interaction
HSI	High-speed Impulsive
PSD	Power Spectral Density
sUAS	Small Unmanned Aerial Systems
RAPP	Rotor Acoustic Prediction Program
BEM	Boundary Element Method
CSD	Computational Structural Dynamics
F1A	Farasat's Formulation 1A
UAM	Urban Aerial Mobility
SHs	Spherical Harmonics
SSHs	Spherical Sector Harmonics
SNR	Signal-to-Noise
PDEs	Partial Differential Equations
NMSE	Normalized Mean Square Error
NSE	Normalized Square Error
MAC	Modal Assurance Criterion
ReTM	Relative Transfer Matrix
MEMS	Microelectromechanical Systems
DC	Direct Current
ROI	Region of Interest
KHCNN	Kirchhoff–Helmholtz-based Convolutional Neural Network
CNN	Convolutional Neural Network
Grad-CAM	Gradient-weighted Class Activation Mapping
STFT	Short-time Fourier Transform

Notations and Symbols

Mathematical Operations and Constants

e	The Euler's number
$i^2 = -1$	The imaginary number
$\widehat{(\cdot)}$	Unit vector
$\overline{(\cdot)}$	Conjugation
$(\cdot)^T$	Transpose
$\lvert \cdot \rvert$	The absolute value of a number
$\lvert\lvert \cdot \rvert\rvert$ or $\lvert\lvert \cdot \rvert\rvert_2$	The ℓ_2-norm or the Euclidean norm
$\lceil \cdot \rceil$	The ceiling function
$(\cdot)!$	Factorial
$\forall x$	For all values of x
$\partial/\partial x$	Partial derivative with respect to x
$g'(x)$	The first order derivative of function g with respect to x
∇	The gradient
∇^2	The Laplacian
$(\cdot)^\dagger$	Moore–Penrose pseudo-inverse
$(\cdot)^*$	Conjugate transpose
$\lVert\cdot\rVert_1$	The ℓ_1-norm
$\mathbb{R}\mathrm{e}\{\cdot\}$	Real part
$\mathbb{I}\mathrm{m}\{\cdot\}$	Imaginary part

Functions and Variables

$\delta(\cdot)$	Dirac delta function
$\delta_{n,m}$	Kronecker delta function
$h_n^{(1)}(\cdot)$	The spherical Hankel function of the first kind
$h_n^{(2)}(\cdot)$	The spherical Hankel function of the second kind
$H_n^{(2)}(\cdot)$	The Hankel function of the second kind
$j_n(\cdot)$	The spherical Bessel function of the first kind
$J_n(\cdot)$	The Bessel function of the first kind
$P_n(\cdot)$	The Legendre polynomial of degree n
$P_n^m(\cdot)$	The associated Legendre polynomial of degree n and order m
$y_n(\cdot)$	The spherical Bessel function of the second kind
$Y_n(\cdot)$	The Bessel function of the second kind (Neuman function)
$Y_n^m(\theta,\phi)$	The spherical harmonic function of degree n and order m evaluated at colatitude θ and azimuth ϕ
$\mathscr{L}(\cdot)$	The cost function
$Y_n^m(\cdot)$	The spherical harmonics of degree n and order m
$T_n^m(\cdot)$	The spherical sector harmonics of degree n and order m

Contents

List of Figures

List of Tables

Chapter 1

Introduction

1.1 Motivation and Scope

In recent years, small-scale unmanned aerial vehicles (UAVs), commonly known as drones, have become increasingly popular in a wide range of applications. For example, drones play an important role in food and parcel delivery [1], mapping [2], search and rescue [3, 4], surveillance [5], agriculture [6], environmental monitoring [7], and video recording and filming [8]. Many companies, including Amazon, UPS, and Domino, are actively investing in expanding the practical use of drones in wider applications [9]. According to the report by the Grand View Research, the market at approximately USD 73.06 billion in 2024, projecting a compound annual growth rate of 14.3 % [10].

Despite the growing importance of drones, the noise pollution from them is strong and can affect daily life and the well-being of communities, as illustrated in Fig. 1.1. Drone noise, especially the high-frequency component, can lead to elevated annoyance levels and stress in affected communities [11]. Exposure to drone noise during nighttime has been linked to disruptions in sleep patterns, leading to poorer sleep quality and related health issues [12]. Moreover, chronic or unexpected exposure to drone noise may trigger psychological stress responses, impacting mood, concentration, and overall mental health [13]. Due to the public concerns over noise pollution, regulatory bodies are beginning to develop standards and operational limits for drone usage to mitigate these effects [14]. Community acceptance of drone operations depends heavily on noise levels, and when noise is perceived as excessive, residents are more likely to oppose drone use in public spaces [15]. Therefore, effective drone noise mitigation strategies are crucial to supporting the sustainable integration of drones into everyday life.

Effective noise mitigation begins with accurate characterization of the drone's acoustic field. Drone noise is typically dominated by the propeller tonal noise whose energy is concentrated on the harmonics of the blade passage frequency (BPF)

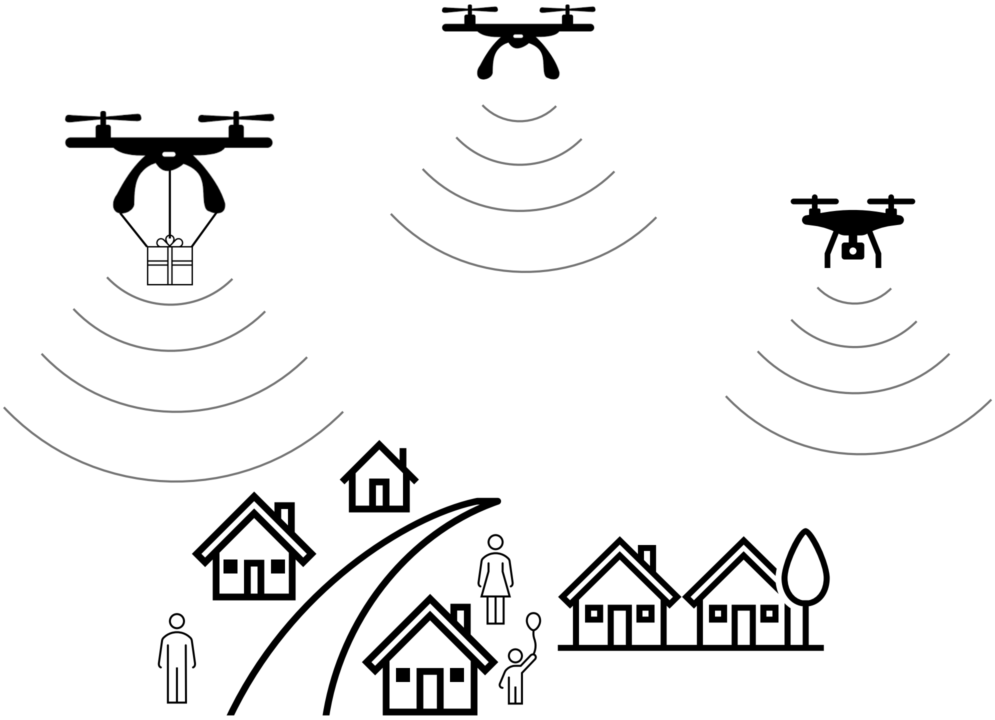

Figure 1.1: Illustration of the drone noise problem to a community.

[16, 17, 18, 19]. To model the drone noise field, researchers mostly utilize computational tools such as Computational Fluid Dynamics (CFD), Vortex methods, Blade Element Theory, Momentum Theory combined with acoustic analogies such as the Ffowcs Williams-Hawkings (FW-H) equation to predict sound emissions from drones [20, 21, 22, 23]. However, these approaches demand significant computational power and yield theoretical estimates that can differ markedly from the actual noise generated by an operating drone. The above drone noise modeling and prediction can inform effective noise reduction strategies, such as redesigning propeller shapes and selecting noise-dampening materials for the airframe.

Drone noise reduction methods can be broadly categorized into passive and active approaches. Passive noise reduction mainly focuses on design modifications and material applications to minimize noise emissions without the need for additional sound sources. One primary approach involves optimizing the design of drone components, including propellers, fuselage, and motors, to reduce noise pollution during operation. By increasing the number of blades of the propeller [24], modifying the blade aerofoil shapes [25], or changing the fuselage geometry [26], the drone noise can be reduced. Another common approach for passive drone noise control incorporates advanced materials and acoustic treatments to dampen noise propagation [27, 28], including sound-absorptive barriers [27] and sound reflectors [29, 30]. Implementing these passive strategies requires careful consideration of their impact on the drone's aerodynamic performance and structural integrity. While they offer the advantage of reducing noise without additional power consumption, these passive methods offer only limited noise reduction and are generally ineffective for low-frequency noise [31].

Drone active noise reduction approach can be further classified into two categories: phase control and active noise control (ANC). Phase control technique reduces noise by adjusting the relative angular blade positions of multiple propellers to achieve optimal alignment, thereby minimizing noise levels in specific target areas [32, 33]. However, this method requires all propellers to have the same rotation speed and is limited to cancelling specific harmonics of tonal noise [34]. Drone ANC approach, on the other hand, employs secondary sources (loudspeakers) to generate anti-noise that destructively interferes with the primary noise [35]. Unlike passive methods, ANC allows for noise cancellation in a controllable region, and with a sufficient number of secondary sources, tonal noise can be effectively mitigated. This makes ANC a highly flexible and promising approach for drone noise reduction. While drone ANC has great potential, most current research on it is limited in the conceptualization stage and mainly focuses on narrow-band and nearfield reduction over some sparse points [27, 36, 37].

As mentioned above, drone active noise reduction is an essential and open research area. To reduce the drone noise influence on residents, we focus on noise reduction over a directional far-field region. For example, in residential areas, reducing drone noise directed downward toward the ground is crucial, while in urban environments with skyscrapers, lateral noise reduction is preferred. In Fig. 1.2, we illustrate a directional drone active noise reduction system, aiming to reduce the drone noise propagating downward. A microphone array is attached to the drone to measure the drone's noise and model the noise field over the target region. Speakers are mounted on the drone to generate the anti-noise based on the onboard microphone measurements to reduce the total noise level over the target region. A phase control system is also embedded to synchronize the relative phases of propellers to maintain the optimal combination to reduce noise pollution further.

Based on the above discussions, we pose the following research question to address in this thesis:

How can on-board microphone measurements and active noise reduction strategies be leveraged to model and suppress drone noise propagating in targeted directions, thereby minimizing its impact on nearby

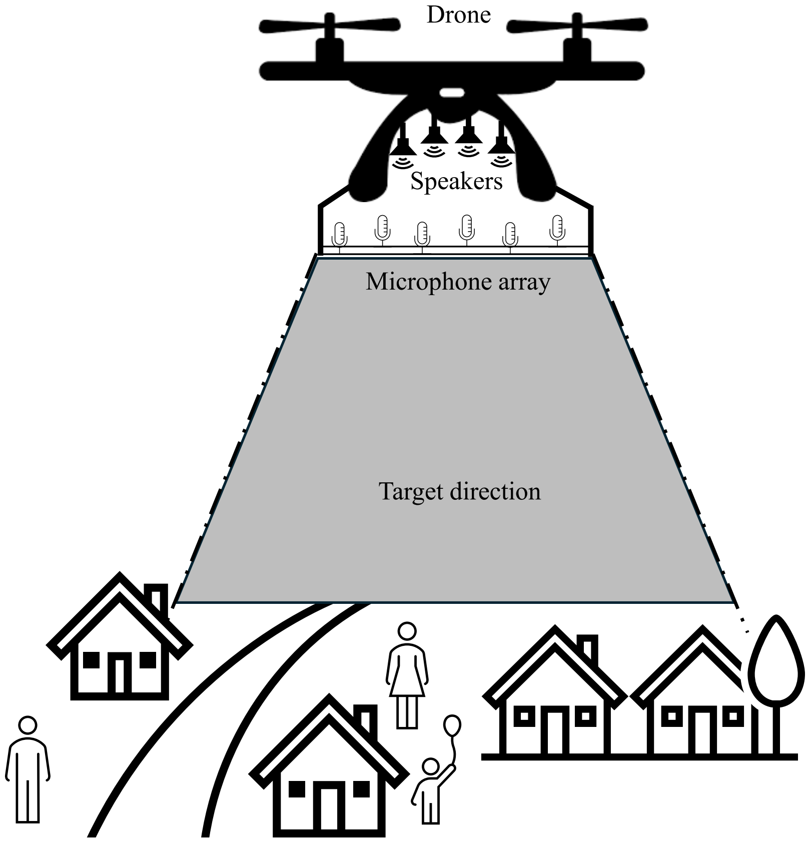

Figure 1.2: Directional drone noise reduction system.

residents?

1.2 Problem Description and Proposed Approaches

We elaborate on the above research problem into three sub-questions and provide some intended solutions to each of the following questions:

How to estimate the drone outgoing sound field in a target set of directions based on the on-board microphone measurement?

Solutions: We generalize this question to a sound field extrapolation problem, aiming to extrapolate the sound field measured from a spherical sector region to another concentrated spherical sector region with the same angular range but different radius. We investigate the properties of spherical sector harmonics in the problem of sound field reconstruction and extrapolation, and further develop the spherical sector sound field extrapolation method. We conduct comprehensive simulations to evaluate the proposed extrapolation method with different frequencies, angular ranges, and extrapolation distances.

We further generalize the problem and remove the spherical sector shape constraint on the measurement region. To this end, we propose a physics-informed machine-learning architecture to reconstruct the sound field from an arbitrary microphone placement. By embedding the free space Green's function into the network architecture, the model adheres to the Helmholtz equation, thereby improving interpretability and generalization to out-of-sample scenarios. We test the performance of the proposed network for a sound field extrapolation problem and a sound field reconstruction problem in a reverberant environment. This method can be applied to many approaches beyond drones.

How to design a feasible drone ANC system that can reduce the drone noise pollution in a certain direction?

Solutions: Once the drone noise field is modelled, an active noise reduction method can be developed accordingly. We develop a theoretical drone directional noise reduction method using the spherical sector harmonics extrapolation model. We derive the wave-domain adaptive ANC algorithm of the proposed noise reduction method. Considering the power and loading restrictions of drones, we define a secondary source to primary source power ratio and analyze it with different secondary source settings.

To experimentally evaluate the directional drone ANC system, we conduct an experiment in the semi-anechoic chamber. Due to the difficulty of building a microphone array in a spherical sector shape, we could not validate the proposed spherical sector harmonics based ANC algorithm. Alternatively, we implement the relative transfer matrix based multi-channel filtered-x least mean square (FxLMS) ANC algorithm and use two planar microphone arrays to validate the noise reduction performance of it.

How to find the optimal relative phase combination of propellers to reduce the drone noise in directional target region?

Solutions: We build a spherical microphone array and use it to measure the outgoing sound field of a drone's propeller. We find the sound field translation relationship between the measured sound field and the sound field over the farfield target region. We develop the sound field model for different propellers with respect to their blade angular positions. Based on the sound field model, we find the optimal relative phase combinations to achieve the best noise reduction over the target region.

1.3 Literature Review

Drones are becoming increasingly popular in both commercial and military applications and are likely to further grow in the future. However, noise generated by drones is strong and annoying, with the potential to cause long-term harm to people's hearing and mental health, which hinders its wider adoption. Therefore, it is important to know the acoustics signature of drone noise and control it based on its characteristics.

Drone noise mainly comes from three sound sources: propeller, motor, and fuselage, with propeller noise representing the most significant contribution [38, 27]. The propeller noise can be further classified into tonal noise and broadband noise. Tonal noise is characterized by energy concentrated at the BPFs, which depend on the number of blades and their rotational speed [16, 17]. Based on the noise generation mechanism, the propeller tonal noise consists of four primary components: thickness noise, loading noise, blade–vortex interaction (BVI) noise, and the high-speed impulsive (HSI) noise. Thickness noise arises from the displacement of air by the finite blade thickness and is typically significant only for large-scale propellers such as ones used in helicopters. Loading noise, the dominant tonal mechanism in small UAVs, is generated by steady aerodynamic forces (lift and drag) acting on the blades. A fixed pressure difference across the rotating blades generates the steady loading noise, while BVI noise occurs when a rotor blade interacts with the tip vortices shed by a preceding blade, which is unsteady [22]. The BVI noise and the loading noise are the major components at low rotating speeds. In contrast, HSI noise is generated when rotor blade tips approach transonic speeds, leading to the formation of shock waves on the advancing blade.

Broadband noise encompasses a wide range of frequencies and is primarily caused by stochastic, or random, aerodynamic processes. Unlike tonal noise, which is linked to periodic events, broadband noise results from irregularities in airflow and blade interactions, including turbulence–blade interaction noise, trailing edge noise, tip vortex interaction noise, and wake interaction noise [39, 40]. In the far field, broadband noise levels are generally lower than tonal components, making the harmonics of the BPF the principal focus for UAV noise mitigation [41, 42, 43].

Researchers investigate the acoustic characteristics of drone noise in two ways: experimental measurements and numerical modeling. Drone noise measurements [44, 45, 46, 47, 48, 49] utilize microphones, microphone arrays, or other types of sensors to measure drone noise field. For drone noise modeling, researchers usually implements computational tools such as CFD, Vortex methods, Blade Element

Theory, Momentum Theory or a combination of them [21, 22, 23]. The acoustic characterization can guide the drone noise reduction, such as the redesign of propeller shape and materials of airframes. We review the research achievements in drone noise measurement, drone noise modeling, and drone noise reduction in the following subsections.

1.3.1 Drone noise measurements

In recent years, many measurements have been conducted for the further acoustic characterisation of drones. Depending on the venue of the measurements, the drone noise measurement study can be classified into laboratory measurements and field measurements. Typically, laboratory measurements are conducted in an anechoic or semi-anechoic chamber, with very low reverberation and background noise. Due to the room size restriction, the drone operation is usually limited to fixed position, hovering, or takeoff [50]. On the other hand, the field measurement provides much more flexibility for drones' operations, including flyovers, hovering, landing and takeoff, but researchers have less control of the outdoor environment, such as the wind gusts and the background noise.

Multiple metrics are used to analyze the measurement data, including power spectral density (PSD), sound pressure level (L_p), sound power level (L_w), A-weighted sound exposure level (L_{AE}), and directivity.

Laboratory measurements

A summary of drone noise laboratory measurements is presented in Table. 1.1. Intaratep *et al.* conducted the measurement in an anechoic chamber with a single stand-mounted microphone, aiming to enhance understanding of noise generation mechanisms in drones [51]. By operating different combinations of the quadcopter's four rotors, the study examined how rotor-rotor interactions affect acoustic output. It was observed that certain rotor configurations lead to increased noise levels due to aerodynamic interference between rotors.

Herreman measured the noise emission from the KittyHawk HDX17 drone by a spherical microphone array with 20 microphones in an anechoic chamber [52]. By choosing different electrical power settings, different operating conditions of the drone can be investigated. The measured sound power data from this method can be employed in modeling techniques to project UAV noise into community environments, aiding in noise impact assessments and mitigation strategies. Herreman *et al.* conducted a similar measurement for an octocopter with a spherical microphone

Table 1.1: Drone noise measurements and acoustic characterisation methods conducted in laboratories.

Study	**Number of rotors**	**Maneuver**	**Microphone setup**	**Metrics**
[51]	4	Hovering, Fixed position	Single stand-mounted microphone	PSD, L_p, L_w
[52]	4	Hovering, Fixed position	20 mics in a sphere	L_p, L_w
[53]	8	Hovering, Fixed position	40 mics in a sphere	L_p, L_w
[54]	4	Fixed position	8 mics, different elevations	L_p
[55]	4	Hovering, Fixed position	18 mics in a hemisphere	L_p
[56]	4	Hovering, takeoff, straight flyover	80 mics in a rectangular array	PSD L_p directivity
[57]	4	Hovering, Fixed position	6 to 12 mics in a hemisphere	Lp Lw directivity

array with 20 and 40 microphones, aiming to establish a standardized methodology for accurately measuring UAV noise [53].

Tinney and Sirohi presented a comprehensive experimental analysis of the acoustic characteristics of multirotor drones during hover conditions [54]. The research investigated the drone noise emission with different drone configurations, rotor sizes.

Alkmim *et al.* analyzed the drone noise directivity pattern and human perception by drone noise measurements [55]. They employed a hemispherical array of microphone to capture the three-dimensional sound field around a hovering quadrotor drone and decomposed the measurement data into the spherical harmonics domain for further analysis. Similarly, Papa, *et al.* also used a hemispherical microphone array to measure the sound power level of a drone in a fixed position [57].

Zhou *et al.* experimentally investigated the noise emissions of a quadcopter UAV during various flight maneuvers with microphone arrays on the ground and vertical line [56]. The research aims to understand how different operational conditions affect the acoustic signature of the drone, which is crucial for developing noise mitigation strategies in urban environments.

Field measurements

An overview of the Field drone noise measurement is described in Table. 1.2, where the number of propellers, maneuver, microphone setup, and metrics are presented in the table.

The study by Humphreys *et al.* presented the design, calibration, and initial deployment of a high-channel-count, field-deployable microphone phased array system. This system is intended for measuring propulsion and airframe noise during aircraft flyovers, addressing the need for accurate, outdoor-capable acoustic measurement tools in aeroacoustic research [58]. Kloet *et al.* investigated the acoustic characteristics of small multi-rotor unmanned aircraft systems (UAS), focusing on how different propeller configurations affect noise emissions. The mini-quad with propellers ranging from 2 to 6 blades was tested in a sheltered outdoor park to assess the impact of blade count on acoustic emissions [59]. Both studies focused on the hovering operation.

Alexander and Whelchel investigated the acoustic characteristics of small unmanned aerial systems (sUAS) during flight, focusing on how different flight maneuvers influence noise emissions and their potential impact on ground-level observers [60]. Acoustic measurements were conducted at the Virginia Tech drone park, providing

Table 1.2: Drone noise measurements and acoustic characterisation methods conducted outside.

Study	**Number of rotors**	**Maneuver**	**Microphone setup**	**Metrics**
[58]	6	Hovering	185 electret microphone array	L_p
[59]	4	Hovering	2 sound level meters	L_p, PSD, directivity
[60]	6	Hovering, straight flyover	5 ground-board microphones	L_{AE}, PSD
[61]	4	Hovering, straight flyover	5 mics on 1 m ground, on grass	L_{AE}, PSD
[62]	4, 6	Hovering, climb, forward flight	microphone array with 64 mics	OSPL, L_p
[63]	8	Hovering, takeoff, landing, straight flyover	12 inverted ground plate mics, 2 tripod-elevated mics	PSD, Lp, L_{AE}
[64]	6	Hovering, takeoff	2 ground mic arrays (linear and circular), 1 elevated array	L_p, directivity
[65]	4	Hovering, climb, descent, flyover, maneuvering	1 mic, and 8 mics for directivity	L_p, L_w

a controlled outdoor setting for capturing sUAS noise during various flight conditions, including hovering and forward flight. Alexander *et al.* conducted extensive acoustic measurements of sUAS during various flight conditions, including hover and forward flight for forecasting the community noise impact of small unmanned aerial systems [61]. These measurements captured the unique noise signatures of multi-rotor drones, which are characterized by tonal components at blade passage frequencies and broadband noise from rotor-airframe interactions.

Besnea offered an in-depth investigation into the acoustic characteristics of drones, focusing on understanding how design and operational parameters influence UAV noise emissions [62]. Noise measurements were performed on four different drones with various flight maneuvers, including hovering and ascending, in an open-field environment to capture realistic acoustic data.

The research conducted by Konzel and Greenwood focused on developing standardized procedures for measuring and characterizing the noise emissions of small multi-rotor unmanned aerial vehicles (UAVs) [63]. 12 inverted ground plate microphones and 2 tripod-elevated microphone were employed to measure the noise emission from an octocopter Tarot X8.

Cutler-Wood *et al.* conducted comprehensive acoustic measurements during hover operations of various types of drones [64]. 19 microphones: 3 microphone arrays, 2 ground-mounted arrays (linear and circular), and 1 elevated array were used to captured sound pressure levels and directivity patterns, providing a detailed acoustic profile of the aircraft in a stationary flight condition.

Treichel and Körper investigated the noise emissions of various drone models during different flight maneuvers to assess their horizontal and vertical directivity patterns [65]. The study involved acoustic measurements of different drones performing various flight operations. The measurements aimed to capture the noise characteristics and directivity of the drones under realistic conditions.

1.3.2 Drone noise prediction and modeling

The noise modeling of a rotating-blade has been thoroughly studied in the past decades [66, 67, 68, 69, 70, 71, 72, 73]. A typical method to predict the rotor noise is to numerically solve the Ffowcs Williams–Hawkings (FW–H) equation [74]. The foundation work of rotor noise prediction was introduced in 1983 by Farassat and Succi, who adept the FW-H equation to modelling the rotor tonal noise [66]. In 1986, a computer program named WOPWOP was developed at NASA Langley Research Center to predict the discrete frequency noise generated by helicopter rotors, which incorporates realistic blade motions and acoustic formulations to improve the prediction accuracy [67]. Gallman introduced the Rotor Acoustic Prediction Program (RAPP), specifically focusing on modeling the BVI noise and low-frequency noise [68]. To computes the far-field acoustic pressure generated by the rotor blades, PARIS was proposed, which also main target the BVI noise prediction [69]. By examining three different primary acoustic formulations: retarded-time, collapsing-sphere, and emission-surface, Brentner addressed the computational challenges in predicting rotorcraft noise [70]. Brentner and Jones further improved the WOP-WOP by integrating the information of aircraft positions, attitudes, rotor blade airloads, and motions, allowing the noise prediction during complex maneuvers [71]. A new noise prediction code PSU-WOPWOP was developed for predicting rotorcraft noise during maneuvering flight, including steady and transient conditions such as hover, descent, and pop-up maneuvers. It also provides flexibility for modeling complex rotor configurations and motions, accommodating multiple rotors and full aircraft movements [73, 72].

Compared to conventional rotorcraft, drones typically employ smaller rotors that operate at lower Reynolds numbers. This scale difference introduces unique aerodynamic characteristics, such as increased sensitivity to transitional flow regimes and a higher susceptibility to unsteady aerodynamics [75]. These factors complicate the accurate prediction of aerodynamic loads and noise emissions using traditional modeling methods. Furthermore, the compact configuration of multi-rotor drones results in significant aerodynamic interactions between rotors and fuselage. Rotor-to-rotor interactions can lead to complex wake interference patterns, causing unsteady loading and fluctuations in thrust and noise levels. Similarly, rotor-to-fuselage interactions can result in acoustic scattering, amplification, or shielding effects, further complicating the noise field [76]. These interactions are particularly challenging to model due to their unsteady and nonlinear nature, necessitating high-fidelity computational methods for accurate analysis. Therefore, compared to conventional rotorcraft, modeling and predicting the noise fields of drones is more challenging due to their unique aerodynamic characteristics and complex interaction effects, requiring advanced methods and simulation techniques.

Ko *et al.* employed a free wake vortex lattice method to simulate wake interactions and utilized the impermeable surface-based FW-H acoustic analogy to predict drone noise emissions in various flight conditions [77]. Jiang *et al.* investigated the acoustic scattering effects of a drone fuselage on rotor-generated noise by an efficient boundary element method (BEM)-based solver. This approach allows for detailed analysis of rotor-to-fuselage interactions [78]. The study conducted by Jia *et al.* employed the Helios software for high-fidelity CFD and Computational Structural Dynamics (CSD) simulations, coupled with the PSU-WOPWOP acoustic prediction tool to investigate the acoustic characteristics of a lift-offset coaxial rotor in high-speed forward flight [79]. Lee and Lee studied how rotor-to-rotor interactions influence the aerodynamic performance, wake structures, and noise emissions of a quadcopter UAV during hover flight using highfidelity OVERFLOW2 CFD and PSU-WOPWOP solvers [80]. The noise emission from different orientations of rotors relative to the airframe was modeled in [81], where the rotor to airframe interaction was considered in the modeling process. The drone noise prediction with rotor to airframe interaction was studied by Whelchel and Alexander who implement the CFD method to solve Farasat's Formulation 1A (F1A) [82, 83].

Recently, drone noise modeling platforms were developed to improve the prediction accuracy under various working conditions and drone configurations. Tan *et al.* introduced a cloud-based simulation platform designed to simulate the environmental noise impact of drones and urban aerial mobility (UAM) systems. The platform utilized cloud computing to enhance the noise modeling efficiency, allowing users to define working conditions and drone configurations through a user-friendly graphical interface [84]. Zhong *et al.* developed an integrated drone noise modeling platform that utilized an in-house computational aeroacoustics solver are employed to develop noise prediction models. The platform implemented the boundary element method accounts for noise scattering due to the fuselage and advanced Gaussian beam tracing techniques to project noise to the far-field, considering factors like atmospheric attenuation and complex boundary reflections [85]. Tan *et al.* further introduced a comprehensive drone noise simulation platform that incorporate various operational parameters—such as flight speed, payload weight, and ground vegetation to model the environmental noise impact of delivery drones in urban residential settings [86].

Research Gaps

Existing drone noise modeling approaches mainly rely on computationally intensive simulations that require detailed knowledge of the drone's design and operating conditions. Such methods require high computational power and long runtimes, making them impractical for drone ANC, which requires real-time noise field information. Moreover, the inability to accurately anticipate in-flight conditions often leads to significant prediction errors. To bridge this gap, there is a clear need to develop physics-based models with measurements from onboard microphones or microphone arrays, enabling estimation of the drone's noise field under actual operating environments.

1.3.3 Drone noise reduction

Drone noise reduction methods can be classified into passive and active approaches. Passive drone noise reduction methods aim to change the design and material of drones' propellers, motors, and airframes to reduce noise generation from drones. On the other hand, active drone noise reduction methods actively counteract and mitigate noise emissions during flight operations. We review the academic achievements of both passive and active drone noise reduction methods in the following subsections.

Passive drone noise reduction

Various studies have been conducted to reduce the noise emission from propellers, which is the major noise source of drones. One simple approach is to increase the number of propeller blades, which changes the acoustic signature of drones and reduces noise emissions from propellers [87]. In addition, by redesigning the shape of the propeller blade, the noise emission can be reduced [88]. Pang *et al.* found that serrated trailing edges can effectively reduce high-frequency broadband noise in the far field [88]. The study conducted by Hersh *et al.* demonstrated that serrated trailing edges can significantly reduce vortex-induced noise. This effect is observed in both stationary and rotating configurations, indicating the broad applicability of the technique [89]. Paruchuri *et al.* proposed a novel serration geometry that more effectively reduces sound waves generated by turbulent interactions at the leading edge [90]. Ning *et al.* investigated the aerodynamic and aeroacoustic characteristics of a novel UAV propeller design inspired by natural flyers like cicadas and maple seeds [91]. By designing a propeller with a planform shape based on cicada wings and maple seeds, the aerodynamic measurements showed that the bio-inspired propeller can provide the same thrust as the baseline propeller under the same power input when hovering and achieve up to 4 dB the noise reduction. Noda *et al.* explored innovative propeller designs inspired by natural flyers to mitigate drone noise [92]. Drawing inspiration from the wing structures of insects and birds, researchers implemented design features such as leading-edge serrations, velvet-like surface textures, and trailing-edge fringes. Compared to DJI Phanton 3 propellers, the proposed propeller can achieve 2 dB noise reduction under the same power efficiency.

Researchers have also investigated the passive noise reduction methods on drones' brushless motors. Most drone motor noise reduction methods focus on improving the design of the stator and motor structure. June *et al.* investigated methods to mitigate noise generated by direct current (DC) motors [93]. The study first identified the primary noise sources in DC motors by experiments and then proposed methods to reduce DC motor noise, such as optimizing motor design parameters, improving manufacturing precision to minimize mechanical imbalances, and incorporating damping materials to absorb vibrations. Byun *et al.* found that the redesigned balance weight effectively reduced both noise and vibration in the DC motor, underscoring the significance of mechanical design optimizations in noise and vibration control of DC motors [94]. Studies have been conducted to investigate the use of micro-perforated panel absorbers made from stainless steel and aluminium to reduce motor noise [95, 96]. Experiments demonstrated that micro-perforated panel absorbers can effectively reduce UAV motor noise, particularly in the 300 Hz to 1 kHz frequency range [95].

Change in the design and structure of the drone fuselage is another popular approach to reduce drone noise. Sound reflectors, also known as acoustic panels or baffles, are positioned on the drone fuselage to block noise propagating to the ground [97]. The design process of reflectors can be incorporated with advanced modelling and simulation techniques to improve the noise reduction while reducing side effects on aerodynamic performance [98]. Ghaffarivardavagh *et al.* introduced ultra-open meta-material design, which is particularly beneficial in scenarios requiring both ventilation and noise reduction, such as sound barriers [99]. Experimental validation demonstrated a reduction in transmitted acoustic energy of up to 94 %.

Active drone noise reduction

The active drone noise reduction approach can be further classified into two branches: phase control and ANC. Phase control, also known as synchro-phaser, manipulates the relative angular blade positions of a set of propellers to mitigate the noise emission from propellers [19]. Under the same rotation speed, controlling the relative angular positions of propeller blades allows the noise generated by different propellers to interfere destructively, thereby reducing the overall emitted noise [100]. Synchro-phaser was developed for large-scale, propeller driven aircraft [101, 102, 103]. Schiller *et al.* adapted this technology into drone's small propellers and experimentally validated that appropriate phase synchronization could achieve a 4–5 dB reduction in sound pressure levels at the blade passage frequency across the ground plane under the dual-propeller system [32]. Smith *et al.* further investigated the influence of increasing rotor numbers for phase control by simulations [104].

The current research on drone ANC is limited, with only a few studies addressing this topic. Kusni initially proposed a propeller noise reduction system, comprising configurations like dipoles and quadrupoles, to generate anti-noise signals that effectively reduce the primary noise from propellers [36]. Numerical simulations were conducted to evaluate the performance of these configurations in free-field conditions. Similarly, Dubravko proposed a multichannel ANC system employing 12 loudspeakers positioned around each propeller to attenuate propeller-generated noise. However, this approach remained at the conceptual stage and was not supported by either simulation or experimental validation [27]. Narine *et al.* implemented a single-channel ANC system to reduce the tonal noise of a single propeller [37]. However, the study was conducted offline and did not consider the causal control constraints inherent to ANC systems [105].

Research gaps

Existing studies on drone propeller phase control are limited in scope and practical applicability. Most approaches rely heavily on numerical noise modeling techniques to simulate the propeller noise field and determine the optimal relative phase configurations. However, the inability to accurately predict in-flight operational conditions often leads to discrepancies between the simulated and actual noise fields, thereby diminishing the effectiveness of phase control strategies. Furthermore, these studies typically focus on noise reduction at a limited number of discrete observer points, rather than evaluating noise suppression over a spatial region, which is more relevant for assessing the impact on communities and residents.

Similarly, current research on ANC systems exhibits several notable limitations: (i) achieving high noise reduction, both spectrally and spatially, with a limited number of transducers; (ii) an exclusive focus on propeller noise, while neglecting contributions from other noise sources such as motors and fuselage; (iii) a primary emphasis on narrowband noise cancellation, which restricts the effectiveness across the broadband spectrum; (iv) a general lack of experimental validation to substantiate theoretical models; and (v) insufficient consideration of practical constraints such as speaker size, drone payload limitations, and power consumption, which are critical for real-world deployment.

1.4 Thesis Overview

Based on the discussion above, this thesis provides multiple approaches to model and reduce drone noise in a certain direction. Figure. 1.3 illustrates the thesis outline and the logical flow of it. The core technical contributions fall into two main

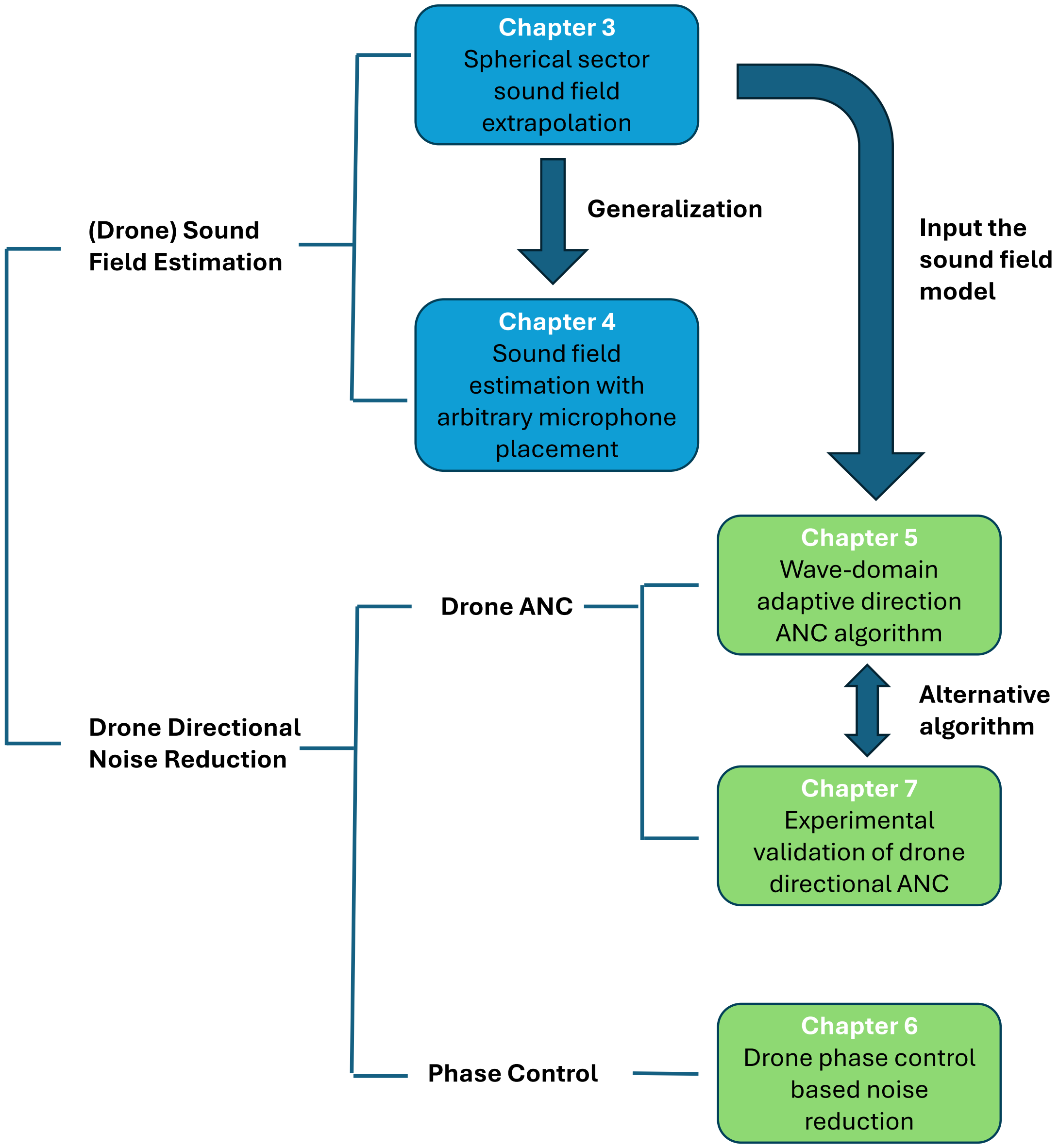

Figure 1.3: Thesis outline.

categories: directional sound field estimation and directional drone noise control, which are detailed across the five body chapters (3–7). Additionally, we begin with a chapter on and theoretical review, and end with a chapter on overall conclusions and future work. We summarise the content and contributions of each chapter as:

Chapter 2: Background Theory

We provide the background theories and mathematical foundations that support the spatial sound field processing methods developed throughout this thesis, including spherical harmonic expansion of a soundfield and its properties, feed-forward active noise control systems, and physics-informed neural networks in audio and acoustics.

Chapter 3: Spherical Sector Harmonics Based Sectorial Sound Field Reconstruction and Extrapolation

In Chapter 3, we tackle the challenge of modeling drone noise fields by reframing the task as a spherical sector sound field extrapolation problem. We begin by thoroughly investigating and evaluating the performance of spherical sector harmonics (SSHs) for reconstructing and extrapolating sectorial sound fields. Our analysis reveals several intrinsic limitations of SSHs: first, they do not exactly satisfy the wave equation because of the shifting and scaling modification in the input arguments of the associated Legendre polynomials and exponential functions; second, significant distortions emerge near the sector boundaries during sound field reconstruction, necessitating a larger measurement region than the target reconstruction area; and third, the spherical Hankel and Bessel functions prove inadequate as radial functions for SSH-based extrapolation. To overcome these challenges, we introduce a mapping-based sectorial extrapolation approach that markedly improves the accuracy of extrapolations, particularly in the interior regions.

Chapter 4: Point Neuron Learning: A New Physics-informed Neural Network Architecture

In this chapter, we break the restriction of confining the measurement area to a spherical sector and expand the scope to the general sound field estimation with microphones placed arbitrarily. We present an innovative physics-informed neural network architecture that incorporates the fundamental solution of the wave equation directly into its design, guaranteeing strict adherence to the underlying physics. This new point neuron learning approach facilitates precise sound field modeling based solely on microphone data, thereby eliminating the need for pre-collected datasets. In contrast to current physics-informed neural network methods, our approach inherently handles complex numbers, improves interpretability, and generalizes well to out-of-sample scenarios. We validate our proposed architecture via simulations on two tasks: (i) sound field reconstruction in reverberant environments, and (ii) sound field extrapolation, demonstrating its applicability to drone noise modeling. The results show that the point neuron method outperforms competing approaches by being more robust to variations in microphone placements and sensor noise, while also delivering excellent versatility across a wide range of acoustic challenges.

Chapter 5: Spherical Sector Harmonics Based Drone Directional Active Noise Control

In Chapter 5, we implement the sound field extrapolation model developed in Chapter 3 to tackle the challenge of reducing directional noise from drones. We first propose a method for reducing drone tonal noise within a targeted spherical sector region. Building on this, we derive a wave-domain adaptive ANC algorithm tailored for directional drone noise reduction. Considering the power and payload limitations inherent to drones, we perform simulations with various secondary source configurations to evaluate both the noise reduction performance and the power consumption of the secondary sources. The simulation results reveal that our method not only effectively suppresses noise in the target sector but also converges rapidly, highlighting its potential as a practical solution for drone noise control.

Chapter 6: Drone Propeller Noise Reduction Based on Phase Control

We introduce a phase control strategy for reducing drone noise by adjusting the relative phase of the propellers in this chapter. Our approach involves three key stages: (i) capturing near-field propeller noise with a custom-designed open spherical microphone array, (ii) developing an extrapolation technique to forecast far-field noise from these near-field measurements, and (iii) simulating far-field noise under different propeller phase configurations. We also examine how various drone configurations affect the efficacy of phase-controlled noise reduction in a specified far-field target zone, demonstrating that noise reductions of up to 6.8 dB at blade passage frequencies are attainable.

Chapter 7: Directional Active Noise Control for Broadband Drone Noise

In Chapter 7, we validate the performance of a broadband directional drone noise ANC system through experiments. We implement an FxLMS algorithm based on a relative transfer matrix, which allows us to control the drone noise over a directional farfield with an onboard monitoring microphone array. Experimental tests conducted in a semi-anechoic chamber revealed an average noise reduction of 4.78 dB in the 1500–2400 Hz frequency band and an approximate 10 dB reduction at harmonic frequencies. These findings underscore the potential of directional ANC strategies for mitigating drone noise propagation, paving the way for quieter drone operations in noise-sensitive environments.

Chapter 8: Conclusion and Future Works

We conclude the thesis in this chapter and discuss potential directions for future research on drone noise field modeling and control.

Chapter 2

Background Theory

Overview: *In this chapter, we review the background theories and mathematical foundations that support the spatial sound field processing methods developed throughout this thesis. We begin by defining the spherical coordinate system used to describe three-dimensional acoustic fields. Then, we introduce the Helmholtz equation, which governs sound propagation in the frequency domain, and present its solution in spherical coordinates, commonly referred to as spherical harmonics. Furthermore, we examine several fundamental sound source models, including their corresponding sound field representations in the spherical harmonic domain. We also provide a brief overview of single-channel and multi-channel feedforward ANC systems, which form the basis for the noise reduction strategies discussed in later chapters. Finally, we introduce PINNs and highlight their emerging applications in audio and acoustics.*

In this chapter, we review the theoretical background and mathematical foundations of spatial sound field representation and processing utilized throughout this thesis. We begin by defining the coordinate system used to describe the spatial sound field domain in Section 2.1. Sections 2.3 and 2.3.2 introduce the Helmholtz equation, which governs sound propagation in space, and its solutions in spherical coordinates—spherical harmonics—which form the basis of spatial sound field representation and processing. In Section 2.4.3, we review several fundamental sound source models, including point sources, plane waves, and mixed-wave sources, along with their spherical harmonics representations. We also provide a brief overview of single-channel and multi-channel feedforward ANC systems in Section 2.6. Finally, we introduce PINNs and highlight their emerging applications in audio and acoustics in Section 2.6.

2.1 Coordinate System

The three-dimensional coordinate system is depicted in Fig. 2.1, where O is the origin of the system. We denote a singular point in the Cartesian coordinates as $\boldsymbol{x} = (x, y, z)$ in meters and in the spherical coordinates as $\boldsymbol{x} = (r, \theta, \phi)$, where $r \in [0, \infty)$ is the radial distance of the point from the origin in meters, $\theta \in [0, \pi]$ is elevation angle downwards from the positive z-axis, and $\phi \in [0, 2\pi)$ is the azimuth angle counterclockwise from the positive x-axis and the projection of the point in the xy-plane. The right-handed Cartesian coordinates are related to the spherical coordinates through

$$x = r\mathrm{sin}\theta\mathrm{cos}\phi, \tag{2.1a}$$

$$y = r\mathrm{sin}\theta\mathrm{sin}\phi, \tag{2.1b}$$

$$z = r\mathrm{cos}\theta. \tag{2.1c}$$

Conversely, spherical coordinates can be related to Cartesian coordinates through.

$$r = \sqrt{x^2 + y^2 + z^2}, \tag{2.2a}$$

$$\theta = \pi/2 + \mathrm{atan}(z, \sqrt{x^2 + y^2}), \tag{2.2b}$$

$$\phi = \mathrm{atan}(y, x). \tag{2.2c}$$

where $\mathrm{atan}(\cdot)$ denotes the four-quadrant inverse tangent.

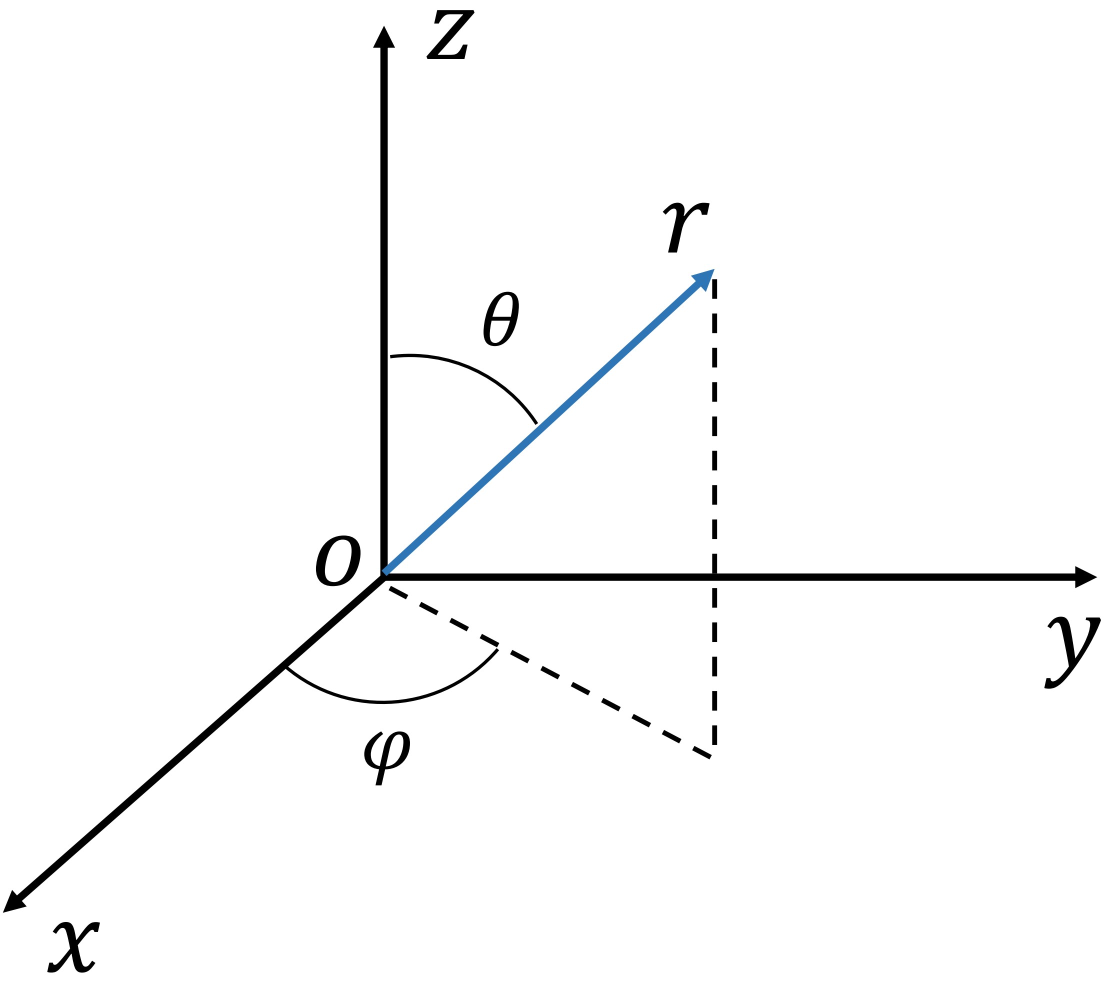

Figure 2.1: The coordinate systems: We denote the Cartesian coordinates and the spherical coordinates of a point as (x, y, z) and (r, θ, ϕ), respectively.

We define the position vector by $\boldsymbol{x} = (x, y, z) = (r, \theta, \phi)$ and the angular direction vector as

$$\hat{\boldsymbol{x}} = (\theta, \phi). \tag{2.3}$$

We have $\|\boldsymbol{x}\| = r$, where $\|\cdot\|$ denotes denotes the Euclidean norm.

2.2 Sound Propagation in Space

In a homogeneous, non-viscous, isotropic medium with stationary initial conditions, the sound propagates through this medium governed by the wave equation [106, 107, 108]

$$\nabla^2 p(t, \boldsymbol{x}) - \frac{1}{c^2} \frac{\partial^2 p(t, \boldsymbol{x})}{\partial t^2} = 0, \tag{2.4}$$

where where ∇^2 represents the Laplacian operator, t is the time index, c is the speed of sound in the given medium, and $p(t, \boldsymbol{x})$ denotes the time domain sound pressure at the position $\boldsymbol{x}$. The right-hand side of (2.4) implies that there are no sources present in the medium.

The acoustic pressure $p(t, \boldsymbol{x})$ has a time dependence expressed as

$$p(t, \boldsymbol{x}) = \int_{-\infty}^{\infty} P(f, \boldsymbol{x}) e^{-i2\pi f t}, \tag{2.5}$$

where f denotes frequency, e is Euler's number, and $i^2 = -1$ is the imaginary number. The Fourier transform of $p(t, \boldsymbol{x})$ from the time domain to the frequency domain is defined as

$$P(f, \boldsymbol{x}) = \int_{-\infty}^{\infty} p(t, \boldsymbol{x}) e^{i2\pi f t}. \tag{2.6}$$

By taking the Fourier transform of the wave equation (2.4), we can get the Helmholtz equation (or reduced wave equation) [106],

$$\nabla^2 P(k, \boldsymbol{x}) + k^2 P(k, \boldsymbol{x}) = 0, \tag{2.7}$$

where k is the wavenumber in radians per meter related to f through

$$k = \frac{2\pi f}{c}. \tag{2.8}$$

We assume that the acoustic waves propagate in a non-dispersive medium such that c is constant and independent of frequency. In this thesis, we only consider air as the medium, and with the 20°C temperature, $c = 343$m/s. Then, the wavenumber is a scalar multiple of the angular frequency ω through

$$k = \frac{\omega}{c} = \frac{2\pi}{\lambda}, \tag{2.9}$$

where $\lambda = c/f$ is the wavelength. Throughout this thesis, we may often use wavenumber k synonymous with "frequency".

The Helmholtz equation given in (2.7) is the foundation of the sound field analysis discussed in this thesis. In the following subsection, we discuss the solution of the Helmholtz equation in the spherical coordinate system using spherical harmonics basis functions to represent $P(k, \boldsymbol{x})$ at all continuous positions $\boldsymbol{x}$ within a spatial region.

2.3 Spherical Harmonic Expansion of Sound Fields

The Helmholtz equation (2.7) in the spherical coordinates becomes

$$\begin{aligned}\frac{1}{r^2}\frac{\partial}{\partial r}\left(r^2\frac{\partial P(k,\boldsymbol{x})}{\partial r}\right)+\frac{1}{r^2\sin\theta}\frac{\partial}{\partial\theta}\left(\sin\theta\frac{\partial P(k,\boldsymbol{x})}{\partial\theta}\right)\\+\frac{1}{r^2\sin^2\theta}\frac{\partial^2 P(k,\boldsymbol{x})}{\partial\phi^2}+k^2P(k,\boldsymbol{x})=0.\end{aligned}\tag{2.10}$$

The solution of (2.10) is given by separation of variables, where the solution is assumed as the product of independent functions of r, θ, and ϕ [108]. With the solution, the sound pressure $P(k,\boldsymbol{x})$ can be represented by two forms:

$$P(k,\boldsymbol{x})=\sum_{n=0}^{\infty}\sum_{m=-n}^{n}[\mathscr{a}_{nm}(k)j_n(kr)+\mathscr{a}_{nm}^{(2)}(k)y_n(kr)]Y_n^m(\theta,\phi),\tag{2.11}$$

and

$$P(k,\boldsymbol{x})=\sum_{n=0}^{\infty}\sum_{m=-n}^{n}[\mathscr{b}_{nm}(k)h_n^{(1)}(kr)+\mathscr{b}_{nm}^{(2)}(k)h_n^{(2)}(kr)]Y_n^m(\theta,\phi),\tag{2.12}$$

where $\boldsymbol{x}\equiv(r,\theta,\phi)$, $\sum_n\sum_m$ denote the double summation over spherical harmonics indexed by their order and mode. The harmonic order n is a non-negative integer that theoretically extends to infinity. However, a finite upper bound is typically imposed in practical applications to ensure computational feasibility. For each order n, the corresponding harmonic mode m is an integer ranging from $-n$ to n, inclusive (note that m is sometimes referred to as degree), $\mathscr{a}_{nm}(k)$ and $\mathscr{b}_{nm}(k)$ represent the spherical harmonic coefficients which are frequency dependent but radially independent, $j_n(\cdot)$ and $y_n(\cdot)$ are the spherical Bessel functions of the first and second kind, respectively, $h_n^{(1)}(\cdot)$ and $h_n^{(2)}(\cdot)$ denote the spherical Hankel functions of the first and second kind, respectively, and $Y_n^m(\cdot)$ is the complex Spherical harmonics basis function of order n and mode m.

Equations (2.11) and (2.12) both represent general solutions to the wave equation in a source-free region. Equation (2.11) is typically employed for modeling standing wave phenomena, while Equation (2.12) is more suitable for representing traveling waves. Depending on the specific boundary conditions and the spatial relationship between the observation region and the sound sources, these general solutions can be tailored to address two special cases: the *interior sound field* and the *exterior sound field*. Before introducing the concepts of the interior sound field and exterior sound field, we first present a detailed discussion of the spherical Bessel functions, spherical Hankel functions, and spherical harmonics in the following Subsections.

2.3.1 Spherical harmonic basis functions

Spherical harmonics are a set of complex orthonormal functions defined on the sphere surface. They are the angular part solutions of (2.10), defined as.

$$Y_n^m(\theta,\phi) = \sqrt{\frac{(2n+1)(n-m)!}{4\pi(n+m)!}}\ \mathscr{P}_n^m(\cos\theta)\ e^{im\phi}, \tag{2.13}$$

where the square root is a normalization term to keep the orthonormal property of spherical harmonics, $(\cdot)!$ represents factorial, $\mathscr{P}_n^m$ denotes the associated Legendre function given by [109]

$$\mathscr{P}_n^m(x) = \begin{cases} (-1)^m(1-x^2)^{(m/2)}\ \frac{d^m}{dx^m}\mathscr{P}_n(x) & \text{for } m \geq 0, \\ \\ (-1)^{|m|}\ \frac{(n-|m|)!}{(n+|m|)!}\ \mathscr{P}_{n|m|}(x) & \text{for } m < 0, \end{cases} \tag{2.14}$$

where $|\cdot|$ denotes the absolute value, and $\mathscr{P}_n$ are the Legendre polynomials, expressed by Rodigues' Formula as [109]

$$\mathscr{P}_n(x) = \frac{1}{2^n n!}\ \frac{d^n}{dx^n}(x^2-1)^n. \tag{2.15}$$

We list some **fundamental properties** of spherical harmonics below [108, 110]:

- Spherical harmonics are orthonormal over the sphere given by

$$\int_0^{2\pi}\int_0^{\pi} Y_n^m(\theta,\phi)(Y_{n'}^{m'}(\theta,\phi))^* \sin(\theta) d\theta d\phi = \delta_{nn'}\delta_{mm'}, \tag{2.16}$$

  where $(\cdot)^*$ denotes complex conjugate, and $\delta_{nn'}$ and $\delta_{mm'}$ are Kronecker delta functions defined as

$$\delta_{nn'} = \begin{cases} 1 & \text{if } n = n', \\ \\ 0 & \text{otherwise.} \end{cases} \tag{2.17}$$

- Complex conjugate:

$$(Y_n^m(\theta,\phi))^* = (-1)^m Y_n^{-m}(\theta,\phi). \tag{2.18}$$

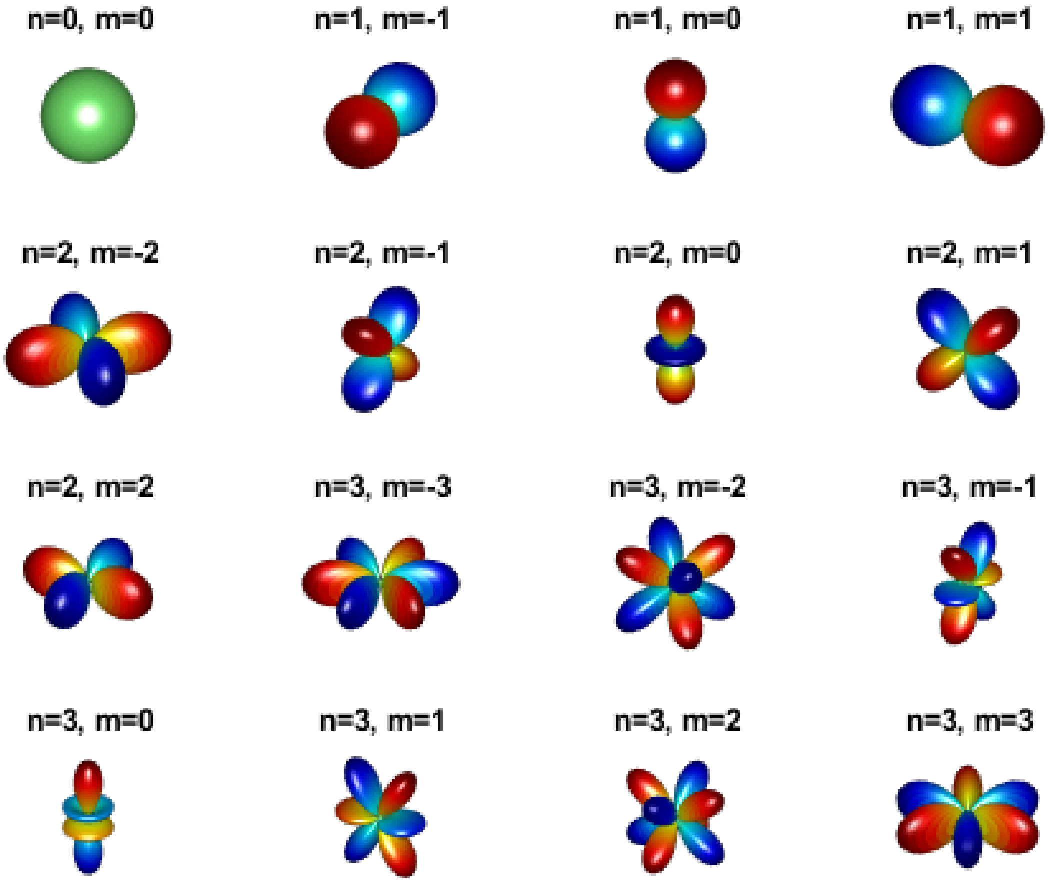

Figure 2.2: Spherical harmonic basis functions up to the 4th order.

- Integration over unit sphere:

$$\int_0^{2\pi}\int_0^{\pi} Y_n^m(\theta,\phi)\sin(\theta)d\theta d\phi = \sqrt{4\pi}\delta_{n0}\delta_{m0}. \tag{2.19}$$

- Limit on the modes: $Y_n^m(\theta,\phi) = 0 \ \ \forall |m| > n$.
- $Y_0^0(\theta,\phi)$ is constant over the sphere.
- When $m = 0$, $Y_n^m(\theta,\phi)$ are independent on ϕ and symmetric relative to the Z-axis.

2.3.2 Spherical Bessel and Hankel functions

The spherical Bessel functions $j_n(kr)$ and $y_n(kr)$ in (2.11) are real-valued function given by [108]

$$j_n(kr) = \frac{1}{\sqrt{kr}}\sqrt{\frac{\pi}{2}}J_{(n+\frac{1}{2})}(kr), \tag{2.20}$$

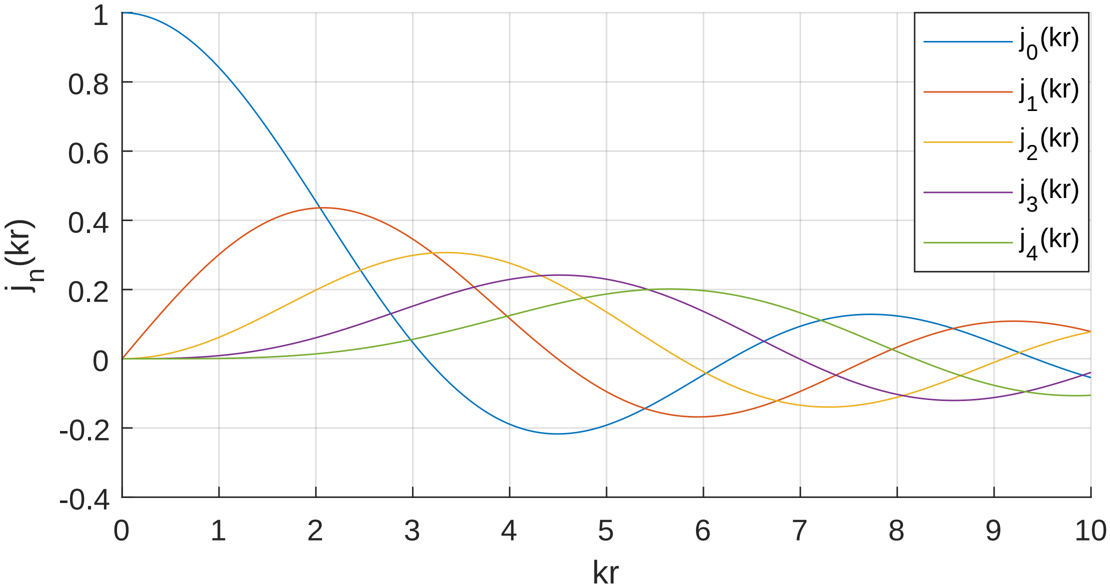

Figure 2.3: Spherical Bessel functions of the first kind up to the 4th order.

$$y_n(kr) = (-1)^{n+1}\frac{1}{\sqrt{kr}}\sqrt{\frac{\pi}{2}}J_{(-n-\frac{1}{2})}(kr), \tag{2.21}$$

where $J_n(\cdot)$ are Bessel functions.

The spherical Hankel functions $h_n^{(1)}(kr)$ and $h_n^{(2)}(kr)$i n (2.12) are complex-valued functions defined by [108]

$$h_n^{(1)}(kr) = j_n(kr) + iy_n(kr), \tag{2.22}$$

$$h_n^{(2)}(kr) = j_n(kr) - iy_n(kr). \tag{2.23}$$

It is clear that $h_n^{(1)}(kr)$ and $h_n^{(2)}(kr)$ are complex conjugate of each other.

Spherical Bessel and Hankel functions reveal the changes of sound fields in radial directions.

Interior sound field

Consider an incoming sound field as shown in Fig. 2.5, where the sound sources are located entirely outside of the region of interest (ROI) and the origin is inside the ROI. For mathematical simplicity, we define the ROI as a three-dimensional sphere of radius R_{int} centered at the origin O. If the pressure at O is finite, (2.11) can be modified to

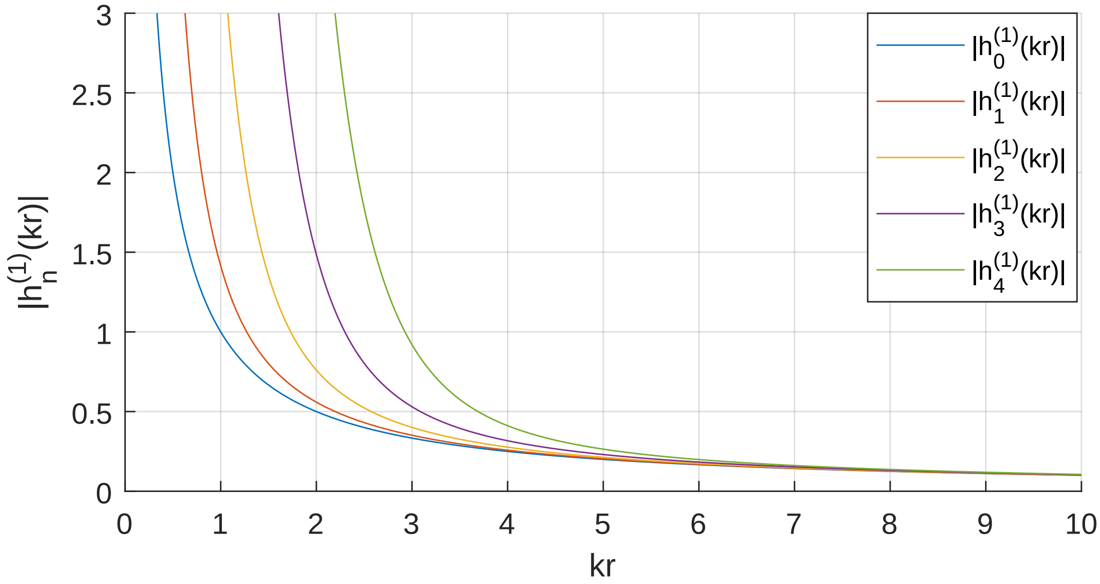

Figure 2.4: Magnitude of spherical Hankel functions of the first kind up to the 4th order.

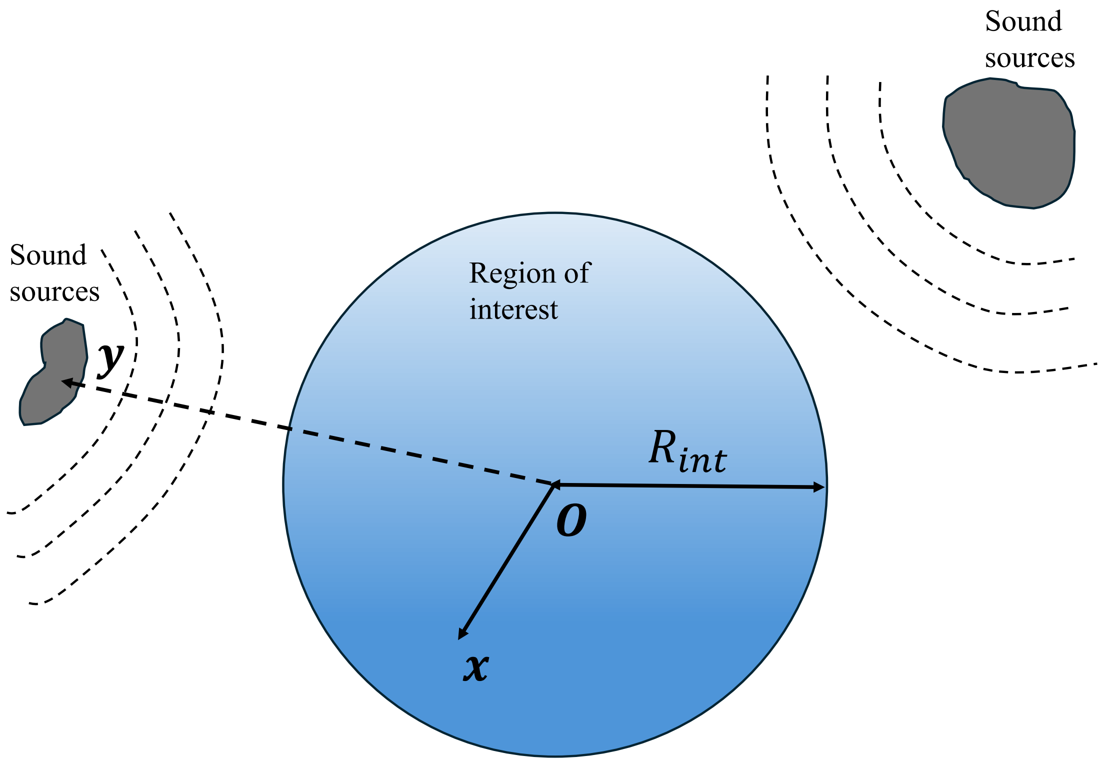

Figure 2.5: Illustration of the interior sound field, in which the valid region lies inside a spherical boundary of radius R_{int} while all sound sources are located outside this boundary. (Note: the schematic is shown in two dimensions for clarity; the actual valid region is a three-dimensional spherical volume.)

$$P(k, \boldsymbol{x}) = \sum_{n=0}^{\infty} \sum_{m=-n}^{n} a_{nm}(k) j_n(kr) Y_n^m(\theta, \phi), \tag{2.24}$$

which is the general solution of $P(k, \boldsymbol{x})$ inside ROI ($\|\boldsymbol{x}\| < R_{int}$) for this interior sound field setup.

2.3.3 Exterior sound field

On the other hand, exterior sound fields refer to an outgoing sound field located outside the outermost sound sources, as illustrated in Fig. 2.6. For mathematical simplicity, the coordinate origin is typically placed at the geometric center of the sound source distribution, and a spherical boundary of radius R_{ext} is defined to enclose all sources. The ROI for the exterior field thus lies beyond this spherical surface, potentially extending to infinity. Given that $h_n^{(2)}(kr)$ represents incoming waves that do not arise in the exterior sound field settings. Therefore, we have $b_{nm}^{(2)}(k) = 0 \; \forall n$ and (2.12) becomes to

$$P(k, \boldsymbol{x}) = \sum_{n=0}^{\infty} \sum_{m=-n}^{n} b_{nm}(k) h_n^{(1)}(kr) Y_n^m(\theta, \phi), \tag{2.25}$$

which is the general solution of $P(k, \boldsymbol{x})$ inside ROI ($\|\boldsymbol{x}\| > R_{ext}$) for this exterior sound field setup

2.4 Basic Sound Source Models

In previous Subsections, we discussed the general sound field solution for arbitrary sound sources. In this Subsection, we introduce three fundamental source models—*point sources, plane waves, and mixed-wave sources*—and present the corresponding expressions for their sound fields.

2.4.1 Point-sources

A point source is idealized as an infinitesimally small object located at a single point in three-dimensional space, which radiates spherical acoustic waves uniformly outward in all directions [108]. The outgoing sound field from a point source is governed by the inhomogeneous Helmholtz equation [111]

$$\nabla^2 P(k, \boldsymbol{x}|\boldsymbol{y}) + k^2 P(k, \boldsymbol{x}|\boldsymbol{y}) = -\delta(\boldsymbol{x} - \boldsymbol{y}), \tag{2.26}$$

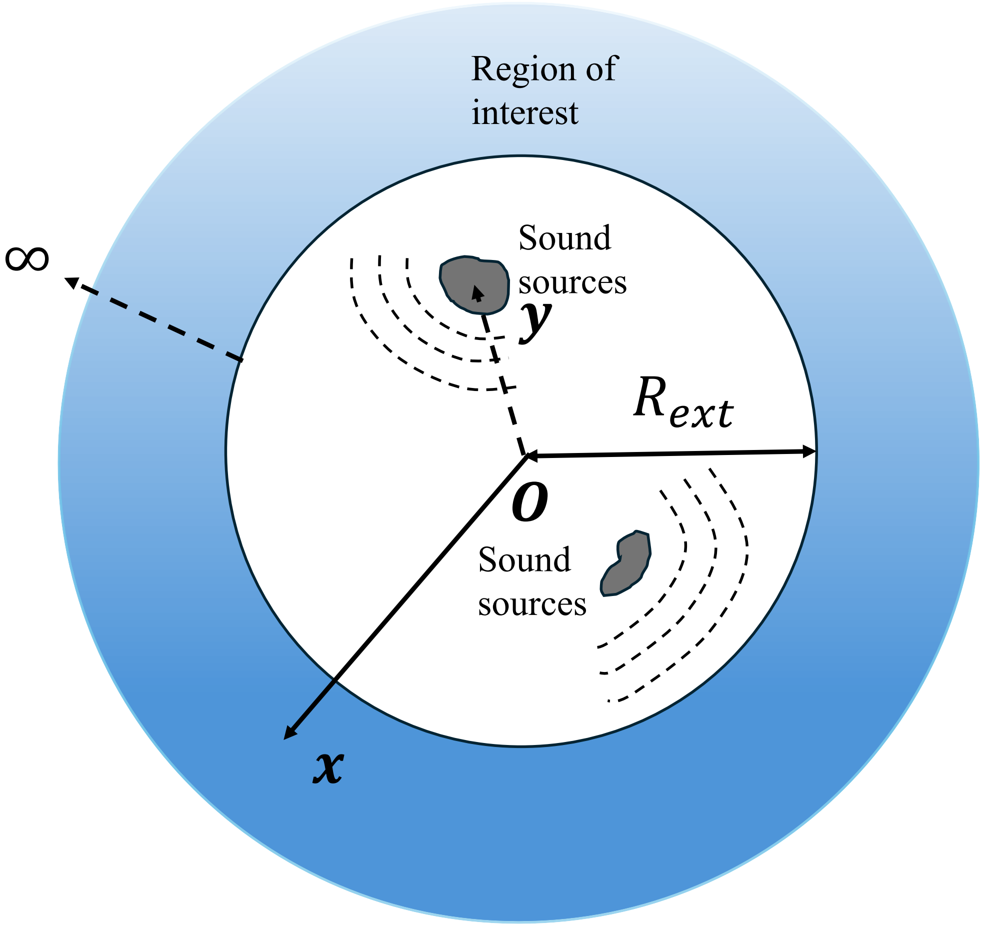

Figure 2.6: Illustration of the exterior sound field, in which the valid region lies outside a spherical boundary of radius R_{ext} that encloses all sound sources. (Note: the schematic is shown in two dimensions for clarity; the actual valid region is a three-dimensional spherical volume.)

where $P(k, \boldsymbol{x}|\boldsymbol{y})$ is the sound pressure at point $\boldsymbol{x}$ generated by a point source located at $\boldsymbol{y}$, $\delta(\cdot)$ denotes the three-dimensional Delta function. Green's function is the solution of (2.26), which satisfies the homogeneous Helmholtz equation (2.7) everywhere except the $\boldsymbol{x} = \boldsymbol{y}$ position. Green's function is given by

$$G(k, \boldsymbol{x}, \boldsymbol{y}) = \frac{e^{ik\|\boldsymbol{x}-\boldsymbol{y}\|}}{4\pi \|\boldsymbol{x}-\boldsymbol{y}\|}. \tag{2.27}$$

The point-source Green's function can be decomposed by spherical harmonics, and the expansion is given by [108]

$$\frac{e^{ik\|\boldsymbol{x}-\boldsymbol{y}\|}}{4\pi\|\boldsymbol{x}-\boldsymbol{y}\|} = \begin{cases} \sum\limits_{n=0}^{\infty}\sum\limits_{m=-n}^{n} ikh_n^{(1)}(k\|\boldsymbol{y}\|)(Y_n^m(\hat{\boldsymbol{y}}))^* j_n(k\|\boldsymbol{x}\|)Y_n^m(\hat{\boldsymbol{x}})), & \text{if } \|\boldsymbol{y}\| > \|\boldsymbol{x}\|, \\ \sum\limits_{n=0}^{\infty}\sum\limits_{m=-n}^{n} ikj_n(k\|\boldsymbol{y}\|)(Y_n^m(\hat{\boldsymbol{y}}))^* h_n^{(1)}(k\|\boldsymbol{x}\|)Y_n^m(\hat{\boldsymbol{x}})), & \text{if } \|\boldsymbol{y}\| < \|\boldsymbol{x}\|. \end{cases} \tag{2.28}$$

Note that the expansion above does not include the sound field evaluated at the source position $\boldsymbol{y}$. Instead, two cases are considered based on the relative radial distance between the observer point $\boldsymbol{x}$ and the source location $\boldsymbol{y}$.

In the first case, when $\|\boldsymbol{y}\| > \|\boldsymbol{x}\|$, the source is located entirely outside the ROI, corresponding to the interior sound field formulation discussed in (2.24). Accordingly, the coefficient is given by

$$a_{nm}(k) = ikh_n^{(1)}(k\|\boldsymbol{y}\|)(Y_n^m(\hat{\boldsymbol{y}}))^*. \tag{2.29}$$

In the second case, when $\|\boldsymbol{y}\| < \|\boldsymbol{x}\|$, the source is enclosed within the ROI, corresponding to the exterior sound field as defined in (2.25). In this case, the coefficient becomes

$$b_{nm}(k) = ikj_n(k\|\boldsymbol{y}\|)(Y_n^m(\hat{\boldsymbol{y}}))^*. \tag{2.30}$$

Note that the above definition of point sources is for the outgoing or outward traveling waves ($e^{-i\omega t}$). For incoming or inward traveling waves ($e^{i\omega t}$), (2.27), (2.28), (2.30), and (2.29) change to

$$G(k,\boldsymbol{x},\boldsymbol{y}) = \frac{e^{-ik\|\boldsymbol{x}-\boldsymbol{y}\|}}{4\pi\|\boldsymbol{x}-\boldsymbol{y}\|}, \tag{2.31}$$

$$\frac{e^{-ik\|\boldsymbol{x}-\boldsymbol{y}\|}}{4\pi\|\boldsymbol{x}-\boldsymbol{y}\|} = \begin{cases} \sum\limits_{n=0}^{\infty}\sum\limits_{m=-n}^{n} -ikh_n^{(2)}(k\|\boldsymbol{y}\|)(Y_n^m(\hat{\boldsymbol{y}}))^* j_n(k\|\boldsymbol{x}\|)Y_n^m(\hat{\boldsymbol{x}})), & \text{if } \|\boldsymbol{y}\| > \|\boldsymbol{x}\|, \\ \sum\limits_{n=0}^{\infty}\sum\limits_{m=-n}^{n} -ikj_n(k\|\boldsymbol{y}\|)(Y_n^m(\hat{\boldsymbol{y}}))^* h_n^{(2)}(k\|\boldsymbol{x}\|)Y_n^m(\hat{\boldsymbol{x}})), & \text{if } \|\boldsymbol{y}\| < \|\boldsymbol{x}\|, \end{cases} \tag{2.32}$$

$$a_{nm}(k) = -ikh_n^{(2)}(k\|\boldsymbol{y}\|)(Y_n^m(\hat{\boldsymbol{y}}))^*, \tag{2.33}$$

and

$$b_{nm}(k) = -ikj_n(k\|\boldsymbol{y}\|)(Y_n^m(\hat{\boldsymbol{y}}))^*, \tag{2.34}$$

respectively.

2.4.2 Plane waves

A plane wave is the limiting case of a spherical wave emitted by a point source located at an infinite distance ($|\boldsymbol{y}| \to \infty$) from the point of observation, such that the curvature of the wavefront becomes negligible and the wavefront appears flat (planar). By performing far-field transition, and handling normalisation, we can model the sound field generated from a unit amplitude plane wave by

$$P(k, \boldsymbol{x}|\boldsymbol{y}) = e^{-ik\hat{\boldsymbol{y}}\cdot\boldsymbol{x}}, \tag{2.35}$$

where $\hat{\boldsymbol{y}}$ denotes the incident direction of the plane wave, and $k\hat{\boldsymbol{y}} \cdot \boldsymbol{x}$ is the inner product between $\boldsymbol{x}$ and the wavenumber vector $\boldsymbol{k} = k\hat{\boldsymbol{y}}$, with magnitude k and propagation direction given by (θ_y, ϕ_y). The dot product can be written explicitly in spherical coordinates as

$$k\hat{\boldsymbol{y}} \cdot \boldsymbol{x} = kr(\sin(\theta_y)\sin(\theta)\cos(\phi_y - \phi) + \cos(\theta_y)\sin(\theta)). \tag{2.36}$$

The spherical harmonics expansion of (2.35) is given as

$$e^{-k\hat{\boldsymbol{y}}\cdot\boldsymbol{x}} = \sum_{n=0}^{\infty}\sum_{m=-n}^{n} 4\pi(-i)^n (Y_n^m(\hat{\boldsymbol{y}}))^* j_n(k\left\|\boldsymbol{x}\right\|) Y_n^m(\hat{\boldsymbol{x}})), \quad \left\|\boldsymbol{y}\right\| \gg \left\|\boldsymbol{x}\right\|. \tag{2.37}$$

As the plane wave source is located at infinity, the sound field generated by a plane wave can be related back to the interior sound field setup, and the SHs coefficients can be found by

$$a_{nm}(k) = 4\pi(-i)^n (Y_n^m(\hat{\boldsymbol{y}}))^*. \tag{2.38}$$

Note that the above definition of point sources is for the outgoing or outward traveling waves ($e^{-i\omega t}$). For incoming or inward traveling waves ($e^{i\omega t}$), (2.35), (2.37), and (2.38) change to

$$P(k, \boldsymbol{x}|\boldsymbol{y}) = e^{ik\hat{\boldsymbol{y}}\cdot\boldsymbol{x}}, \tag{2.39}$$

$$e^{k\hat{\boldsymbol{y}}\cdot\boldsymbol{x}} = \sum_{n=0}^{\infty}\sum_{m=-n}^{n} 4\pi(i)^n (Y_n^m(\hat{\boldsymbol{y}}))^* j_n(k\left\|\boldsymbol{x}\right\|) Y_n^m(\hat{\boldsymbol{x}})), \quad \left\|\boldsymbol{y}\right\| \gg \left\|\boldsymbol{x}\right\|, \tag{2.40}$$

and

$$a_{nm}(k) = 4\pi(i)^n (Y_n^m(\hat{\boldsymbol{y}}))^*, \tag{2.41}$$

respectively.

2.4.3 Mixed-wave sources

The point sources and plane waves that we discussed in previous Subsections represent the near-field and far-field sound propagation model, respectively. The mixed-wave source is proposed to unify the mathematical expression of both near-field and far-field sound fields [112, 113]. The mixed-wave source is not a physical sound source model, but a mathematical expression for equivalent sources. For outgoing or outward traveling waves, the sound pressure at an arbitrary position $\boldsymbol{x}$ generated by a mixed-wave source at $\boldsymbol{y}$ can be expressed by

$$P(k, \boldsymbol{x}|\boldsymbol{y}) = \|\boldsymbol{y}\| \, e^{-ik\|\boldsymbol{y}\|} \frac{e^{ik\|\boldsymbol{x}-\boldsymbol{y}\|}}{4\pi \|\boldsymbol{x}-\boldsymbol{y}\|}. \tag{2.42}$$

In the near-field, (2.42) is equal to the point source Green's function with a scaling factor $e^{-ik\|\boldsymbol{y}\|}$. In the far-field, (2.42) represents a scaled plane-wave sound field as

$$\lim_{\|\boldsymbol{y}\|\to\infty} \|\boldsymbol{y}\| \, e^{-ik\|\boldsymbol{y}\|} \frac{e^{ik\|\boldsymbol{x}-\boldsymbol{y}\|}}{4\pi \|\boldsymbol{x}-\boldsymbol{y}\|} = \frac{e^{-ik\hat{\boldsymbol{y}}\cdot\boldsymbol{x}}}{4\pi}. \tag{2.43}$$

Based on the spherical harmonics decomposition, (2.42) can be expanded as

$$e^{-ik\|\boldsymbol{y}\|} \frac{e^{ik\|\boldsymbol{x}-\boldsymbol{y}\|}}{4\pi \|\boldsymbol{x}-\boldsymbol{y}\|} = \sum_{n=0}^{\infty} \sum_{m=-n}^{n} ik \, \|\boldsymbol{y}\| \, e^{-ik\|\boldsymbol{y}\|} h_n^{(1)}(k \, \|\boldsymbol{y}\|)(Y_n^m(\hat{\boldsymbol{y}}))^* j_n(k \, \|\boldsymbol{x}\|) Y_n^m(\hat{\boldsymbol{x}}). \tag{2.44}$$

As the mixed-wave source satisfies the interior sound field condition. Then, the corresponding spherical harmoncs coefficients can be found by

$$a_{nm}(k) = ik \, \|\boldsymbol{y}\| \, e^{-ik\|\boldsymbol{y}\|} h_n^{(1)}(k \, \|\boldsymbol{y}\|)(Y_n^m(\hat{\boldsymbol{y}}))^*. \tag{2.45}$$

Note that the above definition of point sources is for the outgoing or outward traveling waves ($e^{-i\omega t}$). For incoming or inward traveling waves ($e^{i\omega t}$), (2.42), (2.43), (2.44), and (2.45) change to

$$P(k, \boldsymbol{x}|\boldsymbol{y}) = \|\boldsymbol{y}\| \, e^{ik\|\boldsymbol{y}\|} \frac{e^{-ik\|\boldsymbol{x}-\boldsymbol{y}\|}}{4\pi \|\boldsymbol{x}-\boldsymbol{y}\|}, \tag{2.46}$$

$$\lim_{\|\boldsymbol{y}\|\to\infty} \|\boldsymbol{y}\| \, e^{ik\|\boldsymbol{y}\|} \frac{e^{-ik\|\boldsymbol{x}-\boldsymbol{y}\|}}{4\pi \|\boldsymbol{x}-\boldsymbol{y}\|} = \frac{e^{k\hat{\boldsymbol{y}}\cdot\boldsymbol{x}}}{4\pi}, \tag{2.47}$$

$$e^{ik\|\boldsymbol{y}\|}\frac{e^{-ik\|\boldsymbol{x}-\boldsymbol{y}\|}}{4\pi\|\boldsymbol{x}-\boldsymbol{y}\|}=\sum_{n=0}^{\infty}\sum_{m=-n}^{n}-ik\|\boldsymbol{y}\|e^{ik\|\boldsymbol{y}\|}h_n^{(2)}(k\|\boldsymbol{y}\|)(Y_n^m(\hat{\boldsymbol{y}}))^{*}j_n(k\|\boldsymbol{x}\|)Y_n^m(\hat{\boldsymbol{x}})), \tag{2.48}$$

and

$$a_{nm}(k)=-ik\|\boldsymbol{y}\|e^{ik\|\boldsymbol{y}\|}h_n^{(2)}(k\|\boldsymbol{y}\|)(Y_n^m(\hat{\boldsymbol{y}}))^{*}, \tag{2.49}$$

respectively.

The mixed-wave formulation is sensitive to the choice of coordinate definition. In particular, different choices of the coordinate origin lead to different values of the scaling factor $\|\boldsymbol{y}\|e^{-ik\|\boldsymbol{y}\|}$. Moreover, the observation point cannot coincide with the equivalent source location $\boldsymbol{y}$, and $\boldsymbol{y}$ itself cannot be chosen as the coordinate origin.

2.5 Active Noise Control

In this section, we briefly introduce the background theory of ANC. We take the Filtered-x Least Mean Square (FxLMS) algorithm as an example and introduce the single-channel feed-forward system and the multi-channel feed-forward system in Subsections 2.5.1 and 2.5.2 respectively.

2.5.1 Single-channel feed-forward system

A feedforward adaptive ANC system typically includes a reference microphone, an error microphone, a secondary source, and an adaptive algorithm [114]. A block diagram of FxLMS [115, 116] algorithm is shown in Fig. 2.7, where P is the primary path which is the acoustic impulse responses from the reference sensor to error microphone, S denotes the secondary path which is the impulse response from the secondary source to the error sensor, $\hat{S}$ represents estimated secondary path, $\boldsymbol{W}=[W_0,W_1,...,W_{L_w-1}]^T$ is the adaptive filter with the filter order of L_w, and $e(n)$ is the instantaneous error microphone measurement.

The error signal recorded by the error microphone for each iteration is given by

$$e(n)=v(n)+S*d(n), \tag{2.50}$$

where n is the iteration number, $v(n)$ is the primary noise field at the error microphone, $*$ denotes linear convolution, and $d(n)$ is the secondary source driving signal, given by

$$d(n) = \boldsymbol{x}(n) * \boldsymbol{W}(n), \tag{2.51}$$

where $\boldsymbol{x}(n) = [x(n), x(n-1), ..., x(n-L_M+1)]^T$ are the input reference signal.

By minimizing the mean square value of the error signal $e(n)$, the associated cost function can be expressed as:

$$\mathscr{L}(n) = e(n)^2. \tag{2.52}$$

The update equation is thus derived using the steepest descent method, and is given by

$$\boldsymbol{W}(n+1) = \boldsymbol{W}(n) - \frac{\lambda}{2}\nabla\mathscr{L}(n), \tag{2.53}$$

where λ is the step size, and ∇ is the gradient operator.

By taking the the derivative of $\mathscr{L}(n)$ with respect to $\boldsymbol{W}(n)$, we obtain

$$\nabla\mathscr{L}(n) = 2e(n)\boldsymbol{x}(n) * \hat{S}, \tag{2.54}$$

where $\hat{\boldsymbol{S}}$ can be obtained by measuring the impulse response between the secondary loudspeaker and the error microphone.

By substituting (2.54) into (2.53), we obtain the final update equation for the FxLMS feedforward adaptive filtering algorithm as

$$\boldsymbol{W}(n+1) = \boldsymbol{W}(n) - \lambda e(n)\boldsymbol{x}(n) * \hat{S}. \tag{2.55}$$

From (2.55), we observe that $\boldsymbol{W}$ for the next iteration depends on the current error signal and the filtered reference signal vector.

2.5.2 Multi-channel feed-forward system

The single-channel feedforward adaptive filtering algorithm discussed earlier is limited to reducing noise at only one point. We now consider the multi-channel case, which employs multiple error microphones and secondary loudspeakers to achieve noise reduction over a broader area.

We have a multi-channel feed-forward ANC system with J reference sensors, Q number of error microphones, and L number of secondary loudspeakers. The block diagram of the commonly used FxLMS multi-channel [117, 118] algorithm is shown in Fig. 2.8. The reference input signals are $x_j(n),\ j = 1, ..., J$, and the instantaneous error microphone measurements are $e_q(n),\ q = 1, ..., Q$.

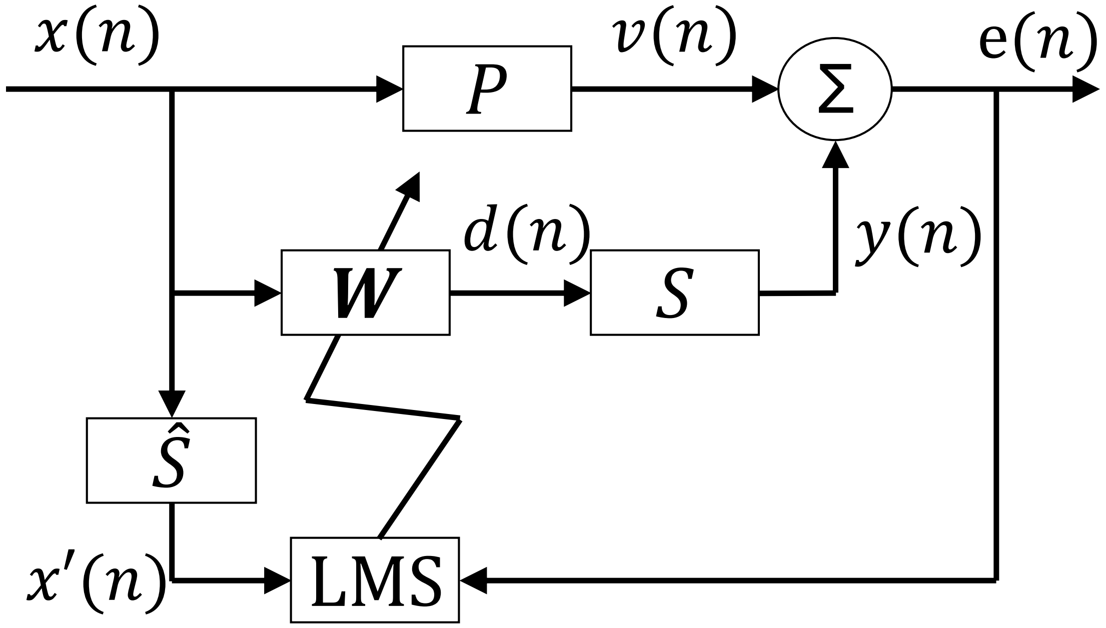

Figure 2.7: Block diagram of a signal channel FxLMS feed-forward ANC system.

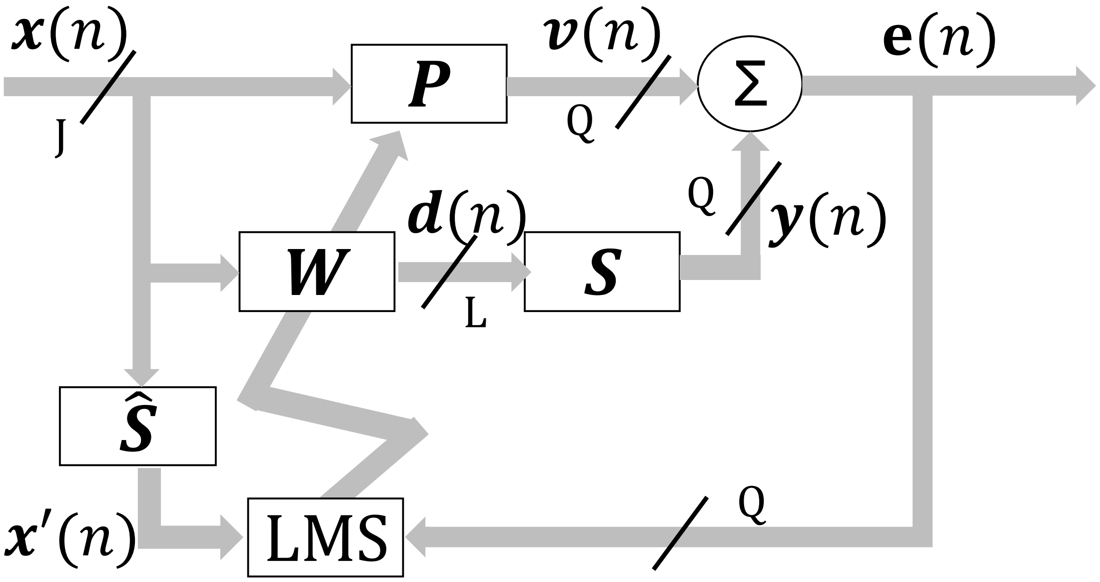

Figure 2.8: Block diagram of a multi-channel FxLMS feed-forward ANC system.

The error signal at the q-th error microphone is given by

$$e_q(n) = v_q(n) + y_q(n), \tag{2.56}$$

where $v_q(n)$ is the primary noise field on the q-th microphone, and $y_q(n)$ is the secondary noise field on the q-th microphone, given by

$$y_q(n) = \sum_{l=1}^{L} d_l(n) * S_{lq}, \tag{2.57}$$

where S_{lq} denotes the impulse response from the l-th secondary source to the q-th error microphone, and $d_l(n)$ is the driving signal of the l-th secondary loudspeaker, $l = 1, 2, ..., L$, generated as

$$d_l(n) = \sum_{j=1}^{J} \boldsymbol{W}_{jl}^T(n)\boldsymbol{x}_j(n), \tag{2.58}$$

where $\boldsymbol{W}_{jl} = [W_{jl,0}, W_{jl,1}, ..., W_{jl,L_w-1}]^T$ are the adaptive filter coefficients of the l-th loudspeaker at the n iteration, and $\boldsymbol{x}_j(n) = [x_j(n), x_j(n-1), ..., x_j(n-Lw+1)]^T$ is the reference signal at the j-th reference microphone.

In a multi-channel feedforward ANC system, the cost function is defined as the sum of the mean squared error signals from all error microphones:

$$\mathcal{L}(n) = \sum_{q=1}^{Q} |e_q(n)|^2. \tag{2.59}$$

Therefore, the update equation of the multi-channel FxLMS algorithm for the filter coefficient $\boldsymbol{W}_{jl}(n)$ is given by:

$$\boldsymbol{W}_{jl}(n+1) = \boldsymbol{W}_{jl}(n) - \lambda \sum_{q=1}^{Q} e_q(n)\boldsymbol{x}_j(n) * \hat{S}_{lq}, \tag{2.60}$$

where $\hat{S}_{lq}$ is the estimated S_{lq}, usually obtained by the impulse response measurement.

Compared to single-channel ANC systems, multi-channel configurations offer improved noise control across multiple locations, making them suitable for spatial ANC applications. However, this comes at the cost of increased computational complexity. The number and placement of microphones and loudspeakers are critical to system performance, with the positioning of error microphones being particularly important for accurately estimating the residual noise field and achieving effective noise reduction.

2.6 Physics-informed Neural Networks in Audio and Acoustics

In this section, we provide a concise overview of physics-informed neural networks (PINNs) and their emerging applications in audio and acoustics.

PINNs are a class of deep learning models that incorporate prior physical knowledge, typically in the form of partial differential equations (PDEs), directly into the learning process [119, 120]. Unlike conventional purely data-driven approaches, PINNs constrain the solution space of neural networks by enforcing the satisfaction of governing equations, boundary conditions, and initial values. PINNs have been widely implemented in diverse scientific fields, including fluid physics [121, 122, 123, 124, 125, 126, 127], thermodynamics [128, 129, 130], and medical imaging [131, 132, 133, 134, 135].

In the field of audio and acoustics, the propagation of sound pressure $p(\boldsymbol{x}, t)$ in a homogeneous medium is often described by the wave equation (2.4). For time-harmonic (steady-state) acoustics, the equation reduces to the Helmholtz equation (2.7). In PINNs, a neural network $\boldsymbol{p}_\beta(t, \boldsymbol{x})$ in the time-domain or $\boldsymbol{p}_\beta(k, \boldsymbol{x})$ in the frequency-domain is trained not only to fit measured data but also to satisfy these equations. The physics is encoded in the loss function $\mathscr{L}(\beta)$, which includes both a data loss and a physics loss, given by

$$\mathscr{L}(\beta) = \mathscr{L}_{\text{Data}} + \lambda_{\text{PDE}} \mathscr{L}_{\text{PDE}}, \tag{2.61}$$

where β denotes model parameters, $\mathscr{L}_{\text{Data}}$ is the date loss, λ_{PDE} is a weighting factor, and $\mathscr{L}_{\text{PDE}}$ is the PDE loss, given by

$$\mathscr{L}_{\text{PDE}} = \begin{cases} \|\nabla^2 \boldsymbol{p}_\beta(t, \boldsymbol{x}) + \frac{1}{c} \frac{\partial^2 \boldsymbol{p}_\beta(t, \boldsymbol{x})}{\partial t^2}\|^2 & \text{in the time-domain,} \\ \\ \|\nabla^2 \boldsymbol{p}_\beta(k, \boldsymbol{x}) + k^2 \boldsymbol{p}_\beta(k, \boldsymbol{x})\|^2 & \text{in the frequency-domain.} \end{cases} \tag{2.62}$$

PINNs have demonstrated their advantages in various topics in audio and acoustics, including sound field estimation and reconstruction [136, 137, 138, 139, 140, 141, 142, 143], nearfield acoustics holography [144], and room impulse response reconstruction [145, 146, 147]. Although PINNs have demonstrated great potential in the field of acoustics, the idea of adding the PDE loss to existing neural network architectures has some limitations, such as susceptibility to local minima, poor interpretability, and limited generalizability beyond the sampled data range. These limitations motivate the development of novel architectures, such as the point-neuron network introduced in Chapter 4, that directly embed known Green's functions or modal solutions into the network design, yielding improved convergence, transparency, and out-of-sample robustness.

2.7 Summary

In this chapter, we first introduced the fundamental concepts of spatial sound field processing, with an emphasis on spherical harmonics representations, which provide the theoretical foundation for the methods developed in the following chapters. Next, we reviewed conventional single-channel and multi-channel feedforward ANC systems, outlining their basic principles and differences. Finally, we provided a brief overview of PINNs and their emerging applications in audio and acoustics.

Chapter 3

Spherical Sector Harmonics Based Sectorial Sound Field Reconstruction and Extrapolation

Overview: *Developing spherical sector harmonics (SSHs) offers a valuable framework for sound field decomposition and analysis within a spherical sector region, which benefits the drone noise modeling over a sectorial region. Despite their potential in spatial audio applications, a comprehensive investigation into their properties and limitations remains absent. This chapter bridges this gap by analyzing SSH performance in two key problems: sectorial sound field reconstruction and extrapolation. First, we identify and prove fundamental limitations of SSHs: (i) SSHs are not exact solutions of the wave equation due to the shifting and scaling of input arguments in the associated Legendre polynomials and exponential functions; (ii) severe distortions occur near the sector boundaries when using SSHs for sound field reconstruction, necessitating a larger measurement region than the target reconstruction area; and (iii) the spherical Hankel and Bessel functions are unsuitable as radial functions for SSH-based extrapolation. To address these limitations, we propose a mapping-based sectoral extrapolation method that significantly enhances extrapolation accuracy, particularly for interior regions. Furthermore, the improved extrapolation method enables the directional drone sound field estimation using an on-board sectorial microphone array, thereby advancing the development of directional drone active noise control.*

3.1 Introduction

Spherical harmonics (SHs) and SH-based spherical microphone array processing [148, 149, 150, 151] are wildly used in various spatial audio applications, including sound source localization [152, 153, 154, 155], beamforming [156, 157], sound field recordings [158], and noise cancellation [159, 160, 161, 162, 163]. However, the construction of spherical arrays can be challenging and infeasible in certain applications, such as drone-related applications in which whole sphere sampling is infeasible. To address the whole sphere sampling challenge, an orthonormal function set was developed for an accurate representation of pressure over an arbitrary spherical sector region, named spherical sector harmonics (SSHs) [164]. Although SSH has the potential to be implemented in various audio and acoustics problems, including using an on-board sectorial microphone array to estimate the drone's outgoing sound field, a thorough investigation of it needs to be included. In this chapter, we conduct comprehensive investigations of SSHs in the problem of sectorial sound field reconstruction and extrapolation, which is the foundation of SSH-based drone directional sound field modeling.

SHs can decompose the sound field into angular-dependent orthonormal functions and corresponding coefficients, allowing the analysis of a spatial sound field with a finite number of SH coefficients. The idea of using an open spherical microphone array to capture high-order sound fields was first introduced by Abhayapala and Ward [148]. Meyer and Elko designed a microphone array over a rigid sphere to realize the above [149]. Rafaely [150] and Duraiswami [165] further contributed to the design and analysis of spherical arrays, and Rafaely later proposed a dual-sphere microphone array [151]. While the concept and ongoing research on SH-based spherical array processing bring significant benefits to the field of spatial audio and acoustics, the whole sphere sampling requirement hinders its implementation in some applications.

To approximate the directivity pattern with data available only within a limited range of directions, Zotter and Pomberger introduced the concept of spherical Slepian functions [166]. These functions form an orthogonal basis specifically designed for the restricted directional range of the sphere, particularly for rotationally symmetric regions such as spherical caps or segments [166, 167]. While spherical Slepian functions enable the decomposition and reconstruction of the sound field within a spherical cap or segment, they require frequency-dependent matrix inversion and may introduce significant errors for sources outside the restricted range [167]. By solving the Helmholtz equation, with sound-soft or sound-hard boundary conditions, the spherical cap and segment harmonics were proposed in [167, 168] and have been validated by the microphone array prototypes [169, 170]. As the spherical cap and segment harmonics satisfy the Helmholtz equation, it can be implemented to interpolate and extrapolate the sound field. However, to apply the spherical cap and segment harmonics, the target region has to be bounded by a sound-soft or sound-hard boundary, significantly limiting its broader implementations, including drone sound field modeling.

Further addressing the need for microphone processing over arbitrary spherical sector regions, Kumari and Kumar developed SSHs that decompose and represent the sound pressure over a spherical sector region [164]. This advancement reduces the sampling requirements, simplifies microphone array construction, and expands its application to ANC [34], beamforming [171, 172], sound source localization [171, 173]. Compared to spherical cap and segment harmonics, SSH does not require the sound-soft or sound-hard boundary to bind the spherical sector region, so that it can be potentially applied to broader applications.

While SSHs have demonstrated potential in spatial audio applications, a thorough investigation of them needs to be included. In this chapter, we delve into the properties and performance of SSHs in the problem of sectorial sound field reconstruction and extrapolation. Firstly, we investigate and prove the following limitations of SSHs: i) SSHs are not solutions of the wave equation due to the shifting and scaling of the input arguments for the associated Legendre polynomials and exponential function; ii) There is a severe distortion around the edge of the sector region when using SSHs for sound field reconstruction, indicating the measurement region should be larger than the target region; iii) The spherical Hankel and Bessel functions are not the corresponding radial functions for SSHs to perform radial extrapolation. Furthermore, we proposed a mapping based sectorial extrapolation method that can improve the extrapolation performance.

The rest of this chapter is organized as follows. In Section 3.2.2, we briefly review the theory of SHs and SSHs and prove that SSHs violate the wave equation. We discuss the sectorial sound field reconstruction and distortion problem in Section 3.4 and demonstrate that the spherical Hankel and Bessel functions are not the corresponding radial functions for SSH to perform radial extrapolation in Section 3.4.2. The mapping based extrapolation method is introduced and evaluated in Section 3.6.

3.2 Spherical Sector Harmonics

This section first reviews the theory of SHs and SSHs, highlighting the differences between them, and then proves that SSHs violate the wave equation. We use the spherical coordinates (r, θ, ϕ) to describe the location of a point, where r is the Euclidean distance to the point from the origin, $\theta \in [0, \pi]$ is the elevation angle measured from the positive z-axis, and $\phi \in [0, 2\pi)$ is the azimuth angle expressed counterclockwise from the positive x-axis on the xy-plane [174].

3.2.1 Spherical sector harmonics sound field processing

A sound field over a spherical region can be decomposed by SHs as

$$P(r, \theta, \phi, k) \approx \sum_{n=0}^{N_h} \sum_{m=-n}^{n} C_n^m(k) F_n(kr) Y_n^m(\theta, \phi), \tag{3.1}$$

where $k = 2\pi f/c$ is the wave number with f the frequency and c the speed of sound propagation, $C_n^m(k)$ is the radial independent SH coefficient, $F_n(kr)$ named the radial function which is the solution of the wave equation for the radial direction in the spherical coordinate, $N_h \geq \lceil kr \rceil (\lceil \cdot \rceil$ is the ceiling operation) [112] is the truncation order of SH decomposition, and $Y_n^m(\cdot)$ is the spherical harmonics of n-th order and m-th degree, defined by

$$Y_n^m(\theta, \phi) = \sqrt{\frac{(2n+1)(n-m)!}{4\pi(n+m)!}} \mathcal{P}_n^m(\cos\theta) e^{im\phi}, \tag{3.2}$$

where $\mathcal{P}_n^m(\cdot)$ is the associated Legendre polynomial of n-th order and m-th degree, and $e^{im\phi}$ is the exponential function of m-th degree.

For the interior case, where the source is located outside of the sphere, $F_n(kr) = j_n(kr)$ is the first kind of spherical Bessel function n-th order; for the exterior case, where the source is inside the sphere, $F_n(kr) = h_n^{(1)}(kr)$ is the spherical Hankel function of the first kind of n-th order. Generally, the sound field can be a combination of these two cases with distinct radial-independent SH coefficients for the interior and exterior parts [108].

Similarly, a sound field over a spherical sector region ($\theta \in [\theta_1, \theta_2]$, $\phi \in [\phi_1, \phi_2]$) can be decomposed by SSHs as [164].

$$P(r, \theta, \phi, k) \approx \sum_{n=0}^{N_s} \sum_{m=-n}^{n} \Gamma_n^m(r, k) T_n^m(\theta, \phi), \tag{3.3}$$

where $T_n^m(\theta,\phi)$ is is the spherical sector harmonics of n-th order and m-th degree, $\Gamma_n^m(r,k)$ are the SSH coefficients, $N_s \geq \lceil kr \rceil$ is the truncation order of SSH decomposition [164]. $T_n^m(\theta,\phi)$ can be expressed as [164]

$$T_n^m(\theta,\phi) = \begin{cases} K_n^m \mathscr{P}_n^m(q_1\text{cos}\theta + q_2)e^{jmu\phi} \\ \qquad \forall\ 0 \leq n \leq \infty, 0 \leq m \leq n, \\ (-1)^{|m|} T_n^{|m|*}(\theta,\phi) \\ \qquad \forall\ -n \leq m < 0, \end{cases} \tag{3.4}$$

where K_n^m is the normalization constant which can be calculated by

$$K_n^m = \sqrt{\frac{(2n+1)(n-m)!q_1 u}{4\pi(n+m)!}}, \tag{3.5}$$

q_1 and q_2 are the shift coefficients that transform $\mathscr{P}_n^m(\cdot)$ to the shifted associated Legendre polynomials $\mathscr{P}_n^m(q_1\text{cos}\theta + q_2)$, and u is the scale coefficient that changes the exponential function $e^{jm\phi}$ to the scaled exponential functions $e^{jmu\phi}$. These coefficients depend on the spherical sector region, represented by

$$\begin{aligned} &q_1 = 2/(\text{cos}\theta_1 - \text{cos}\theta_2), \\ &q_2 = -(\text{cos}\theta_1 + \text{cos}\theta_2)/(\text{cos}\theta_1 - \text{cos}\theta_2), \\ &u = 2\pi/(\phi_2 - \phi_1). \end{aligned} \tag{3.6}$$

As $\theta_2 > \theta_1$ and $\phi_2 > \phi_1$, based on (3.6), we have $q_1 \in [1,\infty), q_2 \in (-\infty,\infty)$ and $u \in [1,\infty)$. When $\theta_1 = 0$, $\theta_1 = \pi$, $\phi_1 = 0$, and $\phi_2 = 2\pi$, SSH reduces to SH.

According to (3.2) and (3.4), SSH is similar to the definition of SH but contains the shifted associated Legendre polynomials $\mathscr{P}_n^m(q_1\text{cos}\theta + q_2)$ and scaled exponential functions $e^{jmu\phi}$ rather than the associated Legendre polynomials $\mathscr{P}_n^m(\text{cos}\theta)$ and exponential functions $e^{jm\phi}$. This transformation effectively maps the sector region onto a whole sphere. However, the mapping process violates the wave equation in the elevational direction and azimuthal direction, which is proved in the following subsection.

3.2.2 Violation of the wave equation

Consider an arbitrary spherical sector region $\theta \in [\theta_1,\theta_2]$, $\phi \in [\phi_1,\phi_2]$. The related SSH function is shown in (3.4), defined in the spherical coordinates. Therefore, if SSHs are solutions of the wave equation, they should satisfy the wave equation in spherical coordinates, shown in (3.7) below:

$$\begin{aligned}&\frac{1}{r^2}\frac{\partial}{\partial r}(r^2\frac{\partial p}{\partial r})+\frac{1}{r^2\sin\theta}\frac{\partial}{\partial\theta}(\sin\theta\frac{\partial p}{\partial\theta})\\&+\frac{1}{r^2\sin^2\theta}\frac{\partial^2 p}{\partial\phi^2}-\frac{1}{c^2}\frac{\partial^2 p}{\partial t^2}=0,\end{aligned}\tag{3.7}$$

where p is the sound pressure at an observation point (r,θ,ϕ) at time t. By separation of variables, we have

$$p(r,\theta,\phi,t)=\mathbf{R}(r)\mathbf{\Theta}(\theta)\mathbf{\Phi}(\phi)\mathbf{T}(t),\tag{3.8}$$

and (3.7) can be rewritten to four ordinary differential equations:

$$\frac{d^2\mathbf{\Phi}}{d\phi^2}+m^2\mathbf{\Phi}=0,\tag{3.9a}$$

$$\frac{1}{\sin\theta}\frac{d}{d\theta}(\sin\theta\frac{d\mathbf{\Theta}}{d\theta})+[n(n+1)-\frac{m^2}{\sin^2\theta}]\mathbf{\Theta}=0,\tag{3.9b}$$

$$\frac{1}{r^2}\frac{d}{dr}(r^2\frac{d\mathbf{R}}{dr})+k^2\mathbf{R}-\frac{n(n+1)}{r^2}\mathbf{R}=0,\tag{3.9c}$$

$$\frac{1}{c^2}\frac{d^2\mathbf{T}}{dt^2}+k^2\mathbf{T}=0.\tag{3.9d}$$

Considering a single frequency case, with (3.3) and (3.4), we have

$$\begin{aligned}p(r,\theta,\phi,t)=&e^{-j\omega t}\sum_{n=0}^{\infty}\sum_{m=-n}^{n}\Gamma_n^m(r,k)K_n^m\\&\times\mathscr{P}_n^m(q_1\mathrm{cos}\theta+q_2)e^{jmu\phi},\end{aligned}\tag{3.10}$$

where $\omega=kc$ is the radial frequency. Then, based on (3.8), (3.9), and (3.10), for SSHs to be considered solutions of the wave equation, $\mathscr{P}_n^m(q_1\mathrm{cos}\theta+q_2)$ should satisfy (3.9b), and $e^{jmu\phi}$ should satisfy (3.9a).

Elevational direction

We first provide our proof in the elevational direction. We use $\mathbf{U}(\theta)$ to represent the shifted associated Legendre polynomials

$$\mathbf{U}(\theta)=\mathscr{P}_n^m(q_1\cos\theta+q_2).\tag{3.11}$$

when $\theta \in [\theta_1, \theta_2]$, $\phi \in [\phi_1, \phi_2]$. Let $\zeta = q_1 \mathrm{cos}\theta + q_2$, and we have $\zeta \in [-1, 1]$. Based on the chain rule [175], the left-hand side of (3.9b) can be rewritten as

$$\begin{aligned} &\frac{1}{\sin\theta}\frac{d}{d\theta}(\sin\theta\frac{d\mathbf{U}}{d\theta}) + [n(n+1) - \frac{m^2}{\sin^2\theta}]\mathbf{U} \\ &= q_1^2\frac{d}{d\zeta}[(1-(\zeta-q_2)^2/q_1^2)\frac{d\mathscr{P}_n^m(\zeta)}{d\zeta}] \\ &+ [n(n+1) - \frac{m^2}{1-(\zeta-q_2)^2/q_1^2}]\mathscr{P}_n^m(\zeta). \end{aligned} \tag{3.12}$$

$\mathscr{P}_n^m(\cdot)$ has the following property [108]

$$\frac{d}{dx}[(1-x^2)\frac{d\mathscr{P}_n^m(x)}{dx} + [n(n+1) - \frac{m^2}{1-x^2}]\mathscr{P}_n^m(x) = 0. \tag{3.13}$$

When $q_1 = 1$ and $q_2 = 0$, (3.12) can be simplified as

$$\frac{d}{d\zeta}[(1-\zeta^2)\frac{d\mathscr{P}_n^m(\zeta)}{d\zeta} + [n(n+1) - \frac{m^2}{1-\zeta^2}]\mathscr{P}_n^m(\zeta). \tag{3.14}$$

From (3.13) and (3.14), we observe that when $q_1 = 1$ and $q_2 = 0$, $\mathbf{U}$ satisfies (3.9b). However, for $q_1 \neq 1$ or $q_2 \neq 0$, (3.12) does not match the left-hand side of (3.13).

To further prove that SSHs are not solutions of the wave equation, we take a specific example $\mathscr{P}_2^0(\zeta) = (3\zeta^2 - 1)/2$ [109] into (3.12) and have

$$12q_2\zeta + 3q_1^2 - 3q_2^2 - 3 \neq 0, \tag{3.15}$$

when $q_1 \neq 1$ or $q_2 \neq 0$. Thus, the shifted associated Legendre polynomials in SSH violate (3.9b) and are not a solution of the wave equation.

Azimuthal direction

The validity of the azimuthal direction is also examined. We use $\mathbf{V}(\phi)$ to represent the scaled exponential function and have

$$\mathbf{V}(\phi) = e^{jmu\phi}. \tag{3.16}$$

By taking (3.16) into the left-hand side of (3.9a), we have

$$-m^2u^2e^{jmu\phi} + m^2e^{jmu\phi}. \tag{3.17}$$

From (3.17), we can find that only when $u = 1$, $\mathbf{V}$ satisfies (3.9a).

Based on the proof provided above, it is evident that SSHs can satisfy the wave equation only when $q_1 = 1$, $q_2 = 0$, and $u = 1$. In this special case, SSHs become SHs, which are indeed solutions of the wave equation. However, for any other values of q_1, q_2, and u, SSHs do not fulfill the wave equation.

3.3 Sectorial Sound Field Reconstruction and Distortion Problem

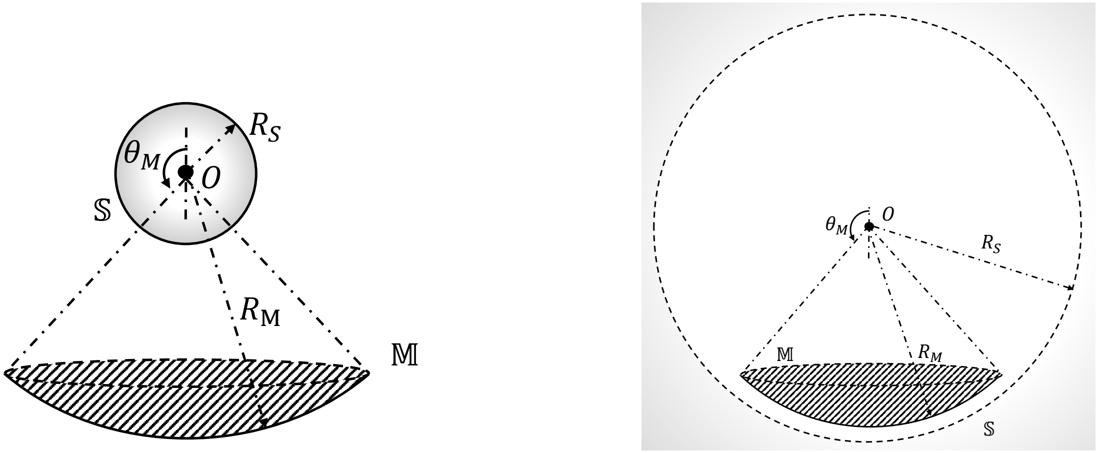

(a) (b)

Figure 3.1: Spherical sector sound field reconstruction setups for (a) exterior case and (b) interior case. Illustration of the sound source region $\mathbb{S}$ and the measurement region $\mathbb{M}$.

The sound field decomposition and reconstruction are fundamental steps in SSH-based sound field processing. We classify the reconstruction problem into exterior and interior cases. As shown in Fig. 3.1, microphones are positioned within the sector region $\mathbb{M}$ to measure the sound field. The target region $\mathbb{T}$ is set to be the same as $\mathbb{M}$, and our goal is to reconstruct the sound field at any arbitrary point within this region. For the exterior case, as shown in Fig. 3.1a, the sound sources are located inside the sphere $\mathbb{S}$ $(\theta \in [0, \pi], \phi \in [0, 2\pi), r \leq R_S, R_S < R_M)$. For the interior case, as shown in Fig. 3.1b, sound sources are located outside of a spherical region $\mathbb{S}$ $(\theta \in [0, \pi], \phi \in [0, 2\pi), r \geq R_S, R_S > R_M)$.

For the measurement region $\mathbb{S}$, the related SSH coefficients $\boldsymbol{\Gamma} = [\Gamma_0^0, \Gamma_1^{-1}, ..., \Gamma_{N_s}^{N_s}]^T$ can be found by

$$\boldsymbol{\Gamma} = \boldsymbol{L}_q^{\dagger} \boldsymbol{p}_q, \tag{3.18}$$

where $(\cdot)^{\dagger}$ denotes the pseudo-inverse operation, $\boldsymbol{p}_q = [P(\boldsymbol{x}_1, k), P(\boldsymbol{x}_2, k), ..., P(\boldsymbol{x}_Q, k)]^T$ is a $Q \times 1$ vector that contains the sound pressure measurements over the sector region by Q microphones $(Q \geq (N_s + 1)^2)$, with the coordinate $\boldsymbol{x}_q = (r_q, \theta_q, \phi_q)$, and $\boldsymbol{L}_q$ denotes the $Q \times (N_s+1)^2$ matrix of SSHs, expressed as

$$\boldsymbol{L}_q = \begin{bmatrix} T_0^0(\theta_1,\phi_1) & \cdots & T_{N_s}^{N_s}(\theta_1,\phi_1) \\ \vdots & \ddots & \vdots \\ T_0^0(\theta_Q,\phi_Q) & \cdots & T_{N_s}^{N_s}(\theta_Q,\phi_Q) \end{bmatrix}. \tag{3.19}$$

After estimating $\boldsymbol{\Gamma}$ with (3.18), the sound field can be reconstructed using (3.3).

While this process is similar to sound field decomposition and reconstruction in SH processing, it can lead to severe distortions around the edges of the spherical sector region. These distortions are caused by mapping the spherical sector to a whole sphere. As illustrated in Fig. 3.2, points over the two latitudinal edges of the sector region ($\theta = \theta_1, \phi \in [\phi_1, \phi_2)$ or $\theta = \theta_2, \phi \in [\phi_1, \phi_2)$) are mapped to the two poles of the sphere ($\theta = 0, \phi = 0$ or $\theta = \pi, \phi = 0$) during the mapping process of shifted associated Legendre polynomials. Similarly, points over the two longitudinal edges of the sector region ($\theta \in [\theta_1, \theta_2]$, $\phi = \phi_1$ or $\theta \in [\theta_1, \theta_2]$, $\phi = \phi_2$) are mapped to one longitude line of the sector region ($\theta \in [\theta_1, \theta_2]$, $\phi = 0$) during the mapping process of scaled exponential functions. These mappings lead to information loss over the edge of the sector region, causing the distortion around the sector edge.

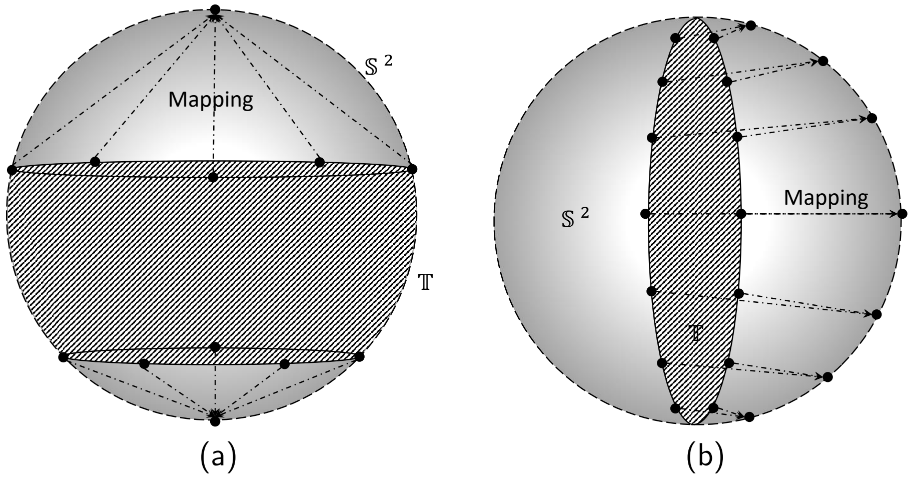

Figure 3.2: Illustration of the mapping process for both elevation angle and azimuth angle perspective: (a) map the target spherical sector region $\mathbb{T}$ ($\theta \in [\theta_1, \theta_2], \phi \in [0, 2\pi)$) to a whole sphere $\mathbb{S}^2$ ($\theta \in [0, \pi], \phi \in [0, 2\pi)$); (b) map the target spherical sector region $\mathbb{T}$ ($\theta \in [0, \pi], \phi \in [\phi_1, \phi_2)$) to a whole sphere $\mathbb{S}^2$ ($\theta \in [0, \pi], \phi \in [0, 2\pi)$).

We investigate this distortion problem by simulations. For the exterior case, we place three unit strength point sources with the Cartesian coordinates $(0.5, 0, 0)$ m, $(0, 0.5, 0)$ m, and $(0, 0, 0.5)$ m. For the interior case, we place three unit strength point sources with the Cartesian coordinates $(3, 0, 0)$ m, $(0, 3, 0)$ m, and $(0, 0, 3)$ m. We analyse the sound field reconstruction distortion over a sector region $\mathbb{T}$ with $\theta_1 = 1/3\pi, \theta_2 = 2/3\pi, \phi_1 = 0, \phi_2 = \pi$, and the radius $R_T = 1$ m. The measurement region $\mathbb{M}$ is the same as $\mathbb{T}$. Microphones are placed over $\mathbb{M}$ with nearly uniform distribution, with $Q = 100$ for the 300 Hz setup and $Q = 300$ for the 700 Hz setup. The reconstruction error over elevation direction $\epsilon_e(\theta, k)$ and azimuth direction $\epsilon_a(\phi, k)$ is defined as

$$\epsilon_e(\theta, k) = 20\log_{10}\Big(\frac{\sum_{u=1}^{U_a} |P_T(R_T, \theta, \phi_u, k) - \hat{P}_T(R_T, \theta, \phi_u, k)|}{\sum_{u=1}^{U_a} |P_T(R_T, \theta, \phi_u, k)|}\Big), \tag{3.20}$$

and

$$\epsilon_a(\phi, k) = 20\log_{10}\Big(\frac{\sum_{u=1}^{U_e} |P_T(R_T, \theta_u, \phi, k) - \hat{P}_T(R_T, \theta_u, \phi, k)|}{\sum_{u=1}^{U_e} |P_T(R_T, \theta_u, \phi, k)|}\Big), \tag{3.21}$$

respectively, where P_T is the exact sound field over the target region, $\hat{P}_T$ is the estimated sound field over the target region, U_a is the number of samples along the azimuth direction, U_e is the number of samples along the elevation direction. In the simulation, we set $U_a = U_e = 203$, then in total, we have 41209 sampling points over $\mathbb{T}$.

The results depicted in Fig. 3.3 and Fig. 3.4 reveal that the distortion appears around all four edges of $\mathbb{T}$ in both the exterior and interior cases, and the distortion is more severe as it approaches the edges. Due to this distortion issue, to enhance the performance of SSH in decomposition and reconstruction, the measurement region $\mathbb{M}$ should be larger than $\mathbb{T}$.

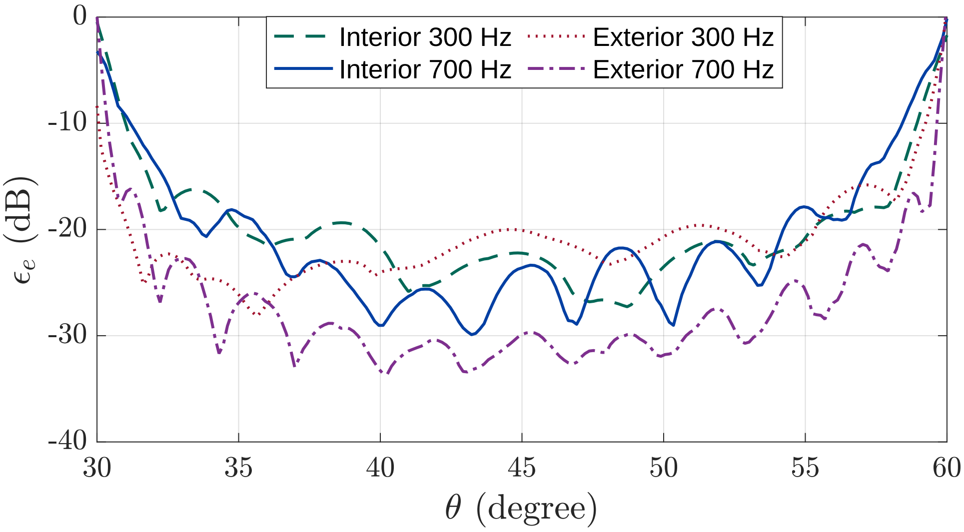

Figure 3.3: Reconstruction error in the elevation direction $\epsilon_e(\theta, k)$ with different θ values.

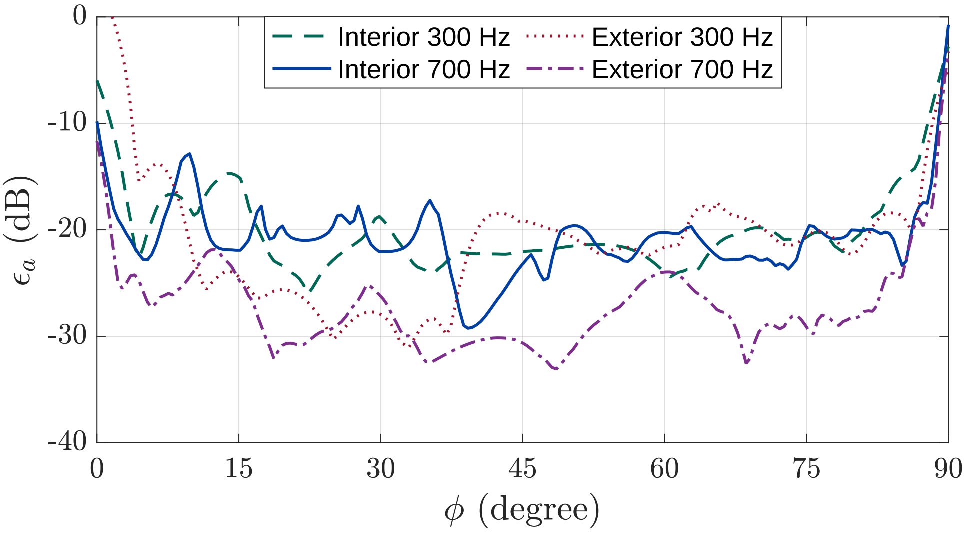

Figure 3.4: Reconstruction error in the azimuth direction $\epsilon_a(\phi, k)$ with different ϕ values.

3.4 Sectorial Sound Field Extrapolation by Spherical Sector Harmonics

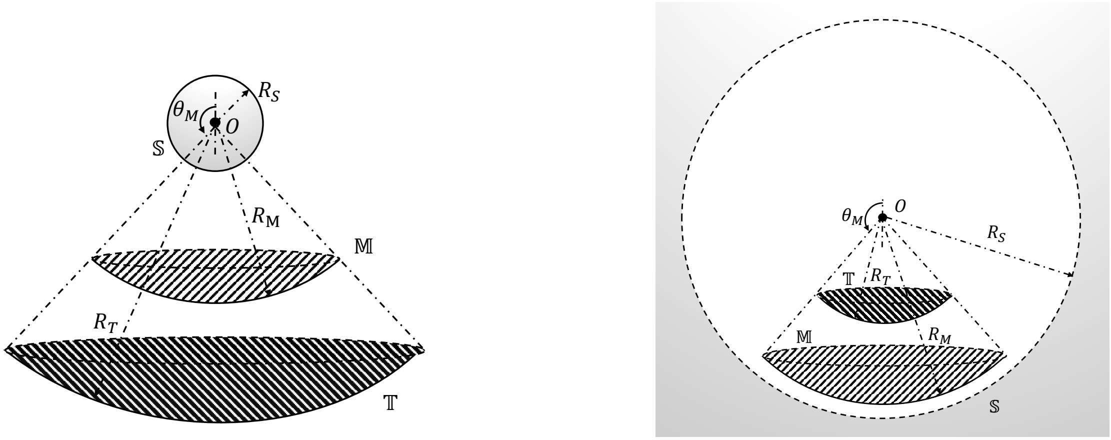

(a) (b)

Figure 3.5: Spherical sector sound field radial extrapolation setups for (a) exterior case and (b) interior case. Illustration of the sound source region $\mathbb{S}$, the measurement region $\mathbb{M}$, and the extrapolation region $\mathbb{T}$.

Sound field radial extrapolation is an essential property of SHs. With (3.1), we can extrapolate the sound field from the measured sphere to another sphere with a different radius. This property enables us to analyze the sound field over the space with a measurement on a sphere and is implemented in many acoustics applications, such as ANC [176, 177, 178] and sound field reproduction [179, 180]. As SSHs are not solutions of the wave equation, shown in Section 3.2.2, the radial function is not theoretically guaranteed to present the sound field changes in the radial direction.

Therefore, analyzing the feasibility of conducting the radial extrapolation with SSHs is important. In this section, we investigate whether SSHs possess a similar extrapolation property to SHs and can decompose the sound field with radially independent coefficients.

As shown in Fig. 3.5, radial extrapolation of spherical sector sound fields involves estimating the sound field at a larger (or smaller) radius based on measurements taken from a spherical sector region. Specifically, the sound field measured on the spherical surface $\mathbb{M}$ (where $\theta \in [\theta_M, \pi]$, $\phi \in [0, 2\pi)$, and $r = R_M$) is extrapolated to a concentric target region $\mathbb{T}$ (with the same angular range but at radius $r = R_T$). Radial extrapolation can be classified into exterior and interior cases. For the exterior case, as shown in Fig. 3.5a, the sound sources are located inside the sphere $\mathbb{S}$ $(\theta \in [0, \pi], \phi \in [0, 2\pi), r \leq R_S, R_S < R_M)$, and we extrapolate the sound field to the outer target region $\mathbb{T}$ $(R_T \geq R_M)$. For the interior case, as shown in Fig. 3.5b, sound sources are located outside of a spherical region $\mathbb{S}$ $(\theta \in [0, \pi], \phi \in [0, 2\pi), r \geq R_S, R_S > R_M)$, and we extrapolate the sound field to the inner target region $\mathbb{T}$ $(R_T \leq R_M)$.

To test the performance of radial functions in SSH radial extrapolation, we create a similar equation (3.22) with reference to (3.1),

$$P(r, \theta, \phi, k) = \sum_{n=0}^{\infty} \sum_{m=-n}^{n} \kappa_n^m(k) F_n(kr) T_n^m(\theta, \phi), \tag{3.22}$$

where $\kappa_n^m(k)$ is the radial independent SSH coefficient. If (3.22) is valid, κ_n^m can be calculated by

$$\boldsymbol{\kappa} = \boldsymbol{M}_q^{\dagger} \boldsymbol{p}_q, \tag{3.23}$$

where $\boldsymbol{\kappa} = [\kappa_0^0, \kappa_1^{-1}, ..., \kappa_{N_s}^{N_s}]^T$, $\boldsymbol{M}_q$ denotes a $Q \times (N_s + 1)^2$ matrix that contains the multiplication of SSHs and the radial function, expressed as

$$\boldsymbol{M}_q = \begin{bmatrix} T_0^0(\theta_1, \phi_1) F_0(kr_1) & \cdots & T_{N_s}^{N_s}(\theta_1, \phi_1) F_{N_s}(kr_1) \\ \vdots & \ddots & \vdots \\ T_0^0(\theta_Q, \phi_Q) F_0(kr_Q) & \cdots & T_{N_s}^{N_s}(\theta_Q, \phi_Q) F_{N_s}(kr_Q) \end{bmatrix}. \tag{3.24}$$

Simulations are conducted to test the validity of (3.22) for both exterior and interior cases. To calculate the extrapolation error, $U = 5214$ points are placed over $\mathbb{T}$ according to the nearly uniform sampling. The extrapolation error $\epsilon(k)$ is defined as

$$\epsilon(k) = 20\log_{10}\left(\frac{\sum_{u=1}^{U} |P_T(\boldsymbol{x}_u, k) - \hat{P_T}(\boldsymbol{x}_u, k)|}{\sum_{u=1}^{U} |P_T(\boldsymbol{x}_u, k)|}\right), \tag{3.25}$$

where $P_T(\cdot)$ is the exact sound field over $\mathbb{T}$, $\hat{P_T}(\cdot)$ is the extrapolated sound field over $\mathbb{T}$.

3.4.1 Exterior case

We test the validity of (3.22) using three unit strength point sources with Cartesian coordinates $(0.5, 0, 0)$ m, $(0, 0.5, 0)$ m, and $(0, 0, 0.5)$ m. First, we investigate the extrapolation performance within a small sector region defined by $\theta_M = 2/3\pi$, $R_M =$ 1 m, $R_T = R_M$, and $R_T = 5R_M$. We then estimate the sound field using (3.22) and (3.23).

Extrapolation results are presented in Fig. 3.6. Notably, when $R_T = R_M$, the sound field estimation is accurate and matches the ground truth. However, when $R_T > R_M$, the extrapolated sound field deviates from the actual sound field, which means we cannot conduct an accurate extrapolation with (3.22) in this example.

Subsequently, we investigate the extrapolation performance under various conditions, including different frequencies (f = 300, 500, 700, and 900 Hz), sizes of $\mathbb{T}$ ($\theta_M = 45°, 75°, 105°$, and $135°$), and distances between R_T and R_M (ranging from 0 to 19 λ, where λ is the wavelength). We keep R_M = 1 m constant, and the distance between R_T and R_M is represented in units of wavelength (λ). Additionally, we ensure an adequate number of microphones ($Q = \lceil 1.3(N_s + 1)^2 \rceil$) for the simulations.

The following observations can be made from the results shown in Fig. 3.7: i) The extrapolation error (ϵ) increases rapidly within a distance of 2λ and gradually saturates as the distance grows; ii) Lower frequencies yield faster convergence of ϵ to smaller values; iii) Smaller sector regions tend to result in larger ϵ values;

Based on simulation results, we find that (3.22) alone cannot accurately extrapolate the sector sound field under the exterior case. However, under certain conditions, such as low frequencies, large sector regions, and small distances from the measurement region, (3.22) can still provide acceptable estimations of the extrapolated sound field.

3.4.2 Interior case

Plane wave

For the interior case, we first validate the sound field extrapolation with a unit-amplitude plane wave source arriving from the direction $\theta_A = \pi$, $\phi_A = 0$. The setups

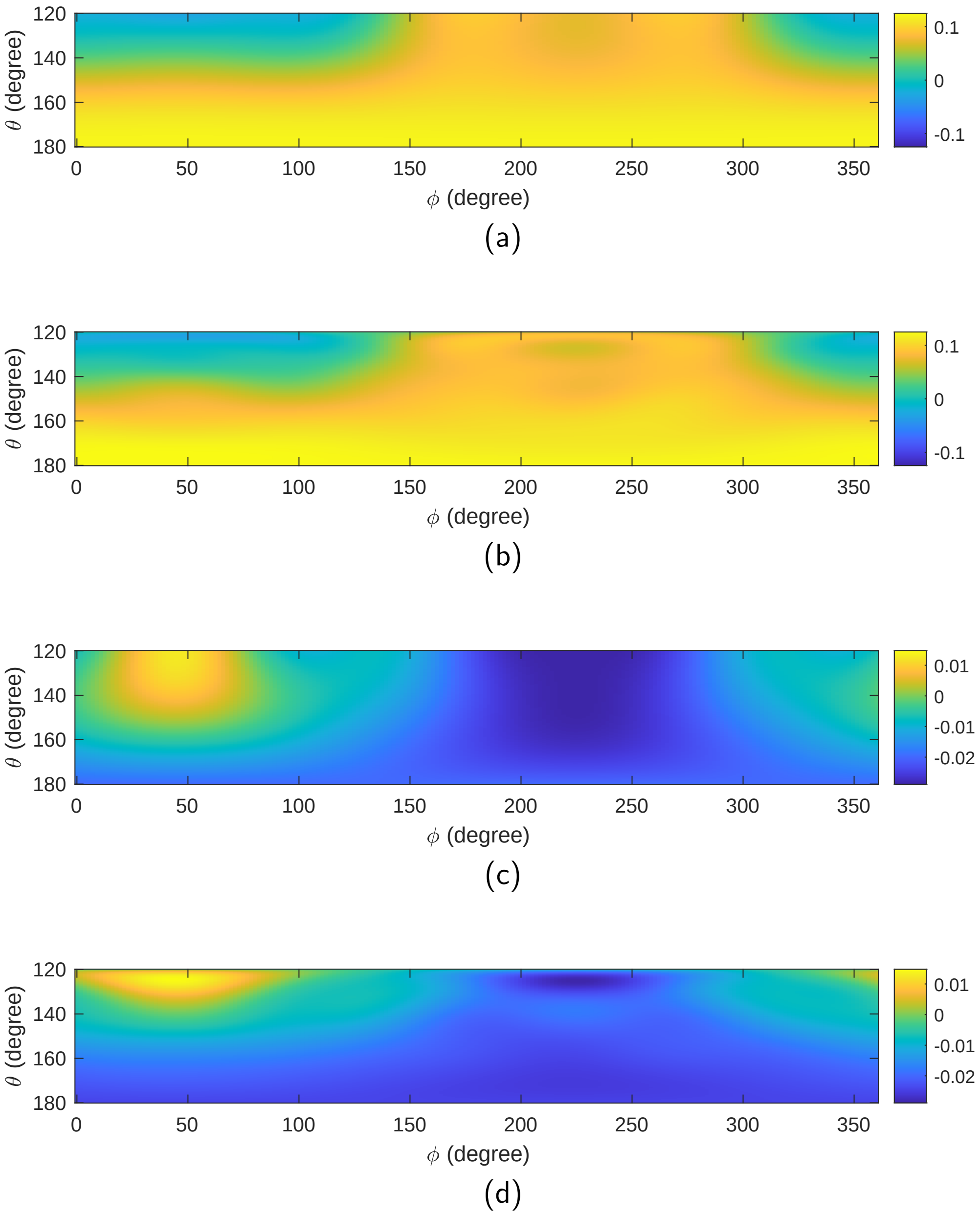

(a)

(b)

(c)

(d)

Figure 3.6: Spherical sector sound field radial extrapolation for the exterior case, with $\theta_M = 120$, $R_M = 1$ m, $f = 300$ Hz, $Q = 100$: (a) sector sound field with $R_T = 1$ m; (b) estimated sound field with $R_T = 1$ m; (c) sector sound field with $R_T = 5$ m; (d) estimated sound field with $R_T = 5$ m.

for $\mathbb{M}$ and microphone placement are the same as in the exterior case. We estimate the sound field for different inner concentric sector regions with $R_T = R_M$ and $0.6R_M$. Results are shown in Fig. 3.8 below. We observe that: i) when $R_T = R_M$, we can accurately estimate the plane wave shape over $\mathbb{T}$; ii) compared to the exterior case, when $R_T \neq R_M$, the estimation error is significantly larger.

Then, we analyze the extrapolation performance with different settings of frequencies

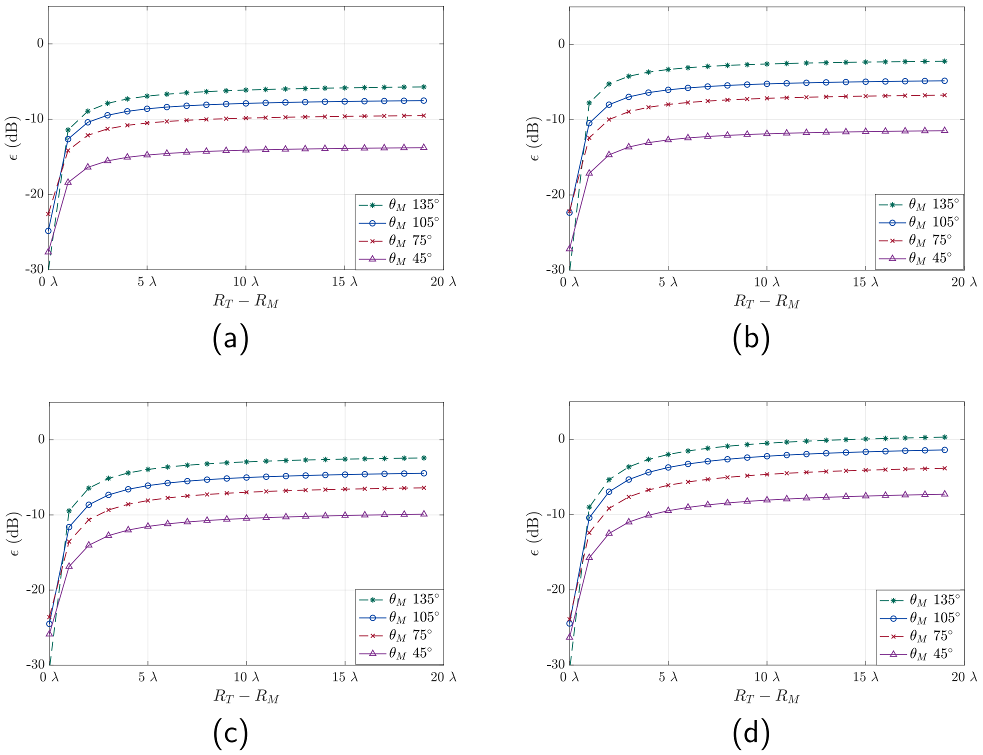

(a) (b)

(c) (d)

Figure 3.7: Extrapolation error ϵ for the exterior case with different settings of frequencies, sizes of $\mathbb{T}$, and distances between R_T and R_M: (a) extrapolation error with 300 Hz; (b) extrapolation error with 500 Hz; (c) extrapolation error with 700 Hz; (d) extrapolation error with 900 Hz.

(f = 300, 500, 700, and 900 Hz), size of $\mathbb{T}$ ($\theta_M = 45°, 75°, 105°$, and $135°$), and distances between R_T and R_M. We consistently set $R_M = 1$ m and $Q = \lceil 1.3(N_s + 1)^2 \rceil$. With $0 < R_T \leq R_M$, we only analyze the distances between R_T and R_M from 0 to 0.7 λ. Results are shown in Fig. 3.9 which demonstrates that: i) ϵ increases sharply within 0.1λ distance; ii) ϵ reaches the largest value when the distance is in the range of 0.3λ to 0.5 λ and decrease or fluctuates around the peak value when the distance further increases; iii) compared to Fig. 3.7, we have larger ϵ in Fig. 3.9, and the dependency of the error on the frequency and the size of $\mathbb{T}$ is less regular Fig. 3.9.

We additionally explore the impact of arrival direction by varying θ_A from 0° to 180° in increments of 10°, while keeping $\phi_A = 0°$ and $f = 300$ Hz. We conduct simulations with varying θ_M settings and distances between $\mathbb{T}$ and $\mathbb{M}$. The results are illustrated in Fig. 3.10, leading us to the following observations: i) The extrapolation error ϵ exhibits symmetry around $\theta_A = 90°$; ii) For $R_T = R_M$, ϵ is small and particularly responsive to changes in θ_A, especially with larger θ_M; iii) When $R_T = R_M$, ϵ rises from its minimum value to a peak at $\theta_A = 90°$, and then descends back to its minimum again; iv) If $R_T \neq R_M$, ϵ is larger and less sensitive to directions in θ_A; v)

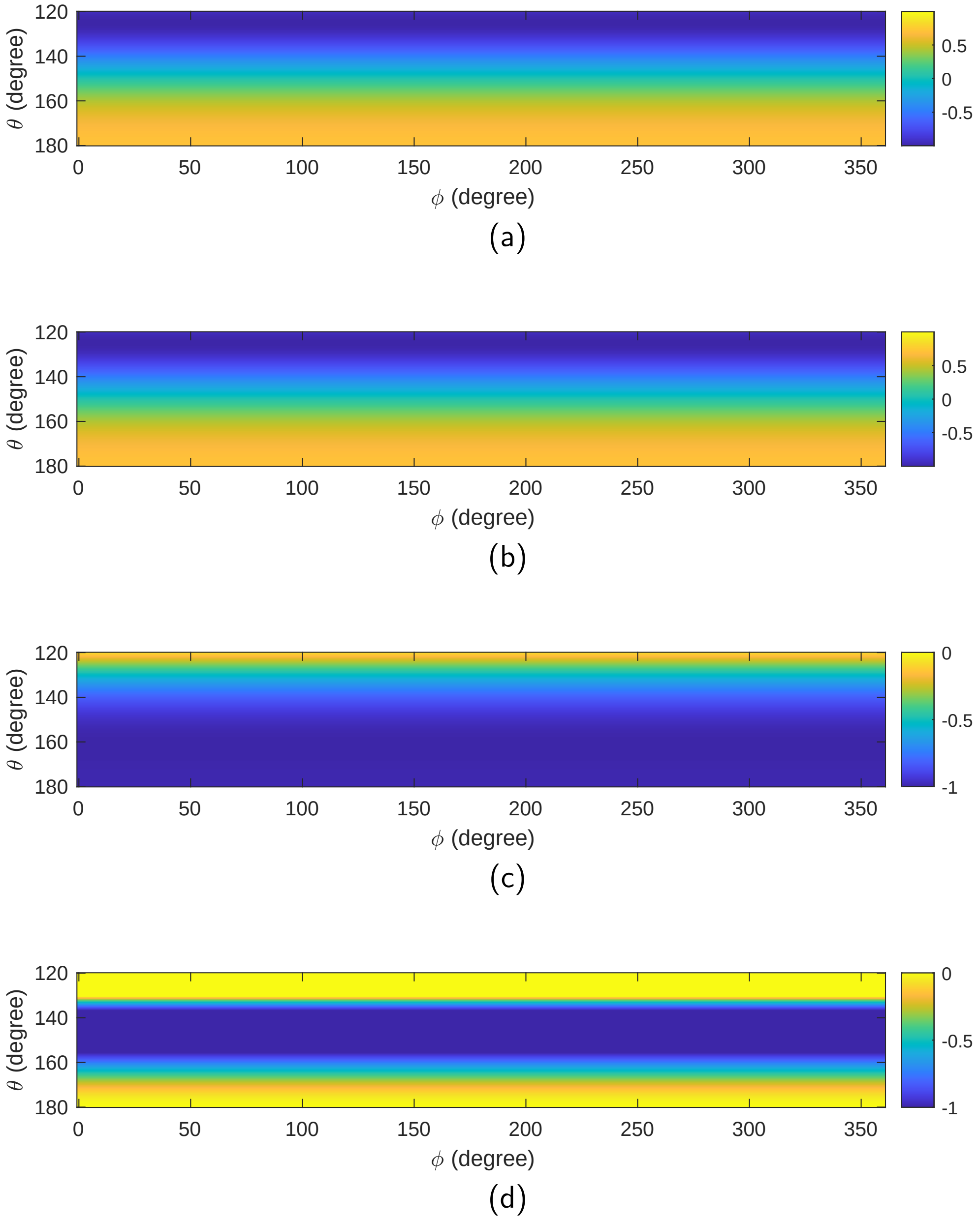

(a)

(b)

(c)

(d)

Figure 3.8: Spherical sector sound field radial extrapolation for the interior case with a plane wave, $\theta_M = 2/3\pi$, $R_M = 1$ m, $f = 300$ Hz, $Q = 100$: (a) true sound field with $R_T = 1$ m; (b) estimated sound field with $R_T = 1$ m; (c) true sound field with $R_T = 0.6$ m; (d) estimated sound field with $R_T = 0.6$ m.

With $R_T = R_M$, ϵ diminishes with the increment of θ_M, whereas with $R_T \neq R_M$, ϵ rises with the increment of θ_M.

Point source

We further investigate the sound field extrapolation performance in the interior case with a unit strength point source, with the Cartesian coordinates $(0, 0, -2)$ m.

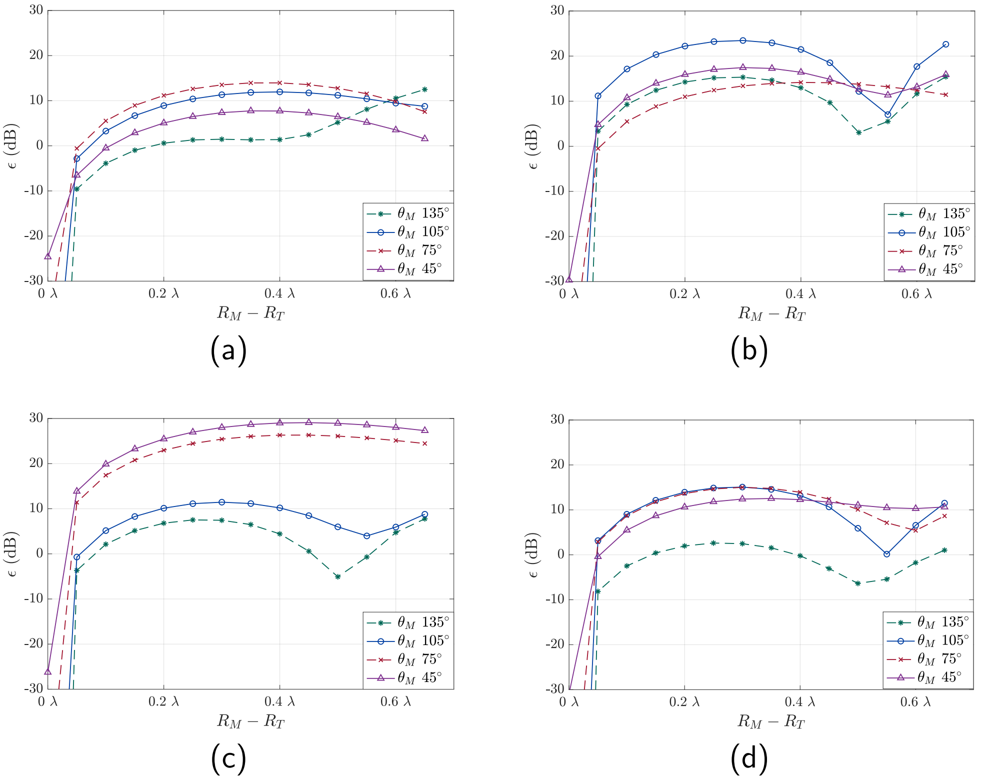

(a) (b) (c) (d)

Figure 3.9: Extrapolation error ϵ for the interior case with a plane wave, different settings of frequencies, sizes of $\mathbb{T}$, and distances between R_T and R_M: (a) extrapolation error with 300 Hz; (b) extrapolation error with 500 Hz; (c) extrapolation error with 700 Hz; (d) extrapolation error with 900 Hz.

The experimental setup, including settings of $\mathbb{M}$ and the microphone placement, is maintained as described in Section 3.4.2. We estimate the sound field for various inner concentric sector regions with $R_T = R_M$ and $0.6R_M$. The results, shown in Fig. 3.11, demonstrate that consistent with the findings in the preceding subsections, accurate estimation of the sector sound field is achievable when $R_T = R_M$. However, significant errors arise when $R_T \neq R_M$.

Continuing our investigation, we conduct additional simulations to analyze the extrapolation error (ϵ) using various setups while maintaining a point source instead of a plane wave. The results are depicted in Fig. 3.12, which reveals: i) the results are similar to those for a plane wave in Fig. 3.9; ii) The impact of frequency and the size of $\mathbb{T}$ on ϵ remains less regular; iii) Compared to Fig. 3.9, the trajectories of ϵ in Fig. 3.12 are more concentrated across different $\mathbb{T}$ setups. This suggests that the size of $\mathbb{T}$ has a relatively minor effect on extrapolation accuracy with point sources, in contrast to plane waves.

In conclusion, the findings from both exterior and interior case simulations underscore the limitations of conducting radial extrapolation with SSHs. While accurate

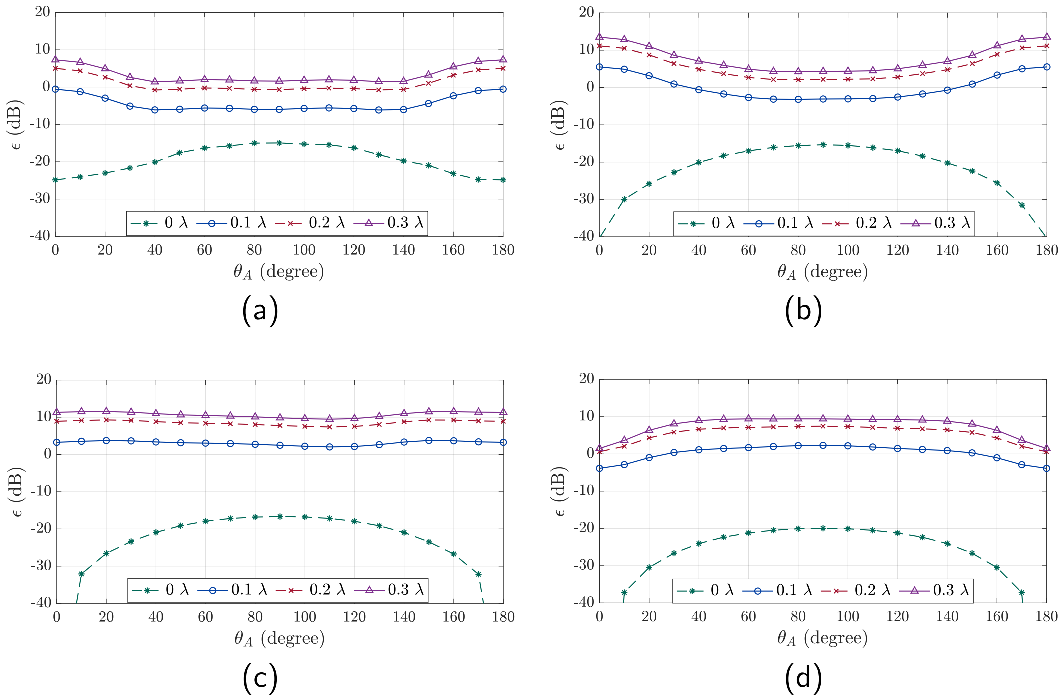

(a) (b)

(c) (d)

Figure 3.10: Extrapolation error ϵ with different arriving direction of the plane wave: (a) extrapolation error with $\theta_M = 45°$; (b) extrapolation error with $\theta_M = 75°$; (c) extrapolation error with $\theta_M = 105°$; (d) extrapolation error with $\theta_M = 135°$.

extrapolation is challenging when $R_T \neq R_M$, (3.22) shows potential for estimating the extrapolation in the exterior case, especially under specific conditions involving low frequencies, large sector regions, and small extrapolation distances.

3.5 Mapping Based Sectorial Sound Field Extrapolation

In this section, we first develop the spherical sector sound field radial extrapolation method based on the mapping between SSHs and SHs. Second, we further defined an error sensitivity ratio to evaluate the robustness of the proposed method. Finally, we evaluated the proposed method by simulations.

3.5.1 Mapping based radial extrapolation

In this section, we aim to find the mapping relationship between the SH coefficients and SSH coefficient.

As the orthonormal function sets, SHs and SSHs have the orthogonal property as

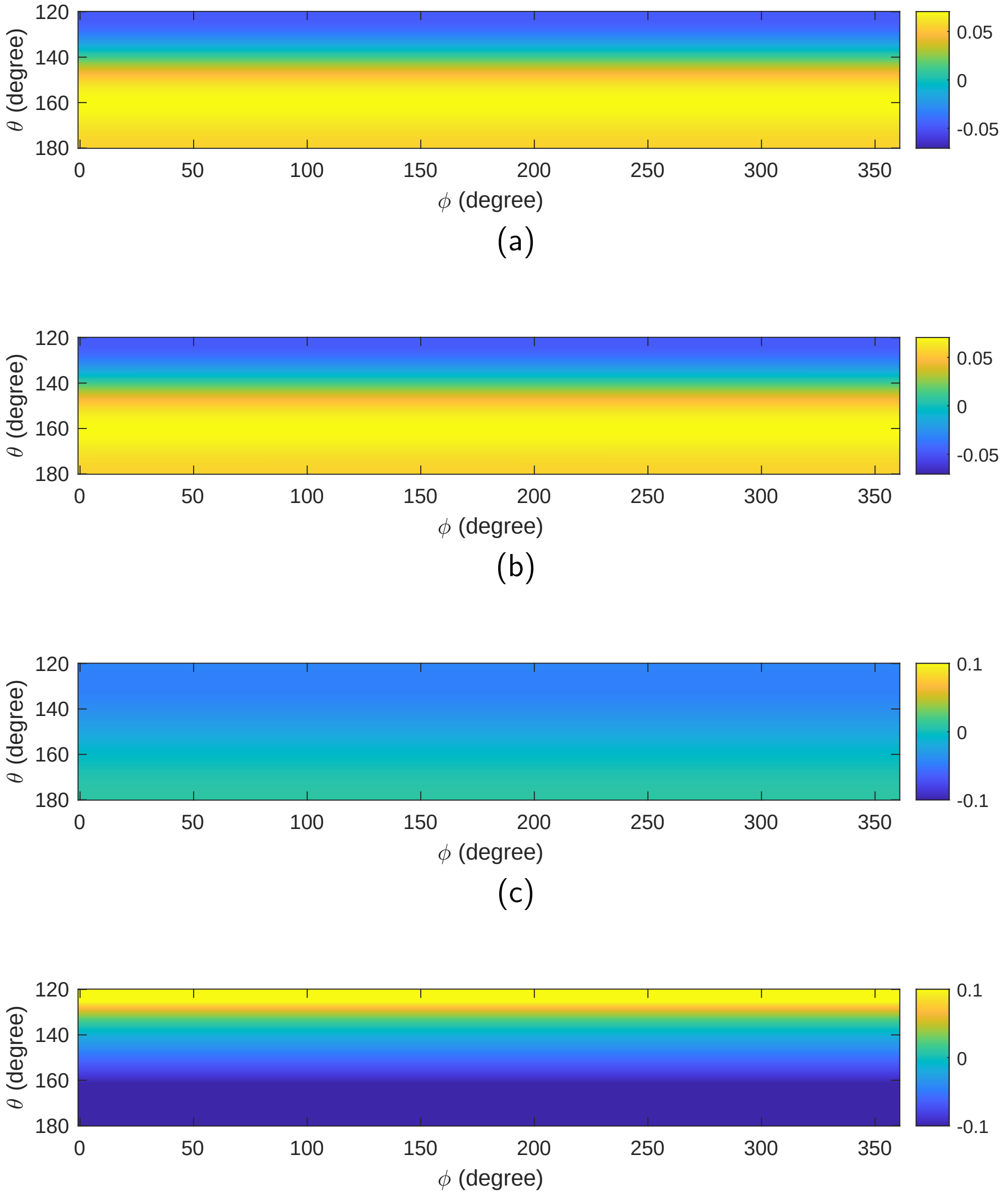

(a)

(b)

(c)

(d)

Figure 3.11: Spherical sector sound field radial extrapolation for the interior case with a point source, $\theta_M = 2/3\pi$, $R_M = 1$ m, $f = 300$ Hz, $Q = 100$: (a) true sound field with $R_T = 1$ m; (b) estimated sound field with $R_T = 1$ m; (c) true sound field with $R_T = 0.6$ m; (d) estimated sound field with $R_T = 0.6$ m.

expressed by

$$\int_0^{\pi} \int_0^{2\pi} Y_n^m(\theta,\phi)[Y_{n'}^{m'}(\theta,\phi)]^* \sin\theta d\theta d\phi = \delta_{nn'}\delta_{mm'}, \tag{3.26}$$

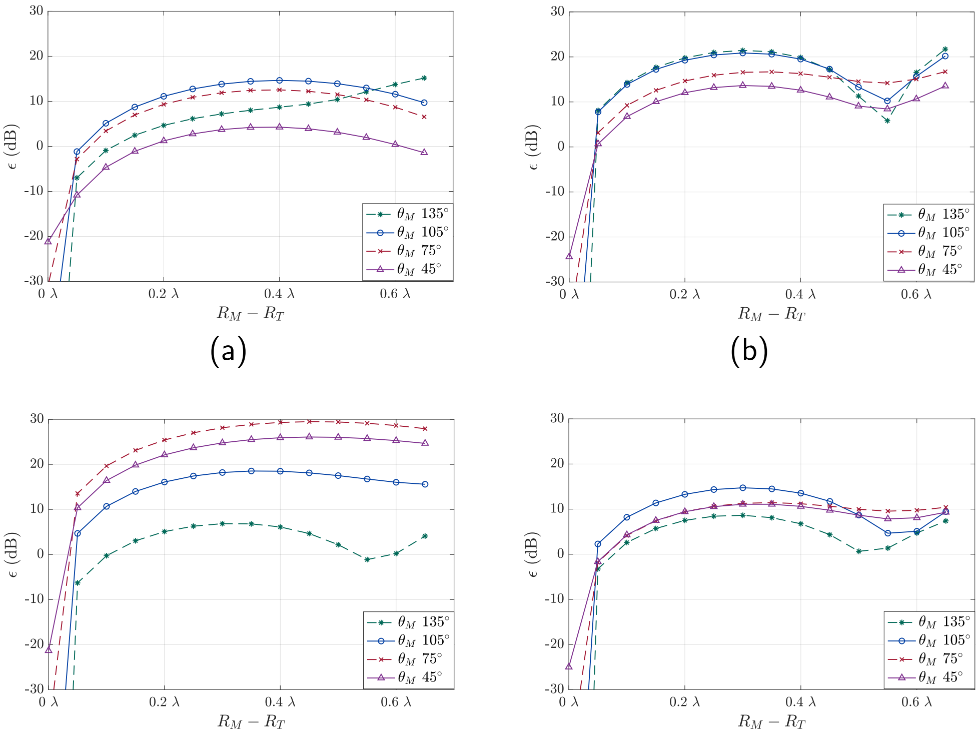

(a) (b)

(c) (d)

Figure 3.12: Extrapolation error ϵ for the interior case with a point source, different settings of frequencies, sizes of $\mathbb{T}$, and distances between R_T and R_M: (a) extrapolation error with 300 Hz; (b) extrapolation error with 500 Hz; (c) extrapolation error with 700 Hz; (d) extrapolation error with 900 Hz.

and

$$\int_{\theta_1}^{\theta_2}\int_{\phi_1}^{\phi_2} T_n^m(\theta,\phi)[T_{n'}^{m'}(\theta,\phi)]^{*}\sin\theta d\theta d\phi = \delta_{nn'}\delta_{mm'}, \tag{3.27}$$

where δ is the Dirac delta function. As we only focus on the $\mathbb{T}$ rather than the whole sphere, a subset of $Y_n^m(\hat{\boldsymbol{x}}), (R_T, \hat{\boldsymbol{x}}) \in \mathbb{T}$ can be represented by SSHs as

$$Y_n^m(\hat{\boldsymbol{x}}) = \sum_{n'=0}^{\infty}\sum_{m'=-n'}^{n'} \mathcal{T}_{nn'}^{mm'} T_{n'}^{m'}(\hat{\boldsymbol{x}}), \quad (R_T, \hat{\boldsymbol{x}}) \in \mathbb{T}, \tag{3.28}$$

where $\mathcal{T}_{nn'}^{mm'}$ is the mapping coefficient between SHs and SSHs. Then, based on (3.27), we can find $\mathcal{T}_{nn'}^{mm'}$ by

$$\mathcal{T}_{nn'}^{mm'} = \int_{\mathbb{T}} Y_n^m(\hat{\boldsymbol{x}}) T_{n'}^{m'}(\hat{\boldsymbol{x}})^{*} d\hat{\boldsymbol{x}}. \tag{3.29}$$

Based on (3.1), (3.3), (3.28), and (3.29), we can find the mapping between SHs and SSHs

$$\boldsymbol{\Gamma}(R_T, k) = \boldsymbol{M}_h \boldsymbol{D}_{R_T} \boldsymbol{\alpha}, \tag{3.30}$$

where $\boldsymbol{\Gamma}(R_T, k) = [\Gamma_0^0(R_T, k), \Gamma_1^{-1}(R_T, k), ..., \Gamma_{N_s}^{N_s}(R_T, k)]^T$ is the SSHs coefficients over $\mathbb{T}$, $\boldsymbol{M}_h$ is the $(N_s+1)^2 \times (N_h+1)^2$ mapping matrix that can map SHs to SSHs, expanded as

$$\boldsymbol{M}_h = \begin{bmatrix} \int_{\mathbb{T}} Y_0^0(\hat{\boldsymbol{x}}) T_0^0(\hat{\boldsymbol{x}})^* d\hat{\boldsymbol{x}} & \cdots & \int_{\mathbb{T}} Y_{N_h}^{N_h}(\hat{\boldsymbol{x}}) T_0^0(\hat{\boldsymbol{x}})^* d\hat{\boldsymbol{x}} \\ \vdots & \ddots & \vdots \\ \int_{\mathbb{T}} Y_0^0(\hat{\boldsymbol{x}}) T_{N_s}^{N_s}(\hat{\boldsymbol{x}})^* d\hat{\boldsymbol{x}} & \cdots & \int_{\mathbb{T}} Y_{N_h}^{N_h}(\hat{\boldsymbol{x}}) T_{N_s}^{N_s}(\hat{\boldsymbol{x}})^* d\hat{\boldsymbol{x}} \end{bmatrix}, \tag{3.31}$$

$\boldsymbol{D}_{R_T}$ is the $(N_h+1)^2 \times (N_h+1)^2$ diagonal matrix, represented by

$$\boldsymbol{D}_{R_T} = \begin{bmatrix} F_0(kR_T) & \cdots & 0 \\ \vdots & \ddots & \vdots \\ 0 & \cdots & F_{N_h}(kR_T) \end{bmatrix}, \tag{3.32}$$

$\boldsymbol{\alpha} = [\alpha_0^0(k), \alpha_1^{-1}(k), ..., \alpha_{N_h}^{N_h}(k)]^T$ is the $(N_h+1)^2 \times 1$ SH coefficients vector, which can be found by microphone measurement, calculated by

$$\boldsymbol{\alpha} = \boldsymbol{L}_m^{\dagger} \boldsymbol{p}_q, \tag{3.33}$$

where $\boldsymbol{L}_m$ denotes the $Q \times (N_h+1)^2$ matrix that contains the multiplication of SHs and the radial function, expressed as

$$\boldsymbol{L}_m = \begin{bmatrix} Y_0^0(\theta_1, \phi_1) F_0(kr_1) & \cdots & Y_{N_h}^{N_h}(\theta_1, \phi_1) F_{N_h}(kr_1) \\ \vdots & \ddots & \vdots \\ Y_0^0(\theta_Q, \phi_Q) F_0(kr_Q) & \cdots & Y_{N_h}^{N_h}(\theta_Q, \phi_Q) F_{N_h}(kr_Q) \end{bmatrix}. \tag{3.34}$$

Based on the above approach, we can find the SSH coefficients of the target region from the SH coefficients.

3.5.2 Robustness assessment

The proposed spherical sector sound field radial extrapolation method can accurately extrapolate the sound field if the sound field can be exactly represented by finite modes of SHs and SSHs, and there is no error in the microphone measurement. However, in reality, the measurement error and the error due to the mode-limited representation always exists. Consider a realistic measurement expressed by

$$\boldsymbol{p}_q = \tilde{\boldsymbol{p}}_q + \boldsymbol{e}, \tag{3.35}$$

where $\tilde{\boldsymbol{p}}_q$ is the mode-limited linear part of the measurement and $\boldsymbol{e}$ is the total error in the measurement. In the current problem of extrapolation, the system needs to remain robust to undesired noise and errors. Due to the restricted measurement region (not covering the whole sphere), process (3.33) will be error sensitive and can not find the accurate SH coefficients, but process (3.30) will shrink the error as we are only interested a sector region $\mathbb{T}$. Thus, the robustness of the whole process is difficult to observe empirically. We define a ratio $\tau(k)$, as the resulting change in $\tilde{\boldsymbol{p}}_q$ due to a small change in $\boldsymbol{p}_q$, showing the robustness of the proposed method to noise

$$\begin{aligned} \tau(k) &= \frac{\|\boldsymbol{M}_h \boldsymbol{D}_{R_T} \boldsymbol{L}_m^{\dagger} \boldsymbol{e}\|_2}{\|\boldsymbol{M}_h \boldsymbol{D}_{R_T} \boldsymbol{L}_m^{\dagger} \boldsymbol{p}_q\|_2} \Big/ \frac{\|\boldsymbol{e}\|_2}{\|\tilde{\boldsymbol{p}}_q\|_2} \\ &= \frac{\|\boldsymbol{M}_h \boldsymbol{D}_{R_T} \boldsymbol{L}_m^{\dagger} \boldsymbol{e}\|_2}{\|\boldsymbol{\Gamma}\|_2} \Big/ \frac{\|\boldsymbol{e}\|_2}{\|\tilde{\boldsymbol{p}}_q\|_2}. \end{aligned} \tag{3.36}$$

The definition of $\xi(k)$ is similar to the definition of the condition number in a linear system, and a larger $\xi(k)$ means less robustness and the process tends to amplify noise.

For a better robustness assessment, it is important to find an upper bound of $\tau(k)$ which only depends on the system setup and does not change with $\boldsymbol{e}$ and $\boldsymbol{p}_q$. Based on (3.3) and (3.27) we can derive that

$$\|\boldsymbol{\Gamma}\|_2 = \frac{\sqrt{\mathrm{E}}}{R_T}, \tag{3.37}$$

where E is the sound energy over $\mathbb{T}$. From Green's function [109] we have

$$G(\boldsymbol{x}|\boldsymbol{y}) = \frac{e^{-jk\|\boldsymbol{y}-\boldsymbol{x}\|_2}}{4\pi\|\boldsymbol{y}-\boldsymbol{x}\|_2}, \tag{3.38}$$

where $\boldsymbol{x} = (r, \theta, \phi)$ is the observe point, $\boldsymbol{y} = (r_s, \theta_s, \phi_s)$ is the point source location. Then, based on (3.36), (3.37), and (3.38), we can find the upper bound of $\tau(k)$ which is defined as the error sensitivity ratio $\Xi(k)$ ($\Xi(k) > \tau(k)$). $\Xi(k)$ can be expressed as

$$\Xi(k) = \begin{cases} (\|\boldsymbol{M}_h \boldsymbol{D}_{R_T} \boldsymbol{L}_m^\dagger\|_2 \frac{(R_T+R_S)\sqrt{Q}}{(R_1-R_S)\sqrt{2\pi(1-\cos\theta_T)}} & \text{for exterior case with point sources,} \\ \|\boldsymbol{M}_h \boldsymbol{D}_{R_T} \boldsymbol{L}_m^\dagger\|_2 \frac{(R_T+R_S)\sqrt{Q}}{(R_S-R_2)\sqrt{2\pi(1-\cos\theta_T)}} & \text{for interior case with point sources,} \\ \|\boldsymbol{M}_h \boldsymbol{D}_{R_T} \boldsymbol{L}_m^\dagger\|_2 \frac{\sqrt{Q}}{\sqrt{2\pi(1-\cos\theta_T)}} & \text{for plane wave incident fields.} \end{cases} \tag{3.39}$$

Based on (3.39), we find that $\Xi(k)$ is related to the placement of microphones, the target region $\mathbb{T}$, and the wave number k.

3.5.3 Performance Analysis

In this section, we assess the robustness and performance of the proposed sound field radial extrapolation method with different configurations based on the error sensitivity ratio $\Xi(k)$. The extrapolation result is also presented for further evaluation and analysis.

Influence of the measurement region and sensor placement

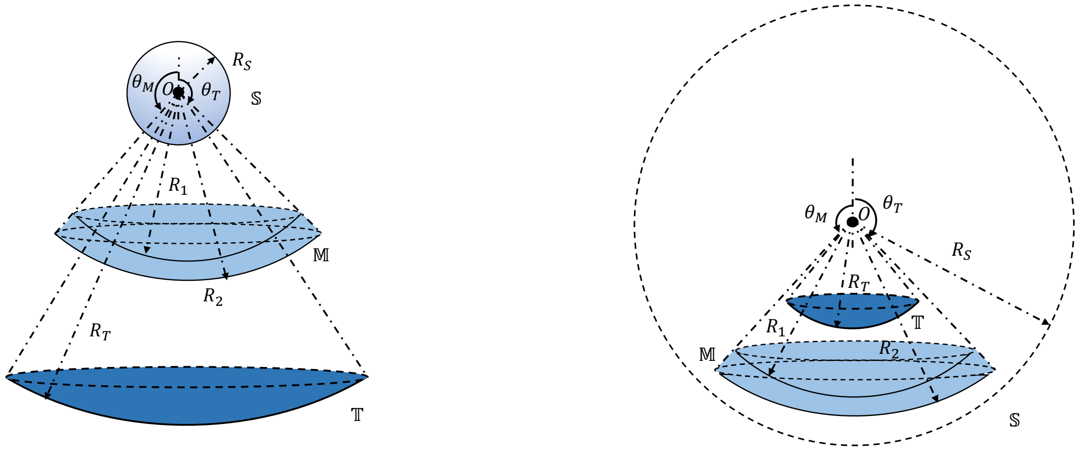

(a) (b)

Figure 3.13: Spherical sector sound field radial extrapolation setups with the dual array setup (a) exterior case and (b) interior case.

We investigate the influence of θ_M and kr to $\Xi(k)$ for two types of microphone placement: a dual array and a single array. As shown in Fig. 3.13, for the dual array, we place $(N+1)^2$ microphones on the inner sector region ($\theta \in [\theta_M, \pi], \phi \in [0, 2\pi), r = R_1$) and another $(N+1)^2$ microphones on the outer sector region ($\theta \in$

$[\theta_M, \pi], \phi \in [0, 2\pi), r = R_2)$ with nearly-uniform sampling, where $N = \lceil kR_2 \rceil$. For the single array, we place $2(N+1)^2$ microphones on the middle sector region ($\theta \in [\theta_M, \pi], \phi \in [0, 2\pi), r = (R_1 + R_2)/2$) with nearly-uniform sampling. In simulations, we set $R_1 = 0.5$ m, $R_2 = 0.7$ m, $R_S = 0.25$ m, $R_T = 5$ m for the exterior case and $R_1 = 0.35$ m, $R_2 = 0.5$ m, $R_T = 0.15$ m, $R_S \to \infty$ for the interior case. θ_M changes from 0° to 150° with a step size of 15°, and $\theta_T = \theta_M$. kr changes from 1 to 8. The speed of sound propagation is $c = 343$ m/s.

The results are shown in Fig. 3.14, where we find that, compared to the single array, the dual array is more robust, especially for large θ_M and kr values. The theory behind it is that $\mathbb{M}$ is an open region, different from a closed spherical region, so it lacks information about sound propagation. Then, the measurement for a different radius can provide more information about the sound propagation and improve the performance. Fig. 3.14 also indicates that $\Xi(k)$ exponentially increases with θ_M and as well as in steps with the kr, which means that with a large θ_M and kr the sound field radial extrapolation is not reliable. The reason for the step shape is that the microphone number increases when kr reaches an integer value. Furthermore, compared to the interior case, $\Xi(k)$ for the exterior case increases relatively smoothly but maintains a large value for a larger range of θ_M and kr. As the dual array is superior to the single array in the spherical sector sound field radial extrapolation, we focus on the dual array setup in the further investigations.

Influence of the distance of target region

As $\Xi(k)$ is also a function of R_T, we further study the influence of R_T on $\Xi(k)$ in this section. We retain most of the settings from the previous section, except we fix $\theta_M = \theta_T = 120°$ and gradually increase R_T. The sensors are arranged in a dual-array configuration. Results are presented in Fig. 3.15, where we find that i) $\Xi(k)$ rises with the kr and the distance between $\mathbb{M}$ and $\mathbb{T}$ for both exterior and interior cases, and the influence of kr is stronger; ii) for the exterior case, the increase of $\Xi(k)$ is relatively smooth and will converge when R_T is large enough, while for the interior case, $\Xi(k)$ maintains a small value for most cases but increases rapidly when kr and the distance between $\mathbb{M}$ and $\mathbb{T}$ become vary large.

Sector sound field radial extrapolation results

To further evaluate the proposed mapping-based extrapolation method, we test it with multiple point sources and mixed plane waves ($R_S \to \infty$). For the exterior case, we randomly place 10 point sources inside a spherical region ($\theta \in [0, \pi], \phi \in [0, 2\pi), r \leq R_S = 0.25$ m), $\theta_M = \theta_T = 105°, R_1 = 0.5$ m, $R_2 = 0.7$ m, $R_T = 5$m. For

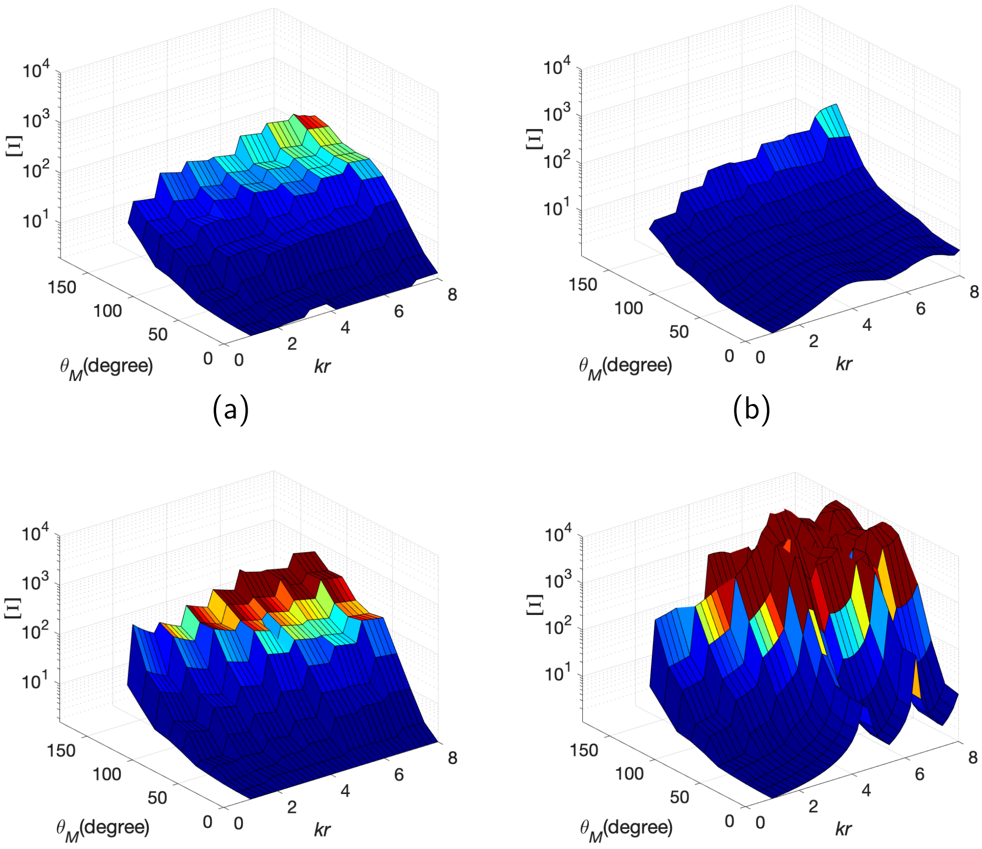

(a) (b)

(c) (d)

Figure 3.14: Error sensitivity ratio $\Xi(k)$ with different configurations: θ_M changing from 0° to 150°, kr changing from 1 to 8: (a) exterior case: dual array; (b) interior case: dual array; (c) exterior case: single array; (d) interior case: single array.

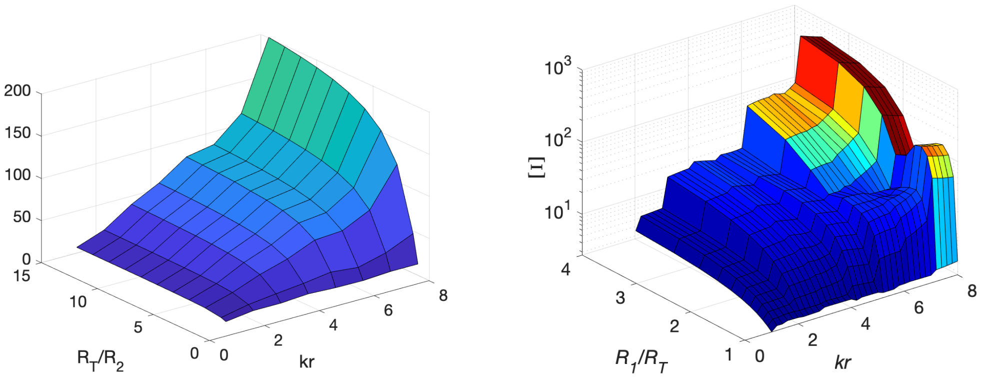

(a) (b)

Figure 3.15: Error sensitivity ratio $\Xi(k)$ with different R_T and kr settings, with the dual array setup: (a) exterior case and (b) interior case.

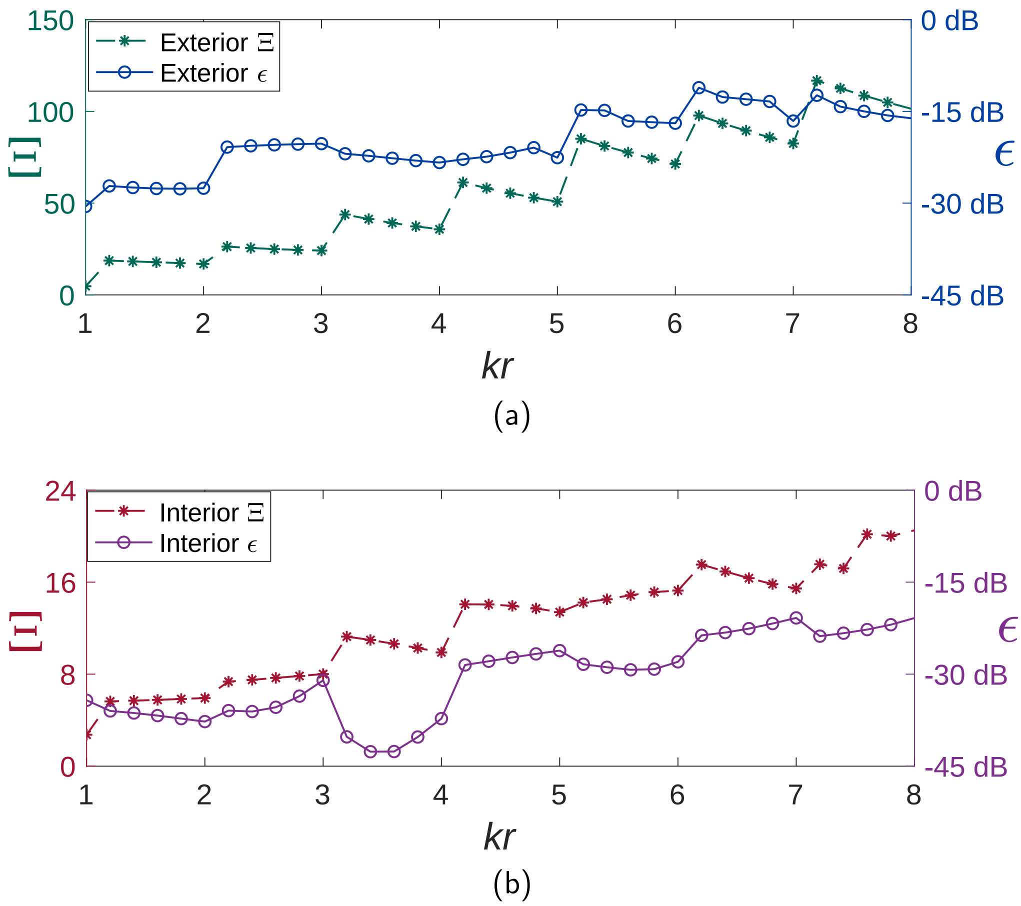

Figure 3.16: Sound field estimation error $\epsilon(k)$ and error sensitivity ratio $\Xi(k)$ with different kr values, with the dual array setup: (a) exterior case (b) interior case.

the interior case, we mix 10 plane waves with random arriving directions, $\theta_M = \theta_T = 105°$, $R_1 = 0.35$ m, $R_2 = 0.5$ m, $R_T = 0.2$ m. We keep the same dual array settings and add Gaussian white noise with a signal-to-noise (SNR) ratio of 30 dB to each microphone recording. To calculate the extrapolation error, $U = 5214$ points are placed over $\mathbb{T}$ by truncated Gaussian sampling. The results are shown in Fig. 3.16, which indicates that i) both $\Xi(k)$ and $\epsilon(k)$ increase with kr in steps. The reason for the step shape is that the microphone number increases when kr reaches integer values; ii) for the given setup, the interior case has a better sound field extrapolation result. A possible reason is that the plane wave has a simpler pattern; iii) for the same $\epsilon(k)$, $\Xi(k)$ for the exterior case is larger than the interior case; iv) there is a strong correlation between $\Xi(k)$ and $\epsilon(k)$ for both interior and exterior cases, and the calculated correlation coefficient between $\Xi(k)$ and $\epsilon(k)$ are 0.81 and 0.89 for interior and exterior cases respectively. The strong correlation means that $\Xi(k)$ is effective in evaluating the proposed spherical sector sound field radial extrapolation method for a given setup.

3.6 Summary and Contributions

In this chapter, we conducted thorough investigations of SSHs in the problem of spherical sector sound field reconstruction and extrapolation. We first proved that SSHs are not solutions to the wave equation. Then, a distortion problem in the sectorial sound field reconstruction was identified, revealing the severe distortion around the edge of the reconstruction sector region. This finding suggests that the measurement region should be larger than the target region to improve accuracy. After that, the spherical sectorial radial extrapolation problem was investigated. Due to the violation of the wave equation, SSHs lack the property to conduct sound field radial extrapolation. Simulations confirm the challenges, especially in interior cases.

To address the radial extrapolation limitation, we propose a mapping-based radial extrapolation method. We analyze its performance and robustness under various conditions, assessing error sensitivity and extrapolation accuracy. Results show that the method performs well, particularly with a dual-array setup, a larger measurement region angle, a lower wave number, and a shorter distance between the measurement and target regions. Moreover, the strong correlation between extrapolation error and the error sensitivity ratio confirms that the latter is a reliable performance metric. The mapping-based extrapolation method also enables directional sound field estimation using an on-board sectorial microphone array, which in turn facilitates the development of directional active noise control for drones.

3.7 Related Publications

- H. Bi, S. Xu, F. Ma, T. D. Abhayapala, and P. N. Samarasinghe, “Limitations and performance analysis of spherical sector harmonics for sound field processing,” Appl. Sci., vol. 14, no. 22, p. 10633, 2024, [Online]. Available: https://doi.org/10.3390/app142210633.
- H. Bi, F. Ma, T. D. Abhayapala, and P. N. Samarasinghe, “Spherical sector harmonics based soundfield radial extrapolation and robustness analysis,” in Proc. ICASSP 2023—2023 IEEE Int. Conf. Acoust., Speech, Signal Process., Rhodes Island, Greece, Jun. 4–10, 2023, pp. 1–5.

Chapter 4

Point Neuron Learning: A New Physics-informed Neural Network Architecture

Overview: *Machine learning and neural networks have driven advancements across numerous research domains, yet challenges such as large training data requirements and inconsistent model performance hinder their application in certain scientific problems. To address these limitations, researchers have explored integrating physics principles into machine learning models, primarily through: (i) physics-guided loss functions, commonly known as physics-informed neural networks (PINNs), and (ii) physics-guided architectural design. While both approaches have demonstrated success, they suffer from issues such as susceptibility to local minima, poor interpretability, and limited generalizability beyond the sampled data range. This chapter introduces a novel PINN architecture that embeds the fundamental solution of the wave equation directly into the network architecture, ensuring strict adherence to wave physics. The proposed point neuron learning method enables accurate sound field modeling solely from microphone observations, eliminating the need for pre-collected datasets. Compared to existing PINN approaches, our method natively handles complex numbers, enhances interpretability, and generalizes effectively to out-of-sample scenarios. We validate our proposed architecture via simulations on two tasks: (i) sound field reconstruction in reverberant environments, and (ii) sound field extrapolation, demonstrating its applicability to drone noise modeling. Results demonstrate that the point neuron method outperforms competing approaches, exhibiting greater robustness to microphone placement variations and sensor noise while maintaining superior versatility across diverse acoustic problems.*

4.1 Introduction

With the explosive growth of available data and computing resources, machine learning and neural networks have been greatly developed and successfully implemented in many research disciplines [181, 182, 183, 184, 185, 186, 187, 188, 189]. However, in some scientific domains, including acoustics, a large amount of observation data is infeasible, and the learned model is unable to produce physically consistent results. To address these challenges, researchers have explored integrating scientific principles into machine learning models, typically through two main approaches: physics-guided loss functions and physics-guided architectural design. Although both approaches have been successfully applied to various discipline specific problems, they have some limitations, including being trapped in a local minimum or converging to a trivial solution [190, 191], poor interpretability [192], and limited ability to generalize to out-of-sample scenarios [192]. In this chapter, we aim to leverage the advantages of both approaches by proposing a neural network architecture that ensures strict adherence to the governing equations from physics, thereby enhancing interpretability and the ability to extend beyond sampled data points. In this way, we can have more flexible microphone placement in modelling the direction of the drone's outgoing sound field compared to the method developed in Chapter 3.

The idea of physics-guided loss functions was proposed in PINNs [119, 120], where partial differential equations (PDEs) related loss terms are added to the neural networks. In the typical PINN, other than the observed data, more data are created to calculate the PDE loss, which can enhance the model robustness and help the learned model fit the governed PDE. PINN has been widely implemented in diverse scientific fields, including fluid physics [121, 122, 123, 124, 125, 126, 127], thermodynamics [128, 129, 130], and medical imaging [131, 132, 133, 134].

Physics-guided architectural design involves integrating principles from physics into neural network architectures to enhance model performance, data efficiency, and interpretability. One straightforward approach is to embed conventional methods into the processing layers of neural networks [193]. Amos and Kolter added a differentiable convex optimization solver layer into the proposed OptNet [194]. In the proposed differentiable physics engine, a rigid body simulator was embedded into the network architecture to enable the network to learn physical parameters from data [195]. Another strategy is encoding invariances and symmetries into network architecture [192]. Ling *et al.* demonstrated that the neural network with the rotational invariance property can improve the prediction accuracy of turbulence modelling [196]. Anderson *et al.* designed a rotationally covariant neural network architecture for better learning of the behaviour and properties of complex many-body physical systems [197].

In the field of acoustics, PINNs have demonstrated successful applications, while research on physics-guided architectural design remains relatively unexplored. Shigemi *et al.* integrated PINN with a bicubic spline interpolation for the sound field estimation problem [136]. Borrel-Jensen, Engsig-Karup, and Jeong implemented PINN with different boundary conditions to predict one-dimensional sound fields [137]. For the problem of nearfield acoustics holography, Olivieri *et al.* proposed a Kirchhoff–Helmholtz-based convolutional neural network (KHCNN) which involved Kirchhoff–Helmholtz equation to calculate loss functions [144], and Kafri *et al.* further combined KHCNN with the famous explainable CNN architecture Gradient-weighted Class Activation Mapping (Grad-CAM) [198] to make it more explainable [135]. For the room impulse response reconstruction, Pezzoli, Antonacci, and Sarti used PINN to reconstruct the early part of room impulse response in time-domain [145], and the network in [146, 147] is able to estimate particle velocity and intensity, in addition to sound pressure. PINNs have also contributed to head-related transfer functions [199], sound field estimation or reconstructions [138, 139, 140, 141, 142], active noise control [200], and ocean acoustics [201, 202].

Although PINNs have demonstrated great potential in the field of acoustics, the idea of adding the PDE loss to existing neural network architectures has some limitations. First, for the frequency-domain approach, most neural networks cannot directly process complex numbers, and the separated training of real and imaginary numbers has the risk of missing phase information. Second, even though the wave equation is involved in the training process, the learned model is still a black box model and hardly interpretable. Third, the working range of the learned model is restricted by the microphone observations or training dataset, resulting in the difficulty of generalizing the learned model to out-of-sample scenarios [192], especially for sound field extrapolation problems [108, 203].

As the PINN is a generalized approach for all PDE-determined systems, the direct adoption of PINN cannot fully utilize features behind the wave equation, and one outstanding feature of the wave equation is that its fundamental solution is known. Therefore, rather than only adding PDE losses in neural networks, we embed the fundamental solution, free space Green function [110], into the network architecture, enabling the learned model to strictly satisfy the wave equation. In the proposed network, the basic processing unit is called a *point neuron* whose weight and biases can be learned by back propagation. The physical meaning of point neurons is equivalent to point sources or plane wave sources, and the weight and distribution of equivalent sources can be updated while training. The proposed *point neuron network* can be implemented to model and estimate an arbitrary sound field purely based on microphone observations without an extra dataset.

The main contribution of this chapter is four-fold. First, the proposed method provides a new way to integrate principles from physics with neural networks. Second, the proposed method can directly process complex numbers, which can maintain the phase information of complex sound fields. Third, point neuron learning is interpretable in physics, and the nature of equivalent sources enables generalizability in out-of-sample scenarios. Finally, the training process only requires a small number of microphone observations, and no extra dataset or pre-training process is required.

The rest of this chapter is organized as follows. In Section 4.2, we formulate a generalized sound field modelling problem. We present the point neuron learning architecture and derive the back propagation for it in Section 4.3. In Section 4.4, we evaluate the proposed method with a sound field estimation problem in a reverberant environment and compare its performance with one conventional method and one typical PINN method. We further evaluate the proposed method with a sound field extrapolation problem in Section 4.5. Finally, Section 4.6 concludes this chapter.

4.2 Problem Formulation

Consider a source-free region of space denoted by $\Omega \subseteq \mathbb{R}^{2\mathrm{or}3}$ surrounded by sound sources as shown in Fig. 4.1. The sound pressure at an arbitrary point in the Cartesian coordinate $\boldsymbol{x} = (x, y, z), \boldsymbol{x} \in \Omega$, can be represented by $P(\boldsymbol{x}, k) \in \mathbb{C}$, where $k = 2\pi f / c$ is the wave number, f is the frequency, and c is the speed of sound propagation. Let there are Q number of observation points $\boldsymbol{x}_q \in \Omega$, $q = 1, ..., Q$, to measure the sound field, as shown in Fig. 4.1.

We aim to build a neural network model $\mathscr{P}(\boldsymbol{x}, k; \boldsymbol{\beta})$ for the sound field $P(\boldsymbol{x}, k)$ over the target region Ω from Q observation points, where $\boldsymbol{\beta} \in \mathbb{C}^S$ are the parameters of the model, S is the number of model parameters. The model $\mathscr{P}(\boldsymbol{x}, k; \boldsymbol{\beta})$ should satisfy the Helmholtz equation which governs the wave propagation over space. We

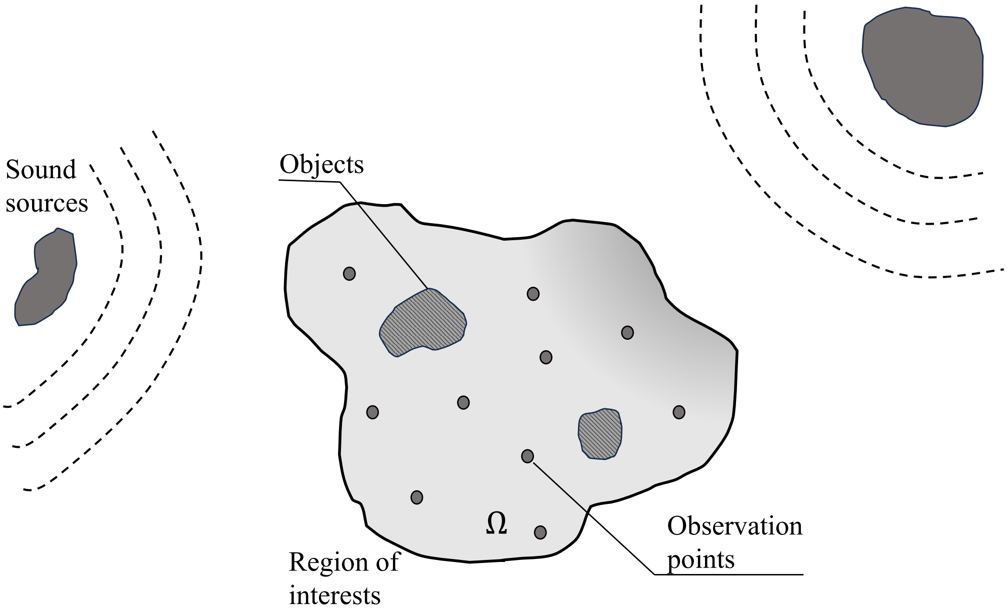

Figure 4.1: Illustration of the target region Ω, observation points, and sound sources.

formulate $\mathscr{P}(\boldsymbol{x}, k; \boldsymbol{\beta})$ by the following optimization problem,

$$\begin{aligned} \underset{\boldsymbol{\beta}\in\mathbb{C}^S}{\arg\min} \quad & \mathscr{L} = \mathscr{L}_{\mathrm{TRN}}(\boldsymbol{\mathscr{p}}_{\mathrm{mic}}, \boldsymbol{p}_{\mathrm{mic}}) + \sigma\mathscr{C}(\boldsymbol{\beta}), && (4.1\mathrm{a}) \\ \mathrm{s.\,t.} \quad & \Delta^2\mathscr{P}(\boldsymbol{x}, k; \boldsymbol{\beta}) + k^2\mathscr{P}(\boldsymbol{x}, k; \boldsymbol{\beta}) = 0 && (4.1\mathrm{b}) \\ & \boldsymbol{x} \in \Omega \\ & \sigma \in [0, \infty) \end{aligned}$$

where $\mathscr{L}$ is the cost function, $\mathscr{L}_{\mathrm{TRN}}$ is the training loss that measures the supervised error between the sound field estimation $\boldsymbol{\mathscr{p}}_{\mathrm{mic}} = [\mathscr{P}(\boldsymbol{x}_1, k), \ldots, \mathscr{P}(\boldsymbol{x}_Q, k)]^T$ and the pressure measurements $\boldsymbol{p}_{\mathrm{mic}} = [P(\boldsymbol{x}_1, k), \ldots, P(\boldsymbol{x}_Q, k)]^T$, σ is a hyper-parameter to control the weight of model complexity loss $\mathscr{C}(\boldsymbol{\beta})$ [192, 204], and

$$\Delta^2 \equiv \frac{\partial^2}{\partial x^2} + \frac{\partial^2}{\partial y^2} + \frac{\partial^2}{\partial z^2}.$$

Then, the research problem becomes how to find the optimal model $\mathscr{P}(\boldsymbol{x}, k; \boldsymbol{\beta})$ based on Q observations that can minimize $\mathscr{L}$ as well as satisfy the wave propagation constrain in (4.1b).

4.3 Point Neuron Learning

The standard PINN approach to solving the optimization problem in Section 4.2 is to combine the constraint in (4.1b) to the cost function in (4.1a). However, the wave propagation constraint in (4.1b) limits the direct adoption of most existing network architecture and models. Therefore, in this section, we propose a new network architecture, termed the point neuron network, which satisfies the Helmholtz equation constraint, and the learned model is explainable using principles in physics.

4.3.1 Point neuron

The propagation of sound is governed by the Helmholtz wave equation (4.1b) which is a natural constraint of any valid sound field and limits the direct adaptation of existing neural network architectures to model the sound field. Therefore, to satisfy (4.1b), we embed the fundamental solution of the Helmholtz equation, i.e., the free space Green function, into a neural network architecture,

$$G(\boldsymbol{x}|\boldsymbol{y},k) = \frac{e^{ik\|\boldsymbol{x}-\boldsymbol{y}\|_2}}{4\pi\|\boldsymbol{x}-\boldsymbol{y}\|_2}, \tag{4.2}$$

where $i^2 = -1$ is the imaginary number, $\|\cdot\|_2$ is ℓ_2-norm, $\boldsymbol{y}$ denotes the location of an omni-directional unit point source, $G(\boldsymbol{x}|\boldsymbol{y},k)$ means the sound field at an observer point $\boldsymbol{x}$ generated by a unit strength point source at $\boldsymbol{y}$.

We add a normalization to unify the treatment of both near-field and far-field sources and make it the building block of our network, named *point neuron unit*, expressed as

$$PN(\boldsymbol{x}|\boldsymbol{y},k) = \|\boldsymbol{y}\|_2 e^{-ik\|\boldsymbol{y}\|_2}\frac{e^{ik\|\boldsymbol{x}-\boldsymbol{y}\|_2}}{4\pi\|\boldsymbol{x}-\boldsymbol{y}\|_2}. \tag{4.3}$$

The point neuron unit works as a virtual source that is capable of modelling both near-field and far-field sound propagation [113]. As shown in Fig. 4.2, we embed V number of point neuron units into a neural network architecture. The network input is the coordinate of an arbitrary point $\boldsymbol{x} = (x, y, z)$, and the output is the sound pressure of that point $P(\boldsymbol{x}, k)$.

The v^{th} point neuron unit has three inputs, x, y, and z co-ordinates of the point $\boldsymbol{x}$, and three biases $B_v^x, B_v^y,$ and $B_v^z \in \mathbb{R}$. In the top path, the three channels of inputs with biases first go through an activation function $(\cdot)^2$ individually and then are fully connected (with unity weights) to pass another activation function $\sqrt{(\cdot)}$ and multiplying with the wave number k (can be considered as a constant weight) before passing through the final activation function $h_0^{(1)}(\cdot)$, which is the 0^{th} order spherical

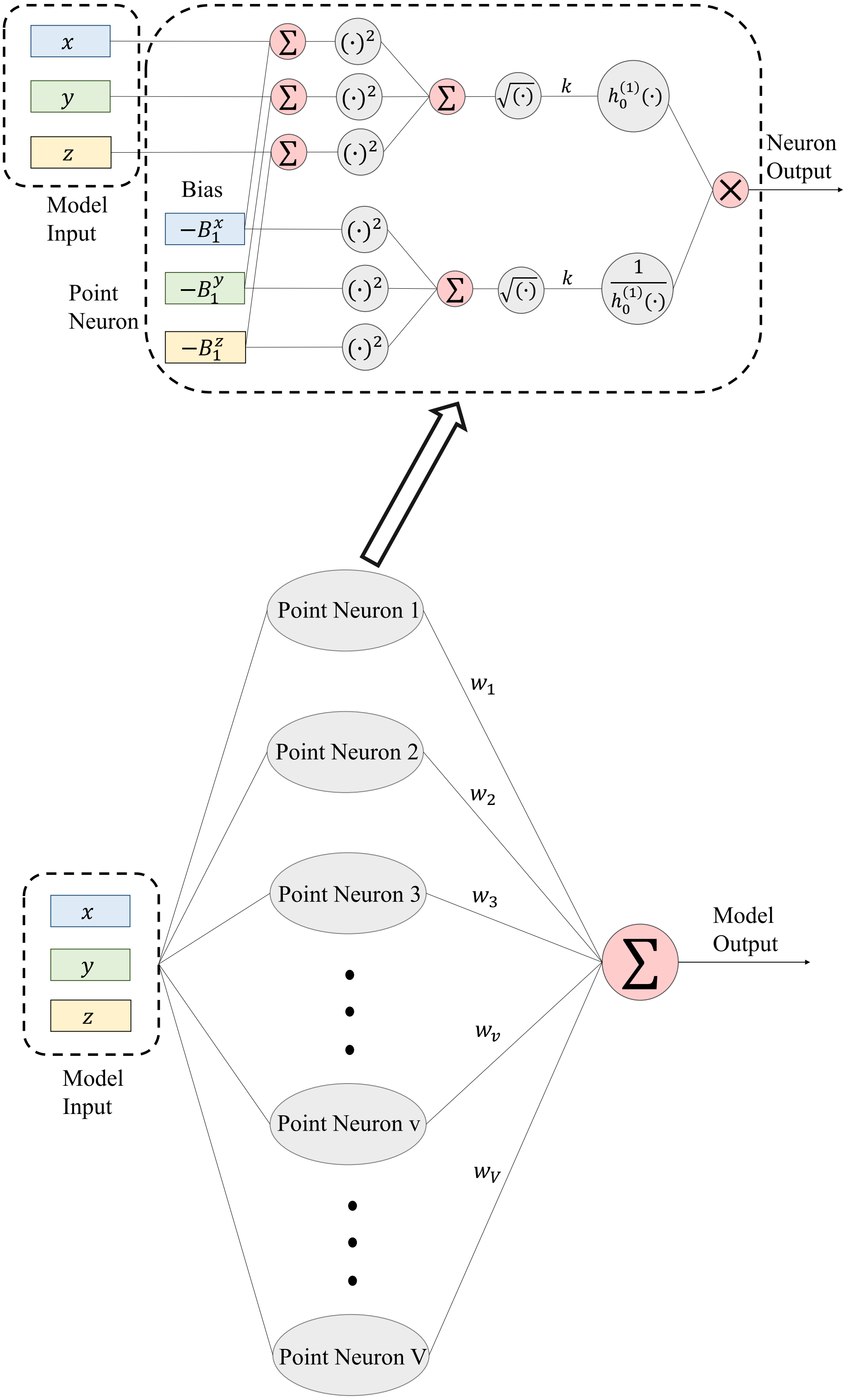

Figure 4.2: Network architecture of point neuron learning. Top: the point neuron building block. Bottom: the architecture overview with V number of point neurons.

Hankel function of the first kind, given by

$$h_0^{(1)}(r) = \frac{e^{ir}}{ir}. \tag{4.4}$$

In the bottom path, the three biases directly undergo the same process as in the top path, followed by the final activation function $1/h_0^{(1)}(\cdot)$ after multiplying the fixed weight k. Finally, the outputs of the top and bottom paths are multiplied together to generate the point neuron output. We construct the point neuron network by fully connecting V point neuron units with neuron weights $w_v \in \mathbb{C}$, $v = 1, \ldots, V$ as shown in Fig. 4.2. The point neuron and its weights are frequency-dependent.

Note that the physical meaning of biases and the weight of the point neuron unit is the location and strength of the corresponding virtual source. The weight and distribution of virtual sources can be learned by the training process. Though the point neuron architecture is a direct mapping from the normalized Green function, the resulting network can be learned (i.e., weights and biases) as any other neural network using established tools. Additionally, embedding Green's function into the network architecture means the proposed method is built on top of the principles of physics rather than learning all information entirely from data, thereby reducing the need for extensive datasets.

4.3.2 Back propagation and training

According to the network architecture and (4.1), we define the system cost function as

$$\begin{aligned}
\underset{\boldsymbol{\beta} \in \mathbb{C}^S}{\arg\min} \quad & \mathscr{L} = \sum_{q=1}^{Q} |\mathscr{P}(\boldsymbol{x}_q, k; \boldsymbol{\beta}) - P(\boldsymbol{x}_q, k)|^2 + \sigma \|\boldsymbol{w}\|_1, && \text{(4.5a)} \\
\text{s.t.} \quad & \Delta^2 \mathscr{P}(\boldsymbol{x}, k; \boldsymbol{\beta}) + k^2 \mathscr{P}(\boldsymbol{x}, k; \boldsymbol{\beta}) = 0 && \text{(4.5b)} \\
& \boldsymbol{x} \in \Omega \\
& \sigma \in [0, \infty)
\end{aligned}$$

where $\|\cdot\|_1$ is ℓ_1-norm, $\boldsymbol{w} = [w_1, \ldots, w_V]^T$ is a $V \times 1$ vector that contains the neuron weights. We apply ℓ_1-norm as the model complexity loss to control the number of activated point neurons and to avoid overfitting. Note that all network parameters are frequency/wave number dependent and for convenience, we omit the dependency on k for the rest of the chapter.

The network parameters can be updated iteratively by back propagation. In specific, for the v^{th} point neuron, weights w_v can be updated by

$$w_v(n+1) = w_v(n) - \mu \frac{\partial \mathscr{L}(n)}{\partial w_v(n)^*}, \tag{4.6}$$

where

$$\frac{\partial \mathscr{L}(n)}{\partial w_v^*(n)} = \sum_{q=1}^{Q} \Big(\mathscr{P}(\boldsymbol{x}_q, n) - P(\boldsymbol{x}_q)\Big) \frac{D_v(n)}{D_v^q(n)}\, e^{-ik\left(D_v^q(n) - D_v(n)\right)} + \frac{1}{2}\sigma e^{i\theta_v(n)}, \tag{4.7}$$

with

$$\begin{aligned} D_v(n) &= \sqrt{B_v^x(n)^2 + B_v^y(n)^2 + B_v^z(n)^2}, \\ D_q^v(n) &= \sqrt{\left(B_v^x(n) - x_q\right)^2 + \left(B_v^y(n) - y_q\right)^2 + \left(B_v^z(n) - z_q\right)^2}, \end{aligned}$$

n is the iteration index of the training process, μ is the learning rate (step size), $(\cdot)^*$ denotes complex conjugation, and $\theta_v(n) \in \mathbb{R}$ is the phases of complex weight w_v. The proof of (4.7) is given in Appendix 4.8.1.

Using back propagation, we can also update bias parameters $B_v^\alpha(\cdot)$ where $\alpha \in \{x, y, z\}$ by

$$B_v^\alpha(n+1) = B_v^\alpha(n) - \mu \frac{\partial \mathscr{L}(n)}{\partial B_v^\alpha(n)}, \tag{4.8}$$

where

$$\begin{aligned} \frac{\partial \mathscr{L}(n)}{\partial B_v^x(n)} = &\sum_{q=1}^{Q} 2\,\mathbb{R}\mathrm{e}\Bigg\{ \big(\mathscr{P}(\boldsymbol{x}_q, n) - P(\boldsymbol{x}_q)\big)^* \; w_v \; \frac{D_v(n)}{D_v^q(n)} \; e^{ik\left(D_v^q(n) - D_v(n)\right)} \\ &\times \Big(\frac{-\big(ikD_v(n) - 1\big)}{D_v(n)^2} B_v^x(n) + \frac{\big(ikD_v^q(n) - 1\big)}{D_v^q(n)^2} \big(B_v^x(n) - x_q\big) \Big) \Bigg\}, \end{aligned} \tag{4.9}$$

$$\begin{aligned} \frac{\partial \mathscr{L}(n)}{\partial B_v^y(n)} = &\sum_{q=1}^{Q} 2\ \mathbb{R}\mathrm{e}\Bigg\{ \big(\mathscr{P}(\boldsymbol{x}_q, n) - P(\boldsymbol{x}_q)\big)^* \; w_v \; \frac{D_v(n)}{D_v^q(n)} \; e^{ik\left(D_v^q(n) - D_v(n)\right)} \\ &\times \Big(\frac{-\big(ikD_v(n) - 1\big)}{D_v(n)^2} B_v^y(n) + \frac{\big(ikD_v^q(n) - 1\big)}{D_v^q(n)^2} \big(B_v^y(n) - y_q\big) \Big) \Bigg\}, \end{aligned} \tag{4.10}$$

$$\begin{aligned} \frac{\partial \mathscr{L}(n)}{\partial B_v^z(n)} = &\sum_{q=1}^{Q} 2\,\mathbb{R}\mathrm{e}\Bigg\{ \big(\mathscr{P}(\boldsymbol{x}_q, n) - P(\boldsymbol{x}_q)\big)^* \; w_v \; \frac{D_v(n)}{D_v^q(n)} \; e^{ik\left(D_v^q(n) - D_v(n)\right)} \\ &\times \Big(\frac{-\big(ikD_v(n) - 1\big)}{D_v(n)^2} B_v^z(n) + \frac{\big(ikD_v^q(n) - 1\big)}{D_v^q(n)^2} \big(B_v^z(n) - z_q\big) \Big) \Bigg\}, \end{aligned} \tag{4.11}$$

where $\mathbb{R}\mathrm{e}\{\cdot\}$ represents the real part of the argument. The proofs of (4.9), (4.10) and (4.11) are given in Appendix 4.8.2.

We have the following comments:

1. In the training process, only microphone observations are used to learn the model, and no extra data or datasets are required. Therefore, the proposed network architecture is feasible in the small data regime where datasets are not accessible, which is common in real sound field model scenarios.

2. From (4.7), (4.9), (4.10), and (4.11), gradients of $w_v(n)$, $B_v^x(n)$, $B_v^y(n)$, and $B_v^z(n)$ become infinity when $D_v(n)$ and $D_v^q(n)$ becomes zero, which means point neurons (virtual sources) cannot be initialized at observer point positions or the origin point. Considering the physical meaning of the network, observer points cannot be on the source positions. Thus, during the training process, we apply a strategy to avoid placing virtual sources on the observer positions nor at the origin. We calculate the $D_v(n)$ and $D_v^q(n)$ in each iteration and replace $B_v^x(n)$, $B_v^y(n)$, and $B_v^z(n)$ to another location when $D_v(n)$ or $D_v^q(n)$ is smaller than a certain threshold.

4.3.3 System initialization

We initialise point neuron weights w_v such that $|w_v|$ in the range of $[-1, 1]$. For the initialization of system biases, we use any Prior-known knowledge about the underlying physical scenario to determine the initial positions of the virtual sources. In general, virtual sources can initially be equally spaced at a distance of half the wavelength $\lambda/2$ as a rule of thumb. The distribution range of the virtual sources should be determined based on the implementation scenario. For example, for modelling the outgoing sound field of a certain sound source, such as a drone, the virtual sources can be initially placed within a sphere that encompasses the sound source. Another initialization example will be discussed in the next section. Initializing the bias with pre-known information can increase the convergence speed of the proposed network and avoid being trapped to a local minimum.

4.4 Simulation Experiments: Scenario One

To illustrate the versatility of the proposed point neuron network architecture, we first apply it to the sound field reconstruction problem, where the goal is to accurately estimate the sound field over a spatial region using a limited set of measurements from microphones.

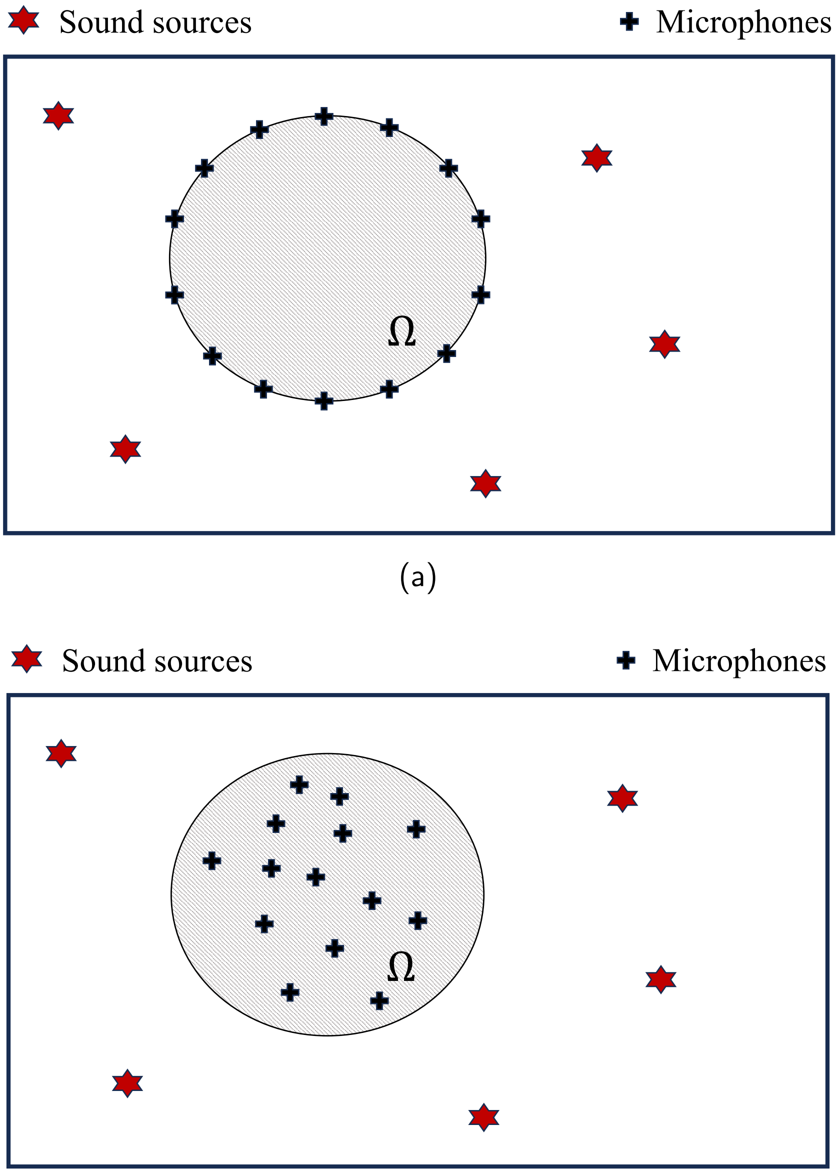

(a)

(b)

Figure 4.3: The example reverberant room used in the simulation in Section 4.4 where the sound sources are outside the observation region Ω with (a) microphones uniformly placed over the edge of the target region and (b) microphones arbitrarily placed in the target region.

4.4.1 Room settings

We evaluate the proposed method in a rectangular reverberant room with dimensions 6.0 m × 4.0 m × 4.0 m where the coordinate origin is in the middle of the room. The target reconstruction region Ω is a horizontal circular region with a radius of $R = 1.0$ m, centred at the point $(-1.0, 0.5, 0.0)$ m. There are five sources with equal strength (set to unity) located at the same horizontal plane, with coordinates $(-2.65, 1.5, 0.0)$ m, $(-2.4, -1.2, 0.0)$ m, $(0.2, -1.5, 0.0)$ m, $(1.7, -0.2, 0.0)$

m, and $(1.0, 1.2, 0.0)$ m. We use the image source method [205] with wall reflection coefficients $[0.8, 0.8, 0.8, 0.8, 0, 0]$ to simulate the sound field over the target reconstruction region. The corresponding reverberation time RT_{60} is 0.537 s [206]. Note that, we set the reflection coefficients of the roof and ground to zero to simplify the illustration.

We consider two different microphone placements to capture the sound field: (i) uniform circular array on the boundary of the target region (Fig. 4.3a), and (ii) randomly selected locations inside the target region (Fig. 4.3b). We initially place $Q = 75$ microphones based on $Q = 2N + 1$ where $N = \lceil k_{f_{\max}} R \rceil$ and $\lceil \cdot \rceil$ is the ceiling operation [207]. In Sec. 4.4.6, we investigate the performance by varying the number of microphones. For all simulations, except Sec. 4.4.7, white Gaussian noise with an SNR of 20 dB is added to each of the microphone measurements.

For reconstruction performance evaluations, we consider the frequency band from 100 to 2000 Hz with 100 Hz increments and use a grid of uniformly spaced 1124 evaluation points over the target region, with a point separation of 5.3 cm.

4.4.2 Network settings

We randomly initialize the network weights by $|w_v| \in [-1, 1]$. For the system biases, we initially place them over a mesh grid on the same horizontal plane as Ω, excluding the target region Ω. The grid has a size of 9.0 m × 9.0 m with a resolution of $\lambda/2$. The number of point neurons increases from $V = 25$ for the lowest frequency to $V = 465$ for the highest frequency. The parameter σ is in the range of $[3 \times 10^{-4}, 3 \times 10^{-3}]$, and $\mu = 3 \times 10^{-2}$.

We compare the proposed sound field reconstruction with a conventional method and a typical PINN method. The conventional method is the orthogonal harmonics-based sound field estimation method that reconstructs any incident sound field by a finite number of harmonic basis functions and corresponding coefficients [208, 108]. We adopt the network architecture proposed in [139] as the typical PINN method since it adds PDE loss to a fully connected network architecture similar to many PINN methods. Similar to the proposed method, the PINN in [139] also only requires microphone observations in the training process. This network contains 3 layers and 15 nodes of each layer, with the activation function being *tanh*, and initializes the trainable parameters with the Xavier initialization. We train the PINN for 108 epochs with a learning rate of 10^{-5} using the ADAM optimizer. The data loss of the network is calculated by all microphones, and the PDE loss is calculated by 437 uniformly arranged sampling points over the target region. Note that PDE loss is not applicable to the proposed method as the proposed method strictly satisfied the Helmholtz equation and has zero PDE loss.

4.4.3 Evaluation metrics

Two different metrics are used to evaluate the overall model estimation. The first metric is the normalized mean square error (NMSE) between the original sound field $P(\boldsymbol{x}, k)$ and the sound field model $\mathscr{P}(\boldsymbol{x}, k)$ for each frequency point k, which is defined by

$$\mathrm{NMSE}(k) = 20\log_{10}\frac{\sum_{u=1}^{U}|\mathscr{P}(\boldsymbol{x}_u, k) - P(\boldsymbol{x}_u, k)|}{\sum_{u=1}^{U}|P(\boldsymbol{x}_u, k)|}, \tag{4.12}$$

where U is the number of evaluation points, $u = 1, ..., U$ be the index of evaluation points, and $\boldsymbol{x}_u \in \Omega$.

The second metric is the Modal Assurance Criterion (MAC) [209], which can assess the overall similarity between the estimated sound field and the original sound field for each frequency. The MAC value is a real scalar bounded by 0 and 1. When the estimated sound field shapes correspond to the original sound field, the resultant MAC estimate is close to 1, but it never reaches 1 unless the same mode shape vectors are compared. MAC(k) can be calculated by

$$\mathrm{MAC}(k) = \frac{\|\boldsymbol{p}_{\mathrm{eval}}^{H}\hat{\boldsymbol{p}}_{\mathrm{eval}}\|_2^2}{(\boldsymbol{p}_{\mathrm{eval}}^{H}\boldsymbol{p}_{\mathrm{eval}})(\hat{\boldsymbol{p}}_{\mathrm{eval}}^{H}\hat{\boldsymbol{p}}_{\mathrm{eval}})}, \tag{4.13}$$

where $\boldsymbol{p}_{\mathrm{eval}} = [P(\boldsymbol{x}_1, k), \ldots, P(\boldsymbol{x}_U, k)]^T$ and $\hat{\boldsymbol{p}}_{\mathrm{eval}} = [\mathscr{P}(\boldsymbol{x}_1, k), \ldots, \mathscr{P}(\boldsymbol{x}_U, k)]^T$ are two $U \times 1$ vectors that contain the original sound pressure (ground truth) and estimated sound pressure of evaluate points, $(\cdot)^H$ denotes the conjugate transpose. Although (4.13) and (4.12) appear similar, they have essential differences. NMSE is calculated point by point, while MAC is calculated from the vector of model estimations. Consequently, MAC can assess the overall similarity between the estimated sound field and the original sound field.

We also visualize the error distribution of the estimated sound field for certain frequencies. The corresponding normalized square error (NSE) is defined as

$$\mathrm{NSE}(\boldsymbol{x}, k) = 20\log_{10}\frac{|\mathscr{P}(\boldsymbol{x}, k) - P(\boldsymbol{x}, k)|}{|P(\boldsymbol{x}, k)|}. \tag{4.14}$$

4.4.4 Circular microphone array placement

Figure 4.4 depicts the performance metrics NMSE (4.12) and MAC (4.13) of the proposed method, harmonics-based method, and PINN method as a function of frequency. Overall, the proposed method outperforms the other two methods for all frequencies, especially when the frequency is higher than 1100 Hz. Specifically, based on the NMSE result as shown in Fig. 4.4a, (i) the proposed method has the lowest NMSE for all frequencies, and it slightly increases from −22 dB in 100 Hz to −13 dB in 2000 Hz, (ii) the PINN method can roughly estimate the sound field under 1100 Hz, while above 1100 Hz the NMSE reaches 0 dB, and (iii) the NMSE for the harmonics-based method fluctuates between −10 dB to 10 dB, and peaks are caused by the zeros of the spherical Bessel function. For small target regions, the harmonics-based method is reliable, but for larger target regions, more basis functions are used to estimate the sound field, and more Bessel zeros are involved in the estimation, resulting in poor performance of the harmonic-based method.

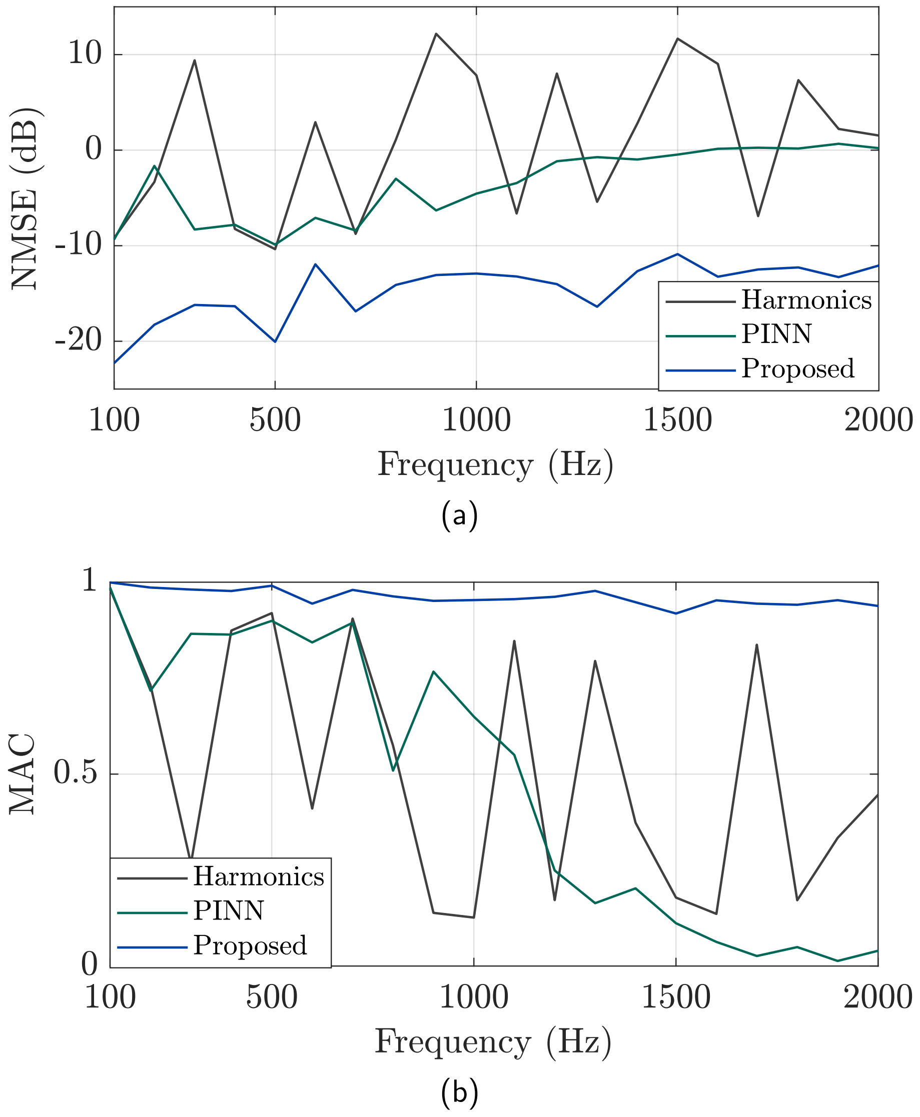

(a)

(b)

Figure 4.4: Evaluation metrics (a) NMSE and (b) MAC with respect to the frequency with circular microphone placement.

From Fig. 4.4b, we find that (i) the proposed method has the highest MAC over all frequencies; (ii) the performance of PINN method degrades after 1100 Hz, indicating that the PINN model cannot estimate the sound field distribution for higher frequencies; (iii) the MAC results for harmonics-based method fluctuates over a large range, indicating the harmonics based method can only work for certain frequencies with the given microphone placement.

Since the dimensionality of the sound field increases with frequency, we observe that the given number of microphones may not be enough to train the PINN to learn the sound field, resulting in its poor performance at higher frequencies. Moreover, the low MAC value for the PINN method over high frequencies also reveals the potential of losing phase information for the learned model.

The sound field reconstruction results and NSE distributions for different methods at 900 Hz are shown in Fig. 4.5, indicating the proposed method can reconstruct the sound field beyond the target region smoothly, demonstrating the proposed method can be generalized to out-of-sample scenarios. Based on Figs. 4.5c and 4.5f, the PINN method can only reconstruct the sound field over the target region but has significant errors for reconstructing the sound field outside of Ω. The reconstruction range is restricted by the distribution range of microphone observations and PDE evaluation points, which is one of the common limitations of typical PINNs.

As shown in Figs. 4.5d and 4.5g, the harmonics-based method can not correctly estimate the sound field at 900 Hz.

4.4.5 Random microphone placement

In some cases, the circular microphone placement is not practical. Therefore, we investigate the performance of different methods with the random microphone placement which can demonstrate the overall performance under more general cases. Results of NMSE and MAC evaluation are presented in Fig. 4.6, illustrating the proposed method outperforms two competing methods for all frequencies, especially when the frequency is higher than 1500 Hz. Compared with Fig. 4.4, we find that with random microphone placement i) the performance of the proposed method is improved by around 3 dB for frequencies under 500 Hz and reduced by around 4 dB for frequencies above 1700 Hz; ii) the outcome of PINN method is enhanced around 7 to 8 dB for frequencies below 1100 Hz, but for high frequencies, it cannot estimate the sound field correctly; iii) the results of the harmonics-based method are more stable and improved by around 8 dB for frequencies below 1500 Hz, but the performance collapses after 1500 Hz.

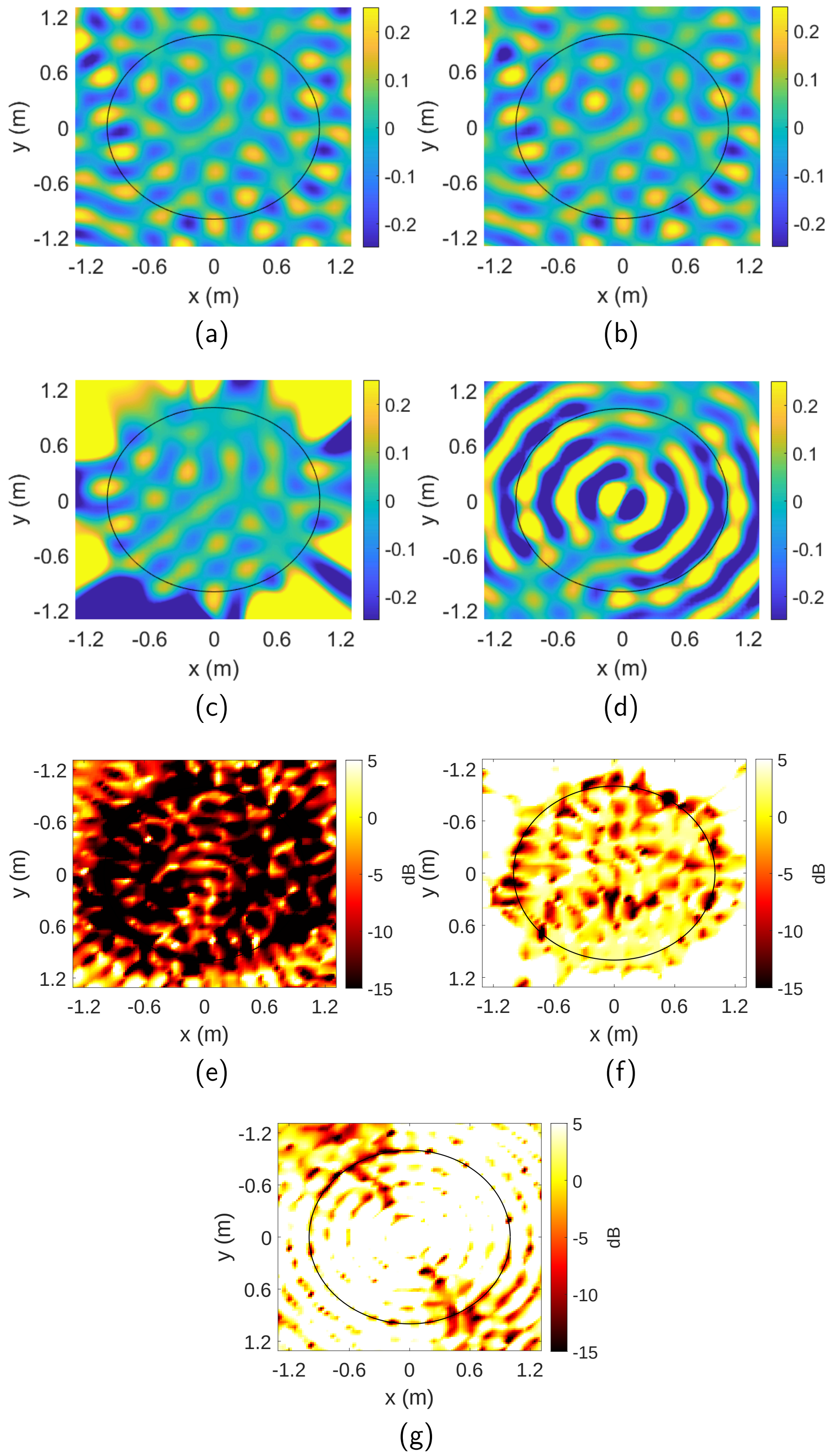

Figure 4.5: Sound field reconstruction and NSE distribution with circular microphone distribution at 900 Hz for different methods, where the black circle bounds the target region: (a) original sound field (b) sound field reconstructed by the proposed method (c) sound field reconstructed by the PINN method (d) sound field reconstructed by the harmonics-based method (e) NSE of the proposed method (f) NSE of the PINN method (g) NSE of the harmonics-based method.

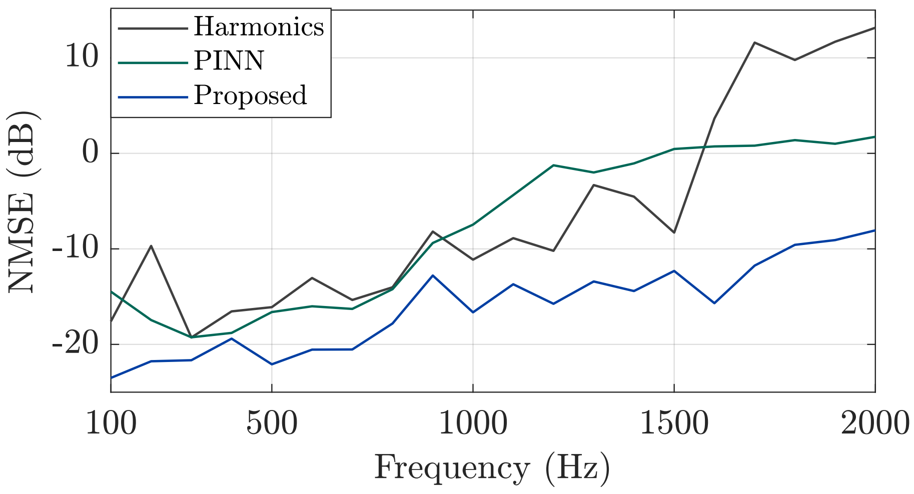

(a)

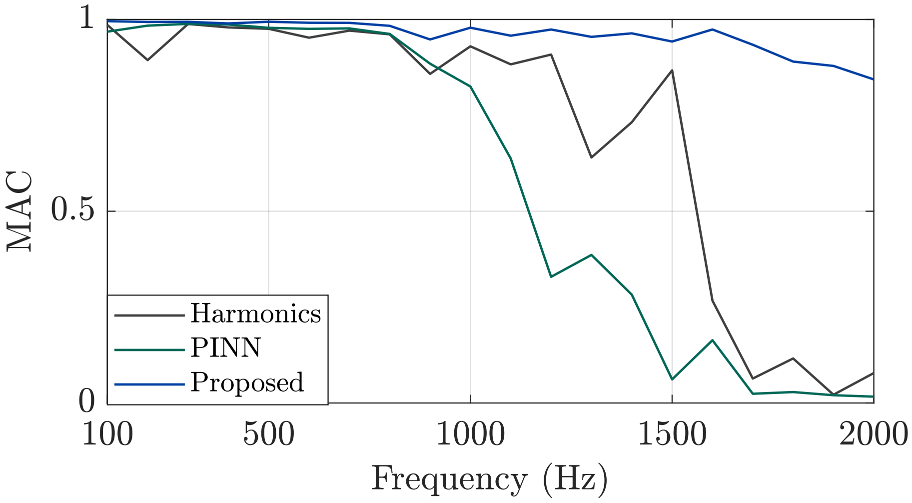

(b)

Figure 4.6: Evaluation metrics (a) NMSE and (b) MAC with respect to the frequency with random microphone placement.

Compared to circular microphone placement, the random microphone distribution samples across the whole target region can benefit the learning process of the proposed method and PINN method, especially for low frequencies. However, the random distribution results in a smaller number of samples in some areas, affecting the estimation of the complex sound field of high frequencies. For the harmonic-based method, the random microphone placement reduces the influence of Bessel zeros and enhance the estimation outcome.

Similar to the investigation in Section 4.4.4, we visualize the original sound field, reconstructed sound fields, and NSE distribution with random microphone placement at 900 Hz in Fig. 4.7. Compared to Fig. 4.5, we find that: i) the proposed method consistently has the best performance that reconstructs the sound field of

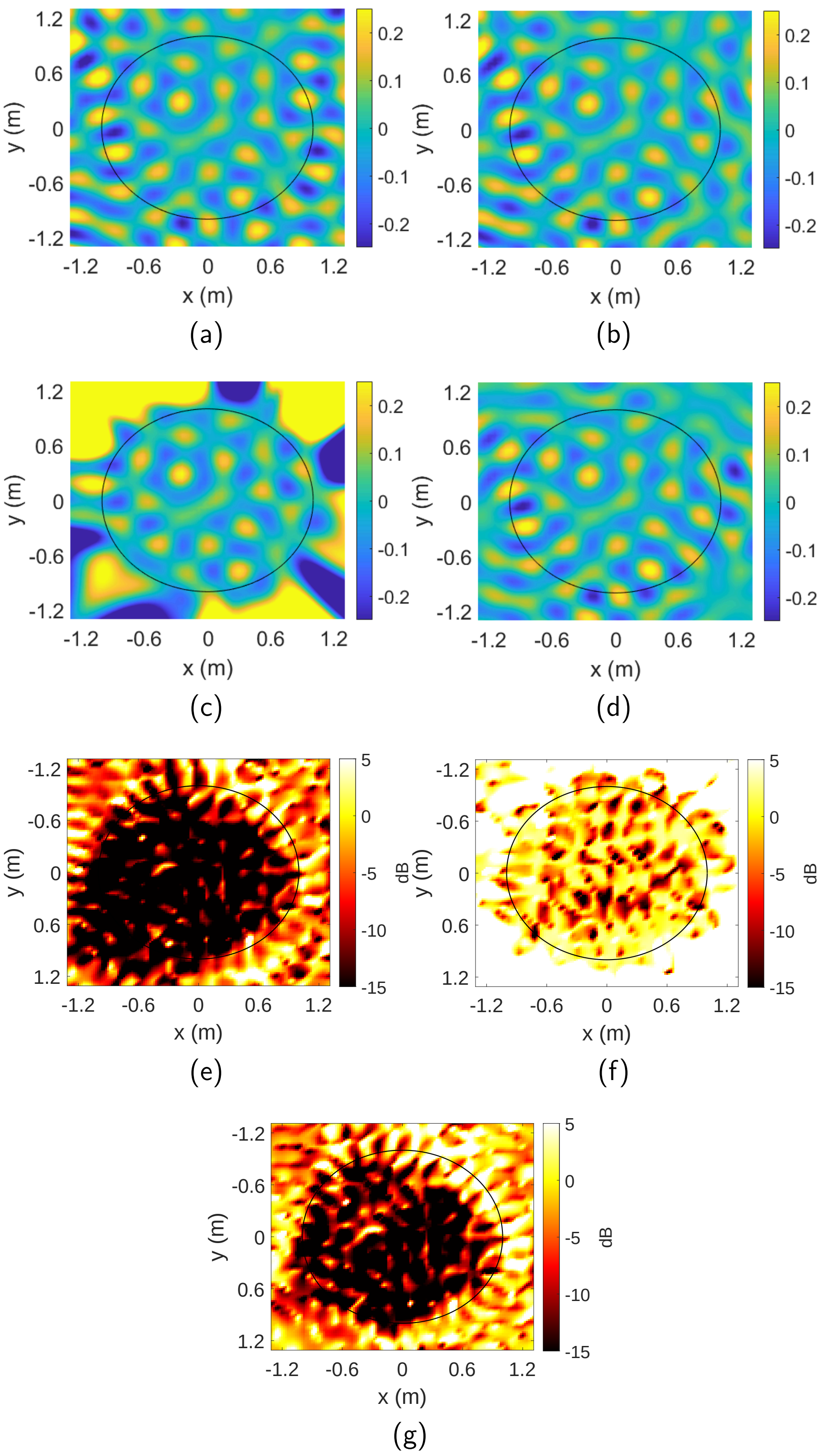

Figure 4.7: Sound field reconstruction and NSE distribution with random microphone distribution at 900 Hz for different methods, where the black circle bounds the target region: (a) original sound field (b) sound field reconstructed by the proposed method (c) sound field reconstructed by the PINN method (d) sound field reconstructed by the harmonics-based method (e) NSE of the proposed method (f) NSE of the PINN method (g) NSE of the harmonics-based method.

the target region accurately; ii) the proposed method estimates the sound field larger than the target region, indicating the generalizability to out-of-sample scenarios; iii) compared to Figs. 4.5d and 4.5g, the reconstruction from harmonics based method is greatly improved with the random distribution and presents the accurate distribution larger than the target region; iv) the reconstruction from PINN method is slightly enhanced over the centre part of the target region.

In section 4.4.4 and section 4.4.5, we demonstrated that the proposed method outperforms two competing methods with both circular and random microphone placements. To further investigate the proposed method, we test its performance with more sparse microphone placement and different strengths of white Gaussian noise in the following subsections.

4.4.6 Impact of varying the number of microphones

We use $Q = 2N + 1$ as the initial guide for choosing the number of microphones in Sections 4.4.4 and 4.4.5. However, for larger target regions and high frequencies, the calculated microphone number is too large which may not be practical. Therefore, in this subsection, we investigate the performance of the proposed method under different microphone numbers with random placement. We keep all settings the same as in Section 4.4.5 except the number of microphones Q which we vary for the following values: $Q = 35,\ 45,\ 55,\ 65, \text{and } 75$.

Results are shown in Fig. 4.8. Overall, the higher the number of microphones, the better the accuracy of the estimation of the sound field.

The difference between NMSE and MAC values are very small for $Q = 55,\ 65, \text{and } 75$, which indicates for $Q \geq 55$ the proposed method accurately estimates the sound field for the whole range of interested frequencies. For $Q = 35$ and 45, the proposed method accurately reconstructs the sound field under 1000 Hz and 1500 Hz, respectively. The required microphone number is a function of the frequency and size of the target region, similar to the truncation rule in [207, 210], but further investigations are required to reveal the relationship among them. Compared to Fig. 4.6, even with $Q = 35$, the proposed method can still outperform the two competing methods.

4.4.7 Robustness analysis under different SNRs and RT_{60}s

We investigate the robustness of the proposed method under different levels of white Gaussian noise and reverberation strength in this section. We first keep all other

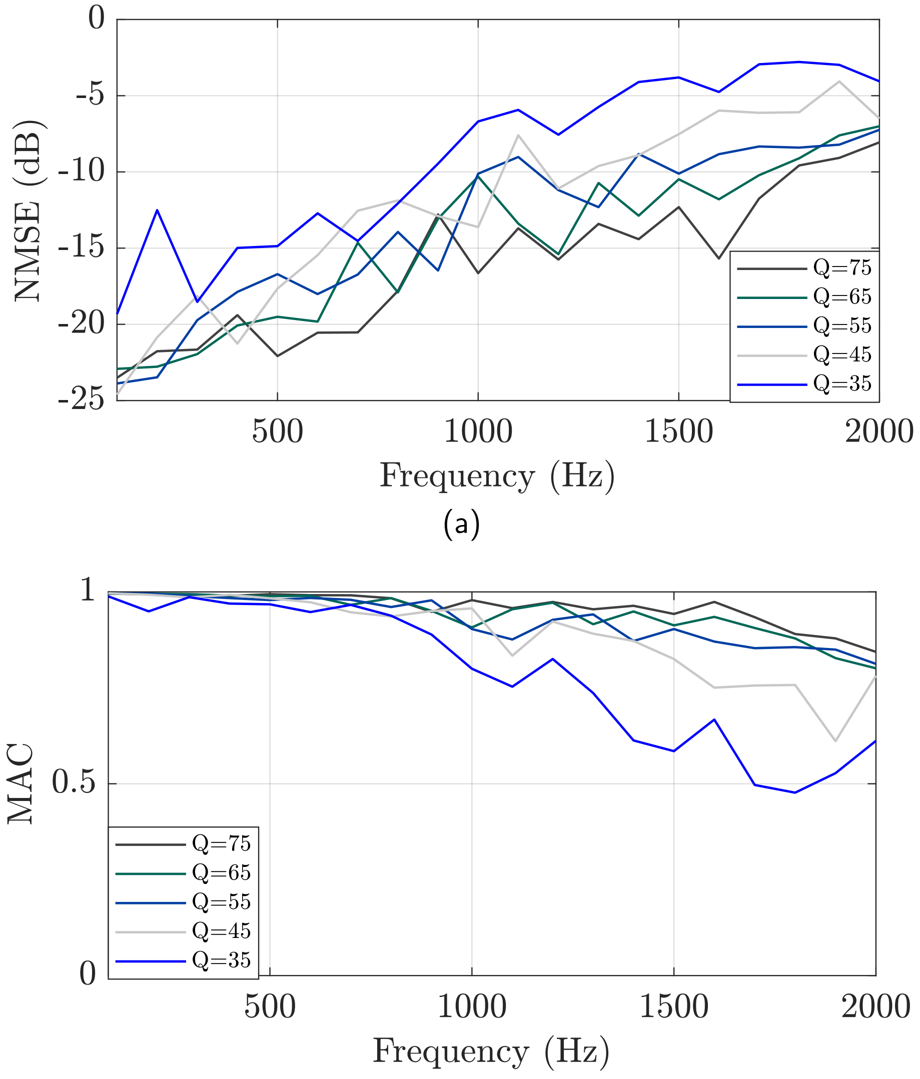

(a)

(b)

Figure 4.8: (a) NMSE and (b) MAC with respect to the frequency with different numbers of randomly placed microphones.

settings the same as in Section 4.4.5 and only change the noise levels added to the microphone observations.

Results are presented in Fig. 4.9, where we find that: i) with noise under 30 dB SNR, the proposed method has similar performance regardless of SNR, meaning a small level of white Gaussian noise has little influence on the proposed method; ii) when SNR $\leq$ 20 dB, the estimation accuracy decreases with the increment of noise level, especially for higher frequencies; iii) compared to the NMSE plot in Fig. 4.10a, the MAC results, shown in Fig. 4.10b, for high frequencies are more sensitive to noise, indicating the estimation for high frequencies tends to lose the overall similarity of the original sound field; iv) when SNR $\leq$ 20 dB, both NMSE and MAC plots among different noise level have similar shape, indicating that the outcome of the

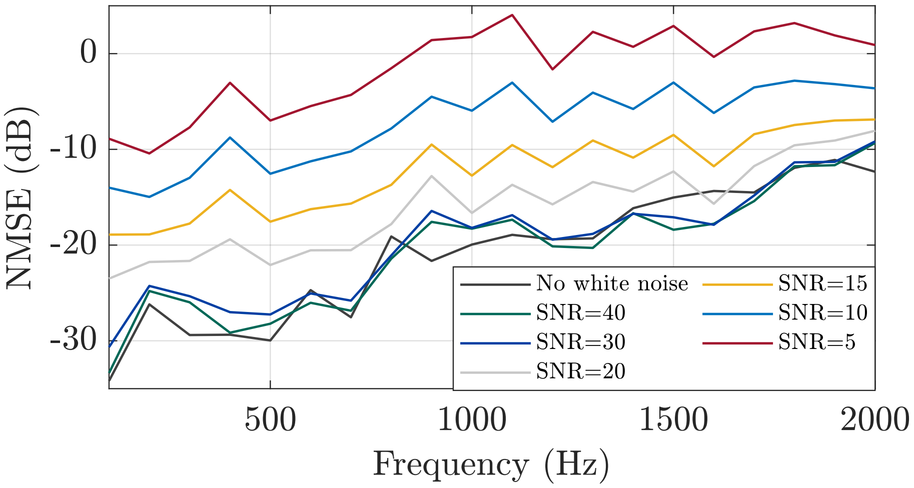

(a)

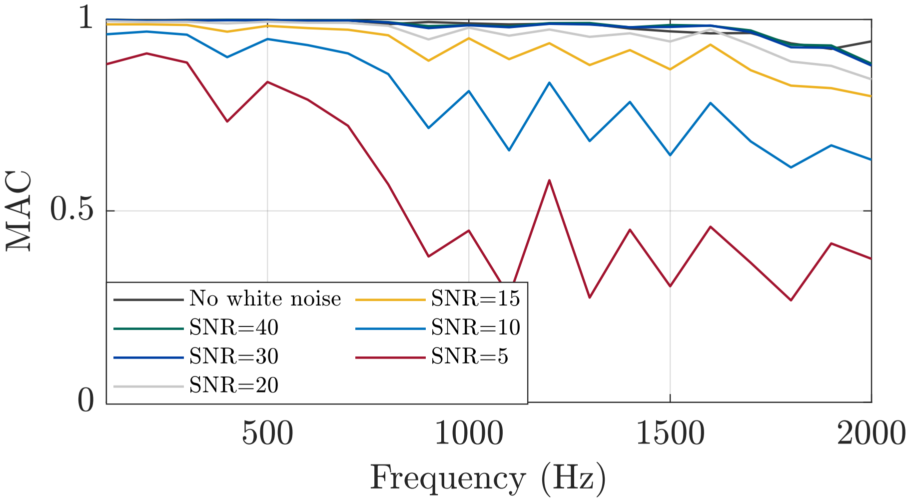

(b)

Figure 4.9: (a) NMSE and (b) MAC with respect to the frequency with different noise levels under random microphone placements.

proposed method is consistent with frequencies; v) compared to Fig. 4.6, even with SNR = 15 dB, the proposed method still outperforms two competing methods.

We further investigate the performance of the proposed method under different reverberation conditions, by keeping all other settings the same as in Section 4.4.5 and only change the value of RT_{60}.

Results are presented in Fig. 4.10, where we find that: i) with small reverberation strength, the estimation is less sensitive to frequency; ii) as the reverberation strength increases, the estimation is more robust for lower frequencies compared to higher ones; and iii) the estimations under $RT_{60} = 0.6$ s and $RT_{60} = 0.9$ s maintain similarly good performance, indicating the proposed method's robustness.

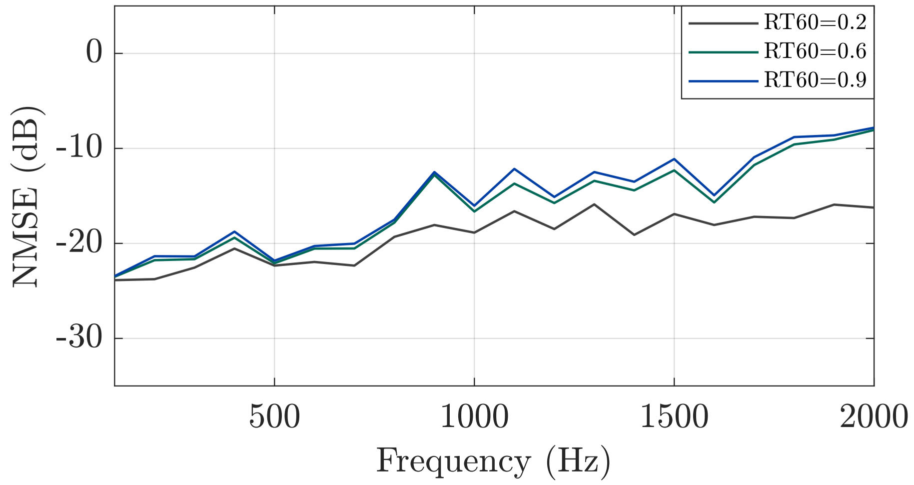

(a)

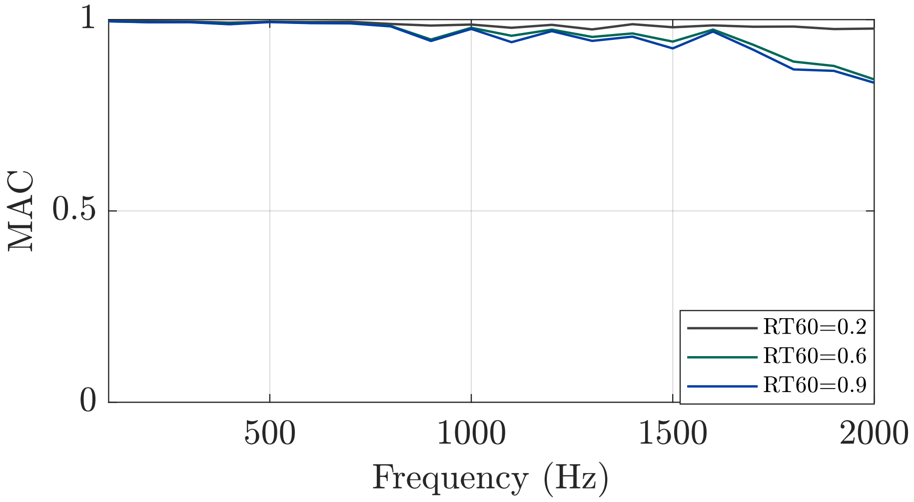

(b)

Figure 4.10: (a) NMSE and (b) MAC with respect to the frequency with different reverberation conditions under random microphone placements.

4.5 Simulation Experiments: Scenario Two

We further evaluate the proposed point neuron network architecture by the sound field extrapolation problem to test the applicability to the drone directional sound field modeling task. As shown in Fig. 4.11, we have sources located in the spherical source region with the radius R_S, marked in gray, and aim to extrapolate the sound field from the measured region to a target region located at a greater radial distance from the origin while maintaining the same angular coverage. This extrapolation task represents a generalization of the spherical sector sound field extrapolation problem discussed in Chapter 3. Unlike the previous case, where both the measurement region and the region of interest (ROI) were strictly constrained to a spherical sector shape, the current problem allows for greater flexibility. The measurement

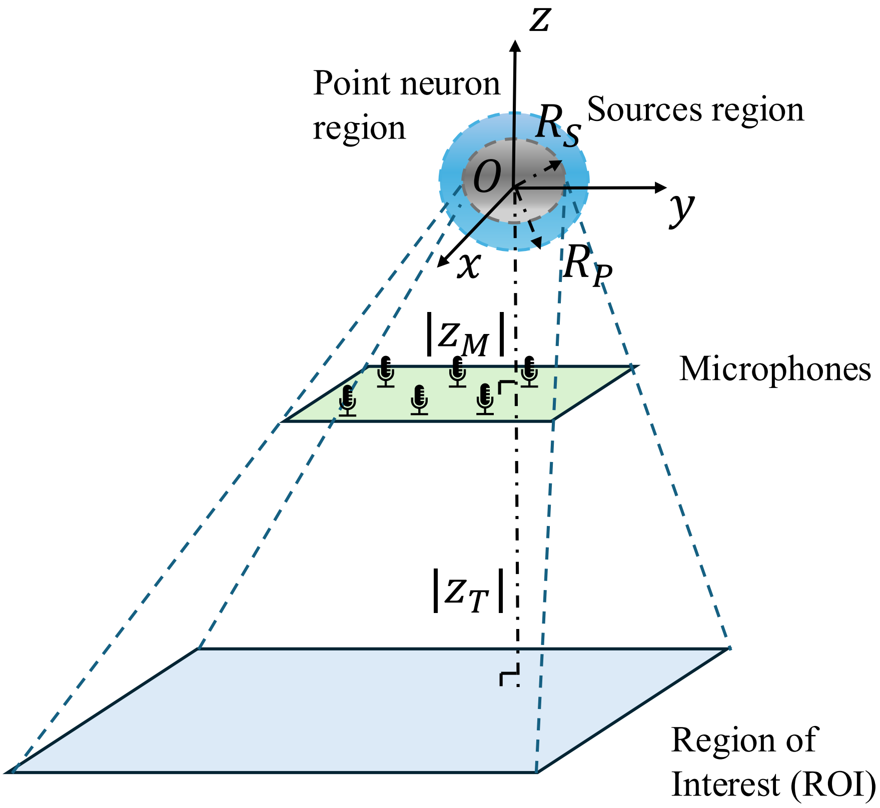

Figure 4.11: Sound field directional extrapolation setup.

and target regions are not limited to spherical sector geometries but can instead take the form of planar surfaces or other arbitrary shapes, provided they share the same angular extent.

In the simulation, we randomly position 50 point sources within the source region, each assigned a random weight, and set the source region radius to $R_S = 0.15$ m. The planar measurement region is placed directly below the source region at $z_M = -0.5$ m, spanning $x_M \in [-0.2, 0.2]$ m and $y_M \in [-0.2, 0.2]$ m. A total of $Q = 25$ microphones are uniformly distributed over this measurement region to capture the sound field. To simulate real-world conditions, white Gaussian noise with a SNR of 30 dB is added to each microphone measurement. Similarly, the planar ROI is located further below the measurement region at $z_T = -5$ m, with the same lateral extent as the measurement region, spanning $x_M \in [-1.325, 1.325]$ m and $y_M \in [-1.325, 1.325]$ m. To evaluate the extrapolation performance, we uniformly place 10,000 evaluation points across the ROI.

Assuming a rough estimation of the source region's size, we define this estimated region as the point-neuron region. During the initialization stage, the network weights are randomly initialized within the range $|w_v| \in [-1, 1]$. The system bi-

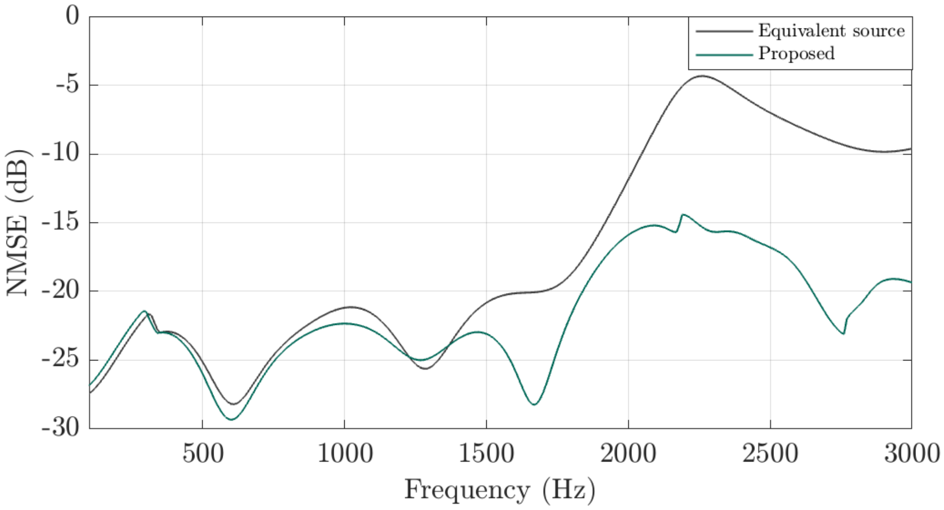

Figure 4.12: Extrapolation NMSE with respect to the frequency.

ases are also randomly initialized within the point-neuron region, with a radius set to $R_T = 0.3$ m. The number of point neurons is fixed at $V = 26$, ensuring a balance between model complexity and computational efficiency. The regularization parameter σ is set within the range of $[1 \times 10^{-1}]$, while the learning rate parameter is set to $\mu = 2 \times 10^{-2}$.

Because there is no sampling point on ROI, the PINN method [139] we compared in Section 3.4.2 failed on this task. We compare the proposed method with the conventional equivalent source method in this task, where the equivalent point sources are placed at the initial position of the point neurons. The evaluated frequency range is 100 - 3000 Hz with a 10 Hz increment.

The NMSE results are presented in Fig. 4.11. Overall, the proposed method outperforms the equivalent source method across most frequencies. Notably, for frequencies above 1500 Hz, where the performance of the equivalent source method deteriorates significantly, the proposed method maintains a consistently low NMSE, ensuring high extrapolation accuracy at higher frequencies. Additionally, we observe fluctuations in NMSE across different frequencies. A possible reason for this is the use of the same parameter settings for all frequencies, which may not be optimal for certain frequencies. Fine-tuning these parameters could further enhance the performance of the proposed method.

The sound field extrapolation results and NMSE distributions at 3000 Hz are shown in Fig. 4.13. Overall, both methods can capture the general wave pattern over the ROI; however, the equivalent source method struggles to reconstruct finer details of the sound field. Since the sources are concentrated in a small region, they generate a wave-like sound field in the far field. The equivalent source method, which places

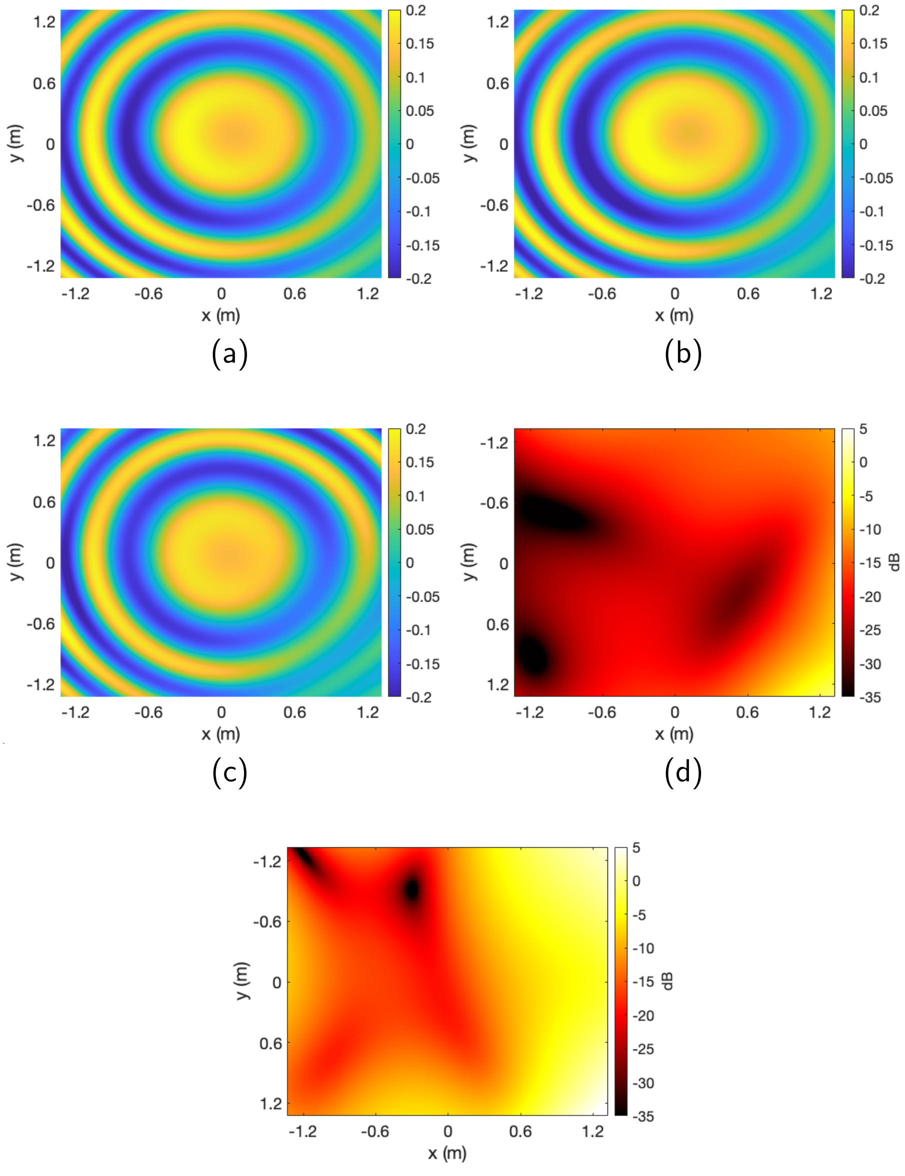

(a) (b) (c) (d) (e)

Figure 4.13: Sound field extrapolation and NSE distribution at 3000 Hz for different methods: (a) original sound field (b) sound field extrapolated by the proposed method (c) sound field extrapolated by the equivalent source method (d) NSE of the proposed method (e) NSE of the equivalent source method.

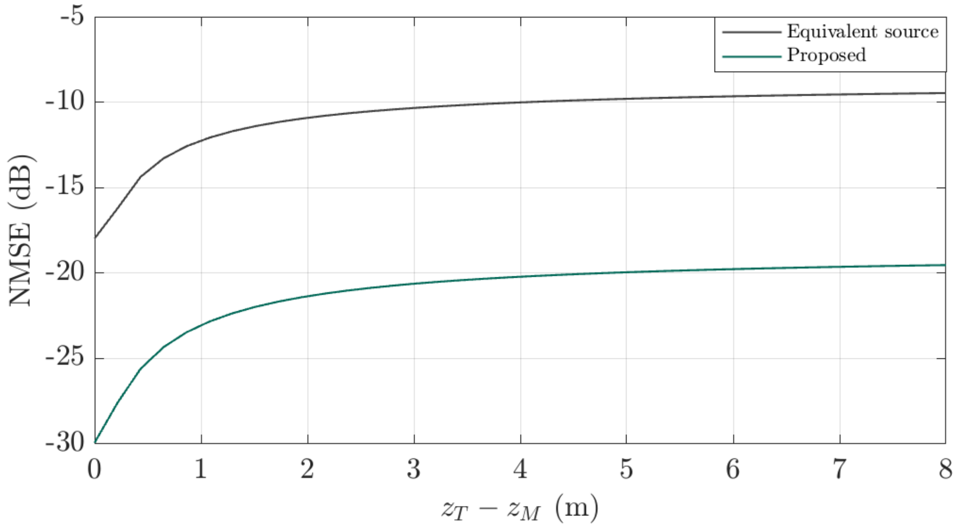

Figure 4.14: Extrapolation NMSE with respect to the extrapolation distance.

equivalent sources around the source region, can approximate this wave pattern but fails to preserve intricate details due to suboptimal source distribution.

A closer examination of Figs. 4.5 and 4.13e reveal that the proposed method provides a more accurate extrapolation of the sound field across the entire ROI, while the equivalent source method introduces noticeable errors, particularly on the right side of the ROI. This discrepancy arises because the equivalent sources fail to fully account for the complex interference patterns present in the original sound field. In contrast, the proposed method captures these intricate details, resulting in significantly improved extrapolation accuracy.

We further investigate the extrapolation performance with respect to the extrapolation distance for the 3000 Hz scenario. The extrapolation distance increases from 0 m ($z_T = z_M$) to 8 m with 0.2 m increment. The result is shown in Fig. 4.14, where we find that: (i) the NMSE of both the proposed method increase rapidly within a small distance and then gradually converge, indicating that the sound field structure stabilizes in the far field; (ii) while both methods follow similar trajectories, the proposed method consistently maintains an NMSE that is approximately 10 dB lower across all extrapolation distances.

4.6 Summary and Contributions

In this chapter, we developed a new PINN architecture that embedded the fundamental solution of the wave equation into the network architecture, enabling the learned model to strictly satisfy the wave equation. The proposed point neuron learning method can estimate an arbitrary sound field based on microphone observations. Compared to other PINN methods, our approach can directly process complex numbers and is fully interpretable in physics, along with improved generalizability to out-of-sample scenarios. The proposed method was first evaluated in a sound field reconstruction problem within a reverberant environment with multiple evaluation metrics. Results indicate that the point neuron learning method outperformed two competing methods over all investigated frequencies. Additionally, the proposed method exhibited robustness to white Gaussian noise and varying reverberation strengths. It also proved effective even with sparse microphone observations. Furthermore, we evaluated the proposed method with a sound field extrapolation problem to highlight the versatility of the proposed point neuron network architecture. While we used sound field reconstruction and the extrapolation problem only as two examples, we expect the proposed point neuron architecture to be suitable for many applications involving wave propagation governed by the wave equation. Compared to the method proposed in Chapter 3, the point-neuron approach offers greater flexibility in microphone placement for estimating the directional drone outgoing sound field and has the potential to be integrated with ANC systems in future applications.

4.7 Related Publications

- H. Bi and T. D. Abhayapala,"Point neuron learning: A new physics-informed neural network architecture," J. Audio Speech Music Process., vol. 2024, no. 56, 2024, [Online]. Available: https://doi.org/10.1186/s13636-024-00376-0.

4.8 Appendix

4.8.1 Derivation of equation (4.7)

We derive the back propagation of point neuron weights in this section. The frequency dependency k and iteration index n are omitted for notational simplicity.

With the input of $\boldsymbol{x}_q$, the output of the v-th point neuron can be expressed by

$$\mathscr{P}_q^v = w_v \frac{D_v}{D_q^v} e^{ik(D_q^v - D_v)}. \tag{4.15}$$

For updating point neuron weights, from (4.5a), we have

$$\frac{\partial \mathscr{L}}{\partial w_v^*} = \frac{\partial \big(\sum_{q=1}^{Q} |\mathscr{P}(\boldsymbol{x}_q) - P(\boldsymbol{x}_q)|^2 \big)}{\partial w_v^*} + \lambda \frac{\partial (\|\boldsymbol{w}\|_1)}{\partial w_v^*}. \tag{4.16}$$

The first term can be further expressed by [211]

$$\begin{aligned}\frac{\partial \big(\sum_{q=1}^{Q} |\mathscr{P}(\boldsymbol{x}_q) - P(\boldsymbol{x}_q)|^2 \big)}{\partial w_v^*} =& \sum_{q=1}^{Q} \Big(\frac{\partial \big((\mathscr{P}_q - P_q)(\mathscr{P}_q - P_q)^* \big)}{\partial \mathscr{P}_q} \frac{\partial \mathscr{P}_q}{\partial w_v^*} \\ &+ \frac{\partial \big((\mathscr{P}_q - P_q)(\mathscr{P}_q - P_q)^* \big)}{\partial {\mathscr{P}_q}^*} \frac{\partial {\mathscr{P}_q}^*}{\partial w_v^*} \Big),\end{aligned} \tag{4.17a}$$

where $\mathscr{P}_q$ and P_q represent $\mathscr{P}(\boldsymbol{x}_q)$ and $P(\boldsymbol{x}_q)$, respectively. We simplify each item separately to get

$$\frac{\partial \big((\mathscr{P}_q - P_q)(\mathscr{P}_q - P_q)^* \big)}{\partial \mathscr{P}_q} = (\mathscr{P}_q - P_q)^*, \tag{4.18a}$$

$$\frac{\partial \mathscr{P}_q}{\partial w_v^*} = 0, \tag{4.18b}$$

$$\frac{\partial \big((\mathscr{P}_q - P_q)(\mathscr{P}_q - P_q)^* \big)}{\partial {\mathscr{P}_q}^*} = (\mathscr{P}_q - P_q), \tag{4.18c}$$

$$\frac{\partial {\mathscr{P}_q}^*}{\partial w_v^*(n)} = \sum_{v'=1}^{V} \frac{\partial \mathscr{P}_q^{v' *}}{\partial w_v^*} = \frac{D_v}{D_q^v} e^{-ik(D_q^v - D_v)}. \tag{4.18d}$$

Substituting (4.18) into (4.17)

$$\frac{\partial \big(\sum_{q=1}^{Q} |\mathscr{P}(\boldsymbol{x}_q) - P(\boldsymbol{x}_q)|^2 \big)}{\partial w_v^*} = \sum_{q=1}^{Q} (\mathscr{P}_q - P_q) \frac{D_v}{D_q^v} e^{-ik(D_q^v - D_v)}. \tag{4.19}$$

For the model complexity loss, we have [211]

$$\frac{\partial(\|\boldsymbol{w}\|_1)}{\partial w_v^*} = \sum_{v'=1}^{V}\Big(\frac{\partial(|w_{v'}|)}{\partial w_v^*}\Big) = \frac{1}{2}\Big(\frac{\partial(|w_v|)}{\partial\,\mathbb{R}\mathrm{e}\{w_v^*\}} + i\frac{\partial(|w_v|)}{\partial\,\mathbb{I}\mathrm{m}\{w_v^*\}}\Big), \tag{4.20a}$$

Given the absolute value of a complex number $|w_v| = \sqrt{\mathbb{R}\mathrm{e}\{w_v^*\}^2 + \mathbb{I}\mathrm{m}\{w_v^*\}^2}$, where $\mathbb{R}\mathrm{e}\{\cdot\}$ and $\mathbb{I}\mathrm{m}\{\cdot\}$ denote the real and imaginary parts of the argument, we have

$$\frac{\partial(|w_v|)}{\partial\,\mathbb{R}\mathrm{e}\{w_v^*\}} = \frac{\mathbb{R}\mathrm{e}\{w_v^*\}}{\sqrt{\mathbb{R}\mathrm{e}\{w_v^*\}^2 + \mathbb{I}\mathrm{m}\{w_v^*\}^2}} = \cos\theta_v, \tag{4.21a}$$

$$\frac{\partial(|w_v|)}{\partial\,\mathbb{I}\mathrm{m}\{w_v^*\}} = \frac{\mathbb{I}\mathrm{m}\{w_v^*\}}{\sqrt{\mathbb{R}\mathrm{e}\{w_v^*\}^2 + \mathbb{I}\mathrm{m}\{w_v^*\}^2}} = \sin\theta_v. \tag{4.21b}$$

Substituting (4.21) into (4.20)

$$\frac{\partial(\|\boldsymbol{w}\|_1)}{\partial w_v^*} = \frac{1}{2}e^{i\theta_v}. \tag{4.22}$$

Based on (4.16), (4.19), and (4.22), we have

$$\frac{\partial\mathscr{L}}{\partial w_v^*} = \sum_{q=1}^{Q}(\mathscr{P}_q - P_q)\frac{D_v}{D_q^v}e^{-ik(D_q^v - D_v)} + \frac{1}{2}\lambda e^{i\theta_v}. \tag{4.23}$$

4.8.2 Derivation of equation (4.9)

For updating biases, we take the derivation of $\partial\mathscr{L}(n)/\partial B_v^x(n)$ as an example,

$$\frac{\partial\mathscr{L}}{\partial B_v^x} = \frac{\partial(\sum_{q=1}^{Q}|\mathscr{P}(\boldsymbol{x}_q) - P(\boldsymbol{x}_q)|^2)}{\partial B_v^x} + \lambda\frac{\partial(\|\boldsymbol{w}\|_1)}{\partial B_v^x}. \tag{4.24}$$

As

$$\frac{\partial(\|\boldsymbol{w}\|_1)}{\partial B_v^x} = 0, \tag{4.25}$$

we have

$$
\begin{aligned}
\frac{\partial \mathcal{L}}{\partial B_v^x} =& \frac{\partial\big(\sum_{q=1}^{Q}|\mathscr{P}(\boldsymbol{x}_q)-P(\boldsymbol{x}_q)|^2\big)}{\partial B_v^x} \qquad (4.26a)\\
=& \sum_{q=1}^{Q}\Big(\frac{\partial\big((\mathscr{P}_q-P_q)(\mathscr{P}_q-P_q)^*\big)}{\partial \mathscr{P}_q}\frac{\partial \mathscr{P}_q}{\partial D_q^v}\frac{\partial D_q^v}{\partial B_v^x}\\
&+\frac{\partial\big((\mathscr{P}_q-P_q)(\mathscr{P}_q-P_q)^*\big)}{\partial \mathscr{P}_q}\frac{\partial \mathscr{P}_q}{\partial D_v}\frac{\partial D_v}{\partial B_v^x}\\
&+\frac{\partial\big((\mathscr{P}_q-P_q)(\mathscr{P}_q-P_q)^*\big)}{\partial \mathscr{P}_q^*}\frac{\partial \mathscr{P}_q^*}{\partial D_q^v}\frac{\partial D_q^v}{\partial B_v^x}\\
&+\frac{\partial\big((\mathscr{P}_q-P_q)(\mathscr{P}_q-P_q)^*\big)}{\partial \mathscr{P}_q^*}\frac{\partial \mathscr{P}_q^*}{\partial D_v}\frac{\partial D_v}{\partial B_v^x}\Big) \qquad (4.26b)
\end{aligned}
$$

We calculate each item individually to get

$$
\begin{aligned}
\frac{\partial\big((\mathscr{P}_q - P_q)(\mathscr{P}_q - P_q)^*\big)}{\partial \mathscr{P}_q} =&(\mathscr{P}_q - P_q)^*, && \text{(4.27a)}\\
\frac{\partial \mathscr{P}_q}{\partial D_q^v} =&\sum_{v'=1}^{V} \frac{\partial \mathscr{P}_q^{v'}}{\partial D_q^v}\\
=&w_v \frac{D_v}{D_q^v} e^{ik(D_q^v - D_v)} \frac{(ikD_q^v - 1)}{D_q^v}, && \text{(4.27b)}\\
\frac{\partial \mathscr{P}_q^*}{\partial D_q^v} =&\sum_{v'=1}^{V} \frac{\partial \mathscr{P}_q^{v'*}}{\partial D_q^v}\\
=&w_v^* \frac{D_v}{D_q^v} e^{-ik(D_q^v - D_v)} \frac{(-ikD_q^v - 1)}{D_q^v},\\
=&(\frac{\partial \mathscr{P}_q}{\partial D_q^v})^*, && \text{(4.27c)}\\
\frac{\partial \mathscr{P}_q}{\partial D_v} =&\sum_{v'=1}^{V} \frac{\partial \mathscr{P}_q^{v'}}{\partial D_v}\\
=&-w_v e^{ik(D_q^v - D_v)} \frac{(ikD_v - 1)}{D_q^v}, && \text{(4.27d)}\\
\frac{\partial \mathscr{P}_q^*}{\partial D_v} =&\sum_{v'=1}^{V} \frac{\partial \mathscr{P}_q^{v'*}}{\partial D_v}\\
=&w_v{}^* e^{-ik(D_q^v - D_v)} \frac{(ikD_v + 1)}{D_q^v},\\
=&(\frac{\partial \mathscr{P}_q^*}{\partial D_v})^*, && \text{(4.27e)}\\
\frac{\partial D_v}{\partial B_v^x} =&\frac{B_v^x}{D_v}, && \text{(4.27f)}\\
\frac{\partial D_q^v}{\partial B_v^x} =&\frac{(B_v^x - x_q)}{D_q^v}. && \text{(4.27g)}
\end{aligned}
$$

Substituting (4.27) into (4.26), we have

$$
\begin{aligned}
\frac{\partial \mathscr{L}}{\partial B_v^x} =&\sum_{q=1}^{Q} 2\,\mathbb{R}\mathrm{e}\Bigg\{(\mathscr{P}_q - P_q)^* w_v e^{ik(D_v^q - D_v)} \frac{D_v}{D_v^q} && \text{(4.28a)}\\
&\times\Big(\frac{-(ikD_v - 1)}{{D_v}^2} B_v^x + \frac{(ikD_v^q - 1)}{D_v^{q2}}(B_v^x - x_q)\Big)\Bigg\}. && \text{(4.28b)}
\end{aligned}
$$

The derivations of (4.10) and (4.11) are similar to the derivation of (4.9).

Chapter 5

Spherical Sector Harmonics Based Drone Directional Active Noise Control

Overview: *Drones have become ubiquitous in various applications, yet their noise pollution remains a significant concern. This chapter explores the feasibility of applying ANC to drones equipped with onboard speakers to mitigate this issue. We first propose a novel method for reducing drone tonal noise within a targeted spherical sector region. Building on this, we derive a wave-domain adaptive ANC algorithm tailored for directional drone noise reduction. Given the power and payload constraints of drones, we conduct simulations under varying secondary source configurations to assess noise reduction performance. Simulation results demonstrate that the proposed method effectively suppresses noise within the designated sector region while achieving fast convergence, offering a potential solution for drone noise control.*

5.1 Introduction

Small scale UAVs, commonly known as drones, are becoming increasingly popular in both commercial and military applications, such as food and parcel delivery [1], mapping [2], search and rescue [3], and surveillance [5]. However, the noise pollution from drones is strong and can damage people's hearing and mental health, which hinders drones' wider adoption. Therefore, drone noise reduction is an essential topic worth further research. As drone noise is typically dominated by tonal noise whose energy is concentrated on the harmonics of the BPF [16, 17, 18, 19, 212], this chapter will particularly focus on drone tonal noise reduction.

There are mainly two kinds of drone noise reduction methods, passive noise reduction, and active noise reduction. Passive drone noise reduction methods do not require additional sound sources, including the optimal propeller and fuselage geometry design [26], ducted (shielded) propeller, and added sound absorptive barriers [27]. However, these methods can only slightly reduce the drone noise and are not suitable for low-frequency noise [31]. Active noise reduction methods contain two branches, phase control and ANC. Phase control manipulates the relative angular blade positions of a set of propellers to reduce the noise level for the target area [32], but it can only cancel some specific harmonics of tonal noise [34]. ANC uses secondary sources (loudspeakers) to produce an anti-noise to destructively interfere with the primary noise [35]. Compared to other methods, ANC can cancel the noise in an adjustable region, and theoretically, the tonal noise can be efficiently canceled with enough numbers of secondary sources. Thus, it has great potential and flexibility.

Research on drone ANC is rare, with a small number of publications on it. Narine *et al.* conduct a single channel ANC system for a single propeller tonal noise [37]. However, this study ignores the causal control constraint of ANC as it conducts the experiment offline [105]. Dubravko proposes a multi-channel ANC system that places 12 loudspeakers surrounding each propeller to cancel the propeller noise, whereas this approach lacks simulation and experimental validations [27]. Muhammad *et al.* develop a propeller noise reduction system using multipole secondary sources, which can reduce the tonal noise on a particular circular region [36]. Most drone ANC research only try to implement ANC technology on drones but does not address two key points. First, there is a power limitation for drones, which means we cannot add too many secondary sources and cannot give too much energy to the secondary sources. Second, as drones fly over residential areas, the noise propagating downwards cause most disturbances. Therefore, directional noise reduction focusing the ground is sufficient, and the noise that propagates in other directions can be ignored. Furthermore, before implementing ANC systems on drones, it would be better to investigate how much energy is needed to reduce the noise in a directional region.

In our study, we develop a novel method that can reduce the drone tonal noise in a directional spherical sector region. First, the SSHs introduced in Chapter 3 are used to find the continuous secondary source distribution function for directional drone tonal noise reduction. Second, the discrete secondary source weights are found by SSH model matching. Third, the wave-domain adaptive ANC algorithm is developed and evaluated. Simulations are conducted to test the directional noise reduction performance with different secondary source setups and analyze the secondary source to primary source power ratio.

The main contributions of this chapter are two-fold:

- We show that directional noise reduction for drone tonal noise is feasible.
- The secondary source to primary source power ratio with different secondary source numbers is investigated, which can be a power consumption reference for future drone ANC research and implementation.

The rest of this chapter is structured as follows. In Section 5.2, we formulate and investigate the directional noise reduction problem. We developed the directional noise reduction method with continuous and discrete secondary sources in Section 5.2.1. The effectiveness of directional noise reduction and the secondary source to primary source power ratio is investigated by simulations in Section 5.2.2. We propose a direction drone ANC system and develop the wave-domain algorithm in Section 5.3, and its performance is evaluated in Section 5.3.2. Section 5.4 concludes the chapter.

5.2 Directional Noise Reduction over Spherical Sector Regions

Consider a flying drone as shown in Fig. 5.1. It is the primary sound source, represented by $\mathbb{P}$, whose noise propagates to the far-field. As the noise propagating to the ground disturbs the residents most, we aim to reduce the noise over a directional spherical sector target region $\mathbb{T}$ $(\theta \in [\theta_2, \pi], \phi \in [0, 2\pi), r = R_T)$ below $\mathbb{P}$. The secondary sources are located in another spherical sector region $\mathbb{S}$ $(\theta \in [\theta_1, \pi], \phi \in [0, 2\pi), r = R_L)$ between $\mathbb{P}$ and $\mathbb{T}$.

The noise at an observer point $\boldsymbol{x} = (R_T, \theta, \phi)$ on the target region $\mathbb{T}$ contains the

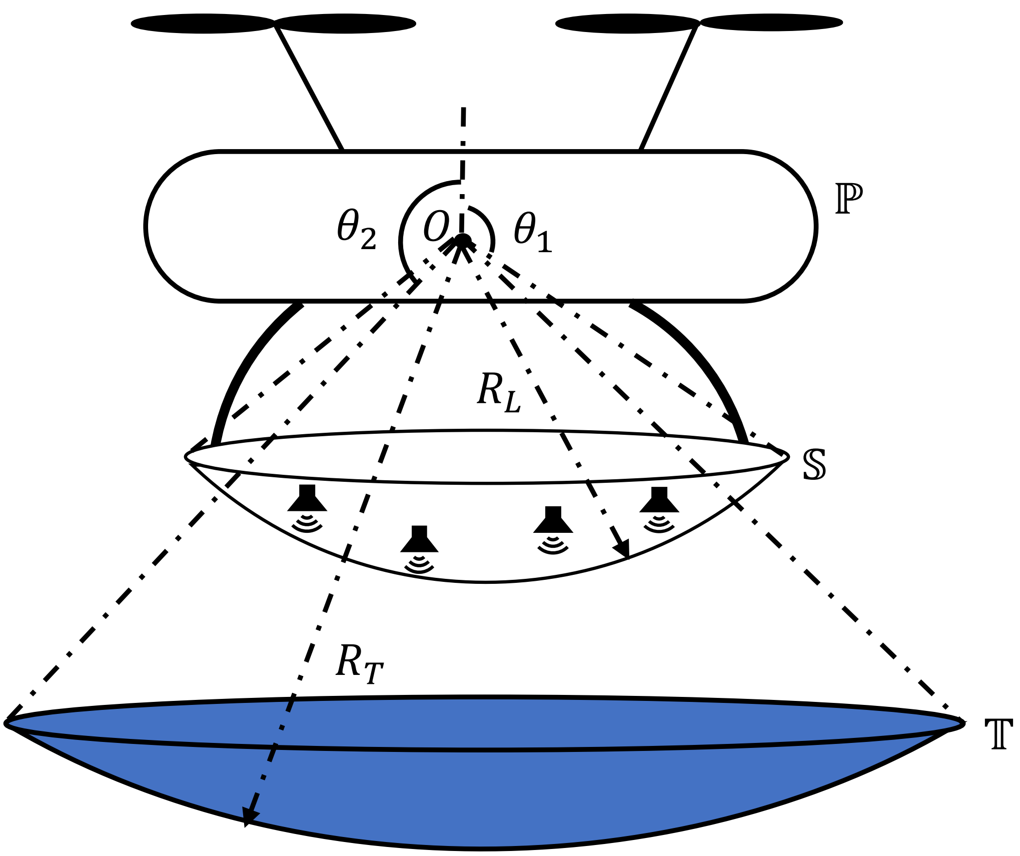

Figure 5.1: System setup: geometric illustration of the primary source $\mathbb{P}$ (drone) , the secondary source region $\mathbb{S}$, and the target directional noise reduction region $\mathbb{T}$.

noise from the primary source and secondary sources, expressed as follow

$$P_{\mathrm{T}}(\boldsymbol{x},k)=\sum_{n=0}^{\infty}\sum_{m=-n}^{n}(A_n^m(k,R_T)+B_n^m(k,R_T))T_n^m(\hat{\boldsymbol{x}}), \tag{5.1}$$

where $k=2\pi f/c$ is the wave number with f the frequency and c the speed of sound propagation, $T_n^m(\hat{\boldsymbol{x}})$ is the SSH basis function defined over the spherical sector region, $A_n^m(\cdot)$ is the SSH coefficient for the noise from the primary source, $B_n^m(\cdot)$ is the SSH coefficient for the noise from secondary sources. To reduce the noise over $\mathbb{T}$, we can adjust secondary sources weights to change $B_n^m(k,R_T)$ to cancel $A_n^m(k,R_T)$.

5.2.1 Directional noise reduction with continuous and discrete secondary sources

In this section, we first develop a method to find the secondary source distribution function for continuous secondary sources, which can provide an ideal noise reduction performance. Then, we find secondary source weights for discrete secondary sources, which reflect the real-world implementation.

Continuous secondary sources

For the continuous secondary sources distributed over the sector region $\mathbb{S}$, the generated sound field for an observer point $\boldsymbol{x} = (R_T, \theta, \phi)$ on $\mathbb{T}$ can be expressed by [208]

$$P_{\mathbb{S}}(\boldsymbol{x}, k) = \int_{\mathbb{S}} \rho(\boldsymbol{y}, k) G(\boldsymbol{x}|\boldsymbol{y}) d\boldsymbol{y}, \boldsymbol{y} \in \mathbb{S}, \tag{5.2}$$

where $\rho(\boldsymbol{y}, k)$ and $G(\boldsymbol{x}|\boldsymbol{y})$ are the continuous source distribution function and the Green function, respectively. Any continuous function defined over a spherical sector region can be expanded in terms of SSHs. Accordingly, $\rho(\boldsymbol{y}, k)$ can be expressed as:

$$\rho(\boldsymbol{y}, k) = \sum_{n=0}^{N_s} \sum_{m=-n}^{n} \Lambda_n^m(k) T_n^m(\hat{\boldsymbol{y}}), \tag{5.3}$$

and $G(\boldsymbol{x}|\boldsymbol{y})$ can be expanded by SHs as [112, 109]

$$G(\boldsymbol{x}|\boldsymbol{y}) = \sum_{n=0}^{N_h} \sum_{m=-n}^{n} ikh_n^{(1)}(kR_T) j_n(kR_L) Y_n^m(\hat{\boldsymbol{y}})^* Y_n^m(\hat{\boldsymbol{x}}), \tag{5.4}$$

where $j_n(\cdot)$ and $h_n^{(1)}(\cdot)$ are the first kind spherical Bessel function and first kind spherical Hankel function of the n-th order, respectively, $Y_n^m(\cdot)$ is the spherical harmonic of n-th order and m-th degree, $\Lambda_n^m(\cdot)$ is the secondary source distribution coefficient, $N_h \geq \lceil kr \rceil$ ($\lceil \cdot \rceil$ is the ceiling operation) and $N_s \geq \lceil kr \rceil$ are truncated orders of SH decomposition and SSH decomposition, respectively.

Then, (5.2) can be rewrite into

$$P_{\mathbb{S}}(\boldsymbol{x}, k) = \int_{\mathbb{S}} \Big(\sum_{n=0}^{N_h} \sum_{m=-n}^{n} \sum_{n'=0}^{N_s} \sum_{m'=-n'}^{n'} \mathcal{G}_n^m Y_n^m(\hat{\boldsymbol{y}})^* Y_n^m(\hat{\boldsymbol{x}}) \Lambda_{n'}^{m'}(k) T_{n'}^{m'}(\hat{\boldsymbol{y}}) \Big) d\boldsymbol{y} \tag{5.5a}$$

$$= \sum_{n=0}^{N_h} \sum_{m=-n}^{n} \Big(\mathcal{G}_n^m \sum_{n'=0}^{N_s} \sum_{m'=-n'}^{n'} \Lambda_{n'}^{m'}(k) \Big(\int_{\mathbb{S}} T_{n'}^{m'}(\hat{\boldsymbol{y}}) Y_n^m(\hat{\boldsymbol{y}})^* d\boldsymbol{y} \Big) \Big) Y_n^m(\hat{\boldsymbol{x}}), \tag{5.5b}$$

where $\mathcal{G}_n^m = ikh_n^{(1)}(kR_T)j_n(kR_L)$. According to (5.5), $P_{\mathbb{S}}(\boldsymbol{x}, k)$ can be decomposed by the SHs, and the corresponding SH coefficients can be represented by

$$\boldsymbol{\alpha}_s = \boldsymbol{I}_g \boldsymbol{M}_s \boldsymbol{\Lambda}, \tag{5.6}$$

where $\boldsymbol{\alpha}_s = [\alpha_{s0}^{\,0}, \alpha_{s1}^{\,-1}, ..., \alpha_{sN_h}^{\,N_h}]^T$ is the $(N_h+1)^2 \times 1$ SH coefficient vector, $\boldsymbol{I}_g$ is the $(N_h+1)^2 \times (N_h+1)^2$ diagonal matrix, represented by

$$\boldsymbol{I}_g = \begin{bmatrix} ikh_0^{(1)}(kR_T)j_0(kR_L) & \cdots & 0 \\ \vdots & \ddots & \vdots \\ 0 & \cdots & ikh_{N_h}^{(1)}(kR_T)j_{N_h}(kR_L) \end{bmatrix} \tag{5.7}$$

$\boldsymbol{M}_s$ is the $(N_h+1)^2 \times (N_s+1)^2$ mapping matrix that can map SSH to spherical coefficients, expressed by

$$\boldsymbol{M}_s = \begin{bmatrix} \int_{\mathbb{S}} Y_0^0(\hat{\boldsymbol{y}})^* T_0^0(\hat{\boldsymbol{y}}) d\boldsymbol{y} & \cdots & \int_{\mathbb{S}} Y_0^0(\hat{\boldsymbol{y}})^* T_{N_s}^{N_s}(\hat{\boldsymbol{y}}) d\boldsymbol{y} \\ \vdots & \ddots & \vdots \\ \int_{\mathbb{S}} Y_{N_h}^{N_h}(\hat{\boldsymbol{y}})^* T_0^0(\hat{\boldsymbol{y}}) d\boldsymbol{y} & \cdots & \int_{\mathbb{S}} Y_{N_h}^{N_h}(\hat{\boldsymbol{y}})^* T_{N_s}^{N_s}(\hat{\boldsymbol{y}}) d\boldsymbol{y} \end{bmatrix} \tag{5.8}$$

$\boldsymbol{\Lambda} = [\Lambda_0^0, \Lambda_1^{-1}, ..., \Lambda_{N_s}^{N_s}]^T$ is $(N_s+1)^2 \times 1$ the secondary source distribution coefficient vector.

Based on the mapping relationship between SHs and SSHs in (3.29) and (3.28), we have

$$\begin{aligned} \boldsymbol{B} =& \boldsymbol{M}_h \boldsymbol{\alpha}_s \\ =& \boldsymbol{M}_h \boldsymbol{I}_g \boldsymbol{M}_s \boldsymbol{\Lambda}, \end{aligned} \tag{5.9}$$

where $\boldsymbol{B} = [B_0^0, B_1^{-1}, ..., B_{N_s}^{N_s}]^T$ is $(N_s+1)^2 \times 1$ the secondary sound field coefficient vector, $\boldsymbol{M}_h$ is the $(N_s+1)^2 \times (N_h+1)^2$ mapping matrix that can map spherical coefficients to SSH, expanded as

$$\boldsymbol{M}_h = \begin{bmatrix} \int_{\mathbb{T}} Y_0^0(\hat{\boldsymbol{x}}) T_0^0(\hat{\boldsymbol{x}})^* d\boldsymbol{x} & \cdots & \int_{\mathbb{T}} Y_{N_h}^{N_h}(\hat{\boldsymbol{x}}) T_0^0(\hat{\boldsymbol{x}})^* d\boldsymbol{x} \\ \vdots & \ddots & \vdots \\ \int_{\mathbb{T}} Y_0^0(\hat{\boldsymbol{x}}) T_{N_s}^{N_s}(\hat{\boldsymbol{x}})^* d\boldsymbol{x} & \cdots & \int_{\mathbb{T}} Y_{N_h}^{N_h}(\hat{\boldsymbol{x}}) T_{N_s}^{N_s}(\hat{\boldsymbol{x}})^* d\boldsymbol{x} \end{bmatrix} \tag{5.10}$$

Based on modeling matching and (5.1), we have

$$A_n^m(k, R_T) + B_n^m(k, R_T) = 0, \tag{5.11}$$

to minimize the sound power over $\mathbb{T}$. Then, from (5.11) and (5.9) we can derive $\boldsymbol{\Lambda}$ by

$$\boldsymbol{\Lambda} = -(\boldsymbol{M}_h \boldsymbol{I}_g \boldsymbol{M}_s)^{\dagger} \boldsymbol{A}, \tag{5.12}$$

where $(\cdot)^{\dagger}$ denotes the pseudo inverse operation, $\boldsymbol{A} = [A_0^0, A_1^{-1}, ..., A_{N_s}^{N_s}]^T$ is $(N_s + 1)^2 \times 1$ is the SSH coefficient vector for the sound field on $\mathbb{T}$ generated by the primary sound source.

Discrete secondary sources

For the discrete secondary sources, assume we have L secondary sources distributed over $\mathbb{S}$. Using point sources as the secondary source, the generated sound field for an observer point $\boldsymbol{x} = (R_T, \theta, \phi)$ on $\mathbb{T}$ can be expressed by

$$P_{\mathrm{S}}(\boldsymbol{x}, k) = \sum_{l=1}^{L} w_l G(\boldsymbol{x}|\boldsymbol{y}_l), \tag{5.13}$$

where w_l is the weight of the l-th secondary source.

Based on (5.4), we have

$$P_{\mathrm{S}}(\boldsymbol{x}, k) = \sum_{n=0}^{N_h} \sum_{m=-n}^{n} \big(\mathcal{G}_n^m \sum_{l=1}^{L} w_l Y_n^m(\hat{\boldsymbol{y}}_l)^*\big) Y_n^m(\hat{\boldsymbol{x}}), \tag{5.14}$$

with the SH coefficient $\boldsymbol{\alpha}_s$ expressed by

$$\boldsymbol{\alpha}_s = \boldsymbol{I}_g \boldsymbol{L}_q \boldsymbol{w}, \tag{5.15}$$

where $\boldsymbol{w} = [w_1, w_2, ..., w_L]^T$ is the $L \times 1$ secondary source weights vector, and $\boldsymbol{L}_q$ denotes the $(N_h + 1)^2 \times L$ matrix that contains the spherical harmonics of secondary sources, expressed as

$$\boldsymbol{L}_q = \begin{bmatrix} Y_0^0(\hat{\boldsymbol{y}}_1) & \cdots & Y_0^0(\hat{\boldsymbol{y}}_L) \\ \vdots & \ddots & \vdots \\ Y_{N_h}^{N_h}(\hat{\boldsymbol{y}}_1) & \cdots & Y_{N_h}^{N_h}(\hat{\boldsymbol{y}}_L) \end{bmatrix}. \tag{5.16}$$

Based on the mapping relationship, we can find the SSH coefficient by

$$\boldsymbol{B} = \boldsymbol{M}_h \boldsymbol{I}_g \boldsymbol{L}_q \boldsymbol{w}. \tag{5.17}$$

Then, to reduce the noise on $\mathbb{T}$, based on (5.17) and (5.1), the secondary source weights can be found by

$$\boldsymbol{w} = -\boldsymbol{T}^{\dagger}\boldsymbol{A}, \tag{5.18}$$

where $\boldsymbol{T} = \boldsymbol{M}_h\boldsymbol{I}_g\boldsymbol{L}_q$ is a $L \times (N_h + 1)^2$ transfer matrix.

5.2.2 Simulation Results

Simulation setup

In this section, we examine the directional tonal noise reduction performance with both continuous and discrete secondary sources. To simulate the complicated sound field generated by a drone, we set 50 random distributed point sources over a 0.25 m radius sphere, as the primary source. The target noise reduction field $\mathbb{T}$ and the secondary source region $\mathbb{S}$ are defined as a sector region with $\theta \in [3\pi/4, \pi]$, $\phi \in [0, 2\pi)$, $R_T = 0.5$ m and $\theta \in [2\pi/3, \pi]$, $\phi \in [0, 2\pi)$, $R_L = 0.35$ m respectively. Assume the rotational speed of the drone's two-blade propellers is 5400 revolutions per minute (90 Hz). Then, the fundamental BPF is 180 Hz, and the tonal frequencies are $180, 360, 540, ..., 1260$ Hz. The speed of sound propagation is $c = 343$ m/s.

To evaluate the noise reduction performance, $U = 4200$ points are nearly uniform placed over $\mathbb{T}$, and we define the noise reduction level $\eta(k)$ as

$$\eta(k) = 10\log_{10}\Big(\frac{\sum_{u=1}^{U}|P_{\mathrm{T}}(\boldsymbol{x}_u, k)|^2}{\sum_{u=1}^{U}|P_{\mathrm{P}}(\boldsymbol{x}_u, k)|^2}\Big), \tag{5.19}$$

where $P_{\mathrm{P}}(\cdot)$ is the sound field over $\mathbb{T}$ generated by the primary source.

To compare the total sound power output from the discrete secondary sources and the primary sound power over the target region $\mathbb{T}$, we define the secondary source to primary source power ratio $\xi(k)$ as

$$\xi(k) = \frac{\sum_{l=1}^{L} E_{\mathrm{unit}}|w_l(k)|^2}{\int_{\mathbb{T}}|P_P(\boldsymbol{x}, k)|^2 d\boldsymbol{x}}, \ \boldsymbol{x} \in \mathbb{T}, \tag{5.20}$$

where E_{unit} is the total power output generated by a unit-strength monopole source. In the real application, $\xi(k)$ can be used to estimate the power consumption of secondary sources.

Noise reduction results

For continuous secondary sources, at the fundamental frequency, the noise over $\mathbb{T}$ before and after control is shown in Fig. 5.2. We find that after control, most of the noise over $\mathbb{T}$ is reduced. The noise reduction level at different frequencies is plotted in Fig. 5.3 which indicates that with continuous secondary sources, most of the tonal noise over the directional target area can be reduced.

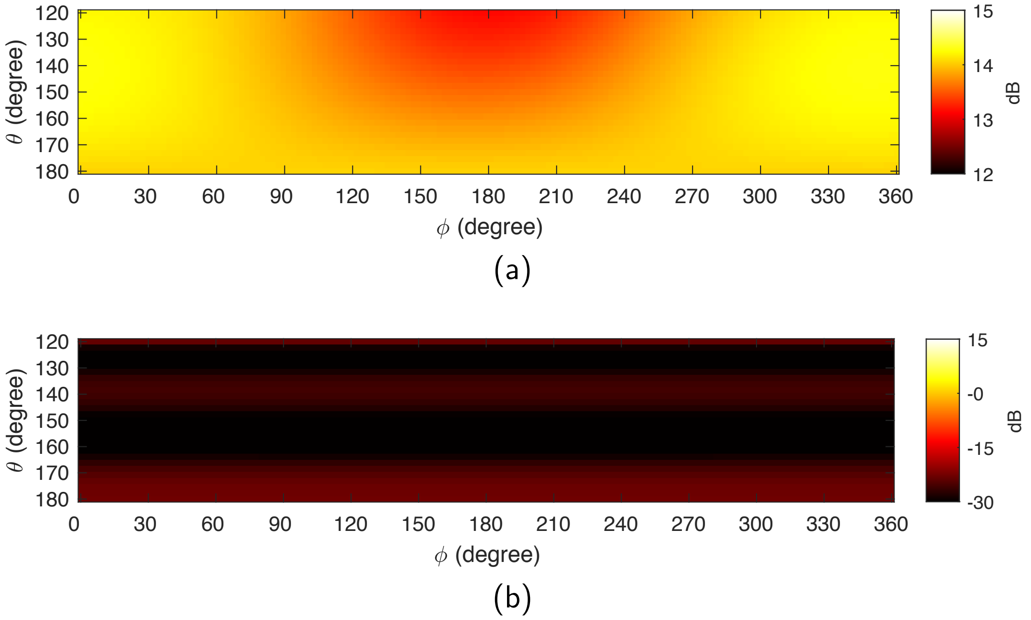

Figure 5.2: Noise reduction results with continuous secondary sources at the fundamental BPF frequency (180 Hz): (a) primary noise field on $\mathbb{T}$ and (b) residual noise on $\mathbb{T}$ after control.

In terms of discrete secondary sources, we nearly uniformly place L point sources over the secondary source region. Theoretically, with $L \geq (N_s + 1)^2$, we can achieve better noise reduction performance, but in reality, drones can not carry too many secondary sources. In our simulation, we set $L = 5, 9, 16, 25$, and 36 to test the reduction performance. Besides, to fully reduce the noise over $\mathbb{T}$, the required secondary source weight is very large, which is infeasible. Ideally, to cancel the directional noise from a monopole source, the most efficient way is to place an overlapped monopole secondary source with the opposite weight. Then, the ideal smallest power ratio is the area ratio of the whole sphere to sector region $\mathbb{T}$. Therefore, we define a power ratio threshold ξ_{th} as 5 times the ideal smallest power ratio and only save results under the threshold. The noise reduction level $\eta(k)$ and the secondary source to primary source power ratio $\xi(k)$ for different tonal noise frequencies are shown in Figs. 5.3 and 5.4 respectively, where we find that: (i) compared to a continuous secondary source, discrete secondary sources cannot achieve the ideal noise reduction, especially for high frequencies; (ii) the noise reduction performance for low-frequency components is much better than the performance for high-frequency components; (iii) with the secondary source power restriction, increasing the secondary source number has little effect on low-frequency components and slight improvement for

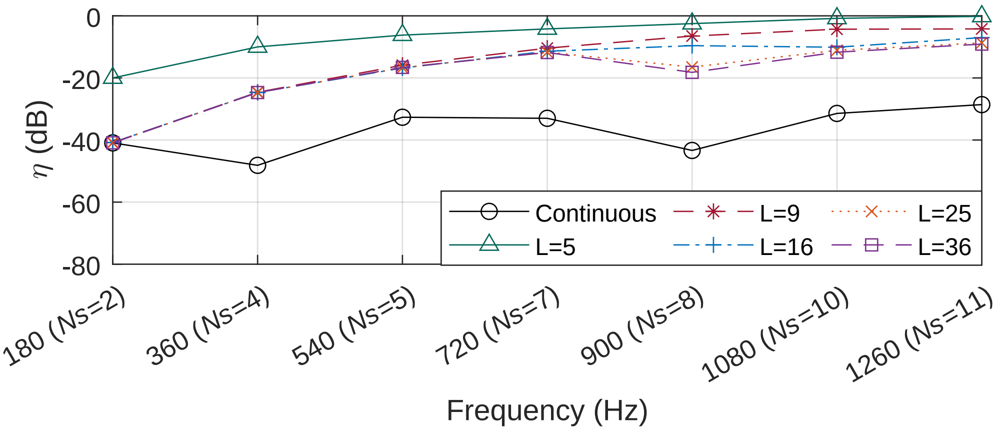

Figure 5.3: Noise reduction level with continuous secondary sources and discrete secondary sources for different BPF frequencies.

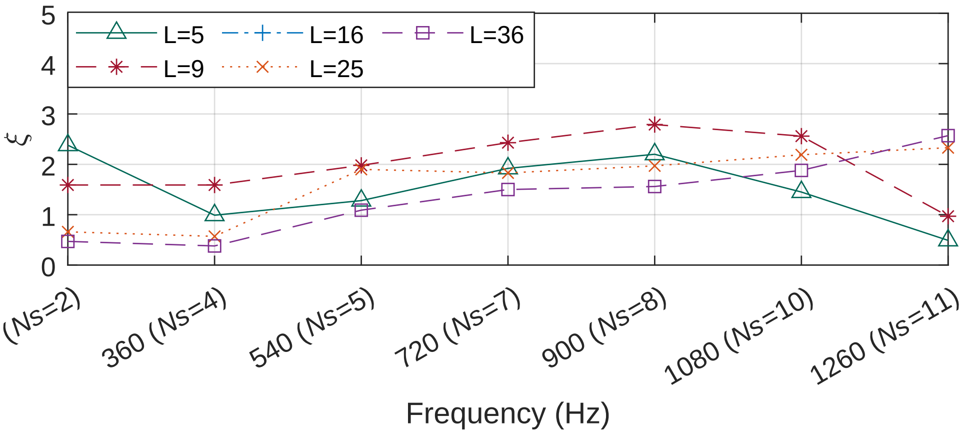

Figure 5.4: Secondary source to primary source power ratio with discrete secondary sources for different BPF frequencies.

high-frequency components; (iv) by increasing the number of secondary sources, we can achieve the same noise reduction performance with less secondary source power.

5.3 Drone Directional ANC System

In this section, we propose a directional drone ANC system and derive the adaptive ANC algorithm for it. The drone ANC system is shown in Fig. 5.5. Compared to the setup in Fig. 5.1, we added an error microphone array on board with the spherical sector shape $\mathbb{M}$ $(\theta \in [\theta_1, \pi], \phi \in [0, 2\pi), r = R_M)$, right below the secondary sources, which can be used to measure and feedback noise reduction performance in real time. Then, with the on-board microphone measurement, we aim to derive the adaptive ANC algorithm to minimize the noise level over the target region

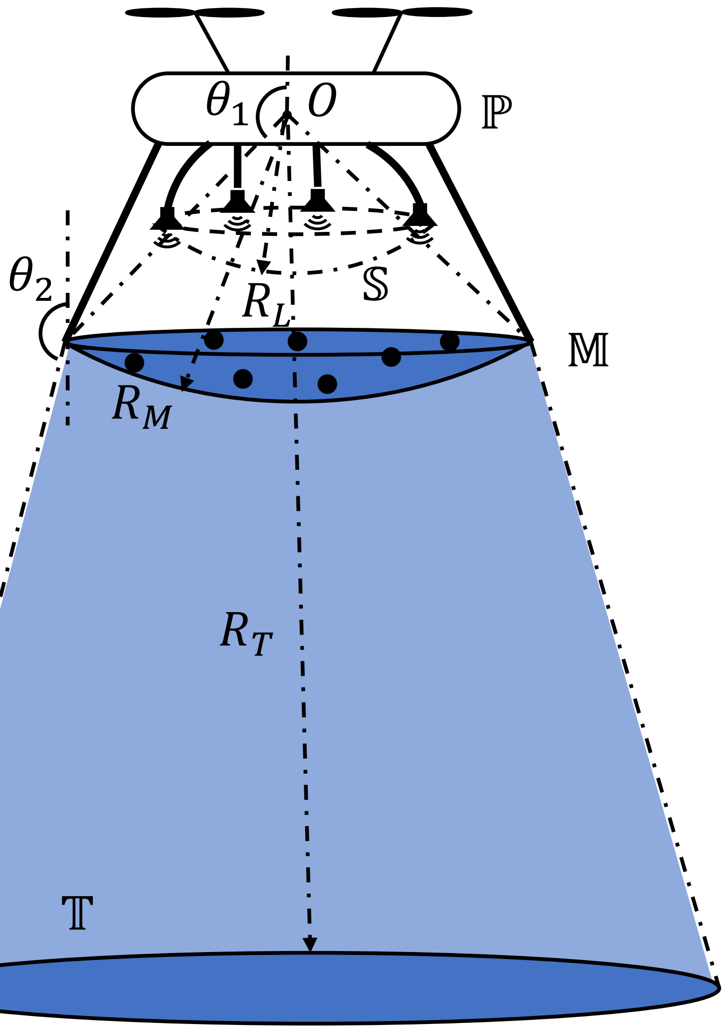

Figure 5.5: Drone ANC system setup: geometric illustration of the primary source $\mathbb{P}$ (drone), the secondary sources $\mathbb{S}$, error microphones $\mathbb{M}$ and the target directional noise reduction region $\mathbb{T}$.

$\mathbb{T}$ $(\theta \in [\theta_2, \pi], \phi \in [0, 2\pi), r = R_T)$ on the ground.

5.3.1 Wave-domain adaptive ANC algorithm

In this section, we first derive an expression that relates the residual signals over the target region $\mathbb{T}$ to the residual noise over the measurement region $\mathbb{M}$. We then use this relationship to formulate an adaptive ANC algorithm that iteratively updates the secondary source weight vector $\boldsymbol{w}$, so as to minimize the residual acoustic energy within $\mathbb{T}$.

Similar to (5.1), the residual noise over $\mathbb{M}$ can be expressed as

$$P_{\mathrm{M}}(\boldsymbol{x},k)=\sum_{n=0}^{N_s}\sum_{m=-n}^{n}(A_n^m(k,R_M)+B_n^m(k,R_M))T_n^m(\hat{\boldsymbol{x}}),\ \boldsymbol{x}\in\mathbb{M}. \tag{5.21}$$

Based on SSHs decomposition, we can also represent $P_{\mathrm{M}}(\boldsymbol{x},k)$ by

$$P_{\mathrm{M}}(\boldsymbol{x},k)=\sum_{n=0}^{N_s}\sum_{m=-n}^{n}\Gamma_n^m(k,R_M)T_n^m(\hat{\boldsymbol{x}}),\ \boldsymbol{x}\in\mathbb{M}, \tag{5.22}$$

where $\Gamma_n^m(k,R_M)$ is the SSH coefficient for the residual noise over $\mathbb{M}$.

From (5.21) and (5.22), the residual SSH coefficients over $\mathbb{M}$ in each iteration (the n^{th} time block) can be expressed as

$$\boldsymbol{\Gamma}(n,k,R_T)=\boldsymbol{A}(n,k,R_M)+\boldsymbol{B}(n,k,R_M), \tag{5.23}$$

where $\boldsymbol{\Gamma}(n,k,R_M)=[\Gamma_0^0(n,k,R_M),\Gamma_1^{-1}(n,k,R_M),...,\Gamma_{N_s}^{N_s}(n,k,R_M)]^T$ is the $(N_s+1)^2\times 1$ SSH coefficients vector for $\mathbb{M}$.

Then, the mapping-based extrapolation method developed in Chapter 3, we have

$$\boldsymbol{\Gamma}(n,k,R_T)=\boldsymbol{M}_e\big(\boldsymbol{A}(n,k,R_M)+\boldsymbol{B}(n,k,R_M)\big), \tag{5.24}$$

where $\boldsymbol{\Gamma}(n,k,R_T)=[\Gamma_0^0(n,k,R_T),\Gamma_1^{-1}(n,k,R_T),...,\Gamma_{N_s}^{N_s}(n,k,R_T)]^T$ is the $(N_s+1)^2\times 1$ SSH coefficients vector for $\mathbb{T}$, and $\boldsymbol{M}_e$ denotes the sound field extrapolation matrix. Based on (3.29) and (3.30), $\boldsymbol{M}_e$ can be expressed by

$$\boldsymbol{M}_e=\boldsymbol{M}_h\boldsymbol{D}_{R_T}\boldsymbol{M}_h^{\dagger}. \tag{5.25}$$

For notational simplicity, we omit the dependency k, R_M, and R_T in each vector, thus have

$$\boldsymbol{\Gamma}(n)=\boldsymbol{M}_e(\boldsymbol{A}(n)+\boldsymbol{B}(n)). \tag{5.26}$$

We derive the wave-domain adaptive algorithms by minimizing squared residual energy over $\mathbb{T}$. Hence, the cost function becomes

$$\mathcal{L}(n)=\int_{\mathbb{T}}P_{\mathrm{T}}(\boldsymbol{x},k)P_{\mathrm{T}}(\boldsymbol{x},k)^*d\boldsymbol{x}. \tag{5.27}$$

Based on (5.22) and (3.27), we can simplify (5.27) as

$$\begin{aligned}\mathscr{L}(n) =& \int_{\mathbb{T}} (\sum_{n=0}^{N_s} \sum_{m=-n}^{n} \Gamma_n^m(n) T_n^m(\hat{\boldsymbol{x}}) \sum_{n'=0}^{N_s} \sum_{m'=-n'}^{n'} \Gamma_{n'}^{m'}(n)^* T_{n'}^{m'}(\hat{\boldsymbol{x}})^*) d\boldsymbol{x} \\ =& \sum_{n=0}^{N_s} \sum_{m=-n}^{n} \sum_{n'=0}^{N_s} \sum_{m'=-n'}^{n'} \Gamma_{n'}^{m'}(n) \Gamma_n^m(n)^* (\int_{\mathbb{T}} T_n^m(\hat{\boldsymbol{x}}) T_{n'}^{m'}(\hat{\boldsymbol{x}})^* d\boldsymbol{x}) \\ =& \sum_{n=0}^{N_s} \sum_{m=-n}^{n} |\Gamma_n^m(n)|^2 \\ =& \, \boldsymbol{\Gamma}(n)^H \boldsymbol{\Gamma}(n) \end{aligned} \tag{5.28}$$

Using the steepest descent algorithm, the update equation can be expressed by

$$\boldsymbol{d}(n+1) = \boldsymbol{d}(n) + \frac{\mu}{2} \nabla \mathscr{L}(n), \tag{5.29}$$

where $\boldsymbol{d}$ is the update variable, and μ denotes the step size.

We derive the wave-domain update function for two cases, (1) loudspeaker weights are updated directly, and (2) secondary sound field coefficients are updated.

Update the loudspeaker weights

We first aim to update the speaker weights $\boldsymbol{w}$ directly. Then, the update variable $\boldsymbol{d}$ in (5.29) becomes $\boldsymbol{w}$.

Based on complex LMS algorithm [213], we take a derivative of $\mathscr{L}(n)$ with respect to $\boldsymbol{w}^*$ and have

$$\nabla \mathscr{L} = 2 \frac{\partial \mathscr{L}}{\partial \boldsymbol{w}^*} = 2 \frac{\boldsymbol{\Gamma}^H \boldsymbol{\Gamma}}{\partial \boldsymbol{w}^*}, \tag{5.30}$$

where we omit the iteration index n for notational simplicity.

Substituting (5.18) and (5.26) into (5.30), we have

$$\begin{aligned}\nabla \mathscr{L} = 2 \Big(& \frac{\partial (\boldsymbol{A}^H \boldsymbol{M}_e^H \boldsymbol{M}_e \boldsymbol{A})}{\partial \boldsymbol{w}^*} - \frac{\partial (\boldsymbol{w}^H \boldsymbol{T}^H \boldsymbol{M}_e^H \boldsymbol{M}_e \boldsymbol{A})}{\partial \boldsymbol{w}^*} \\ & - \frac{\partial (\boldsymbol{A}^H \boldsymbol{M}_e^H \boldsymbol{M}_e \boldsymbol{T} \boldsymbol{w})}{\partial \boldsymbol{w}^*} + \frac{\partial (\boldsymbol{w}^H \boldsymbol{T}^H \boldsymbol{M}_e^H \boldsymbol{M}_e \boldsymbol{T} \boldsymbol{w})}{\partial \boldsymbol{w}^*} \Big). \end{aligned} \tag{5.31}$$

By calculating each item separately, we obtain

$$\begin{aligned}\frac{\partial(\boldsymbol{A}^H\boldsymbol{M}_{\boldsymbol{e}}^H\boldsymbol{M}_e\boldsymbol{A})}{\partial\boldsymbol{w}^*}&=0,\\ \frac{\partial(\boldsymbol{w}^H\boldsymbol{T}^H\boldsymbol{M}_{\boldsymbol{e}}^H\boldsymbol{M}_e\boldsymbol{A})}{\partial\boldsymbol{w}^*}&=\boldsymbol{T}^H\boldsymbol{M}_{\boldsymbol{e}}^H\boldsymbol{M}_e\boldsymbol{A},\\ \frac{\partial(\boldsymbol{A}^H\boldsymbol{M}_{\boldsymbol{e}}^H\boldsymbol{M}_e\boldsymbol{T}\boldsymbol{w})}{\partial\boldsymbol{w}^*}&=0,\\ \frac{\partial(\boldsymbol{w}^H\boldsymbol{T}^H\boldsymbol{M}_{\boldsymbol{e}}^H\boldsymbol{M}_e\boldsymbol{T}\boldsymbol{w})}{\partial\boldsymbol{w}^*})&=\boldsymbol{T}^H\boldsymbol{M}_{\boldsymbol{e}}^H\boldsymbol{M}_e\boldsymbol{T}\boldsymbol{w}.\end{aligned} \tag{5.32}$$

Based on (5.18), (5.31), and (5.32), we have

$$\nabla\mathscr{L}(n)=2\boldsymbol{T}^H\boldsymbol{M}_{\boldsymbol{e}}^H\boldsymbol{\Gamma}(n). \tag{5.33}$$

Note that $\boldsymbol{T}$ and $\boldsymbol{M}_{\boldsymbol{e}}$ are only related to the system setup, not time varying. Substituting (5.33) into (5.29), the adaptive equation can be written as

$$\boldsymbol{w}(n+1)=\boldsymbol{w}(n)+\mu\boldsymbol{T}^H\boldsymbol{M}_{\boldsymbol{e}}^H\boldsymbol{\Gamma}(n). \tag{5.34}$$

We further normalize (5.34) to obtain the normalized version of adaptive equation

$$\boldsymbol{w}(n+1)=\boldsymbol{w}(n)+\mu\frac{\boldsymbol{T}^H\boldsymbol{M}_{\boldsymbol{e}}^H}{\|\boldsymbol{T}^H\boldsymbol{M}_{\boldsymbol{e}}^H\|_2^2}\boldsymbol{\Gamma}(n). \tag{5.35}$$

Update the secondary sound field coefficients

We aim to first update the secondary source coefficients $\boldsymbol{B}$ and then update $\boldsymbol{w}$ based on the updated $\boldsymbol{B}$. Therefore, the update variable $\boldsymbol{d}$ in (5.29) changes to $\boldsymbol{B}$.

We take a derivative of $\mathscr{L}(n)$ with respect to $\boldsymbol{B}^*$ and have

$$\nabla\mathscr{L}=2\frac{\partial\mathscr{L}}{\partial\boldsymbol{B}^*}=2\frac{\boldsymbol{\Gamma}^H\boldsymbol{\Gamma}}{\partial\boldsymbol{B}^*}. \tag{5.36}$$

Substituting (5.26) into (5.36), we have

$$\begin{aligned}\nabla\mathscr{L}=2(&\frac{\partial(\boldsymbol{A}^H\boldsymbol{M}_{\boldsymbol{e}}^H\boldsymbol{M}_e\boldsymbol{A})}{\partial\boldsymbol{B}^*}+\frac{\partial(\boldsymbol{B}^H\boldsymbol{M}_{\boldsymbol{e}}^H\boldsymbol{M}_e\boldsymbol{A})}{\partial\boldsymbol{B}^*}\\ &+\frac{\partial(\boldsymbol{A}^H\boldsymbol{M}_{\boldsymbol{e}}^H\boldsymbol{M}_e\boldsymbol{B})}{\partial\boldsymbol{B}^*}+\frac{\partial(\boldsymbol{B}^H\boldsymbol{M}_{\boldsymbol{e}}^H\boldsymbol{M}_e\boldsymbol{B})}{\partial\boldsymbol{B}^*}).\end{aligned} \tag{5.37}$$

By calculating each item separately, we get

$$\begin{aligned}
\frac{\partial(\boldsymbol{A}^H\boldsymbol{M_e}^H\boldsymbol{M}_e\boldsymbol{A})}{\partial\boldsymbol{B}^*} &= 0,\\
\frac{\partial(\boldsymbol{B}^H\boldsymbol{M_e}^H\boldsymbol{M}_e\boldsymbol{A})}{\partial\boldsymbol{B}^*} &= \boldsymbol{M_e}^H\boldsymbol{M}_e\boldsymbol{A}\\
\frac{\partial(\boldsymbol{A}^H\boldsymbol{M_e}^H\boldsymbol{M}_e\boldsymbol{T}\boldsymbol{B})}{\partial\boldsymbol{B}^*} &= 0\\
\frac{\partial(\boldsymbol{B}^H\boldsymbol{M_e}^H\boldsymbol{M}_e\boldsymbol{B})}{\partial\boldsymbol{B}^*}) &= \boldsymbol{M_e}^H\boldsymbol{M}_e\boldsymbol{B}.
\end{aligned} \tag{5.38}$$

Based on, (5.37), and (5.38), we have

$$\nabla\mathscr{L}(n) = 2\boldsymbol{M_e}^H\boldsymbol{\Gamma}(n). \tag{5.39}$$

Substituting (5.39) into (5.29), the adaptive equation for $\boldsymbol{B}$ can be given by

$$\boldsymbol{B}(n+1) = \boldsymbol{B}(n) + \mu\boldsymbol{M_e}^H\boldsymbol{\Gamma}(n). \tag{5.40}$$

We further normalize (5.40) to get the normalized version of adaptive equation

$$\boldsymbol{B}(n+1) = \boldsymbol{B}(n) + \mu\frac{\boldsymbol{M_e}^H}{\|\boldsymbol{M_e}^H\|_2^2}\boldsymbol{\Gamma}(n). \tag{5.41}$$

Then, based on (5.18) and (5.23), the speaker weight can be obtained by

$$\boldsymbol{w}(n+1) = \boldsymbol{T}^\dagger\boldsymbol{B}(n+1). \tag{5.42}$$

5.3.2 Simulation results

Simulation setup

In this section, we evaluate the proposed adaptive directional ANC algorithm through simulations. The primary source settings remain consistent with Section 5.2.2.

The target noise reduction field, $\mathbb{T}$, and the secondary source region, $\mathbb{S}$, are both defined as sector regions. Specifically, $\mathbb{T}$ is given by $\theta \in [3\pi/4, \pi]$, $\phi \in [0, 2\pi)$, with a radius of $R_T = 5$ m. The secondary source region $\mathbb{S}$ is defined by $\theta \in [2\pi/3, \pi]$, $\phi \in [0, 2\pi)$, with a radius of $R_L = 0.35$ m.

A total of $Q = 36$ microphones are placed in the measurement region, $\mathbb{M}$, with $R_M = 0.5$ m and $\theta \in [2\pi/3, \pi]$, $\phi \in [0, 2\pi)$. White Gaussian noise with a SNR of 30 dB is added to each microphone recording.

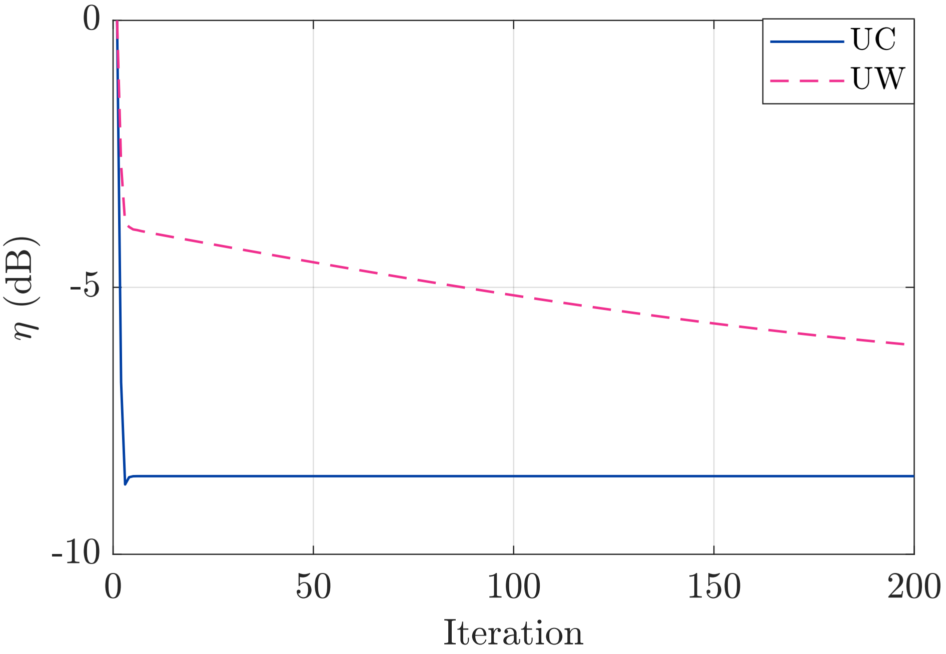

Figure 5.6: Convergence performance with: (a) update secondary sound field coefficient (UC) and (b) update loudspeaker weights (UW).

Assuming the drone's two-blade propellers rotate at 5400 revolutions per minute (90 Hz), the fundamental BPF is 180 Hz. Given the physical size and loading constraints of the drone, incorporating a large number of secondary sources is impractical. Therefore, we evaluate cases where the number of secondary sources is limited to $L = 4, 6$, and 8. The target frequency range includes up to the fifth harmonic (180, 360, 540, 720, 900 Hz). The number of evaluation points and evaluation metrics are kept consistent with Section 5.2.2.

ANC results

We first examine the convergence speed of the two proposed methods: updating the loudspeaker weights (UW) and updating the secondary sound field coefficients (UC). To analyze their performance, we fix the number of secondary sources at $L = 6$ and evaluate the third harmonic ($f = 540$ Hz). The results, shown in Fig. 5.6, indicate that the UC algorithm converges significantly faster than the UW algorithm. Specifically, the UC method achieves full convergence within 10 iterations, whereas the UW method fails to fully converge even after 200 iterations. This difference arises because updating the secondary sound field coefficients enables decomposition using the orthogonal basis functions of the sound field, facilitating a more efficient gradient descent process.

We further evaluate the noise reduction performance over the target region after

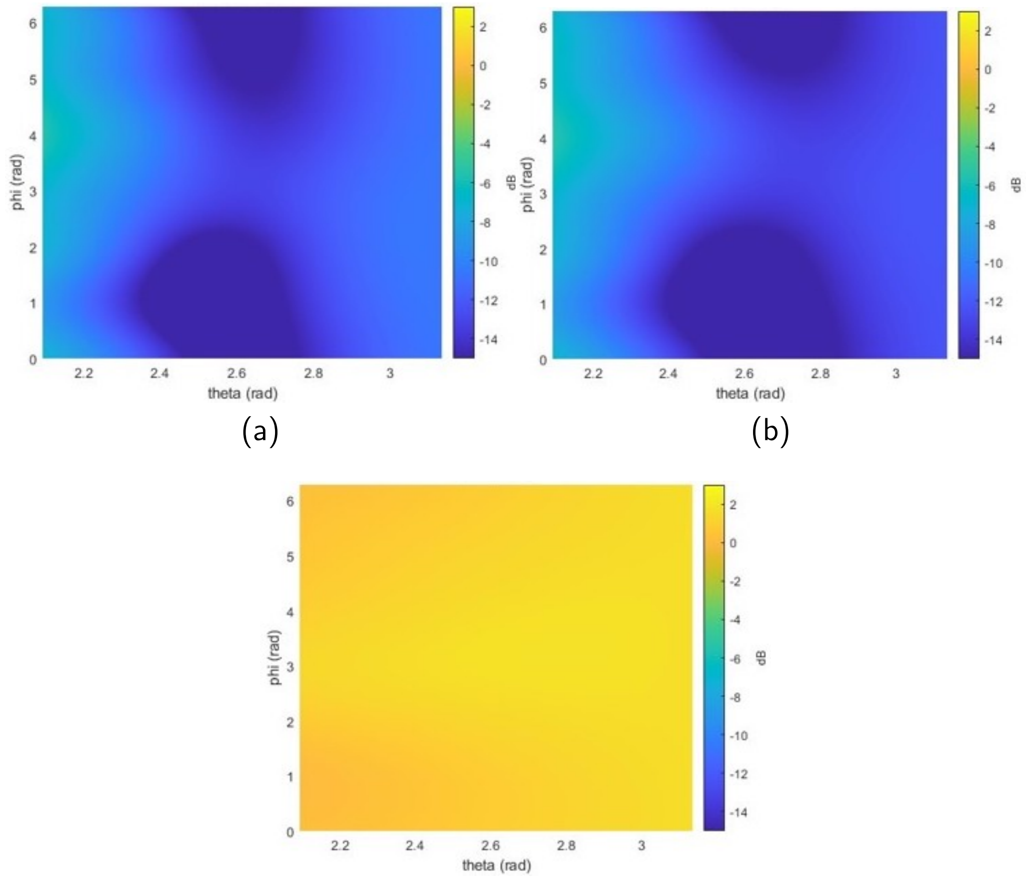

(a)

(b)

(c)

Figure 5.7: Noise Reduction performance over the target region after convergence with 6 secondary speakers: (a) update secondary sound field coefficient, (b) update loudspeaker weights, and (c) primary sound field (360 Hz).

convergence. The sound power distribution within $\mathbb{T}$ is illustrated in Fig. 5.7, where we observe the following: (i) The noise reduction performances of the two proposed methods are comparable after convergence. (ii) The noise reduction over the target region is smooth, indicating effective suppression of noise without abrupt variations.

The noise reduction results for different numbers of secondary sources and frequencies are summarized in Table 5.1. From these results, we find that: (i) Both proposed methods achieve similar levels of converged noise reduction. (ii) Increasing the number of secondary sources significantly enhances noise reduction at lower frequencies, whereas its effect is less pronounced at higher frequencies. (iii) Compared to Fig. 5.3, the noise reduction performance in Table 5.1 is slightly diminished due to extrapolation errors, which have a greater impact at higher frequencies.

Additionally, Table 5.2 presents the secondary-to-primary source power ratio for the two adaptive algorithms across different numbers of secondary sources and harmonics. The results indicate that both methods exhibit similar power ratios. Compared to Fig. 5.4, the adaptive algorithms maintain the same level of power consumption as the theoretical noise reduction, suggesting that the extrapolation process and adaptive algorithm have minimal impact on the secondary-to-primary source power ratio.

Table 5.1: Noise reduction level η (dB) of different BPF frequencies with different numbers of secondary sources.

Freq	UC				UW			
	4	6	8	10	4	6	8	10
180 Hz	-9.5	-13.2	-17.8	-18.2	-9.3	-13.3	-17.9	-18.2
360 Hz	-7.0	-9.8	-14.2	-14.8	-7.2	-9.6	-14.1	-14.9
540 Hz	-4.5	-5.7	-10.2	-10.9	-4.3	-5.8	-10.3	-11.1
720 Hz	-2.4	-3.6	-6.5	-6.7	-2.3	-3.3	-6.3	-6.6
900 Hz	-1.1	-2.7	-4.5	-4.5	-1.1	-2.8	-4.4	-4.5

Table 5.2: Secondary source to primary source power ratio ξ of different BPF frequencies with different numbers of secondary sources.

Freq	UC				UW			
	4	6	8	10	4	6	8	10
180 Hz	2.4	2.4	2.1	2.3	2.3	2.5	2.0	2.2
360 Hz	1.2	1.5	1.9	2.0	1.2	1.4	1.8	1.9
540 Hz	1.3	1.4	2.1	2.1	1.4	1.4	2.1	2.2
720 Hz	2.2	2.3	2.5	2.4	2.2	2.3	2.4	2.3
900 Hz	1.9	2.0	2.2	2.2	1.9	2.1	2.2	2.2

5.4 Summary and Contributions

In conclusion, this chapter introduced a spherical sector harmonics-based directional noise reduction method for drone noise control. Building on this approach, we further derived the update equations with respect to two variables: (a) the loudspeaker weights and (b) wave-domain secondary source coefficients. Simulations were conducted to evaluate both theoretical noise reduction and the effectiveness of the adaptive algorithms. The theoretical noise reduction results indicate that, in the absence of secondary source power constraints, most of the drone's tonal noise can be effectively cancelled given a sufficient number of secondary sources. However, when power limitations are considered, noise reduction is more effective at lower frequencies, while performance at higher frequencies is relatively limited. Additionally, increasing the number of secondary sources has little effect on low-frequency reduction but provides a slight improvement for higher frequencies. For the adaptive algorithms, the results demonstrate that updating secondary source coefficients leads to significantly faster convergence. Both proposed algorithms achieve similar final noise reduction performance. Furthermore, increasing the number of secondary sources substantially enhances noise reduction at lower frequencies but has a minimal impact at higher frequencies.

5.5 Related Publications

- H. Bi, F. Ma, T. D. Abhayapala and P. N. Samarasinghe,“Spherical Sector Harmonics Based Directional Drone Noise Reduction,” 2022 International Workshop on Acoustic Signal Enhancement (IWAENC), Bamberg, Germany, 2022, pp. 1-5, doi: 10.1109/IWAENC53105.2022.9914790.
- H. Bi, T. D. Abhayapala, F. Ma, and P. N. Samarasinghe, “Directional active noise control for drones,” J. Acoust. Soc. Am., vol. 154, no. 4_Suppl., p. A162, Oct. 2023, doi: 10.1121/10.0023134.

Chapter 6

Drone Propeller Noise Reduction Based on Phase Control

Overview: *This chapter investigates the control of far-field drone noise by manipulating the relative phase of propellers. Our methodology consists of three key steps: (i) measuring near-field propeller noise using a specially designed open spherical microphone array, (ii) developing an extrapolation method to predict far-field noise based on near-field measurements, and (iii) simulating far-field noise under varying propeller phase configurations. We further analyze the influence of drone configurations on phase-controlled noise reduction in a far-field target region, demonstrating that a noise reduction of up to -6.8 dB can be achieved at blade passage frequencies. Additionally, the analysis of residual noise highlights the potential benefits of integrating phase control with active noise control for enhanced drone noise mitigation.*

6.1 Introduction

UAVs, also known as drones, are becoming popular in both civil and military applications, such as parcel delivery [1], wild animal survey [214], search and rescue, and surveillance [5]. However, noise generated by drones is annoying, with the potential to cause long-term harm to people's hearing and mental health [11, 13]. This hinders further applications of drones, evoking the need for new research on efficient methods to control drone noise. In addition to the drone ANC method developed in Chapter 5, this chapter explores an active noise reduction approach that does not require adding extra weights, such as loudspeakers, to the drone.

Drone noise is typically dominated by the propeller tonal noise whose energy is concentrated on the harmonics of the BPF [16, 17, 18, 19]. Characteristics of propeller tonal noise were investigated by many researchers [215, 216, 217]. Zhou and Fattah found that the interaction of propellers will redistribute the energy of the noise among BPF harmonics [215]. Zhong *et al.* proposed a farfield approximation formulation for the propeller tonal noise in the frequency domain [216]. Roger and Moreau simulated the three-dimensional directivity patterns of forward-flight propeller tonal noise [217].

In terms of drone noise reduction, there are two potential methods: (1) ANC and (2) phase control. ANC uses secondary sources (loudspeakers) to produce the anti-noises to destructively interfere with the primary noises [35]. Narine *et al.* achieve 43.82 % noise reduction for a single propeller noise using one loudspeaker as the secondary source [37]. However, this is an offline implementation that violates the causal control constraint of ANC [105]. Phase control manipulates the relative angular blade positions of a set of propellers to reduce the noise level for the target area [19]. Researchers from NASA simulated and validated the performance of phase control by a dual rotor system [32]. The influence of increasing rotor numbers for phase control noise reduction has been investigated in [104]. A drawback of existing phase control studies is that they mainly rely on theoretically developed drone noise prediction equations [218, 219], which may not predict the sound field of a drone accurately.

In this chapter, rather than relying on propeller noise prediction equations, we investigate the potential of phase control based on real measurements. First, we measure the nearfield noise of a single propeller using a spherical microphone array and extrapolate the nearfield recording to the farfield sound pressure of all propellers. Second, we find the optimal relative phase through minimizing the farfield sound power level of a target area. Third, simulations are conducted to investigate the phase control noise reduction for a given target area for different drone configurations.

The main contributions of this chapter are threefold. First, as it is difficult to directly measure the farfield sound pressure of a propeller, we develop a method that can estimate the farfield sound pressure based on the nearfield measurement. Second, we show that 90° phase difference in propellers can always achieve the optimal noise reduction level for all drone configurations. Third, we find that phase control can only cancel specific orders of BPF noise, and we can decide which orders of noise to eliminate by selecting the relative phases of the propellers. This implies that for more effective noise control, phase control shall be integrated with an ANC system, such as that developed in Chapter 5.

The rest of this chapter is structured as follows. The problem formulation is in Section. 6.2. We develop the noise prediction method based on a single propeller noise measurement in Section. 6.3. The effectiveness of phase control for different drone configurations and the insights of phase control are presented in Section. 6.4. Section. 6.5 concludes the chapter.

6.2 Problem Formulation

Consider a drone in hovering condition as shown in Fig. 6.1. Its noise propagates to a farfield target region $\mathbb{T}$ (a part of the large hemisphere $\mathbb{H}$) where people present. The sound field over $\mathbb{T}$ can not be measured directly, and thus we use a number of microphones $\diamondsuit$ placed on the small hemisphere $\mathbb{H}^{'}$ to record the sound pressure of a single propeller and extrapolate the nearfield recording to the farfield $\mathbb{T}$. We denote the spherical coordinates and the Cartesian coordinates with respect to the origin O as (r, θ, ϕ) and (x, y, z), respectively.

The sound field, [1] with synchronized propeller rotational speed, at an observer point $\boldsymbol{x} = (r, \theta, \phi)$ on $\mathbb{T}$ is

$$p_{\mathrm{T}}(\boldsymbol{x}, t) = \sum_{n_p=1}^{N_p} p_{n_p}(\boldsymbol{x}, t + \frac{\psi_{n_p}}{2\pi f_0}), \tag{6.1}$$

where N_p is the number of propellers, n_p is the index of propellers, $p_{n_p}(\boldsymbol{x}, t)$ is the sound field over the target region generated by propeller n_p, ψ_{n_p} is the relative phase of propeller n_p with respect to propeller 1 when propeller 1 is parallel to the y axis[2], f_0 is the propeller rotation frequency.

---

[1] we only consider the noise emitted from drones' propellers, neglecting fuselage scattering.

[2] ψ_1 is always zero.

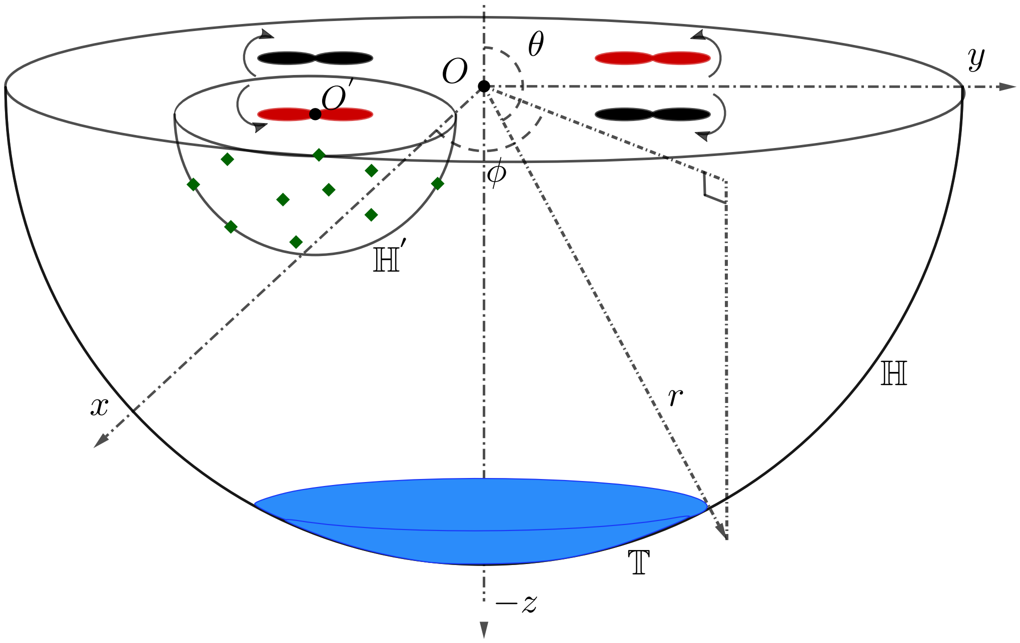

Figure 6.1: System setup: geometric illustration of the drone configuration, microphones on the small hemisphere $\mathbb{H}'$, target region $\mathbb{T}$ represented by the colored part of the hemisphere $\mathbb{H}$.

We aim to reduce the sound (noise) power level over the target region $\mathbb{T}$ by controlling the relative phases ψ_{n_p} of propellers.

6.3 Propeller Sound Field Representation by Spherical Harmonics

In this section, we first introduce an extrapolation method that projects the nearfield noise measurement of a single propeller to a farfield area. After that, according to the geometric relationship between the propellers, we estimate the nearfield sound field for other propellers and then use the extrapolation method to obtain the total farfield sound field. Finally, we find the optimal relative phases through an optimization process.

6.3.1 Sound field extrapolation method

Here, we first introduce the basic theory of signal processing based on the spherical harmonics, and then present the sound field extrapolation method.

We view a propeller as an outgoing sound source. The outgoing sound field at a point in the frequency domain and in the time domain can be represented as

[108, 159]

$$P(\omega, r, \theta, \phi) \approx \sum_{n=0}^{N_h} \sum_{m=-n}^{n} C_n^m(\omega) h_n^{(1)}(\omega r/c) Y_n^m(\theta, \phi), \tag{6.2}$$

and

$$p(t, r, \theta, \phi) \approx \sum_{n=0}^{N_h} \sum_{m=-n}^{n} c_n^m(t, r) Y_n^m(\theta, \phi), \tag{6.3}$$

respectively, where $N_h = \lceil \omega r/c \rceil$ ($\lceil \cdot \rceil$ is the ceiling operation) is the order of sound field [112, 109], $h_n^{(1)}(\cdot)$ is the spherical Hankel function of the first kind [220], $Y_n^m(\theta, \phi)$ denotes for the spherical harmonic functions with order n and degree m, $C_n^m(\omega)$ and $c_n^m(t, r)$ are the frequency domain outgoing field coefficients and the time domain spherical harmonic coefficients, respectively. The relationship between $C_n^m(\omega)$ and $c_n^m(t, r)$ is

$$c_n^m(t, r) = \mathscr{F}^{-1}[C_n^m(\omega) h_n^{(1)}(\omega r/c)], \tag{6.4}$$

where $\mathscr{F}^{-1}$ represents the inverse Fourier transform [221].

As shown in Fig. 6.1, we denote the center of measured propeller O' as the origin. The sound field at the point (R_T, θ_T, ϕ_T) on the farfield target area $\mathbb{T}$ is

$$p(t, R_T, \theta_T, \phi_T) \approx \sum_{n=0}^{N_h} \sum_{m=-n}^{n} c_n^m(t, R_T) Y_n^m(\theta_T, \phi_T), \tag{6.5}$$

where $c_n^m(t, R_T)$ is the spherical harmonic coefficients.

In the frequency domain, based on (6.2) and (6.4), we have

$$\mathscr{F}[c_n^m(t, R_T)] = [\frac{h_n^{(1)}(\omega R_T/c)}{h_n^{(1)}(\omega R_M/c)}] \mathscr{F}[c_n^m(t, R_M)], \tag{6.6}$$

where $\mathscr{F}[\cdot]$ denote the Fourier transform. Then, in the time domain, we have

$$c_n^m(t, R_T) = c_n^m(t, R_M) * g(t, R_T, R_M), \tag{6.7}$$

where $*$ denotes convolution, and $g(t, R_T, R_M)$ is the function that relates the spherical harmonic coefficients between different radii

$$g(t, R_T, R_M) = \mathscr{F}^{-1}[\frac{h_n^{(1)}(\omega R_T/c)}{h_n^{(1)}(\omega R_M/c)}]. \tag{6.8}$$

.

In (6.7), the spherical harmonic coefficients $c_n^m(t, R_M)$ over $\mathbb{H}'$ are obtained through

[222, 109]

$$c_n^m(t, R_M) = \sum_{q=1}^{Q} \gamma_q p(t, R_M, \theta_q, \phi_q) Y_n^m(\theta_q, \phi_q), \tag{6.9}$$

where R_M is the radius of $\mathbb{H}'$, Q is the number of microphones over the hemisphere $\mathbb{H}'$, γ_q are the sampling weights, $p(t, R_M, \theta_q, \phi_q)$ is the time domain sound pressure at the sampling point (R_M, θ_q, ϕ_q).

6.3.2 Sound fields for all propellers

Drones have two sets of propellers and motors to balance their fuselage. One is designed to rotate clockwise, while the other is designed to rotate counter-clockwise, and the shapes of two sets of propellers are mirror-symmetric. Note the relative angle between clockwise and counter-clockwise propellers is time-varying. Therefore, in this chapter, we define the relative phase as angular blade positions between other propellers to propeller 1^{st} when propeller 1^{st} is parallel to the y axis. In the hovering condition, two sets of propellers spin at the same speed in opposite directions. For propellers with the same shape and rotation direction as the measured propeller, they generate the same sound field as the measured propeller. With the propeller center as the origin, the nearfield noise $p_s(\cdot)$ generated by the same set of propellers over a hemisphere with radius R_M is shown by

$$p_s(t, R_M, \theta, \phi) \approx \sum_{n=0}^{N_h} \sum_{m=-n}^{n} (c_n^m(t, R_M) + n(t)) Y_n^m(\theta, \phi), \tag{6.10}$$

where $c_n^m(t, R_M)$ is the spherical harmonic coefficient we found for the measured propeller, $n(t)$ is the measurement noise. Similarly, for mirror-symmetric propellers, based on the symmetry characteristics, the nearfield sound field $p_o(\cdot)$ over a hemisphere with radius R_M is shown by

$$p_o(t, R_M, \theta, \phi) \approx \sum_{n=0}^{N_h} \sum_{m=-n}^{n} (c_n^m(t, R_M) + n(t)) Y_n^m(\theta, 2\pi - \phi). \tag{6.11}$$

After obtaining the nearfield sound field of each propeller, we can use the extrapolation method to obtain the sound field $p_{n_p}(\boldsymbol{x}, t)$ over the target region $\mathbb{T}$ for each propeller. Based on (6.1), as $p_{n_p}(\boldsymbol{x}, t)$ is known, the total drone sound field over $\mathbb{T}$ can be found.

6.3.3 Optimization

The optimization problem is to minimize the sound power level over the target region $\mathbb{T}$ by controlling propeller relative phases. We define the total sound power over $\mathbb{T}$ as the cost function

$$\mathcal{L}(\boldsymbol{\psi}^{\mathbf{d}}) = \sum_{s=1}^{S}\sum_{u=1}^{U}(\sum_{n_p=1}^{N_p} p_{n_p}(\Psi(\boldsymbol{x}_{n_p}, \boldsymbol{x}_u), s + \psi^d_{n_p}))^2, \tag{6.12}$$

where $\boldsymbol{\psi}^{\mathbf{d}} = [\psi^d_1, \psi^d_2, ..., \psi^d_{N_p}]^T$, $\psi^d_1, \psi^d_2, ..., \psi^d_{N_p} \in [0, S]$ denote the discrete relative phase for propeller 1 to propeller N_p, $S = \lfloor f_{\mathrm{s}}/f_0 \rfloor$ ($\lfloor \cdot \rfloor$ is the floor operation) is the sample number for one rotation period, f_{s} is the sampling frequency, U is the evaluation point number for the given target area, $\Psi(\cdot)$ indicates the coordinate transfer function which can transfer the evaluation point on $\mathbb{T}$ with global coordinate (with origin O) to the local coordinate with the origin of the center of propeller n_p, $\boldsymbol{x}_{n_p} = (x_{n_p}, y_{n_p}, 0)$ express the global Cartesian coordinate for the center of propeller n_p, $\boldsymbol{x}_u = (\theta_u, \phi_u, R)$ is the Spherical coordinate for the evaluation point u. We define the optimization problem as

$$\begin{aligned} &\underset{\boldsymbol{\psi}^{\mathbf{d}} \in \mathbb{C}^{N_p}}{\arg\min} && \mathcal{L}(\boldsymbol{\psi}^{\mathbf{d}}), \\ &\text{s. t.} && \psi^d_1, \psi^d_2, ..., \psi^d_{N_p} \in [0, S]. \end{aligned} \tag{6.13}$$

Because $c_n^m(t, R_M)$ is obtained purely from measurements and lacks an analytical representation, the optimization problem cannot be solved in closed form. Therefore, we determine the optimal relative phases by exhaustively searching over all possible phase combinations.

6.4 Experimental Measurements and Simulations

In this section, we measure the nearfield noise of a single propeller and demonstrate the performance of phase control for drone noise reduction through simulations.

6.4.1 Setup for the single propeller noise measurement

The experiment setup is shown in Fig. 6.2, where we place the propeller in the center of a $R_M = 0.5$ m radius microphone array and lift it 1.7 m above the ground. A

Figure 6.2: The setup for single propeller noise measurement. The propeller is placed at the center of microphone array, and 32 microphones are nearly uniformed arranged over the lower hemisphere.

two-blade Gemfan 1045 Carbon Nylon propeller, with a diameter of 254 mm, and A2212/13T 1000KV brushless motor are used in this measurement. The rotational speed of the propeller is 5400 RPM. Thirty-two TDK ICS-43434 microphones are nearly uniformed placed over the lower hemisphere of the microphone array [223], and the sampling frequency is $f_s = 48000$ Hz. The measurement is conducted in an outdoor environment, with the temperature 26.3 degree Celsius and wind speed 8 km/h. The speed of sound is $c \approx 347$ m/s.

6.4.2 Results for different drone configurations

Different drone configurations are illustrated in Fig. 6.3. We first implement phase control to the typical configuration for the quadcopter drone, shown in Fig. 6.3 (c). We find that the optimal relative phases fluctuate round $[0°, 90°, 0°, 90°]$ during different time slots. The sound power level (SPL) over the large hemisphere $\mathbb{H}$, with a radius of 7 m, is illustrated in Fig. 4, where we can find the noise over the target area ($\theta \in [155°, 180°]$, $\phi \in [0°, 360°)$) is reduced.

To further understand the noise reduction performance, we define noise reduction level η as

$$\eta = 10\log_{10}\left(\frac{\mathcal{L}(\psi_1^d, \psi_2^d, ..., \psi_{N_p}^d)}{\mathcal{L}(0, 0, ..., 0)}\right), \tag{6.14}$$

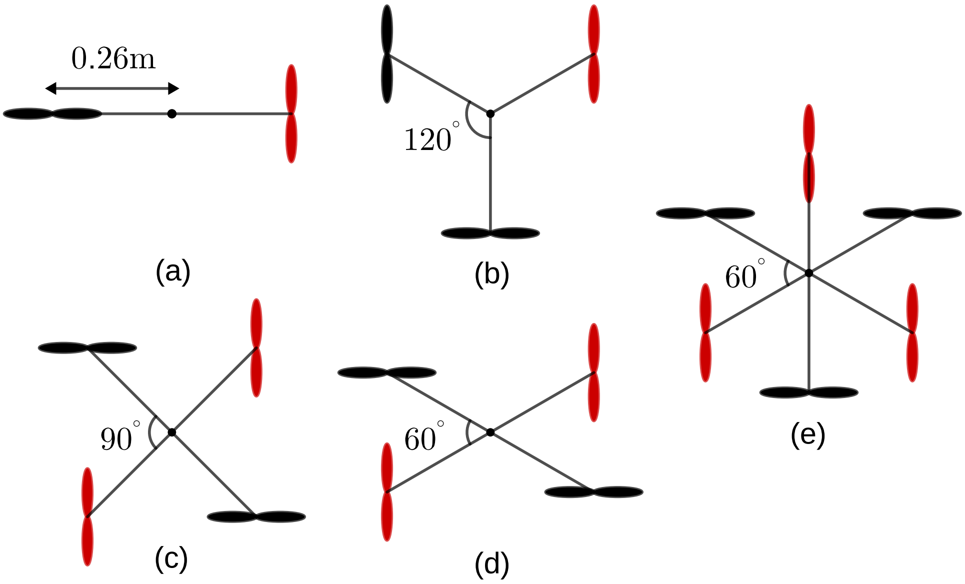

Figure 6.3: Drones with different propeller configurations, with the distance between the propeller's center and the drone's center is 0.26 m: (a) A two propellers, (b) three propellers, (c) four propellers with 90° angle between two adjacent arms, (c) four propellers with 60° angle between two adjacent arms, and (e) six propellers.

which means the ratio of total sound power over $\mathbb{T}$ after and before phase control. With the noise reduction level, we can test the phase control performance over time. We test the noise reduction level with $[0°, 90°, 0°, 90°]$ relative phases over 10 seconds and find that the performance is stable, with the average noise reduction level -6.80 ± 1.25 dB. This indicates that when we implement phase control to real drones, the control system only needs to maintain the pre-determined relative phase combination rather than determine the optimal relative combination in real-time.

We also implement the phase control method to different drone configurations which are shown in Fig. 6.3. The result is presented in Table 6.1, where we find that the 90° relative phase difference can achieve the best noise reduction performance for the given target area. Besides, for configurations (a), (c), and (d), configuration (a) has the largest distance between two adjacent propellers, and configuration (d) has the smallest distance between two adjacent propellers. Comparing the results of these three configurations, we find that phase control can reduce more noise when the two adjacent propellers are close to each other.

6.4.3 Residual noise analysis

In Fig. 6.5, we analyze the residual noise for the drone configuration (c) by plotting the SPL at an observer point in the target region before and after phase control. We

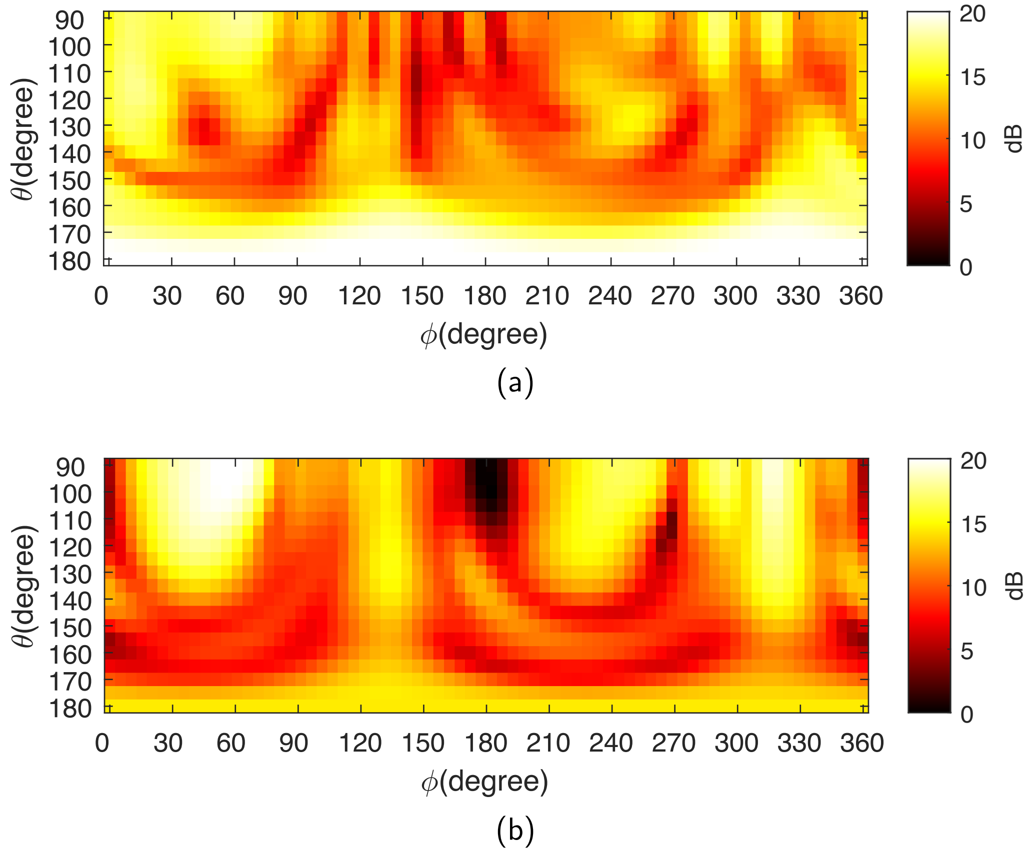

(a)

(b)

Figure 6.4: SPL over large hemisphere $\mathbb{H}$ with different relative phases for configuration (c) of Fig. 6.3: (a) the SPL with relative phase combination $[0°, 0°, 0°, 0°]$ and (b) the SPL with relative combination $[0°, 90°, 0°, 90°]$.

notice that when we set relative phases to the optimal combination $[0°, 90°, 0°, 90°]$, it can only cancel the noise for odd BPF harmonics, which is true for all observer points. This finding can be briefly explained by the relationship between relative phase and BPF harmonics. As the propeller we used has two blades, the fundamental BPF frequency can be calculated by $f_1 = 2f_0$. Therefore, the 90° relative phase difference actually preforms as $2 \times 90° \times b$ phase difference for the b-th order of BPF harmonics, and for the odd order of BPF harmonics, the phase difference can be represented as $\pi + (b-1)\pi$, so the odd order of BPF harmonic can be canceled. Consequently, even-order harmonics suffer a 2π phase shift, which is the same as a 0 phase shift, so there are no changes for even harmonics in Fig. 6.5. Based on this relationship, we predict that for the relative phase combination $[0°, 90°/l, 0°, 90°/l]$, where l is an integer number, the $b = l, 3l, 5l, 7l, ...$ order of BPF harmonics can be canceled. To validate this assumption, we analyze two other relative phase combinations $[0°, 45°, 0°, 45°]$ and $[0°, 22.5°, 0°, 22.5°]$. The result is shown in Figs. 6.5b and 6.5c, which are in line with our prediction. This finding means that we can control the specific order of propeller tonal noise, where most of the drone noise energy concentrate.

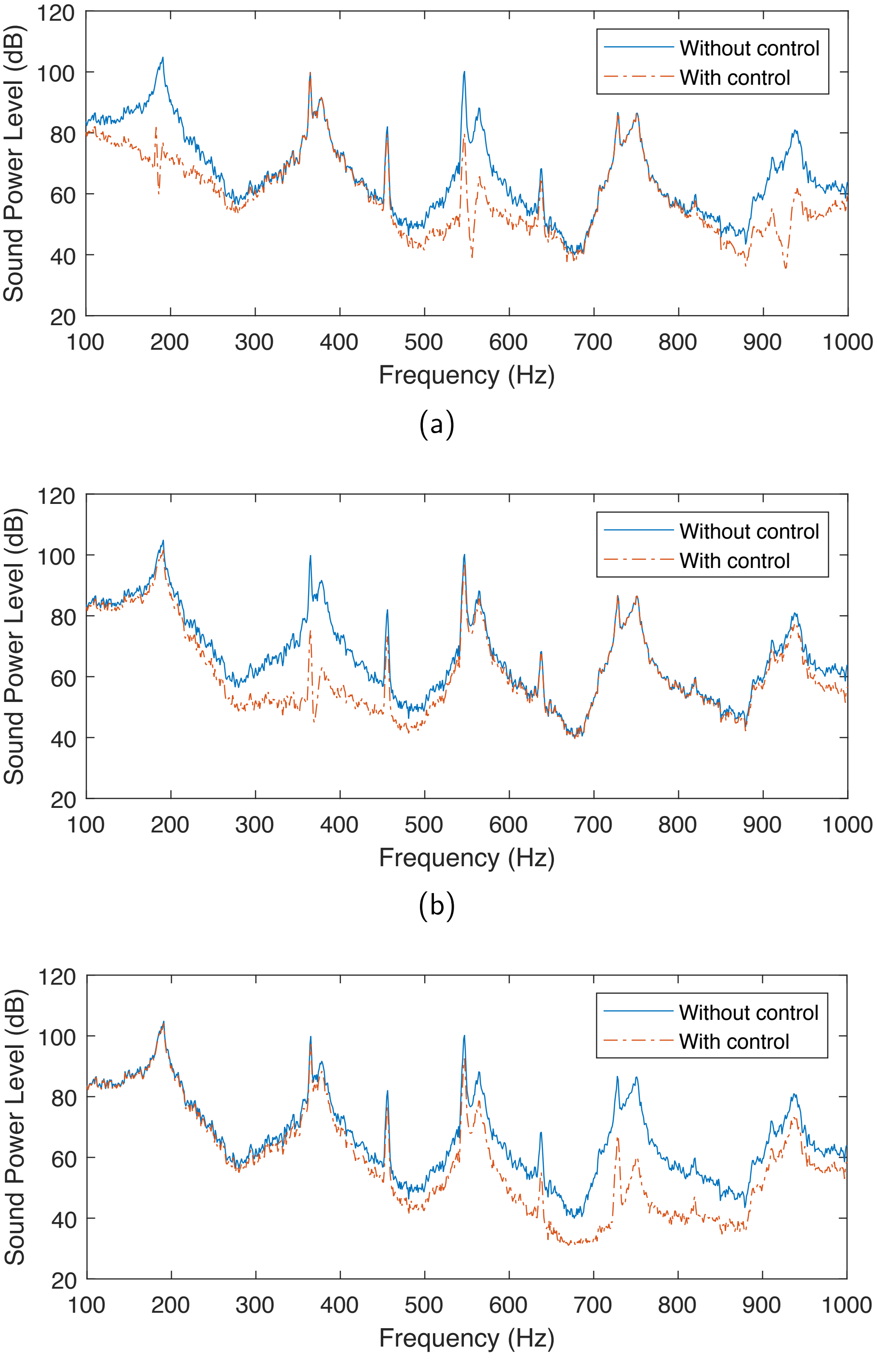

(a)

(b)

(c)

Figure 6.5: SPL with and without phase control for an observer point on the target region $\mathbb{T}$, with $\theta = 180°$, $\phi = 0°$: (a) SPL with $[0°, 90°, 0°, 90°]$ relative phases, (b) SPL with $[0°, 45°, 0°, 45°]$ relative phases, and (c) SPL with $[0°, 22.5°, 0°, 22.5°]$ relative phases.

Table 6.1: Phase control results for different drone configurations.

Configuration	Optimal relative phases	Noise reduction level
a	$[0°, 90°]$	-1.72 dB
b	$[0°, 90°, 90°]$	-2.57 dB
c	$[0°, 90°, 0°, 90°]$	-6.80 dB
d	$[0°, 90°, 0°, 90°]$	-6.96 dB
e	$[0°, 90°, 0°, 90°, 0°, 90°]$	-7.40 dB

6.5 Summary and Contributions

This chapter examined the noise reduction potential for drones in the hovering condition using the phase control method. For the typical quadcopter configuration, phase control can achieve -6.8 dB noise reduction for a farfield target region. Based on extensive simulations for different drone configurations, we find that the 90° phase difference can always result the best performance, and when the two adjacent propellers are close to each other, we can get better noise reduction results. Furthermore, we can flexibly control specific orders of propeller tonal noise, which can alleviate the burden of the ANC method and maximize the overall performance of a phase control-ANC drone noise control system.

6.6 Related Publications

- H. Bi, F. Ma, T. D. Abhayapala and P. N. Samarasinghe,“Spherical Array Based Drone Noise Measurements and Modelling for Drone Noise Reduction via Propeller Phase Control,” 2021 IEEE Workshop on Applications of Signal Processing to Audio and Acoustics (WASPAA), New Paltz, NY, USA, 2021, pp. 286-290, doi: 10.1109/WASPAA52581.2021.9632719.

Chapter 7

Directional Active Noise Control for Broadband Drone Noise

Overview: *In Chapters 5 and 6, we proposed two active noise reduction methods targeting tonal drone noise in specific directional regions. In this chapter, we move beyond tonal components and propose a directional broadband ANC framework designed to selectively attenuate broadband drone noise in a targeted far-field region of interest. Experimental validation in a semi-anechoic chamber demonstrates* 4.78 *dB average noise reduction in the 1500- 2400 Hz range, and approximately* 10 *dB over harmonic frequencies. These results demonstrate the potential of directional ANC strategies in mitigating drone noise propagation, which could enable quieter operations in noise-sensitive environments. The main contributions of this chapter are twofold:*

- *We propose the first drone-based ANC system capable of attenuating broadband noise in a far-field region.*
- *To the best of our knowledge, we conduct the first experimental validation of a drone ANC system's effectiveness in far-field noise reduction.*

7.1 Introduction

Drones have become increasingly popular for applications such as food and parcel delivery [1], mapping [2], search and rescue [3], and wildlife surveys [214]. Despite the growing importance of drones, the noise pollution from them is strong and can affect daily life and the health of residents. At the equivalent sound level, drone noise might be perceived as more annoying than road vehicles [224]. Therefore, effective drone noise mitigation strategies are crucial to supporting the sustainable integration of drones into everyday life.

Drone noise reduction methods can be broadly categorized into passive and active approaches. Passive noise reduction methods aim to change the design and material of drone's propellers, motors, and airframes to reduce noise generation from drones, and include techniques such as optimizing propeller and fuselage geometry [26], using ducted (shielded) propellers, and incorporating sound-absorptive barriers [27]. However, these methods offer only limited noise reduction and are generally ineffective for low-frequency noise [31]. In contrast, active drone noise reduction methods actively counteract and mitigate noise emissions during flight operations. These can be further divided into phase control and ANC. The phase control technique reduces noise by adjusting the relative angular blade positions of multiple propellers, thereby minimizing noise levels in specific target areas [32]. However, as mentioned in Chapter 6, this method is limited to canceling specific harmonics of tonal noise. ANC, on the other hand, employs secondary sources (loudspeakers) to generate anti-noise that destructively interferes with the primary noise [35]. ANC allows for noise cancellation in a controllable region, and with a sufficient number of secondary sources, noise can be effectively mitigated. This makes ANC a highly flexible and promising approach for drone noise reduction.

The current research on drone ANC is limited, with only a few studies addressing this topic. Muhammad *et al.* initially proposed a propeller noise reduction system that effectively reduced tonal noise over a circular target region based on simulations [36]. However, this approach required multiple secondary sources for each propeller, making it impractical for drone applications. Similarly, Dubravko introduced a multichannel ANC system using 12 loudspeakers positioned around each propeller to cancel the noise of the propeller, but the concept remained theoretical, lacking both simulation and experimental validation [27]. Narine *et al.* implemented a preliminary single-channel ANC system targeting the tonal noise generated by a single propeller [37]. However, the system was designed to cancel noise at a single spatial point near the propeller using a loudspeaker positioned at a long distance from the propeller, making the setup impractical for use on a flying drone. Moreover, in

Chapter 5, we proposed a narrow-band directional ANC system designed to reduce drone noise propagating downward. While effective, this system required a speaker and microphone array arranged in a spherical sector shape, limiting its practical implementation. Despite these efforts, most drone ANC research has certain limitations: i) focusing solely on propeller noise, neglecting other sources of drone noise; ii) targeting only narrow-band cancellation; iii) lacking experimental validation.

To address these research gaps, this chapter proposes and experimentally validates a broadband directional ANC system for drones. Given the weight and power constraints of drones, fully canceling all outgoing noise would require an impractically large number of secondary sources. Instead, to minimize disturbances to residents, this work focuses on drone noise reduction in a directional far-field region based on the near-field measurement from an on-board microphone array. Since deploying microphones in the far-field region is impractical, the proposed system incorporates the remote-sensing ANC algorithm from [225], which enables noise reduction in the target region using only near-field measurements. The algorithm is detailed in Section 7.5.4. The main contribution of this chapter is two-fold:

- We present the first drone ANC system capable of canceling broadband noise over a far-field region.
- To the best of our knowledge, we provide the first experimental evaluation of a drone ANC system's performance in the far field.

7.2 Problem Formulation

Consider a drone ANC system as shown in Fig. 7.1. Drone is the primary noise source with J reference sensors placed near the its propellers. Let there be Q monitoring microphones hanging on the drone to physically measure the near-field drone noise and V virtual microphones sampling the ROI in the farfield. L secondary sources are mounted on the drone fuselage, between the drone and the monitoring microphone, to control the noise propagating towards the ROI. Figure 7.3a shows a scenario where the drone flies over a residential area; in this case, the goal is to suppress noise directed downward toward the ground. Figure 7.3b illustrates an urban environment with high-rise buildings, where the objective is to reduce lateral noise propagation toward surrounding structures.

In the short-time Fourier transform (STFT) domain, we can represent the monitoring microphone signals and virtual microphone signals as:

$$\mathbf{e}_{\mathrm{M}}(f,t) = \mathbf{P}_{\mathrm{M}}(f)\mathbf{x}(f,t) + \mathbf{S}_{\mathrm{M}}(f)\mathbf{y}(f,t), \tag{7.1}$$

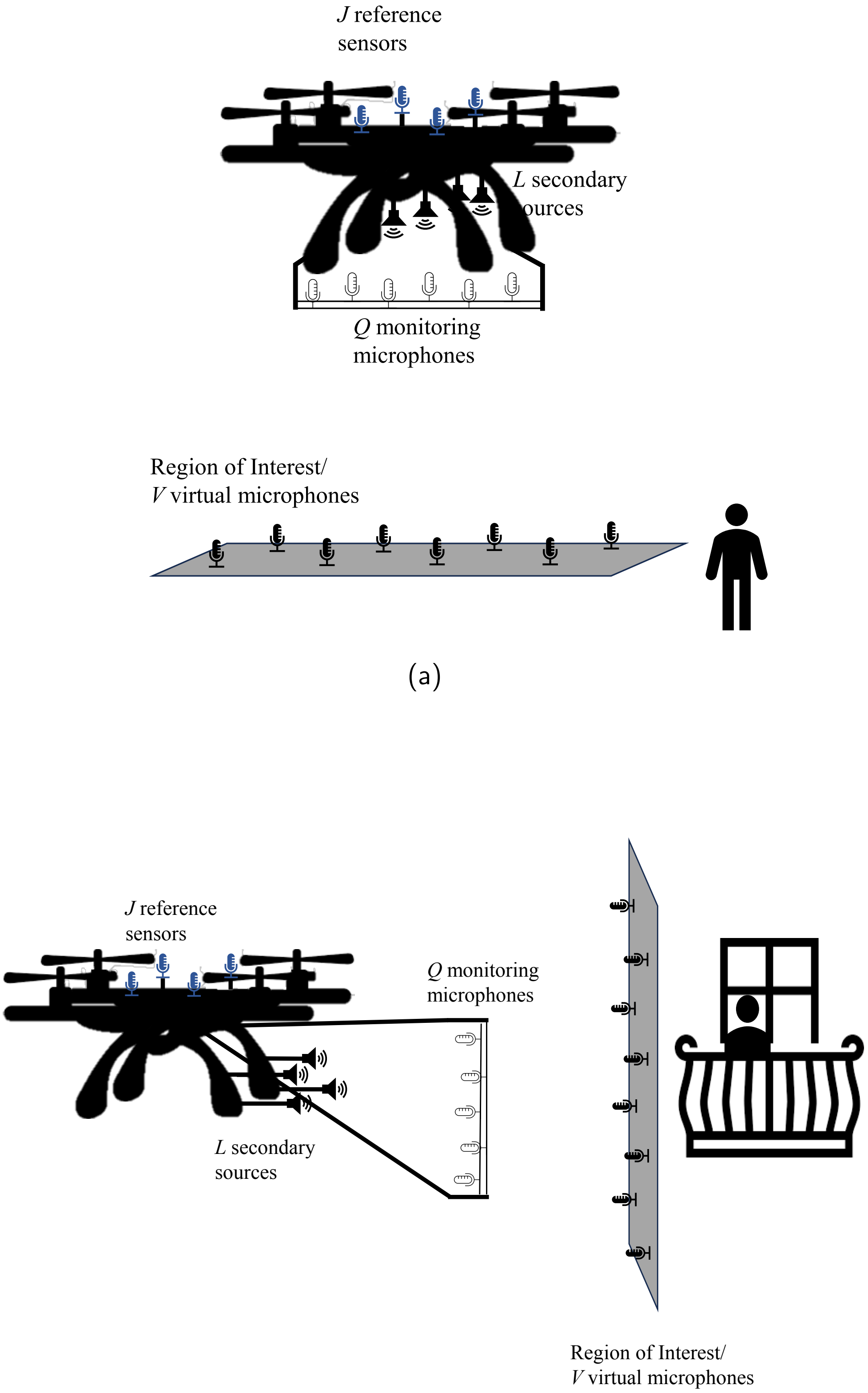

(a)

(b)

Figure 7.1: Drone directional ANC system setup (a) reducing noise downward and (b) reducing noise sideward: Q monitoring microphones hanging on the drone, L secondary sources mounted on the drone fuselage, J reference sensors placed near the drone propellers, and V virtual microphones sampled the ROI in the farfield.

$$\mathbf{e}_{\mathrm{V}}(f,t) = \mathbf{P}_{\mathrm{V}}(f)\mathbf{x}(f,t) + \mathbf{S}_{\mathrm{V}}(f)\mathbf{y}(f,t), \tag{7.2}$$

where $\mathbf{e}_{\mathrm{M}}(f,t)$ denotes the $Q \times 1$ monitoring microphone signals, $\mathbf{e}_{\mathrm{V}}(f,t)$ represents the $V \times 1$ virtual microphone signals, $\mathbf{x}(f,t)$ is the reference signals with the size of $J \times 1$, $\mathbf{y}(f,t)$ is the secondary source signals with the size of $L \times 1$, $\mathbf{P}_{\mathrm{M}}(f)$ and $\mathbf{S}_{\mathrm{M}}(f)$ are the primary channel response matrices and the secondary channel response matrices to monitoring microphones of sizes $Q \times J$ and $Q \times L$, respectively. $\mathbf{P}_{\mathrm{V}}(f)$ and $\mathbf{S}_{\mathrm{V}}(f)$ are the primary channel response matrices and the secondary channel response matrices to virtual microphones of sizes $V \times J$ and $V \times L$, respectively.

Since measurements from virtual microphones are not directly accessible, the research problem becomes how to derive an adaptive ANC algorithm that iteratively updates $\mathbf{y}$ based on the available information from $\mathbf{x}$, with the objective of minimizing the residual noise observed at the virtual microphone positions, represented by $\mathbf{e}_{\mathrm{V}}$.

7.3 The Relative Transfer Matrix

The relative transfer matrix (ReTM) is defined as the spatial mapping between the two microphone groups that are arbitrarily distributed within a given spatial region [225], which is independent of the source signals and is solely determined by the spatial properties (i.e., the acoustic transfer functions). The ReTM $\mathbf{R}_{\mathrm{VM}}$ between the recorded signals at the physical microphone group and the virtual microphone group is given by

$$\mathbf{e}_{\mathrm{V}}(f,t) = \mathbf{R}_{\mathrm{VM}}(f)\mathbf{e}_{\mathrm{M}}(f,t). \tag{7.3}$$

Based on (7.1), (7.2), and (7.8), the theoretical definition of ReTM is given by

$$\mathbf{R}_{\mathrm{VM}}(f) = [\mathbf{P}_{\mathrm{V}}(f)\mathbf{S}_{\mathrm{V}}(f)][\mathbf{P}_{\mathrm{M}}(f)\mathbf{S}_{\mathrm{M}}(f)]^{\dagger}. \tag{7.4}$$

where $(\cdot)^{\dagger}$ is the pseudo-inverse, assuming validity.

In practice, the ReTM can be estimated by the correlation-based approach [225]:

$$\mathbf{R}_{\mathrm{VM}}(f) \approx \mathbf{P}_{\mathrm{VV}}(f){\mathbf{P}_{\mathrm{MV}}}^{\dagger}(f), \tag{7.5}$$

where $\mathbf{P}_{\mathrm{VV}}(f) \triangleq \mathbb{E}\{\mathbf{e}_{\mathrm{V}}(f,t)\mathbf{e}_{\mathrm{V}}^{*}(f,t)\}$ is the auto-correlation matrix, $\mathbf{P}_{\mathrm{MV}}(f)$ is the cross-correlation matrix, which can calculated by $\mathbf{P}_{\mathrm{MV}}(f) \triangleq \mathbb{E}\{\mathbf{e}_{\mathrm{M}}(f,t)\mathbf{e}_{\mathrm{V}}^{*}(f,t)\}$, in which, $(\cdot)^{*}$ denotes the conjugate transpose, and $\mathbb{E}$ is the expectation obtained by averaging over T time frames as

$$\mathbf{P}_{\mathrm{VV}}(f) \cong \frac{1}{T}\sum_{t=1}^{T}\mathbf{e}_{\mathrm{V}}(f,t)\mathbf{e}_{\mathrm{V}}^{*}(f,t), \tag{7.6}$$

and

$$\mathbf{P}_{\mathrm{MV}}(f) \cong \frac{1}{T}\sum_{t=1}^{T}\mathbf{e}_{\mathrm{M}}(f,t)\mathbf{e}_{\mathrm{V}}^{*}(f,t), \tag{7.7}$$

respectively.

It is worth noting that in this chapter, we implement the ReTM solely as a method to model far-field drone noise based on onboard microphone measurements and incorporate it into the FxLMS algorithm. The point neuron learning method introduced in Chapter 4 could serve as an alternative to ReTM and may be used to develop a corresponding ANC algorithm for a similar task in future work.

7.4 Drone ANC with ReTM

In this section, we introduce the algorithm used in the drone directional ANC system.

The ANC algorithm has two stages, the tuning stage and the control stage. In the tuning stage, which can be done in the drone factory before launching to the market, the drone hovers at a certain height, and secondary sources play white noise. We place physical microphones at both the monitoring microphone and virtual microphone positions to measure $\mathbf{e}_{\mathrm{M}}$ and $\mathbf{e}_{\mathrm{V}}$. Then, we estimate the $\mathbf{R}_{\mathrm{VM}}$ by (7.5). Since the ReTM is independent of the source signals and is solely determined by the spatial properties of the acoustic environment, it remains unchanged as long as the drone's operating environment and the relative positions between the drone, the monitoring microphones, and the virtual microphones remain the same.

In the control stage, we assume the $\mathbf{R}_{\mathrm{VM}}$ stays unchanged from the tunning stage and use (7.8) to estimate $\mathbf{e}_{\mathrm{V}}$ from $\mathbf{e}_{\mathrm{M}}$. The adaptive ANC algorithm is illustrated in Fig. 7.2, where there are no physical microphones at the virtual microphone locations. With the estimated $\mathbf{R}_{\mathrm{VM}}$, we can estimate the far-field noise over the ROI by the on-board microphone measurement through

$$\hat{\mathbf{e}_{\mathrm{V}}}(f,t) = \mathbf{R}_{\mathrm{VM}}(f)\mathbf{e}_{\mathrm{M}}(f,t), \tag{7.8}$$

where $\hat{\mathbf{e}_{\mathrm{V}}}$ is the estimated virtual microphone signals.

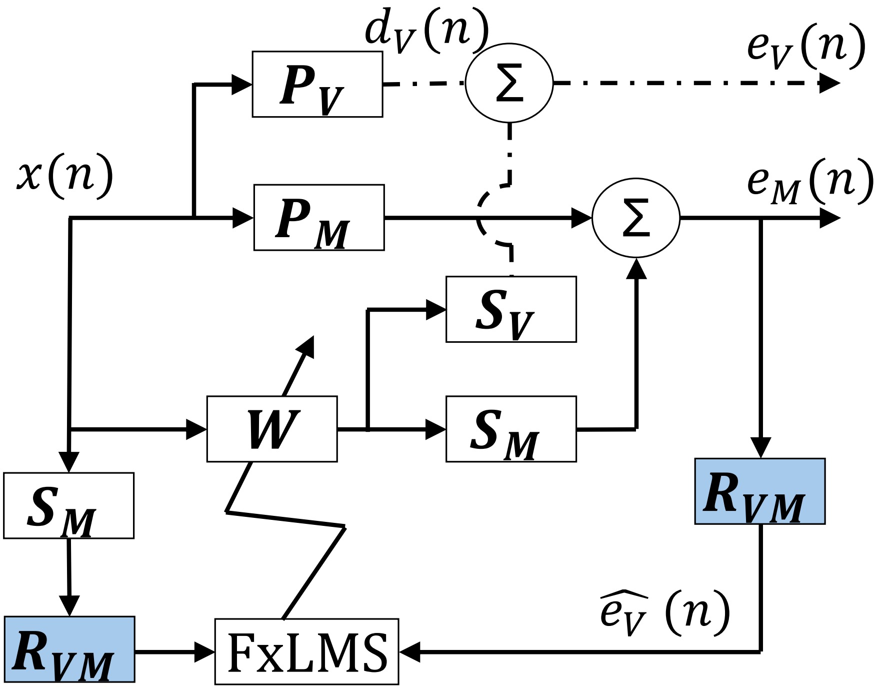

Figure 7.2: Illustration of control stage of the ReTM-based FxLMS ANC algorithm.

The loudspeaker signal is computed as

$$\mathbf{y}(f,t) = \sum_{j=1}^{J} \mathbf{W}_{\mathrm{j}}^{T}(f,t) * x'_{\mathrm{j}}(f,t), \tag{7.9}$$

where $x'_{\mathrm{j}}(f,t)$ represents the j-th reference signal $x_{\mathrm{j}}(f,t)$ filtered by the secondary path model to the monitoring microphone array $\mathbf{S}_{\mathrm{M}}(f)$ and the estimated ReTM $\mathbf{R}_{\mathrm{VM}}(f)$, $\mathbf{W}_{\mathrm{j}}$ is the $L \times 1$ adaptive filter.

We derive the updating equation below, and omit the dependency f and t for notational simplicity.

The residual signal $\mathbf{e}_{\mathrm{V}}$ can be represented by

$$\mathbf{e}_{\mathrm{V}} = \mathbf{d}_{\mathrm{V}} + \mathbf{S}_{\mathrm{V}}\Big(\sum_{j=1}^{J} x_{\mathrm{j}}\mathbf{W}_{\mathrm{j}}\Big), \tag{7.10}$$

where $\mathbf{d}_{\mathrm{V}}$ is the primary noise field over the virtual microphones.

The cost function is given by

$$\mathcal{L} = \mathbf{e}_{\mathrm{V}}^{H}\mathbf{e}_{\mathrm{V}}. \tag{7.11}$$

Based on (7.10), we can expand (7.11) as

$$\begin{aligned}\mathcal{L} =&\mathbf{d}_{\mathrm{V}}^{H}\mathbf{d}_{\mathrm{V}} + \mathbf{d}_{\mathrm{V}}^{H}\mathbf{S}_{\mathrm{V}}\big(\sum_{j=1}^{J} x_{\mathrm{j}}\mathbf{W}_{\mathrm{j}}\big) + \big(\sum_{j=1}^{J} x_{\mathrm{j}}^{*}\mathbf{W}_{\mathrm{j}}^{H}\big)\mathbf{S}_{\mathrm{V}}^{H}\mathbf{d}_{\mathrm{V}}\\ &+\big(\sum_{j=1}^{J} x_{\mathrm{j}}^{*}\mathbf{W}_{\mathrm{j}}^{H}\big)\mathbf{S}_{\mathrm{V}}^{H}\mathbf{S}_{\mathrm{V}}\big(\sum_{l=1}^{J} x_{\mathrm{l}}\mathbf{W}_{\mathrm{l}}\big).\end{aligned} \tag{7.12}$$

Then, we take a derivative of $\mathcal{L}$ with respect to $\mathbf{W}_{j}^{*}$ and calculate each item separately as

$$\frac{\partial\big(\mathbf{d}_{\mathrm{V}}^{H}\mathbf{d}_{\mathrm{V}}\big)}{\partial\mathbf{W}_{\mathrm{j}}^{*}} = 0, \tag{7.13}$$

$$\frac{\partial\big(\mathbf{d}_{\mathrm{V}}^{H}\mathbf{S}_{\mathrm{V}}\big(\sum_{j=1}^{J} x_{\mathrm{j}}\mathbf{W}_{\mathrm{j}}\big)\big)}{\partial\mathbf{W}_{\mathrm{j}}^{*}} = 0, \tag{7.14}$$

$$\frac{\partial\big((\sum_{j=1}^{J} x_{\mathrm{j}}^{*}\mathbf{W}_{\mathrm{j}}^{H})\mathbf{S}_{\mathrm{V}}^{H}\mathbf{d}_{\mathrm{V}}\big)}{\partial\mathbf{W}_{\mathrm{j}}^{*}} = x_{\mathrm{j}}^{*}\mathbf{S}_{\mathrm{V}}^{H}\mathbf{d}_{\mathrm{V}}, \tag{7.15}$$

$$\frac{\partial\big((\sum_{j=1}^{J} x_{\mathrm{j}}^{*}\mathbf{W}_{\mathrm{j}}^{H})\mathbf{S}_{\mathrm{V}}^{H}\mathbf{S}_{\mathrm{V}}(\sum_{l=1}^{J} x_{\mathrm{l}}\mathbf{W}_{\mathrm{l}})\big)}{\partial\mathbf{W}_{\mathrm{j}}^{*}} = x_{\mathrm{j}}^{*}\mathbf{S}_{\mathrm{V}}^{H}\mathbf{S}_{\mathrm{V}}\big(\sum_{l=1}^{J} x_{\mathrm{l}}\mathbf{W}_{\mathrm{l}}\big). \tag{7.16}$$

By summing these items together and simplifying the equation, we have

$$\nabla\mathcal{L} = 2x_{\mathrm{j}}^{*}\mathbf{S}_{\mathrm{V}}^{H}\mathbf{e}_{\mathrm{V}}. \tag{7.17}$$

Substituting (7.17) into (5.29), and replacing $\mathbf{e}_{\mathrm{V}}$ by (7.8) and $\mathbf{S}_{\mathrm{V}}$ by $\mathbf{R}_{\mathrm{VM}}[\mathbf{0}\ \mathbf{S}_{\mathrm{M}}]$, the adaptive equation can be written as

$$\mathbf{W}_{\mathrm{j}}(f,t+1) = \mathbf{W}_{\mathrm{j}}(f,t) - \mu x_{\mathrm{j}}(f,t)\mathbf{R}_{\mathrm{VM}}{}^{H}(f)\mathbf{S}_{\mathrm{M}}{}^{H}(f)\mathbf{e}_{\mathrm{M}}(f,t)\mathbf{R}_{\mathrm{VM}}(f). \tag{7.18}$$

7.5 Experiments

To test the proposed ANC system, in this section, we conduct experiments in a semi-anechoic acoustics chamber at the Australian National University with dimensions of 6.2 m × 4.8 m × 3.2 m and $T_{60} = 0.126$s.

7.5.1 Experiment Setup

A quadrotor UAV with a diagonal size of 32 cm was used in the experiment, as shown in Fig. 7.3a. A 16-channel UMA-16 microphone array (13.2 cm × 13.2 cm) was

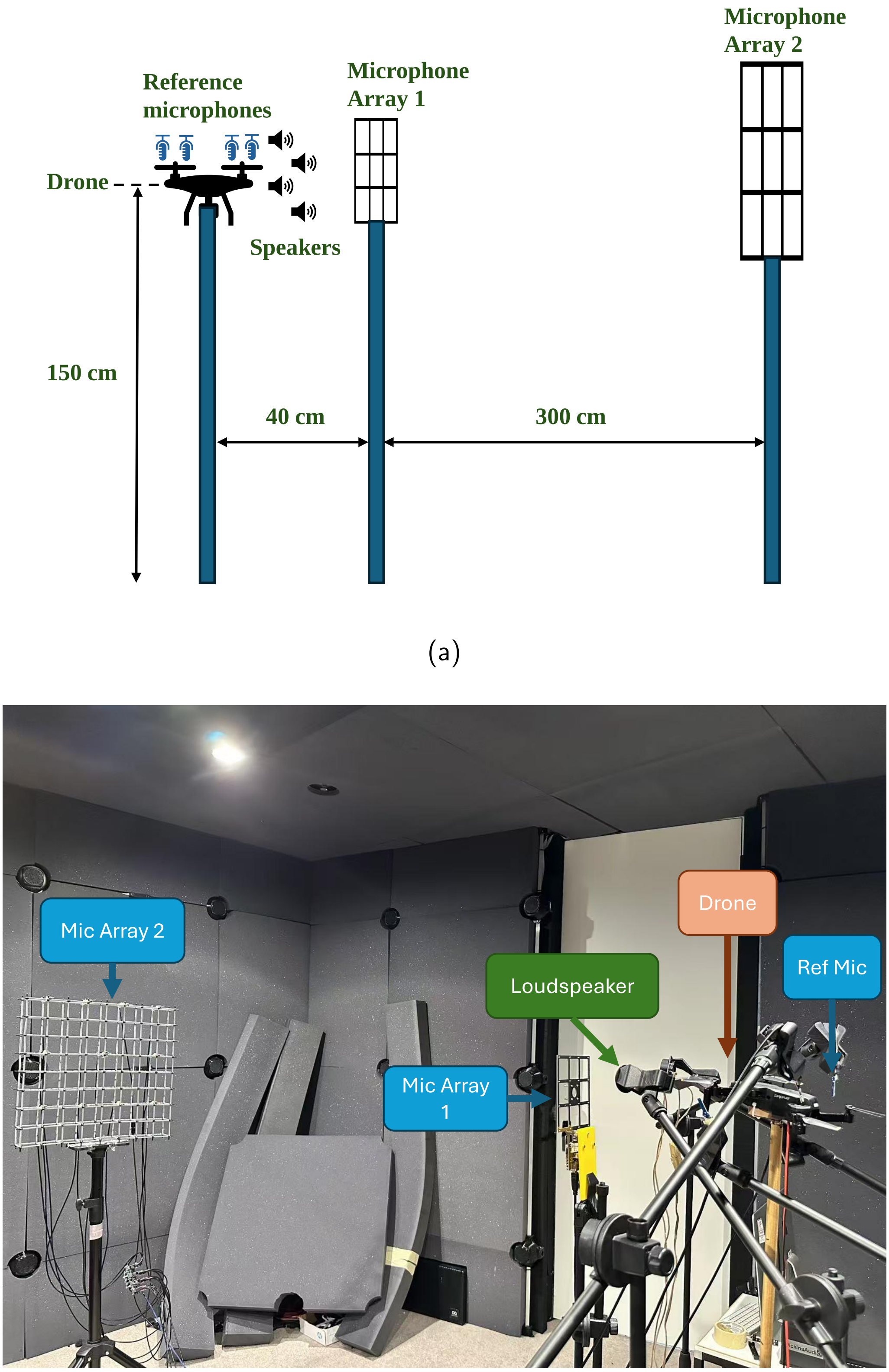

(a)

(b)

Figure 7.3: Drone directional ANC system experiment setup (a) experiment layout (b) experiment photo.

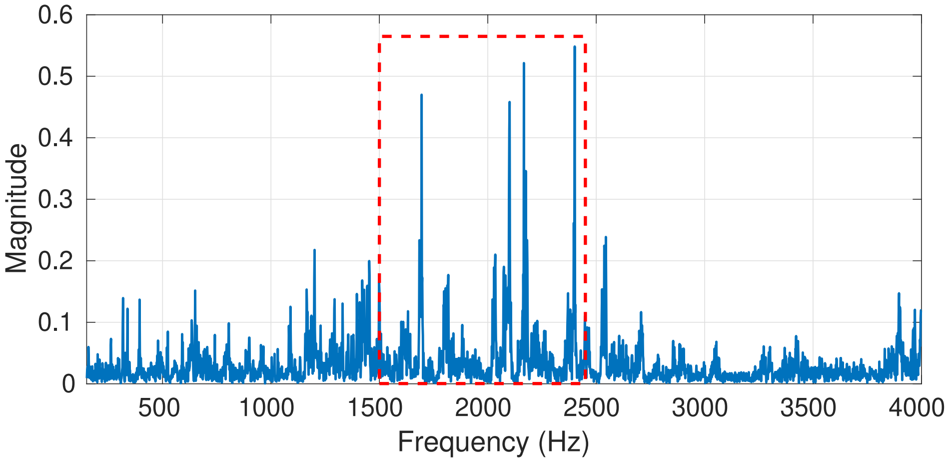

Figure 7.4: Drone noise spectrum observed at one of the virtual microphones, highlighting dominant BPFs within 1500–2400 Hz.

employed to monitor the near-field sound field, while a 9-channel microphone array (36 cm × 36 cm) was used to measure the sound field over the ROI. Four MEMS microphone chips served as reference microphones, located next to four propellers. The ND20FA-6 loudspeakers from DAYTON AUDIO, with a diameter of 4 cm, were used as the secondary sources.

We set $J = 4$ reference sensors, $L = 4$ secondary sources, $Q = 16$ monitoring microphones, $V = 9$ virtual microphones. We consider the 16-channel microphone array and the 9-channel microphone as the monitoring microphone group and virtual microphone group, respectively. Fig. 7.3 shows the experiment setup. The drone was mounted on a 150 cm wooden bar to remain stationary. The centers of the two microphone arrays are aligned vertically with the drone, positioned at the same height, and placed horizontally at 40 cm and 300 cm from the drone, respectively. The four reference microphones were placed at each of the four propellers, and the four secondary sources were positioned between the drone fuselage and the monitoring microphone array.

7.5.2 Experiment Procedure

We recorded two 40-second clips of the drone propeller noise under identical experimental conditions at a sampling rate of 48 kHz. Each recording was first filtered using a band-pass filter between 1500 Hz and 2400 Hz (a justification for this subband is provided below) and then transformed using STFT for ANC analysis. From each 40-second recording, we extracted a 30-second segment. These two 30-second segments were combined to form the tuning dataset, which was used to compute the ReTM between the monitoring and virtual microphone groups via (7.5). The

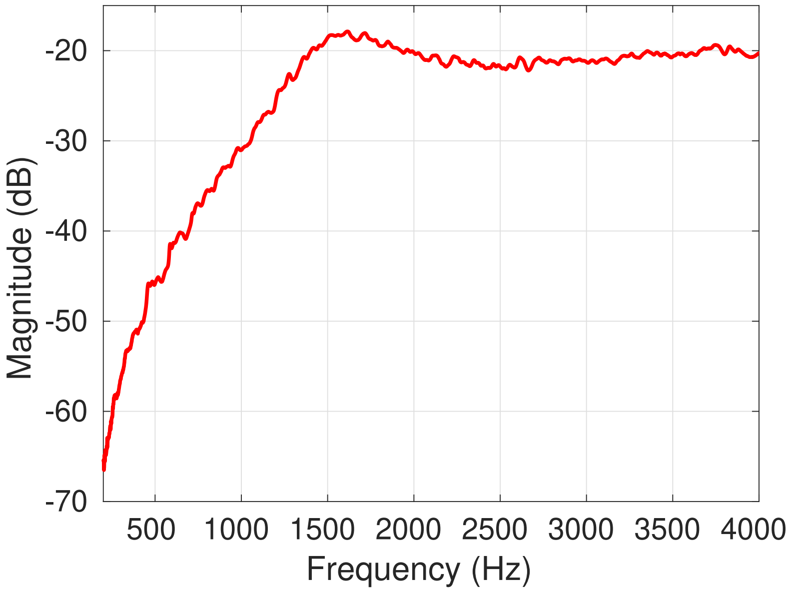

Figure 7.5: Measured magnitude response of the ND20FA-6 loudspeaker, showing flat response characteristics above 1500 Hz and roll-off below.

estimated ReTM and the measured monitoring microphone signals were then used to estimate the virtual microphone signals during the ANC control stage. The remaining 8-second segments from each recording were similarly combined to form the testing dataset, which was used to evaluate ANC performance. We applied a constant step size $\mu = 0.03$ in the FxLMS algorithm and report the preliminary noise reduction results in both the frequency and time domains.

7.5.3 Justification for Sub-band Processing

To determine an effective ANC frequency range, we examined the drone noise characteristics from Fig. 7.4 and observed that the BPFs were particularly prominent in the mid-frequency range of 1500–2400 Hz. Additionally, the magnitude response of the ND20FA-6 loudspeaker was found to be approximately flat within this range, as shown in Fig. 7.5. In contrast, the response below 1500 Hz decreases rapidly, making it unsuitable for low-frequency ANC applications due to insufficient speaker performance. Low-frequency sounds have long wavelengths, requiring a larger cone to move enough air to produce them, which makes it difficult for small-sized speakers to perform well at low frequencies. Given the combined considerations of noise dominance and loudspeaker characteristics, we restricted the ANC processing to this 1500–2400Hz sub-band to improve ANC efficiency. Note that the optimal ANC frequency range may vary depending on the specific drone and speaker hardware.

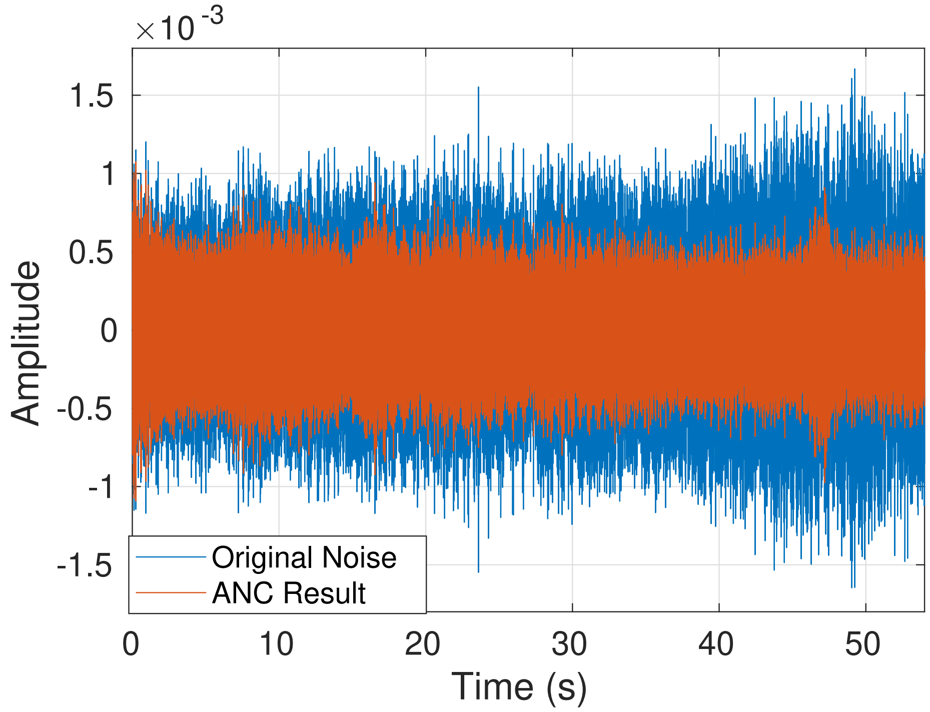

(a)

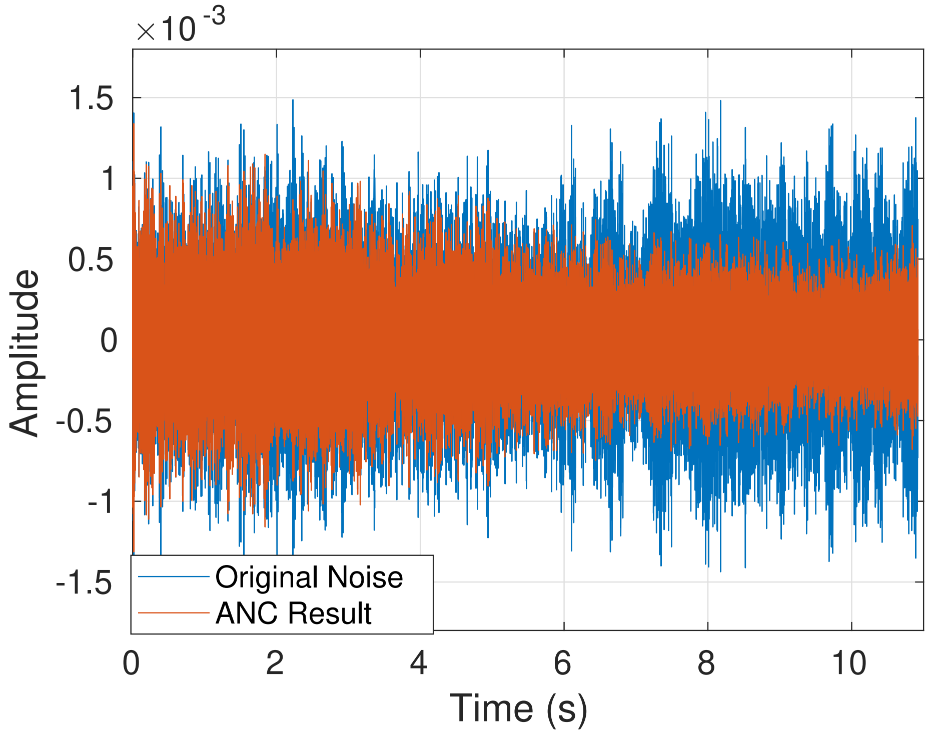

(b)

Figure 7.6: Time-domain error signal (filtered) at one of the virtual microphones. (a) Tuning dataset: ANC performance with the same noise recording as in the tuning stage. (b) Testing dataset: performance using a different segment of noise recording.

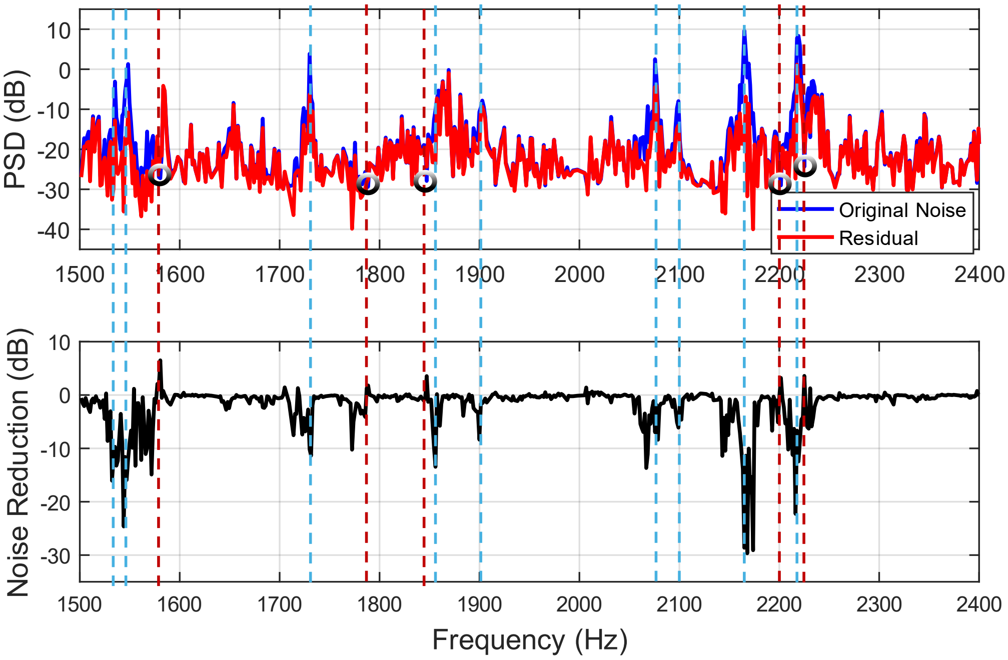

Figure 7.7: Power spectral density and noise reduction at one of the virtual microphones, illustrating around 10 dB attenuation in the target frequency band. The dotted lines indicate positive noise reduction values, which occur where the original noise level was very low.

7.5.4 Experiment Results

Figure 7.6a and Figure 7.6b show the time-domain error signals at one of the virtual microphones for the tuning and testing datasets, respectively. Note that the signals have been band-pass filtered to show only the activity within the ANC frequency range. In Fig. 7.6a, we show the ANC performance when the noise field in the control stage is the tuning dataset (the recording used to estimated ReTM). The system achieves an average noise reduction of -5.63 dB, with the error signal converging to a stable level within approximately 3 seconds. In Fig. 7.6b, we present a more realistic scenario, where the noise field during the control stage is the ANC testing set. Here, the ANC system achieves an average noise reduction of -4.78 dB, with convergence occurring around 5 seconds.

Figure 7.7 illustrates the power spectral density (PSD) and the corresponding noise reduction at a virtual microphone. The system achieves around 10 dB reduction at the dominant BPFs, highlighted by the blue dotted lines, which are the most prominent and perceptually significant components of drone noise [17]. At frequencies marked with red dotted lines, slight positive reduction values appear. However, the original noise levels at these frequencies are already low at around -25 to -30 dB (black circles), making even small residuals appear as an increase. The residual

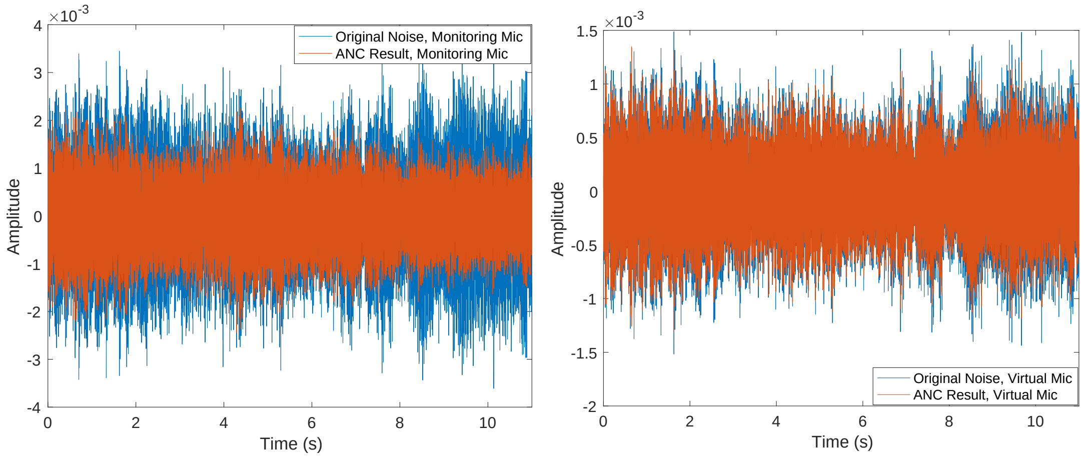

(a) (b)

Figure 7.8: Time domain performance of the baseline method on a single microphone: (a) monitoring microphone and (b) virtual microphone.

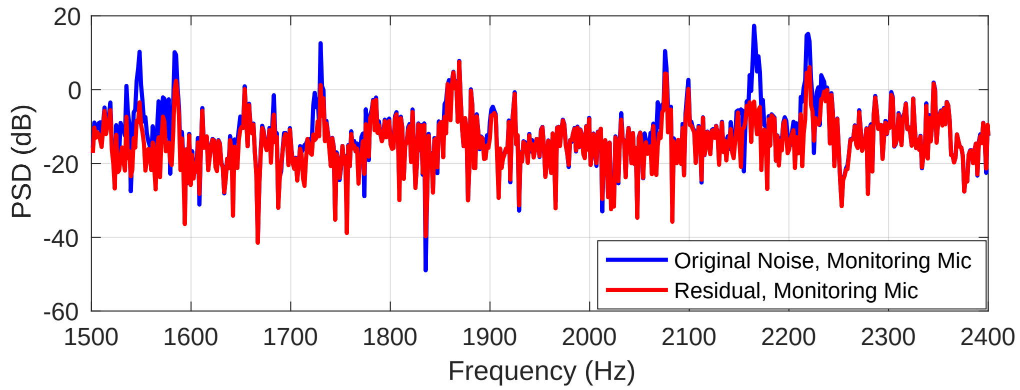

(a)

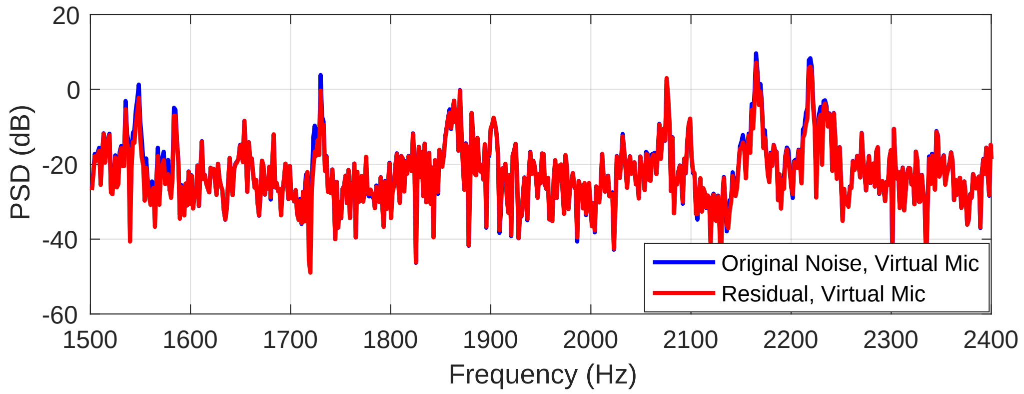

(b)

Figure 7.9: Power spectral density and noise reduction of the baseline method for a single microphone: (a) monitoring microphone and (b) virtual microphone.

noise remains around -20 dB, indicating that the remaining noise is minimal and unlikely to be perceptible in typical environments.

We also investigated the noise reduction performance of the baseline method, the FxLMS algorithm based solely on the monitoring microphone array without ReTM. The noise reduction results in the time domain and frequency domain are shown in Figs. 7.8 and 7.9, respectively. The baseline method achieves an overall noise reduction of 5.9 dB and approximately 10 dB reduction at the BPFs on the monitoring microphone array, which is comparable to the performance of the proposed method on the virtual microphone array. However, the noise reduction of the baseline method on the virtual microphone array is very limited, with only a 1.6 dB overall reduction, and the reduction at the BPFs is also negligible, indicating that the baseline method is only effective over the monitoring microphones. These results demonstrate the advantage of the proposed method in enabling effective noise reduction control in the far field based on near field noisy measurements.

7.6 Summary and Contributions

In this work, we propose a directional broadband ANC framework to mitigate drone noise propagating toward predefined far-field regions, addressing urban noise pollution concerns. Experimental validation in a semi-anechoic chamber demonstrates the system's capability to deliver an average noise reduction of 4.78 dB across 1500-2400 Hz within the region of interest, with a 10 dB noise reduction at drone BPFs. These findings demonstrate the efficacy of directional ANC strategies in attenuating drone noise and suggest their applicability in practical settings.

7.7 Related Publications

- **H. Bi**, Y. Zhang, T. D. Abhayapala, and P. N. Samarasinghe, "Directional Active Noise Control for Drone Noise," *JASA Express Lett*, 1 December 2025; 5 (12): 124801. [Online]. Available: `https://doi.org/10.1121/10.0039953`

Chapter 8

Conclusion and Future Works

Overview: *In this final chapter, we summarize the major contributions and key findings of the thesis, and revisit the central research question outlined at the outset. Finally, we conclude with a discussion on potential directions for future work and improvements to address remaining challenges and enhance the applicability of the proposed methods.*

8.1 Conclusion

In this thesis, we investigated two primary research problems: drone noise field modeling and directional drone noise reduction. For the noise modeling problem, instead of relying on computational aeroacoustic methods, which are typically resource-intensive and require detailed prior knowledge of flight conditions, we proposed a data-driven approach that leverages on-board microphone measurements. This problem was reformulated as a sound field extrapolation task. For the noise reduction problem, we focused on directional noise mitigation in the far-field and developed two ANC approaches and one phase control approach tailored to this objective. The key contributions of this thesis are summarized in the following conclusions:

(i) A spherical sector harmonics-based sound field extrapolation method was developed and analyzed in Chapter 3. This method enables the extrapolation of sectorial sound fields from on-board measurements to concentrated far-field regions with the same angular coverage. The proposed approach is particularly suited for modeling drone noise propagation in directional regions of interest.

(ii) In Chapter 4, a novel physics-informed neural network architecture, termed the *point neuron network*, was introduced for sound field interpolation and extrapolation tasks. Compared to existing PINN frameworks, the proposed network offers enhanced interpretability and demonstrates robust generalization to out-of-sample conditions. Unlike the spherical sector harmonics method from Chapter 3, the point neuron network does not require the microphone array to conform to a specific geometric configuration, making it more practical for real-world drone noise modeling. This approach has wider applicability in the sound field problems beyond drone-related topics.

(iii) A directional active noise control system for drones was developed in Chapter 5 to effectively attenuate tonal drone noise in a targeted far-field spherical region. This system builds upon the sectorial sound field extrapolation method introduced in Chapter 3. Furthermore, practical constraints such as drone payload capacity and power consumption were addressed through an analysis of the secondary-to-primary source power ratio under varying numbers of secondary sources.

(iv) A propeller phase control strategy was proposed in Chapter 6 to reduce tonal drone noise in the far-field region beneath the drone. This method leverages the phase relationships among multiple propellers to achieve destructive interference, thereby suppressing radiated noise in targeted directions.

(v) A directional broadband drone noise control system was developed and experimentally validated in Chapter 7. This system demonstrates effective attenuation of broadband drone noise propagating toward specific regions. Unlike the ANC method introduced in Chapter 5, the proposed system does not require the microphone array to follow a predefined geometric configuration, offering greater flexibility for practical deployment.

Collectively, the above contributions constitute a comprehensive framework for drone noise modeling and directional noise reduction. Therefore, we believe this thesis successfully addresses the research question posed: ***How can on-board microphone measurements and active noise control strategies be leveraged to model and suppress drone noise propagating in targeted directions, thereby minimizing its impact on nearby residents?***

Although this thesis demonstrates the great potential of active noise reduction methods for drones, achieving truly quiet drones with integrated phase control and ANC systems remains a significant challenge. A key concern is whether these systems might compromise the drone's flight stability. Addressing this issue requires careful design and strategic placement of the phase control and ANC components tailored to specific drone designs, as well as close collaboration with experts in aerodynamics, aeroacoustics, and drone manufacturing.

8.2 Future Research

This section first outlines future research directions that are closely related to this thesis. Due to hardware and time constraints, several aspects could not be fully investigated. In addition, potential research problems that naturally arise from the findings of this thesis are identified and discussed.

Feasibility study of drone noise reduction systems

The feasibility of the proposed drone noise reduction methods has not been fully investigated in several key aspects that are essential for practical deployment on real drones:

(i) Real-time feasibility of the proposed ANC algorithms on embedded drone platforms.

(ii) Feasibility of integrating loudspeakers on small drones, with particular emphasis on payload capacity, energy consumption, and flight stability.

(iii) ANC performance under real in-flight conditions, including aerodynamic effects and stability considerations.

(iv) Potential side effects in non-target regions associated with the proposed directional drone noise reduction methods.

Drone noise modeling by the multi-model framework

In Chapters 3 and 4, two drone noise modeling methods were proposed based solely on on-board microphone measurements. In future work, these methods can be extended by integrating the microphone measurements with computational aeroacoustic models within a multi-model framework. Given the high computational demands of such hybrid approaches, a practical solution is to pre-train a model using prior knowledge of the drone's design specifications and operating conditions, and subsequently refine this model in real-time using on-board microphone data. This hybrid strategy has the potential to significantly enhance modeling accuracy while maintaining computational efficiency.

Drone noise modeling based drone audio recording enhancement

Many modern drones are equipped with microphones for aerial audio recording. However, the high-intensity rotor noise severely degrades recording quality. An accurate drone noise model can be used to subtract the noise component from the recorded signal, thereby enhancing audio fidelity. The primary challenge in this approach lies in achieving precise synchronization between the real-time noise model and the recorded audio, ensuring that the modeled noise aligns temporally and spectrally with the captured signal. Therefore, the drone noise modeling approach developed in Chapters 3 and 4 can be implemented in the problem to obtain the real-time drone noise model. After that, the noise-subtracted recording can be further enhanced by learning-based methods.

Optimize the secondary source number and locations for drone ANC systems

In Chapters 5 and 7, two directional drone ANC systems were proposed. Due to the strict power and payload constraints inherent to drone platforms, it is impractical to deploy a large number of secondary sources. Therefore, under these limitations, identifying the optimal spatial configuration of a limited number of secondary sources becomes critical for maximizing noise reduction performance. To address this challenge, sparsity-constrained optimization techniques offer a promising direction for future research, enabling the selection of effective source placements that balance performance with resource efficiency.

Drone ANC systems with multiple microelectromechanical systems speakers

For small drones, integrating conventional loudspeakers presents significant challenges due to strict payload limitations. Microelectromechanical systems (MEMS) speakers, which employ thin-film piezoelectric or electrostatic actuation mechanisms to generate sound, offer an attractive alternative. These devices feature ultra-compact form factors, low weight, and high power efficiency. Compared to traditional loudspeakers, MEMS speakers are significantly lighter, occupy less physical space, and provide greater flexibility in placement. Consequently, MEMS speaker technology holds strong potential for application in drone ANC systems, particularly for lightweight and power-constrained aerial platforms.

Directional drone noise reduction system

We develop two directional drone ANC systems in Chapters 5 and 7, and the phase control noise reduction system in Chapter 6. For future work, these methods can be integrated into a unified, comprehensive system that leverages the strengths of each approach. Such integration has the potential to deliver more effective and adaptive directional noise reduction performance.

Bibliography

[1] W. C. Chiang, Y. Li, J. Shang, and T. L. Urban, "Impact of drone delivery on sustainability and cost: Realizing the uav potential through vehicle routing optimization," *Appl. Energy*, vol. 242, pp. 1164–1175, 2019.

[2] D. Ventura, M. Bruno, G. Jona Lasinio, A. Belluscio, and G. Ardizzone, "A low-cost drone based application for identifying and mapping of coastal fish nursery grounds," *Estuar. Coast. Shelf Sci.*, vol. 171, pp. 85–98, 2016.

[3] B. Mishra, D. Garg, P. Narang, and V. Mishra, "Drone-surveillance for search and rescue in natural disaster," *Comput. Commun.*, vol. 156, pp. 1–10, 2020.

[4] M. Erdelj and E. Natalizio, "Uav-assisted disaster management: Applications, architectures, and design challenges," *IEEE Access*, vol. 5, pp. 7337–7350, 2017.

[5] E. Semsch, M. Jakob, D. Pavlicek, and M. Pechoucek, "Autonomous uav surveillance in complex urban environments," in *IEEE/WIC/ACM Int. Jt. Conf. Web Intell. Intell. Agent Technol.* IEEE, 2009, vol. 2, pp. 82–85.

[6] Chao Zhang and J. Michael Kovacs, "The application of small unmanned aerial systems for precision agriculture: a review," *Precision Agriculture*, vol. 13, no. 6, pp. 693–712, 2012.

[7] K. Anderson and K. J. Gaston, "Lightweight unmanned aerial vehicles will revolutionize spatial ecology," *Biological Conservation*, vol. 158, pp. 205–209, 2013.

[8] Ying Liu, Xian Chen, and Qian Wang, "Aerial cinematography for unmanned aerial vehicles: A survey and future trends," *IEEE Access*, vol. 9, pp. 12345–12365, 2021.

[9] Wageesha Nilmini Manamperi, *Parameterisation, Localisation, and Enhancement of Spatial Soundfield from Drone On-Board Microphones*, Ph.d. thesis, The Australian National University, 2024.

[10] Grand View Research, "Drone market size, share & trends analysis report by product (commercial, military), by application (filming & photography,

inspection), by region, and segment forecasts, 2024 - 2030," 2024, Accessed: 2025-05-25.

[11] P. McDonald, M. Spencer, and Y. Zhang, "Assessing the impact of drone noise on community well-being: A preliminary study," *Science of the Total Environment*, vol. 710, pp. 136–142, 2020.

[12] R. Pijpers and M. Van den Berg, "Drone noise and sleep disturbance: An exploratory study," *Journal of Urban Health*, vol. 95, no. 2, pp. 235–243, 2018.

[13] L. Jones and T. Brown, "Psychological responses to novel noise sources: A case study on drone noise," *Environmental Psychology*, vol. 42, pp. 80–88, 2019.

[14] F. Rodriguez and S. Patel, "Towards regulatory frameworks for drone operations: Addressing noise pollution," *Journal of Air Transport Management*, vol. 92, pp. 101–109, 2022.

[15] M. Garcia and R. Chen, "Public perception and acceptance of drone technology in urban areas," *Technology in Society*, vol. 65, pp. 101–110, 2021.

[16] G. Sinibaldi and L. Marino, "Experimental analysis on the noise of propellers for small uav," *Appl. Acoust.*, vol. 74, no. 1, pp. 79–88, 2013.

[17] N. Intaratep, W. N. Alexander, W. J. Devenport, S. M. Grace, and A. Dropkin, "Experimental study of quadcopter acoustics and performance at static thrust conditions," in *22nd AIAA/CEAS Aeroacoustics Conference*, 2016, p. 2873.

[18] A. Christian, D. D. Boyd Jr, N. S. Zawodny, and S. A. Rizzi, "Auralization of tonal rotor noise components of a quadcopter flyover," in *Inter-Noise Noise-Con Proc.* Institute of Noise Control Engineering, 2015, vol. 250, pp. 3983–3994.

[19] K. A. Pascioni, S. A. Rizzi, and N. Schiller, "Noise reduction potential of phase control for distributed propulsion vehicles," in *AIAA Scitech 2019 Forum*, 2019, p. 1069.

[20] Q. Tan, H. Bian, J. Guo, P. Zhou, H. K. Lo, S. Zhong, and X. Zhang, "Virtual flight simulation of delivery drone noise in the urban residential community," *Transportation Research Part D: Transport and Environment*, vol. 118, pp. 103686, 2023.

[21] O. Gur and A. Rosen, “Comparison between blade-element models of propellers,” *The Aeronautical Journal*, vol. 112, no. 1138, pp. 689–704, Dec 2008.

[22] D. H. Kim, C. H. Park, and Y. J. Moon, “Aerodynamic analyses on the steady and unsteady loading-noise sources of drone propellers,” *International Journal of Aeronautical and Space Sciences*, vol. 20, pp. 611–619, 2019.

[23] T. Zhou and R. Fattah, “Tonal noise characteristics of two small-scale propellers,” in *Proc. AIAA/CEAS Aeroacoustics Conference*, Jun 2017, vol. 4054, p. 2017.

[24] H. Ben-Gida, M. Faran, T. Kogan, and O. Stalnov, “Noise reduction of a uav propeller using grit-type boundary layer tripping,” in *Proc. 57th Israel Annual Conf. on Aerospace Sciences*, Mar. 2017, pp. 15–16.

[25] Z. Ning, R. W. Wlezien, and H. Hu, “An experimental study on small uav propellers with serrated trailing edges,” in *Proceedings of the 47th AIAA Fluid Dynamics Conference*, June 2017, p. 3813.

[26] O. Gur and A. Rosen, “Design of quiet propeller for an electric mini unmanned air vehicle,” *J. Propuls. Power*, vol. 25, no. 3, pp. 717–728, 2009.

[27] D. Miljkovic, “Methods for attenuation of unmanned aerial vehicle noise,” in *Proc. 41st Int. Conv. Inf. Commun. Technol., Electron. Microelectron. (MIPRO).* IEEE, 2018, pp. 0914–0919.

[28] M. V. Mane, P. D. Sonawwanay, M. Solanki, and M. Others, “A comprehensive review on advancements in noise reduction for unmanned aerial vehicles (uavs),” *Journal of Vibration Engineering & Technologies*, vol. 12, no. Suppl 2, pp. 1375–1397, 2024.

[29] E. Pang, A. Cambray, D. Rezgui, M. Azarpeyvand, and S. A. S. Ali, “Investigation towards a better understanding of noise generation from uav propellers,” in *Proceedings of the 2018 AIAA/CEAS Aeroacoustics Conference*, June 2018, p. 3450.

[30] A. M. N. Malgoezar, A. Vieira, M. Snellen, D. G. Simons, and L. L. M. Veldhuis, “Experimental characterization of noise radiation from a ducted propeller of an unmanned aerial vehicle,” *International Journal of Aeroacoustics*, vol. 18, no. 4–5, pp. 372–391, 2019.

[31] F. A. Everest and K. C. Pohlmann, *Master handbook of acoustics*, McGraw-Hill Education, 2022.

[32] N. Schiller, K. Pascioni, and N. Zawodny, "Tonal noise control using phased rotors," 2019.

[33] V. Štorch, J. Nožička, M. Brada, J. Gemperle, and J. Suchý, "Measurement of noise and its correlation to performance and geometry of small aircraft propellers," in *EPJ Web of Conferences*. 2016, vol. 114, p. 02112, EDP Sciences.

[34] H. Bi, F. Ma, T. D. Abhayapala, and P. N. Samarasinghe, "Spherical array based drone noise measurements and modelling for drone noise reduction via propeller phase control," in *Proc. IEEE Workshop Appl. Signal Process. Audio Acoust.*, 2021, pp. 286–290.

[35] S. J Elliott and P. A Nelson, "Active noise control," *IEEE Signal Process. Mag.*, vol. 10, no. 4, pp. 12–35, 1993.

[36] M. Kusni, "The active noise control of propeller noise using a multipole secondary source," in *Proceedings of the 24th International Council of the Aeronautical Sciences (ICAS 2002)*, Toronto, Canada, 2002.

[37] Michael Narine, "Active noise cancellation of drone propeller noise through waveform approximation and pitch-shifting," M.S. thesis, Georgia State University, Atlanta, GA, 2020, Master's Thesis.

[38] X. Geng, X. Liu, H. Liu, Y. Yao, and Y. Wang, "Noise prediction of a uav propeller using computational fluid dynamics and aeroacoustic analogy," *Journal of Sound and Vibration*, vol. 498, pp. 115949, 2021.

[39] W. Chen, Z. Ma, É. Spieser, J. Guo, P. Zhou, S. Zhong, X. Zhang, and X. Huang, "Acoustic imaging of the broadband noise arising in contra-rotating co-axial propellers," *Aerospace Science and Technology*, vol. 141, pp. 108531, 2023.

[40] J. Whelchel and W. N. Alexander, "suas rotor-airframe interaction," in *Proceedings of the AIAA 2021-2212, Session: Emerging Urban and Advanced Air Mobility Noise II*. July 2021, AIAA.

[41] X. Xu, Y. Lu, J. Ma, and M. Shao, "A global rotor noise control method based on near-field acoustic holography and sound field reproduction," *Aerospace Science and Technology*, vol. 124, pp. 107549, 2022.

[42] J. E. Marte and D. W. Kurtz, "A review of aerodynamic noise from propellers, rotors, and lift fans," Technical Report NASA-32-7462, NASA, Washington, DC, 1970.

[43] A. J. Torija, P. Chaitanya, and Z. Li, "Psychoacoustic analysis of contra-rotating propeller noise for unmanned aerial vehicles," *The Journal of the Acoustical Society of America*, vol. 149, no. 2, pp. 835–846, Feb 2021.

[44] M. Strauss, P. Mordel, V. Miguet, and A. Deleforge, "Dregon: Dataset and methods for uav-embedded sound source localization," in *2018 IEEE/RSJ International Conference on Intelligent Robots and Systems (IROS).* Oct 2018, pp. 5735–5742, IEEE.

[45] L. Wang, R. Sanchez-Matilla, and A. Cavallaro, "Audio-visual sensing from a quadcopter: Dataset and baselines for source localization and sound enhancement," in *2019 IEEE/RSJ International Conference on Intelligent Robots and Systems (IROS).* Nov 2019, pp. 5320–5325, IEEE.

[46] L. Wang and A. Cavallaro, "Microphone-array ego-noise reduction algorithms for auditory micro aerial vehicles," *IEEE Sensors Journal*, vol. 17, no. 8, pp. 2447–2455, 2017.

[47] L. Wang and A. Cavallaro, "A blind source separation framework for ego-noise reduction on multi-rotor drones," *IEEE/ACM Transactions on Audio, Speech, and Language Processing*, vol. 28, pp. 2523–2537, Aug 2020.

[48] M. J. B. Lotinga, C. Ramos-Romero, N. Green, and A. J. Torija, "Noise from unconventional aircraft: A review of current measurement techniques, psychoacoustics, metrics and regulation," *Curr. Pollution Rep.*, vol. 9, pp. 724–745, 2023.

[49] C. Ramos-Romero, N. Green, A. J. Torija, and C. Asensio, "On-field noise measurements and acoustic characterisation of multi-rotor small unmanned aerial systems," *Aerospace Science and Technology*, vol. 141, pp. 108537, 2023.

[50] M. J. B. Lotinga, C. Ramos-Romero, N. Green, et al., "Noise from unconventional aircraft: A review of current measurement techniques, psychoacoustics, metrics and regulation," *Current Pollution Reports*, vol. 9, pp. 724–745, 2023.

[51] N. Intaratep, W. N. Alexander, W. J. Devenport, S. M. Grace, and A. Dropkin, "Experimental study of quadcopter acoustics and performance at static thrust conditions," in *Proc. 22nd AIAA/CEAS Aeroacoustics Conf.*, Lyon, France, May 2016, American Institute of Aeronautics and Astronautics.

[52] K. Herreman, "Proposed measurement method for uav sound levels," in *Proc. Noise-Con*, Providence, RI, USA, June 2016, pp. 15–622.

[53] K. Herreman, C. Taylor, and Y. Paya, "Anechoic chamber measurement of

an octocopter," in *Proc. NOISE-CON 2020*, New Orleans, USA, Nov. 2020, vol. 262 of *INTER-NOISE and NOISE-CON Congress and Conference Proceedings*, pp. 511–518, Institute of Noise Control Engineering.

[54] C. E. Tinney and J. Sirohi, "Multirotor drone noise at static thrust," *AIAA Journal*, vol. 56, no. 7, pp. 2816–2826, 2018.

[55] M. Alkmim, J. Cardenuto, E. Tengan, T. Dietzen, T. Van Waterschoot, J. Cuenca, et al., "Drone noise directivity and psychoacoustic evaluation using a hemispherical microphone array," *Journal of the Acoustical Society of America*, vol. 152, no. 5, pp. 2735–2745, 2022.

[56] T. Zhou, H. Jiang, Y. Sun, R. J. Fattah, X. Zhang, B. Huang, and L. Cheng, "Acoustic characteristics of a quad-copter under realistic flight conditions," in *Proc. 25th AIAA/CEAS Aeroacoustics Conf.*, Delft, The Netherlands, May 2019, American Institute of Aeronautics and Astronautics.

[57] U. Papa, G. D. Core, and G. Giordano, "Determination of sound power levels of a small uas during flight operations," in *Proc. Inter-Noise 2016, 45th Int. Congress and Exposition on Noise Control Engineering*, Hamburg, Germany, Aug. 2016, pp. 692–702.

[58] W. M. Humphreys, D. P. Lockard, M. R. Khorrami, W. Culliton, R. McSwain, P. A. Ravetta, et al., "Development and calibration of a field-deployable microphone phased array for propulsion and airframe noise flyover measurements," in *Proc. 22nd AIAA/CEAS Aeroacoustics Conf.*, Lyon, France, May 2016, American Institute of Aeronautics and Astronautics.

[59] N. Kloet, S. Watkins, and R. Clothier, "Acoustic signature measurement of small multi-rotor unmanned aircraft systems," *International Journal of Micro Air Vehicles*, vol. 9, no. 1, pp. 3–14, 2017.

[60] W. N. Alexander and J. Whelchel, "Flyover noise of multi-rotor suas," in *Proc. Inter-Noise 2019, 48th Int. Congress and Exhibition on Noise Control Engineering*, Madrid, Spain, June 2019.

[61] W. N. Alexander, J. Whelchel, N. Intaratep, and A. Trani, "Predicting community noise of suas," in *Proc. 25th AIAA/CEAS Aeroacoustics Conf.*, Delft, The Netherlands, May 2019, American Institute of Aeronautics and Astronautics.

[62] I. Besnea, "Acoustic imaging and spectral analysis for assessing uav noise," Master's thesis, Delft University of Technology, Delft, The Netherlands, 2020.

[63] N. Konzel and E. Greenwood, “Ground-based acoustic measurements of small multirotor aircraft,” in *Proc. Vertical Flight Society’s 78th Annual Forum & Technology Display*, Fort Worth, US, May 2022, Vertical Flight Society.

[64] C. Cutler-Wood, M. Barzach, R. Downs, C. M. Hobbs, and S. Shirayama, “Estimating unmanned aircraft takeoff noise using hover measurement data,” in *Proc. Quiet Drones 2022*, Internet, June 2022, INCE-Europe.

[65] J. Treichl and S. Körper, “Untersuchung der geräuschemission von drohnen / investigation of the noise emission of drones,” *Lärmbekämpfung*, vol. 14, pp. 108–114, 2019.

[66] F. Farassat and G. P. Succi, “The prediction of helicopter discrete frequency noise,” *Vertica*, vol. 7, no. 4, pp. 309–320, 1983.

[67] K. S. Brentner, “Prediction of helicopter rotor discrete frequency noise,” Tech. Rep. NASA TM 87721, NASA, 1986.

[68] J. M. Gallman, “The validation and application of a rotor acoustic prediction computer program,” Tech. Rep. NASA TM 101794, NASA, 1990.

[69] P. Spiegel, “Prediction and analysis of the noise emitted by a main rotor of a helicopter in case of bvi,” Tech. Rep. Publication No. 1996-1, ONERA, 1996.

[70] K. S. Brentner, “Numerical algorithms for acoustic integrals with examples for rotor noise prediction,” *AIAA Journal*, vol. 35, no. 4, pp. 625–630, 1997.

[71] K. S. Brentner and H. E. Jones, “Noise prediction for maneuvering rotorcraft,” in *6th AIAA/CEAS Aeroacoustics Conference*. American Institute of Aeronautics and Astronautics, 2000, number AIAA Paper 2000-2031.

[72] G. A. Bresa, “Modeling the noise of arbitrary maneuvering rotorcraft: Analysis and implementation of the psu-wopwop noise prediction code,” M.S. thesis, Department of Aerospace Engineering, The Pennsylvania State University, University Park, PA, 2002.

[73] G. A. Bresa, K. S. Brentner, G. Perez, and H. E. Jones, “Maneuvering rotorcraft noise prediction,” *Journal of Sound and Vibration*, vol. 275, pp. 719–738, 2004.

[74] J. E. Ffowcs Williams and D. L. Hawkings, “Sound generation by turbulence and surfaces in arbitrary motion,” *Philosophical Transactions of the Royal Society of London. Series A, Mathematical and Physical Sciences*, vol. 264, no. 1151, pp. 321–342, 1969.

[75] G. Romani and D. Casalino, “Rotorcraft blade-vortex interaction noise prediction using the lattice-boltzmann method,” *Aerospace Science and Technology*, vol. 88, pp. 147–157, 2019.

[76] P. Ventura Diaz and S. Yoon, “High-fidelity computational aerodynamics of multi-rotor unmanned aerial vehicles,” in *Proceedings of the AIAA SciTech Forum 2018 (56th AIAA Aerospace Sciences Meeting)*, Kissimmee, FL, Jan 2018.

[77] J. Ko, J. Kim, and S. Lee, “Computational study of wake interaction and aeroacoustic characteristics in multirotor configurations,” in *INTER-NOISE and NOISE-CON Congress and Conference Proceedings*, Madrid, Spain, 2019, vol. 259, pp. 5145–5156, Institute of Noise Control Engineering.

[78] H. Jiang, T. Zhou, R. J. Fattah, X. Zhang, and X. Huang, “Multi-rotor noise scattering by a drone fuselage,” in *25th AIAA/CEAS Aeroacoustics Conference*, Dallas, TX, USA, 2019, number 2019-2586, American Institute of Aeronautics and Astronautics.

[79] Z. Jia, S. Lee, K. Sharma, and K. S. Brentner, “Aeroacoustic analysis of a lift-offset coaxial rotor using high-fidelity cfd/csd loose coupling simulation,” *Journal of the American Helicopter Society*, vol. 65, no. 1, pp. 011501, 2020.

[80] H. Lee and D.-J. Lee, “Rotor interactional effects on aerodynamic and noise characteristics of a small multirotor unmanned aerial vehicle,” *Physics of Fluids*, vol. 32, no. 4, pp. 047107, 2020.

[81] Z. Wang, Q. Henricks, M. Zhuang, A. Pandey, M. Sutkowy, B. Harter, M. McCrink, and J. Gregory, “Impact of rotor–airframe orientation on the aerodynamic and aeroacoustic characteristics of small unmanned aerial systems,” *Drones*, vol. 3, no. 3, pp. 56, 2019.

[82] J. Whelchel and W. N. Alexander, “suas rotor-airframe interaction,” in *Proceedings of the 25th AIAA/CEAS Aeroacoustics Conference*, Delft, The Netherlands, 2019, American Institute of Aeronautics and Astronautics.

[83] F. Farassat, “Derivation of formulations 1 and 1a of farassat,” Tech. Rep. NASA/TM-2007-214853, NASA Langley Research Center, Hampton, Virginia, Mar. 2007.

[84] Q. Tan, H. Bian, S. Zhong, and X. Zhang, “Simulation of multi-rotor powered urban aerial mobility noise for environmental assessment,” in *Proceedings of*

NOISE-CON 2021, Washington, D.C., USA, 2021, pp. 3854–3860, Institute of Noise Control Engineering.

[85] S. Zhong, P. Zhou, Y. Fang, and X. Zhang, "A hybrid and efficient low-noise assessment platform for urban aerial mobility (helpu)," in *Proceedings of INTER-NOISE 2021 - 50th International Congress and Exposition of Noise Control Engineering*, Washington, D.C., USA, 2021, pp. 3756–3768, Institute of Noise Control Engineering of the USA, Inc.

[86] Q. Tan, H. Bian, J. Guo, P. Zhou, H. K. Lo, S. Zhong, and X. Zhang, "Virtual flight simulation of delivery drone noise in the urban residential community," *Transportation Research Part D: Transport and Environment*, vol. 118, pp. 103686, 2023.

[87] F. B. Metzger, "An assessment of propeller aircraft noise reduction technology," Tech. Rep. NASA/CR-198237, NASA Langley Research Center, Hampton, VA, USA, Aug. 1995.

[88] E. Pang, A. Cambray, D. Rezgui, M. Azarpeyvand, and S. A. Showkat Ali, "Investigation towards a better understanding of noise generation from uav propellers," in *Proceedings of the 24th AIAA/CEAS Aeroacoustics Conference*, Atlanta, GA, USA, June 2018.

[89] A. S. Hersh, P. T. Soderman, and R. E. Hayden, "Investigation of acoustic effects of leading-edge serrations on airfoils," *Journal of Aircraft*, vol. 11, no. 4, pp. 197–202, 1974.

[90] C. C. Paruchuri, S. Narayanan, P. F. Joseph, and J. W. Kim, "Leading edge serration geometries for significantly enhanced leading edge noise reductions," in *Proceedings of the 22nd AIAA/CEAS Aeroacoustics Conference*, Lyon, France, June 2016, number AIAA 2016-2736.

[91] Z. Ning and H. Hu, "An experimental study on the aerodynamic and aeroacoustic performances of a bio-inspired uav propeller," in *35th AIAA Applied Aerodynamics Conference*, Denver, CO, USA, June 2017, number AIAA 2017-3747.

[92] R. Noda, T. Nakata, T. Ikeda, D. Chen, Y. Yoshinaga, K. Ishibashi, C. Rao, and H. Liu, "Development of bio-inspired low-noise propeller for a drone," *Journal of Robotics and Mechatronics*, vol. 30, no. 3, pp. 337–343, 2018.

[93] I. H. Jung, J. H. Seo, H. S. Han, T. W. Park, and J. Y. Kim, "A study

on dc motor noise reduction," *Key Engineering Materials*, vol. 270-273, pp. 1434–1439, 2004.

[94] K. W. Byun, C. S. Kim, and K. B. Oh, "A study on the reduction of noise and vibration of dc motor by the redesign of balance weight," in *Proceedings of the 2011 Spring Academic Conference of the Korea Precision Engineering Society*. 2011, pp. 1219–1220, Korea Precision Engineering Society.

[95] Y. J. Qian, Y. L. Wei, D. Y. Kong, and H. Xu, "Experimental investigation on motor noise reduction of unmanned aerial vehicles," *Applied Acoustics*, vol. 176, pp. 107873, 2021.

[96] H. Xu, D. Kong, Y. Qian, and X. Tang, "Motor noise reduction of unmanned aerial vehicles," *Applied Acoustics*, vol. 198, pp. 108979, 2022.

[97] N. Intravartolo, T. Sorrells, N. Ashkharian, and R. Kim, "Attenuation of vortex noise generated by uav propellers at low reynolds numbers," in *55th AIAA Aerospace Sciences Meeting*, 2017, p. 2019.

[98] A. C. Demoret and C. F. Wisniewski, "The impact of a notched leading edge on performance and noise signature of unmanned aerial vehicle propellers," in *AIAA SciTech 2019 Forum*, 2019, p. 0159.

[99] R. Ghaffarivardavagh, J. Nikolajczyk, S. Anderson, and X. Zhang, "Ultra-open acoustic metamaterial silencer based on fano-like interference," *Physical Review B*, vol. 99, no. 2, pp. 024302, 2019.

[100] A. Mahashabde, P. Wolfe, A. Ashok, C. Dorbian, Q. He, A. Fan, S. Lukachko, A. Mozdzanowska, C. Wollersheim, S. R. H. Barrett, M. Locke, and I. A. Waitz, "Assessing the environmental impacts of aircraft noise and emissions," *Progress in Aerospace Sciences*, vol. 47, no. 1, pp. 15–52, 2011.

[101] J. D. Jones and C. R. Fuller, "Noise control characteristics of synchrophasing. ii—experimental investigation," *AIAA Journal*, vol. 24, no. 8, pp. 1271–1276, 1986.

[102] J. D. Jones and C. R. Fuller, "An experimental investigation of the interior noise control effects of propeller synchrophasing," Tech. Rep. NAS 1.26:178185, NASA, 1986.

[103] D. Hammond, R. McKinley, and B. Hale, "Noise reduction efforts for special operations c-130 aircraft using active synchrophaser control," Tech. Rep. AD-A434029, Air Force Research Laboratory, Wright-Patterson Air Force Base, OH, 1998.

[104] B. Smith, R. Niemiec, and F. Gandhi, "A comparison of multicopter noise characteristics with increasing number of rotors," in *76th VFS Annual Forum, Virginia Beach, VA*, 2020.

[105] S. M. Kuo and D. R. Morgan, *Active noise control systems*, vol. 4, Wiley, New York, 1996.

[106] D. L. Colton and R. Kress, *Inverse Acoustic and Electromagnetic Scattering Theory*, vol. 93 of *Applied Mathematical Sciences*, Springer, New York, 1998.

[107] T. D. Abhayapala, *Modal Analysis and Synthesis of Broadband Nearfield Beamforming Arrays*, Ph.D. thesis, The Australian National University, Canberra, Australia, December 1999.

[108] E. G. Williams, *Fourier Acoustics: Sound Radiation and Nearfield Acoustical Holography*, Academic Press, London, UK, 1999.

[109] B. Rafaely, *Fundamentals of spherical array processing*, vol. 8, Springer, 2015.

[110] E. Skudrzyk, *The foundations of acoustics: basic mathematics and basic acoustics*, Springer Science & Business Media, New York, 2012.

[111] H. Teutsch, *Modal Array Signal Processing: Principles and Applications of Acoustic Wavefield Decomposition*, vol. 348 of *Lecture Notes in Control and Information Sciences*, Springer, Berlin, Heidelberg, 2007.

[112] D. B Ward and T. D. Abhayapala, "Reproduction of a plane-wave sound field using an array of loudspeakers," *IEEE Trans. Speech Audio Process.*, vol. 9, no. 6, pp. 697–707, 2001.

[113] L. Birnie, T. D. Abhayapala, V. Tourbabin, and P. N. Samarasinghe, "Mixed source sound field translation for virtual binaural application with perceptual validation," *IEEE/ACM Trans. Audio Speech Lang. Process.*, vol. 29, pp. 1188–1203, 2021.

[114] Huiyuan Sun, *Theory and Design of Feasible Active Noise Control Systems for 3D Regions*, Ph.d. thesis, The Australian National University, 2022.

[115] S.-C. Chan and Y. Chu, "Performance analysis and design of fxlms algorithm in broadband anc system with online secondary-path modeling," *IEEE Transactions on Audio, Speech, and Language Processing*, vol. 20, no. 3, pp. 982–993, March 2012.

[116] Y. Chu, S. Zhao, L. He, and F. Niu, "Wind noise suppression in filtered-x

least mean squares-based active noise control systems," *The Journal of the Acoustical Society of America*, vol. 152, no. 6, pp. 3340–3345, 2022.

[117] D. Shi, W.-S. Gan, B. Lam, and C. Shi, "Two-gradient direction fxlms: An adaptive active noise control algorithm with output constraint," *Mechanical Systems and Signal Processing*, vol. 116, pp. 651–667, 2019.

[118] D. Shi, W.-S. Gan, B. Lam, and S. Wen, "Active noise control based on the momentum multichannel normalized filtered-x least mean square algorithm," in *INTER-NOISE and NOISE-CON Congress and Conference Proceedings*. 2020, vol. 261, pp. 709–719, Institute of Noise Control Engineering.

[119] M. Raissi, P. Perdikaris, and G. E. Karniadakis, "Physics informed deep learning (part i): Data-driven solutions of nonlinear partial differential equations," 2017, Preprint at arXiv:1711.10561.

[120] M. Raissi, P. Perdikaris, and G. E. Karniadakis, "Physics-informed neural networks: A deep learning framework for solving forward and inverse problems involving nonlinear partial differential equations," *J. Comput. Phys.*, vol. 378, pp. 686–707, 2019.

[121] S. Cai, Z. Wang, F. Fuest, Y. J. Jeon, C. Gray, and G. E. Karniadakis, "Flow over an espresso cup: inferring 3-d velocity and pressure fields from tomographic background oriented schlieren via physics-informed neural networks," *J. Fluid Mech.*, vol. 915, pp. A102, 2021.

[122] D. Li, K. Xu, J. M. Harris, and E. Darve, "Coupled time-lapse full-waveform inversion for subsurface flow problems using intrusive automatic differentiation," *Water Resour. Res.*, vol. 56, no. 8, pp. e2019WR027032, 2020.

[123] N. B. Erichson, M. Muehlebach, and M. W. Mahoney, "Physics-informed autoencoders for lyapunov-stable fluid flow prediction," *arXiv preprint arXiv:1905.10866*, 2019.

[124] M. Raissi, A. Yazdani, and G. E. Karniadakis, "Hidden fluid mechanics: Learning velocity and pressure fields from flow visualizations," *Science*, vol. 367, no. 6481, pp. 1026–1030, 2020.

[125] A. M. Tartakovsky, C. O. Marrero, P. Perdikaris, G. D. Tartakovsky, and D. Barajas-Solano, "Physics-informed deep neural networks for learning parameters and constitutive relationships in subsurface flow problems," *Water Resour. Res.*, vol. 56, no. 5, pp. e2019WR026731, 2020.

[126] W. Zhu, K. Xu, E. Darve, and G. C. Beroza, "A general approach to seismic

inversion with automatic differentiation," *Computers & Geosciences*, vol. 151, pp. 104751, 2021.

[127] M. Rasht-Behesht, C. Huber, K. Shukla, and G. E. Karniadakis, "Physics-informed neural networks (pinns) for wave propagation and full waveform inversions," *J Geophysical Res: Solid Earth.*, vol. 127, no. 5, pp. e2021JB023120, 2022.

[128] R. G. Patel, I. Manickam, N. A. Trask, M. A. Wood, M. Lee, I. Tomas, and E. C. Cyr, "Thermodynamically consistent physics-informed neural networks for hyperbolic systems," *J. Comput. Phys.*, vol. 449, pp. 110754, 2022.

[129] X. Jia, J. Willard, A. Karpatne, J. S. Read, J. A. Zwart, M. Steinbach, and V. Kumar, "Physics-guided machine learning for scientific discovery: An application in simulating lake temperature profiles," *ACM/IMS Trans. Data Sci.*, vol. 2, no. 3, pp. 1–26, 2021.

[130] K. M. Kim, P. Hurley, and J. P. Duarte, "Physics-informed machine learning-aided framework for prediction of minimum film boiling temperature," *Int. J. Heat Mass Transf.*, vol. 191, pp. 122839, 2022.

[131] M. Sarabian, H. Babaee, and K. Laksari, "Physics-informed neural networks for brain hemodynamic predictions using medical imaging," *IEEE Trans. Med. Imaging.*, vol. 41, no. 9, pp. 2285–2303, 2022.

[132] G. Kissas, Y. Yang, E. Hwuang, W. R. Witschey, J. A. Detre, and P. Perdikaris, "Machine learning in cardiovascular flows modeling: Predicting arterial blood pressure from non-invasive 4d flow mri data using physics-informed neural networks," *Comput. Methods Appl. Mech. Eng.*, vol. 358, pp. 112623, 2020.

[133] K. Hammernik, T. Küstner, B. Yaman, Z. Huang, D. Rueckert, F. Knoll, and M. Akçakaya, "Physics-driven deep learning for computational magnetic resonance imaging: Combining physics and machine learning for improved medical imaging," *IEEE Signal Process. Mag.*, vol. 40, no. 1, pp. 98–114, 2023.

[134] R. LM. van Herten, A. Chiribiri, Ma. Breeuwer, M. Veta, and C. M. Scannell, "Physics-informed neural networks for myocardial perfusion mri quantification," *Med. Image Anal.*, vol. 78, pp. 102399, 2022.

[135] H. Kafri, M. Olivieri, F. Antonacci, M. Moradi, A. Sarti, and S. Gannot, "Grad-cam-inspired interpretation of nearfield acoustic holography us-

ing physics-informed explainable neural network," in *Proc. IEEE Int. Conf. Acoust., Speech, Signal Process.* IEEE, 2023, pp. 1–5.

[136] K. Shigemi, S. Koyama, T. Nakamura, and H. Saruwatari, "Physics-informed convolutional neural network with bicubic spline interpolation for sound field estimation," in *Proc. Int. Workshop Acoust. Signal Enhancement.* IEEE, 2022, pp. 1–5.

[137] N. Borrel-Jensen, A. P. Engsig-Karup, and C. Jeong, "Physics-informed neural networks for one-dimensional sound field predictions with parameterized sources and impedance boundaries," *Jasa Express Lett.*, vol. 1, no. 12, 2021.

[138] X. Chen, F. Ma, A. Bastine, P. N. Samarasinghe, and H. Sun, "Sound field estimation around a rigid sphere with physics-informed neural network," in *Proc. Asia-Pacific Signal Inf. Process. Assoc. Annu. Summit Conf.* IEEE, 2023, pp. 1984–1989.

[139] F. Ma, T. D. Abhayapala, and P. N. Samarasinghe, "Circumvent spherical bessel function nulls for open sphere microphone arrays with physics informed neural network," *Preprint at arXiv:2308.00242*, 2023.

[140] X. Karakonstantis and E. Fernandez-Grande, "Advancing sound field analysis with physics-informed neural networks," *J. Acoust. Soc. Amer.*, vol. 154, no. 4_supplement, pp. A98–A98, 2023.

[141] M. Olivieri, X. Karakonstantis, M. Pezzoli, F. Antonacci, A. Sarti, and E. Fernandez-Grande, "Physics-informed neural network for volumetric sound field reconstruction of speech signals," *Preprint at arXiv:2403.09524*, 2024.

[142] F. Miotello, F. Terminiello, M. Pezzoli, A. Bernardini, F. Antonacci, and A. Sarti, "A physics-informed neural network-based approach for the spatial upsampling of spherical microphone arrays," *Preprint at arXiv:2407.18732*, 2024.

[143] S. A. Verburg Riezu, E. Fernandez Grande, and P. Gerstoft, "Optical interferometry based acoustic field characterization using physics informed neural networks," in *Proceedings of INTER-NOISE 2024*, Nantes, France, Aug 2024, pp. 8852–8858.

[144] M. Olivieri, M. Pezzoli, F. Antonacci, and A. Sarti, "A physics-informed neural network approach for nearfield acoustic holography," *Sensors*, vol. 21, no. 23, pp. 7834, 2021.

[145] M. Pezzoli, F. Antonacci, and A. Sarti, "Implicit neural representation with

physics-informed neural networks for the reconstruction of the early part of room impulse responses," *Preprint at arXiv:2306.11509*, 2023.

[146] X. Karakonstantis, D. Caviedes-Nozal, A. Richard, and E. Fernandez-Grande, "Room impulse response reconstruction with physics-informed deep learning," *J. Acoust. Soc. Amer.*, vol. 155, no. 2, pp. 1048–1059, 2024.

[147] X. Karakonstantis and E. Fernandez-Grande, "Room impulse response reconstruction using physics-constrained neural networks," in *10th Convention of the European Acoustics Association*. European Acoustics Association, 2023.

[148] T. D. Abhayapala and D. B. Ward, "Theory and design of high order sound field microphones using spherical microphone array," *Proc. IEEE Int. Conf. Acoust., Speech, Signal Process.*, vol. 2, pp. 1949–1952, 2002.

[149] J. Meyer and G. Elko, "A highly scalable spherical microphone array based on an orthonormal decomposition of the soundfield," *Proc. IEEE Int. Conf. Acoust., Speech, Signal Process.*, vol. 2, pp. 1781–1784, 2002.

[150] B. Rafaely, "Analysis and design of spherical microphone arrays," *IEEE Trans. Speech Audio Process.*, vol. 13, no. 1, pp. 135–143, 2004.

[151] B. Rafaely, "The spherical-shell microphone array," *IEEE Trans. Audio, Speech, Language Process.*, vol. 16, no. 4, pp. 740–747, 2008.

[152] V. Varanasi, H. Gupta, and R. M. Hegde, "A deep learning framework for robust doa estimation using spherical harmonic decomposition," *IEEE/ACM Trans. Audio, Speech, Language Process.*, vol. 28, pp. 1248–1259, 2020.

[153] D. Salvati, C. Drioli, and G. L. Foresti, "Diagonal unloading beamforming in the spherical harmonic domain for acoustic source localization in reverberant environments," *IEEE/ACM Trans. Audio, Speech, Language Process.*, vol. 28, pp. 2001–2012, 2020.

[154] G. Ping, E. Fernandez-Grande, P. Gerstoft, and Z. Chu, "Three-dimensional source localization using sparse bayesian learning on a spherical microphone array," *J. Acoust. Soc. Amer.*, vol. 147, no. 6, pp. 3895–3904, 2020.

[155] Y Hu and S Gannot, "Closed-form single source direction-of-arrival estimator using first-order relative harmonic coefficients," in *Proc. IEEE Int. Conf. Acoust., Speech, Signal Process.* IEEE, 2022, pp. 726–730.

[156] G. Huang, J. Chen, and J. Benesty, "A flexible high directivity beamformer

with spherical microphone arrays," *J. Acoust. Soc. Amer.*, vol. 143, no. 5, pp. 3024–3035, 2018.

[157] L. Wang and J. Zhu, "Regularized beamformer for the spherical microphone array to cope with the white noise amplification," *Proc. IEEE Int. Conf. Acoust., Speech, Signal Process.*, pp. 4657–4661, 2020.

[158] K. Wakayama, J. Trevino, H. Takada, S Sakamoto, and Y. Suzuki, "Extended sound field recording using position information of directional sound sources," *Proc. IEEE Workshop Appl. Signal Process. Audio Acoust.*, pp. 185–189, 2017.

[159] F. Ma, W. Zhang, and T. D. Abhayapala, "Active control of outgoing noise fields in rooms," *J. Acoust. Soc. Amer.*, vol. 144, no. 3, pp. 1589–1599, 2018.

[160] B. Bu, C. Bao, and M. Jia, "Design of a planar first-order loudspeaker array for global active noise control," *IEEE/ACM Trans. Audio, Speech, Language Process.*, vol. 26, no. 11, pp. 2240–2250, 2018.

[161] Jihui Zhang, Thushara D Abhayapala, Prasanga N Samarasinghe, Wen Zhang, and Shouda Jiang, "Multichannel active noise control for spatially sparse noise fields," *J. Acoust. Soc. Amer.*, vol. 140, no. 6, pp. EL510–EL516, 2016.

[162] H. Bi, F. Ma, T. D. Abhayapala, and P. N. Samarasinghe, "Spherical array based drone noise measurements and modelling for drone noise reduction via propeller phase control," *Proc. IEEE Workshop Appl. Signal Process. Audio Acoust.*, pp. 286–290, 2021.

[163] T Peleg and B Rafaely, "Investigation of spherical loudspeaker arrays for local active control of sound," *J. Acoust. Soc. Amer.*, vol. 130, no. 4, pp. 1926–1935, 2011.

[164] D. Kumari and L. Kumar, "Spherical sector harmonics representation of sound fields using a microphone array over spherical sector," *J. Acoust. Soc. Amer.*, vol. 149, no. 1, pp. 145–157, 2021.

[165] R. Duraiswami, Zhiyun L., D.N. Zotkin, E. Grassi, and N.A. Gumerov, "Plane-wave decomposition analysis for spherical microphone arrays," in *Proc. IEEE Workshop Appl. Signal Process. Audio Acoust.*, 2005, pp. 150–153.

[166] F. Zotter and H. Pomberger, "Spherical slepian functions for approximation of spherical measurement data," *Fortschritte der Akustik*, 2012.

[167] H. Pomberger and F. Zotter, "Modal sound field decomposition applicable for a limited range of directions," *Fortschritte Der Akustik, AIA-DAGA*, 2013.

[168] H Pomberger, *Acoustic boundary value problems and their application to partial spherical microphone arrays*, Ph.D. thesis, Ph. D. thesis, University of Music and Performing Arts Graz, Graz, Austria, 2017.

[169] H. Pomberger and F. Pausch, "Design and evaluation of a spherical segment array with double cone," *Acta Acustica united with Acustica*, vol. 100, no. 5, pp. 921–927, 2014.

[170] B. D. Keller and F. Zotter, "A new prototype for sound projection," *Fortschritte Der Akustik-DAGA*, 2015.

[171] D. Kumari and L. Kumar, "$\mathbf{S}^2$H domain processing for acoustic source localization and beamforming using microphone array on spherical sector," *IEEE Trans. Signal Process.*, vol. 69, pp. 1983–1994, 2021.

[172] D. Kumari and L. Kumar, "Optimal beamformer design in spherical sector harmonics domain," *"Appl.Acoust.*, vol. 200, pp. 109070, 2022.

[173] Chibuzo J Nnonyelu, Meng Jiang, and Jan Lundgren, "Spherical-sector harmonics domain processing for wideband source localization using spherical-sector array of directional microphones," *J. Acoust. Soc. Amer.*, vol. 153, no. 3_supplement, pp. A54–A54, 2023.

[174] R. A. Kennedy and P. Sadeghi, *Hilbert space methods in signal processing*, Cambridge University Press, 2013.

[175] J. Stewart, *Calculus*, Cengage Learning, 2015.

[176] H Sun, T. D Abhayapala, and P. N Samarasinghe, "Time domain spherical harmonic analysis for adaptive noise cancellation over a spatial region," in *Proc. IEEE Int. Conf. Acoust., Speech, Signal Process.* IEEE, 2019, pp. 516–520.

[177] H Sun, N Murata, J Zhang, T Magariyachi, P. N. Samarasinghe, S Hayashi, T. D. Abhayapala, and T Itabashi, "Secondary channel estimation in spatial active noise control systems using a single moving higher order microphone," *J. Acoust. Soc. Amer.*, vol. 151, no. 3, pp. 1922–1931, 2022.

[178] F. Ma, W. Zhang, and T. D. Abhayapala, "Active control of outgoing broadband noise fields in rooms," *IEEE/ACM Trans. Audio, Speech, Language Process.*, vol. 28, pp. 529–539, 2019.

[179] J Zhang, W Zhang, T. D Abhayapala, J Xie, and L Zhang, "2.5 d multizone

reproduction with active control of scattered sound fields," in *Proc. IEEE Int. Conf. Acoust., Speech, Signal Process.* IEEE, 2019, pp. 141–145.

[180] J Zhang, W Zhang, T. D. Abhayapala, and L Zhang, "2.5 d multizone reproduction using weighted mode matching: Performance analysis and experimental validation," *J. Acoust. Soc. Amer.*, vol. 147, no. 3, pp. 1404–1417, 2020.

[181] K. He, X. Zhang, S. Ren, and J. Sun, "Deep residual learning for image recognition," in *Proc. IEEE Comput. Soc. Conf. Comput. Vis. Pattern Recognit.*, 2016, pp. 770–778.

[182] A. Voulodimos, N. Doulamis, A. Doulamis, and E. Protopapadakis, "Deep learning for computer vision: A brief review," *Comput. Intell. Neurosci.*, vol. 2018, 2018.

[183] Y. Goldberg, *Neural network methods for natural language processing*, Springer Nature, New York, 2022.

[184] Alex Sherstinsky, "Fundamentals of recurrent neural network (rnn) and long short-term memory (lstm) network," *Phys. D: Nonlinear Phenom.*, vol. 404, pp. 132306, 2020.

[185] P. Dwivedi, G. Routray, and R. M. Hegde, "Octant spherical harmonics features for source localization using artificial intelligence based on unified learning framework," *IEEE Trans. Artif. Intell.*, 2024.

[186] P. Dwivedi, S. B. Hazare, G. Routray, and R. M. Hegde, "Long-term temporal audio source localization using sh-crnn," in *Natl. Conf. Commun.* IEEE, 2023, pp. 1–6.

[187] Z. Luo, D. Shi, W.-S. Gan, and Q. Huang, "Delayless generative fixed-filter active noise control based on deep learning and bayesian filter," *IEEE/ACM Trans. Audio, Speech, Language Process.*, 2023.

[188] Y. LeCun, Y. Bengio, and G. Hinton, "Deep learning," *nature*, vol. 521, no. 7553, pp. 436–444, 2015.

[189] J. Ribeiro, S. Koyama, and H. Saruwatari, "Sound field estimation based on physics-constrained kernel interpolation adapted to environment," *Authorea Preprints*, 2023.

[190] D. Feng, Z. Tan, and Q. He, "Physics-informed neural networks of the saint-

venant equations for downscaling a large-scale river model," *Water Resour. Res.*, vol. 59, no. 2, pp. e2022WR033168, 2023.

[191] J. C. Wong, C. Ooi, A. Gupta, and Y. Ong, "Learning in sinusoidal spaces with physics-informed neural networks," *IEEE trans. artif. intell.*, 2022.

[192] J. Willard, X. Jia, S. Xu, M. Steinbach, and V. Kumar, "Integrating physics-based modeling with machine learning: A survey," *Preprint at arXiv:2003.04919*, vol. 1, no. 1, pp. 1–34, 2020.

[193] H. Robinson, S. Pawar, A. Rasheed, and O. San, "Physics guided neural networks for modelling of non-linear dynamics," *Neural Netw.*, vol. 154, pp. 333–345, 2022.

[194] B. Amos and J. Z. Kolter, "Optnet: Differentiable optimization as a layer in neural networks," in *Proc. Int. Conf. Mach. Learn.* PMLR, 2017, pp. 136–145.

[195] F. de Avila Belbute-Peres, K. Smith, K. Allen, J. Tenenbaum, and J. Z. Kolter, "End-to-end differentiable physics for learning and control," *Adv. Neural Inf. Process. Syst.*, vol. 31, 2018.

[196] J. Ling, A. Kurzawski, and J. Templeton, "Reynolds averaged turbulence modelling using deep neural networks with embedded invariance," *J. Fluid Mech.*, vol. 807, pp. 155–166, 2016.

[197] B. Anderson, T. S. Hy, and R. Kondor, "Cormorant: Covariant molecular neural networks," *Adv. Neural Inf. Process. Syst.*, vol. 32, 2019.

[198] R. R. Selvaraju, M. Cogswell, A. Das, R. Vedantam, D. Parikh, and D. Batra, "Grad-cam: Visual explanations from deep networks via gradient-based localization," in *Proc. IEEE Int. Conf. Comput. Vis.*, 2017, pp. 618–626.

[199] F. Ma, T. D. Abhayapala, P. N. Samarasinghe, and X. Chen, "Physics informed neural network for head-related transfer function upsampling," 2023.

[200] Y. A. Zhang, F Ma, T. D. Abhayapala, P. N. Samarasinghe, and A. Bastine, "An active noise control system based on soundfield interpolation using a physics-informed neural network," in *Proc. IEEE Int. Conf. Acoust., Speech, Signal Process.*, 2024, pp. 506–510.

[201] S. Yoon, Y. Park, P. Gerstoft, and W. Seong, "Predicting ocean pressure field with a physics-informed neural network," *J. Acoust. Soc. Amer.*, vol. 155, no. 3, pp. 2037–2049, 2024.

[202] S. Yoon, Y. Park, P. Gerstoft, and W. Seong, “Physics-informed neural network for predicting unmeasured ocean acoustic pressure field,” *J. Acoust. Soc. Amer.*, vol. 154, no. 4_supplement, pp. A97–A97, 2023.

[203] H. Bi, T. D. Abhayapala, F. Ma, and P. N. Samarasinghe, “Spherical sector harmonics based soundfield radial extrapolation and robustness analysis,” in *Proc. IEEE Int. Conf. Acoust., Speech, Signal Process.* IEEE, 2023, pp. 1–5.

[204] A. Karpatne, G. Atluri, J. H. Faghmous, M. Steinbach, A. Banerjee, A. Ganguly, S. Shekhar, N. Samatova, and V. Kumar, “Theory-guided data science: A new paradigm for scientific discovery from data,” *IEEE Trans. Knowl. Data Eng.*, vol. 29, no. 10, pp. 2318–2331, 2017.

[205] J. B. Allen and D. A. Berkley, “Image method for efficiently simulating small-room acoustics,” *J. Acoust. Soc. Amer.*, vol. 65, no. 4, pp. 943–950, 1979.

[206] E. AP. Habets, “Room impulse response generator,” *Technische Universiteit Eindhoven, Tech. Rep*, vol. 2, no. 2.4, pp. 1, 2006.

[207] R. A. Kennedy, P. Sadeghi, T. D. Abhayapala, and H. M. Jones, “Intrinsic limits of dimensionality and richness in random multipath fields,” *IEEE Trans. Signal Process.*, vol. 55, no. 6, pp. 2542–2556, 2007.

[208] Y. J. Wu and T. D. Abhayapala, “Theory and design of soundfield reproduction using continuous loudspeaker concept,” *IEEE Trans. Audio, Speech, Language Process.*, vol. 17, no. 1, pp. 107–116, 2008.

[209] M. Pastor, M. Binda, and T. Harčarik, “Modal assurance criterion,” *Procedia Eng.*, vol. 48, pp. 543–548, 2012.

[210] D.B. Ward and T.D. Abhayapala, “Reproduction of a plane-wave sound field using an array of loudspeakers,” *IEEE Trans. Audio, Speech, Language Process.*, vol. 9, no. 6, pp. 697–707, 2001.

[211] D. Sarason, *Complex function theory*, American Mathematical Soc., Providence, 2007.

[212] W. Manamperi, T. D. Abhayapala, J. Zhang, and P. N. Samarasinghe, “Estimating drone motor related acoustic transfer function: A preliminary investigation,” in *Proc. Asia-Pacific Signal and Inf. Process. Assoc. Annu. Summit and Conf.* IEEE, 2020, pp. 156–160.

[213] B. Widrow, J. McCool, and M. Ball, “The complex lms algorithm,” *Proc. IEEE*, vol. 63, no. 4, pp. 719–720, Apr. 1975.

[214] G. P. Jones, L. G. Pearlstine, and H. F. Percival, "An assessment of small unmanned aerial vehicles for wildlife research," *Wildl. Soc. Bull.*, vol. 34, no. 3, pp. 750–758, 2006.

[215] T. Zhou and R. Fattah, "Tonal noise characteristics of two small-scale propellers," *AIAA Pap.*, vol. 4054, pp. 2017, 2017.

[216] S. Zhong, P. Zhou, R. Fattah, and X. Zhang, "A revisit of the tonal noise of small rotors," *Proc. R. Soc. Lond. A*, vol. 476, no. 2244, pp. 20200491, 2020.

[217] M. Roger and S. Moreau, "Tonal-noise assessment of quadrotor-type uav using source-mode expansions," in *Acoustics*. Multidisciplinary Digital Publishing Institute, 2020, vol. 2, pp. 674–690.

[218] F. Farassat, *Theory of noise generation from moving bodies with an application to helicopter rotors*, National Aeronautics and Space Administration, 1975.

[219] L. C. Nguyen and J. J. Kelly, "A users guide for the nasa anopp propeller analysis system," Tech. Rep. NASA CR 4768, NASA, Hampton, VA, 1997.

[220] Daniel W Lozier, "Nist digital library of mathematical functions," *Annals of Mathematics and Artificial Intelligence*, vol. 38, no. 1, pp. 105–119, 2003.

[221] A. V. Oppenheim, *Discrete-time signal processing*, Pearson Education India, 1999.

[222] N.P. Samarasinghe, T.D Abhayapala, and M. Poletti, "Wavefield analysis over large areas using distributed higher order microphones," *IEEE/ACM Trans. Audio, Speech, Language Process.*, vol. 22, no. 3, pp. 647–658, 2014.

[223] R. H. Hardin and N. J. Sloane, "Mclaren's improved snub cube and other new spherical designs in three dimensions," *Discrete Comput. Geometry*, vol. 15, no. 4, pp. 429–441, 1996.

[224] A. Christian and R. Cabell, "Initial investigation into the psychoacoustic properties of small unmanned aerial system noise," in *Proceedings of the 23rd AIAA/CEAS Aeroacoustics Conference*, Denver, CO, USA, June 2017.

[225] T. D. Abhayapala, L. Birnie, M. Kumar, D. Grixti-Cheng, and P. N. Samarasinghe, "Generalizing the relative transfer function to a matrix for multiple sources and multichannel microphones," in *Proceedings of the 31st European Signal Processing Conference (EUSIPCO)*, Helsinki, Finland, September 2023, pp. 336–340.